UNIVERSITY OF OKLAHOMA

GRADUATE COLLEGE

ACTIVE GALACTIC NUCLEI

IN THE ULTRAVIOLET SPECTRUM

A DISSERTATION

SUBMITTED TO THE GRADUATE FACULTY

in partial fulfillment of the requirements for the

Degree of

DOCTOR OF PHILOSOPHY

By

ERIN M. COOPER
Norman, Oklahoma
2016

Downloaded from SHAREOK. Persistent Handle URL: https://hdl.handle.net/11244/34702

ACTIVE GALACTIC NUCLEI
IN THE ULTRAVIOLET SPECTRUM

A DISSERTATION APPROVED FOR THE
HOMER L. DODGE DEPARTMENT OF PHYSICS AND ASTRONOMY

BY

Dr. Karen Leighly, Chair

Prof. Karen Antell

Dr. Richard Henry

Dr. Edward Baron

Dr. Xinyu Dai

Dr. Eric Abraham

© Copyright by ERIN M. COOPER 2016
All Rights Reserved.

This is for those who believed in me
at times when I could not believe in myself.

Acknowledgements

I would like to thank, first and foremost, my advisor, Dr. Karen Leighly, for her patience and guidence in both directing and funding my research. I thank also Tarryn Kahre, one of many students involved in the P V absorption project, without whose countless hours of dedication and organization, this project would not have been completed.

To all the countless fellow graduate students I have come to know in my career both before and after me, whose role I thank you in joining and helping me through it all, including the many late, research filled nights.

I thank my committee, my department, and my university for allowing me the opportunity to accomplish such a task.

Most of all, I thank my friends and family for encouraging me in this path, especially when times were tough.

Table of Contents

List of Tables viii

List of Figures ix

Abstract xii

1 Introduction 1
- 1.1 What is an Active Galactic Nucleus (AGN)? . . . 1
- 1.2 AGN in the Ultraviolet . . . 3
  - 1.2.1 Resonance Lines . . . 3
  - 1.2.2 Fe Emission & Eigenvector 1 . . . 5
- 1.3 This Work . . . 5

2 Phosphorus V Broad Absorption in HST Observed AGN 7
- 2.1 Introduction . . . 7
- 2.2 The Data . . . 9
- 2.3 Processing . . . 13
  - 2.3.1 Downloading . . . 13
  - 2.3.2 Extracting and Combining . . . 13
  - 2.3.3 Wavelength Calibration . . . 16
  - 2.3.4 Binning . . . 17
  - 2.3.5 Finalizing Spectra - De-redden & De-redshift . . . 17
- 2.4 Continuum and Emission Modeling . . . 17
  - 2.4.1 Direct Modeling: CIAO Sherpa . . . 18
  - 2.4.2 Composite Modeling: FOS Quasar Composite . . . 18
  - 2.4.3 Intervening Geocoronal Lyα Damping Wings . . . 19
- 2.5 Absorption Modelling . . . 20
  - 2.5.1 Derive Absorption Profile from Ion . . . 20
  - 2.5.2 Apply Absorption Profile to Pv . . . 22
  - 2.5.3 Levels of Detection . . . 24
- 2.6 Results & Discussion . . . 25
  - 2.6.1 Sample Characteristics . . . 25
  - 2.6.2 Validation Check to Combine Ions and Detector Subsamples . . . 39
  - 2.6.3 Comparison with Other Samples . . . 43
- 2.7 Summary & Conclusions . . . 51

3 WPVS007: BAL Variability in a NLS1 Galaxy 52
- 3.1 Introduction . . . 52
- 3.2 Observations . . . 55
  - 3.2.1 HST COS Observations . . . 55
  - 3.2.2 Swift UVOT Observations . . . 58
- 3.3 Analysis . . . 58
  - 3.3.1 Size Scales . . . 59
  - 3.3.2 Absorber Location . . . 67
  - 3.3.3 Occulter Location . . . 68
  - 3.3.4 The Bigger Picture . . . 68

3.4 Summary . . . 70

4 Ultraviolet Iron Emission in Strong Iron Emitting AGN in the SDSS 72
4.1 "Normal" vs. "PHL 1811-like" Emission: The Puzzle . . . 73
4.2 A Thermal Model . . . 74
4.3 Spectral Fitting . . . 78
4.4 Results . . . 85
4.4.1 Departure Coefficients . . . 88
4.5 Comparison to Other Templates . . . 89
4.5.1 Vestergaard & Wilkes: 1Zw1 . . . 89
4.5.2 Bruhweiler & Verner . . . 92
4.6 Conclusions . . . 93

5 Conclusions 94

References 95

Appendices 98

A Acronyms 99

B P V Project: Parameters of Interest and Their Estimated Errors 101
B.1 Direct Parameters . . . 101
B.1.1 log luminosity . . . 101
B.1.2 $v_{min,ION}$, $v_{max,ION}$, and $width_{ION}$ . . . 104
B.1.3 $depth_{ION}$ . . . 106
B.1.4 Measured Values . . . 107
B.2 Derived Parameters . . . 107
B.2.1 $\bar{\tau}_{ION}$ . . . 107
B.2.2 f, $(\tau_{PV} = f * \tau_{ION})$ . . . 112
B.2.3 τ_{PV} . . . 114
B.2.4 $\bar{\tau}_{PV}$ . . . 115
B.2.5 $depth_{PV}$ . . . 115
B.2.6 Measured Values . . . 116

C P V Project: Spectral and τ Profile Data 120

D P V Project: Removed Targets 187
D.1 Slit-less Observations . . . 187
D.2 No Apparent Absorption . . . 187
D.3 Narrow Lines with Un-Physical τ Ratios . . . 187
D.4 Narrow Lines without Partial Covering . . . 188
D.5 O VI BAL blended with Lyα Damping Wings . . . 188
D.6 Other . . . 188

E WPVS007: ISM Line Measurements 189

F WPVS007: Modeling Normalized Flux **194**
F.1 Singlet 194
F.2 Doublet 195
F.2.1 Full Covering, $C_f(v) = 1$ 197
F.2.2 Constant Partial Covering, $C_f(v) = constant$ 198
F.2.3 Non-Constant Partial Covering 200

G Measures of Balnicity **206**
G.1 Balnicity Index 206
G.2 Absorption Index 206
G.3 Detection Index 207

List of Tables

1.1 Resonance Line Data 4

2.1 Target Information 10
2.2 KS test p-value results for the sample absorption properties by ion. 42
2.3 KS test p-value results for the sample absorption properties by detector. . 42
2.4 Summary of P Vincidence in Filiz Ak et al. (2014). 46

3.1 Observation Log 56

4.1 Sample Information. 74
4.2 Upper Level Energy Ranges for Template Partitions. 77
4.3 Fe IIResults: Fraction of the fitted Fe IIflux from each upper level energy bin. 87
4.4 Total Fe Results: Fraction of the fitted Fe flux from each ion, Fe IIand Fe III. 88
4.5 Fe IIlevel contribution compared to Thermal Equilibrium, relative to the lowest upper energy level bin. 89

B.1 Cosmological Parameters from *WMAP* Final Results, Bennett et al. (2013). 102
B.2 Direct Parameters. Measurements not relying on derived optical depth profile.108
B.3 Indirect Parameters. Measurements requiring derived optical depth profile. 117

E.1 WPVS007 HST COS June 2010 ISM Line Measurements 190
E.2 WPVS007 HST COS June 2013 ISM Line Measurements 191
E.3 WPVS007 HST COS December 2013 ISM Line Measurements 192
E.4 WPVS007 HST COS March 2015 ISM Line Measurements 193

F.1 Resonance Line Data 196

List of Figures

1.1 Anatomy of an AGN 2

2.1 Derivation of τ profile: PG 1254+047 23
2.2 Log Width vs. Log v_{max} 27
2.3 Log v_{max} vs. Maximum Depth 28
2.4 Log Width vs. Maximum Depth 29
2.5 $\bar{\tau}$ vs. Maximum Depth 31
2.6 $\bar{\tau}$ vs. v_{max} 32
2.7 Log v_{max} vs. Log Luminosity at 1121Å 34
2.8 v_{max} vs. Log λ Luminosity at 1121Å 36
2.9 Log Luminosity at 1121Å vs. Maximum Depth 37
2.10 $\bar{\tau}$ vs. Log Luminosity at 1121Å 38
2.11 depth_{PV} vs. Log $\bar{\tau}_{PV}$ 40
2.12 depth_{PV} and $\bar{\tau}_{PV}$ vs. v_{max} and width 41
2.13 Cumulative histograms of subsample properties by ion. 44
2.14 Cumulative histograms of subsample properties by detector. 45
2.15 Histogram of monochromatic luminosities in comparison to other samples. 48
2.16 Histogram of redshifts in comparison to other samples. 49
2.17 Histogram of maximum velocities in comparison to other samples 50

3.1 HST COS Observations 57
3.2 Swift UVOT Observations: UVM2 and E(B − V) 60
3.3 Swift UVOT Observations: color-magnitude plots 61
3.4 Combined HST spectra and Swift photometry 62
3.5 Size Scales 64
3.6 Simultaneous continuum fitting, powerlaw + emission line lorentzians . . 66
3.7 Cartoon of variability implied by WPVS007 69

4.1 Fe Shape Examples: Typical vs. PHL 18111-like 75
4.2 Fe II Models and A_{ki}s separated by upper level energy of transition. . . . 79
4.3 Fe III Models and A_{ki}s separated by upper level energy of transition. . . . 80
4.4 Ni II Models and A_{ki}s separated by upper level energy of transition. . . . 81
4.5 Ni III Models and A_{ki}s separated by upper level energy of transition. . . . 82
4.6 Spectral Fits: Typical Fe Shape 83
4.7 Spectral Fits: PHL 1811-like Fe Shape 84
4.8 Spectral Fits: Fe II Breakdown 86
4.9 Spectral Fits: 1Zw1 Fe II and Fe III Breakdown 90
4.10 Spectral Fits: Comparison Models Fe II Breakdown 91

C.1 FIRST-J020930.7-043826 121
C.2 HS-0033+4300 122
C.3 IRAS-F22456-5125 123
C.4 RBS542 124
C.5 IRAS13349+2438 125
C.6 NGC520.40 126
C.7 PG1114+445 127

C.8 IRAS11598-0112 . . . 128
C.9 PG1001+054 . . . 129
C.10 PG1322+659 . . . 130
C.11 SDSSJ13205941+295728.1 . . . 131
C.12 SDSSJ093653.84+533126.8 . . . 132
C.13 SDSSJ001224.01-102226.5 . . . 133
C.14 SDSSJ075620.08+304535.3 . . . 134
C.15 SDSSJ120944.81+023212.7 . . . 135
C.16 SDSSJ092837.98+602521.0 . . . 136
C.17 3C57 . . . 137
C.18 3C207 . . . 138
C.19 Q2208-1720 . . . 139
C.20 Q1239+0028 . . . 140
C.21 HE0436-2614 . . . 141
C.22 1714+5757 . . . 142
C.23 PG0946+301 . . . 143
C.24 3C351.0 . . . 144
C.25 PKS2251+11 . . . 145
C.26 HE0238-1904 . . . 146
C.27 PG2112+059 . . . 147
C.28 QSO-1431+3952 . . . 148
C.29 PG1404+226 . . . 149
C.30 4C40-24 . . . 150
C.31 0110+0019 . . . 151
C.32 1306+3021 . . . 152
C.33 HE0409-5004 . . . 153
C.34 MC1146+111 . . . 154
C.35 SDSSJ110312.93+414154.9 . . . 155
C.36 SDSSJ095000.73+483129.3 . . . 156
C.37 SDSSJ080359.23+433258.4 . . . 157
C.38 SDSSJ121037.56+315706.0 . . . 158
C.39 SDSSJ100902.06+071343.8 . . . 159
C.40 4C63.22 . . . 160
C.41 SDSSJ143511.53+360437.2 . . . 161
C.42 SDSSJ134206.56+050523.8 . . . 162
C.43 3C196.0 . . . 163
C.44 1225-0052 . . . 164
C.45 3C288.1 . . . 165
C.46 PG2302+029 . . . 166
C.47 MC1118+12 . . . 167
C.48 SDSSJ161916.54+334238.4 . . . 168
C.49 SDSSJ111754.31+263416.6 . . . 169
C.50 PKS0454-22 . . . 170
C.51 SDSSJ133053.27+311930.5 . . . 171
C.52 SDSSJ094733.21+100508.7 . . . 172
C.53 RXJ0439.6-5311 . . . 173
C.54 PG1309+355 . . . 174
C.55 SDSSJ115758.72-002220.8 . . . 175

C.56 SDSSJ122534.79-024757.1 176
C.57 PG1115+407 177
C.58 RXJ1230.8+0115 178
C.59 IOandQSO0045+3926 179
C.60 3C186 180
C.61 PKS1004+130 181
C.62 1631+3930 182
C.63 SDSSJ015530.02-085704.0 183
C.64 CT344 184
C.65 PG0804+761 185
C.66 PG 1254+47 186

Abstract

Active Galactic Nucleus (AGN) produce rich, luminescent spectra across the electromagnetic spectrum. This work focuses on topics in the ultraviolet region, where lie the broad absorption line outflows innate to Broad Absorption Line Quasi-Stellar Objects (BALQSOs) and the Fe II bump, characteristic of strong Fe emitters.

We find the incidence of P V absorption in AGN to be $\sim 10\%$ and only observe P V absorption in Broad Absorption Lines (BALs), never in narrow lines. Our troughs exhibit envelope behavior in v_{max} versus Luminosity, as previously observed, with P V detected troughs forming the upper edge of the envelope.

The spectral and photometric variabilities in the low luminosity, narrow line Seyfert 1 galaxy WPVS007 are consistent with the BAL wind ablating off the edge of a variable scale height torus. WPVS 007 underwent the first ultraviolet occultation yet observed for an AGN.

The differences in ultraviolet spectral shape of the Fe emission shape observed in strong Fe emitting AGN is attributable to higher excitation Fe II and excess Fe III in PHL1811-like objects, but photoionization is not sufficient to fit the observed emission.

Chapter 1

Introduction

1.1 What is an Active Galactic Nucleus (AGN)?

Active Galactic Nucleus (AGN) are some of the most distant (up to $z \approx 6$), luminous (on the order of $10^{12} L_{\odot}$) objects in the observable universe (Osterbrock & Ferland (2006)). Thought to be powered by the active accretion of matter onto a central supermassive black hole, AGN are considered remarkable for their luminescence across the entire electromagnetic spectrum, often outshining their host galaxy.

The anatomy of an AGN resembles that in figure 1.1. The central supermassive black hole is surrounded by an accretion disk, actively accreting matter, transforming gravitational potential energy into radiation and kinetic energy. The X-ray corona is a sea of hot electrons that can Compton up-scatter photons from the accretion disk into the X-ray band. Jets may form in the polar regions and transport energy and momentum into what appear as extended radio lobe features, though not all AGN exhibit radio jets and may exhibit only weak X-ray emission. The broad line region consists of clumps of matter reprocessing continuum emission into line emission radiation. The narrow line region lies at a greater radius and thus experiences less Doppler broadening. Its lines therefore appear narrower, but the processes are the same. A thick, dusty torus surrounds the central engine.

Roughly $10 - 20\%$ of optically observed AGN present outflowing winds, observed as blue-shifted broad absorption lines (e.g. Gibson et al. (2009), Pâris et al. (2012),

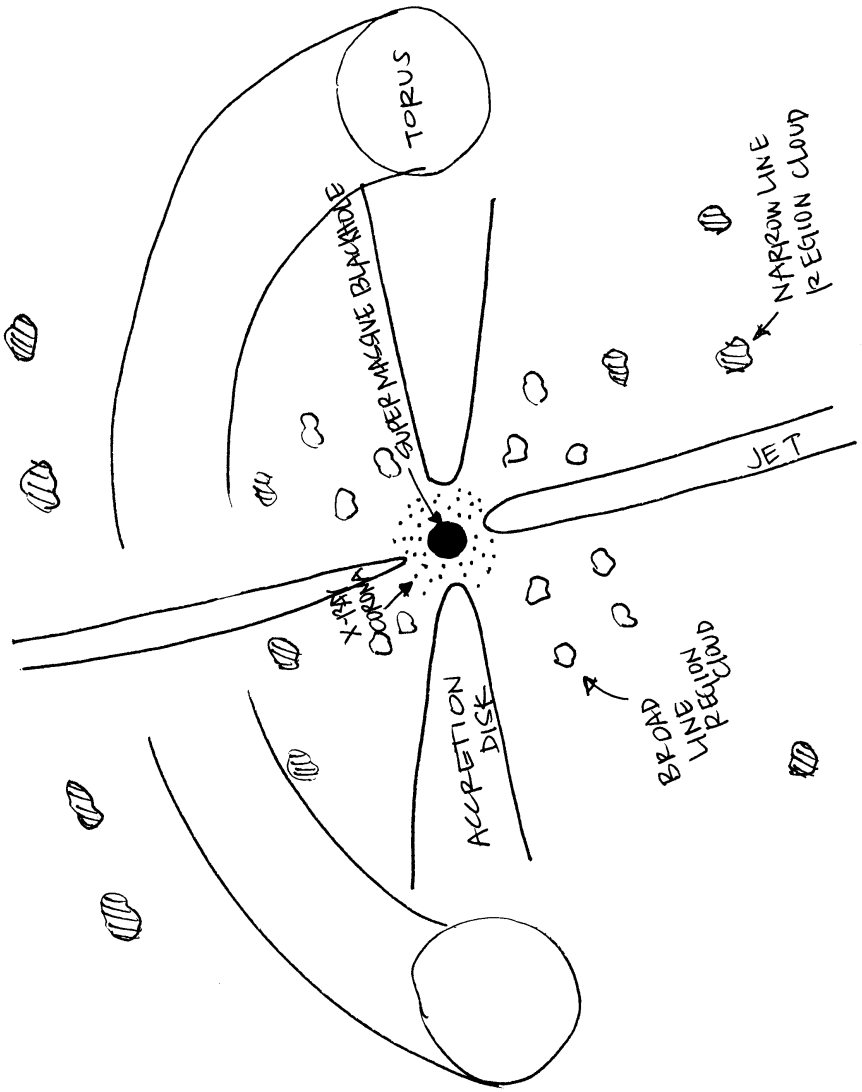

Figure 1.1: Anatomy of an AGN.

Pâris et al. (2014)). The fraction is substantially higher when considering radio observed AGN, upwards of $\sim 40\%$ (e.g. Dai et al. (2008) and Shankar et al. (2008)). Such outflows potentially aid galactic evolution by imparting energy, momentum, and chemically enriched gas to the surrounding galaxy. They also serve as a possible feedback mechanism that drives the co-evolution of the black hole mass and the host galaxy stellar bulge (as evidenced by the $M - \sigma$ relation, e.g. Ferrarese & Merritt (2000)). The stellar bulge lies outside the sphere of influence of the black hole, therefore some method of communication is required to explain the co-evolution.

1.2 AGN in the Ultraviolet

While AGN are notable for their significant emission across the electromagnetic spectrum, this work focuses on features in the ultraviolet portion of the spectrum.

1.2.1 Resonance Lines

Broad absorption lines are most often identified in the UV resonant doublet C IV $\lambda\lambda 1548, 1551$Å and also observed in other nearby resonant doublet features, described in table F.1.

These lines share the common theme of their ionic species having a single valence electron, and therefore being isoelectronic with neutral lithium (C^{+3}, N^{+4}, and O^{+5}, ground state: $1s^2s$) or sodium (Si^{+3} and P^{+4}, ground state: $1s^22s^22p^63s$). As a result, their resonant transitions arise from the same levels. The ground state term for these ions is all ${}^2S_{\frac{1}{2}}$ and the upper level terms of the doublet transitions are all ${}^2P^o_{\frac{3}{2}}$ and ${}^2P^o_{\frac{1}{2}}$. These are the D_1 and D_2 lines, first observed in neutral sodium in the

λ(Å)	f_{ij}	τ_b/τ_r
O VI		
1031.912	0.133	2.00
1037.613	0.0660	
P V		
1117.98	0.450	2.02
1128.01	0.221	
N V		
1238.821	0.156	1.99
1242.804	0.0780	
Si IV		
1393.76	0.513	2.00
1402.77	0.255	
C IV		
1548.202	0.190	1.99
1550.774	0.0952	

Table 1.1: Resonance Line Data

Fraunhofer spectrum of the sun. For the rest of this work, we refer to the short wavelength of the doublet, D_1, as the blue line and its counterpart, D_2, as the red line.

For an absorption line, the optical depth, τ, is related to the column density (number of paricles per unit area), N, by: $\tau \propto f\lambda N$, where f is the oscillator strength and λ is the wavelength of the transition. The ratio τ_b/τ_r is therefore equal to the ratio $f_b\lambda_b/f_r\lambda_r$ and for these resonant lines, that ratio between the doublet lines is ~ 2 (blue:red). While atomic physics tells us the true theoretical ratio is always 2:1, the apparent ratio can be reduced to as low as 1:1 due to the effects of partial covering (see appendix F). Knowing the apparent ratio allows us to deconvolve the doublet absorption line profile.

Because C^{+3} is a common ion in the gas, the C IV absorption line profile can

easily become saturated. When the profile becomes saturated, we lose information and are only able to derive lower limits on the column density. In this scenario, less abundant ions, such as P^{+4} can be important tracers of the real column density in the gas.

1.2.2 Fe Emission & Eigenvector 1

Additionally, this work explores the UV Fe emission pseudo-continuum, a densely packed region of overlapping emission lines forming an almost continuum, between the Si II, Al III, C III emission complex near 1909Å and the Mg II resonant doublet $\lambda\lambda 2798, 2803$Å as it relates to strong and peculiarly emitting Fe AGN from the Sloan Digital Sky Survey (SDSS). With its vast catalog of possible transitions, Fe can be an important coolant of the broad emission line gas. Optical Fe emission line strength contributes to the relationships in the Boroson & Green (1992) eigenvector 1, along with the [O III] 5007Å intensity and the full width at half maximum broad line component of Hβ. Leighly et al. (2007) identified two shapes of ultraviolet Fe emission in strong Fe emitting AGN, one arising from normal Fe II emission, the other from potentially excited Fe II and additional Fe III emission.

1.3 This Work

The studies in this work are broken into three parts. Chapter 2 explores the incidence of P V absorption in Hubble Space Telescope (HST) observed AGN as well as properties of the absorption profiles in companion ions: Si IV, C IV, and O VI. Chapter 3 explains the broad absorption and emission line variability from HST

Cosmic Origins Spectrograph (COS) observations and Swift UV-optical Telescope (Swift UVOT) photometric variability in the low luminosity, narrow line Seyfert 1 galaxy WPVS007. Chapter 4 uses the catalog of Fe emission lines in the Kurucz & Bell (1995) database to probe the differences in Fe emission among the two classes of strong Fe emitting AGN, identified in Leighly et al. (2007).

Chapter 2

Phosphorus V Broad Absorption in HST Observed AGN

2.1 Introduction

Galaxies and their AGN are known to experience a shared evolution, evidenced by the observed correlation of central black hole mass with bulge stellar velocity dispersion or bulge luminosity Ferrarese & Merritt (2000). However, how this shared evolution proceeds is still not well known. One possible mechanism for this interaction is via feedback, observed as blue-shifted absorption lines in AGN spectra. These outflowing winds are crucial to AGN physics and galaxy evolution in that they can potentially carry away angular momentum, thereby facilitating the accretion thought to power the central engine, as well as drive both chemically enriched gas (Cavaliere et al. (2002)) and kinetic energy (Scannapieco & Oh (2004)) into the host galaxy, thereby influencing its evolution.

But what drives the outflow? One popular and potentially obvious mechanism is acceleration via radiative line driving. Ionic species absorb line radiation preferentially in the outward direction, but emit in random ones, thereby driving the gas outward. A link between maximum outflow velocity and luminosity has been shown (Laor & Brandt (2002), Ganguly & Brotherton (2008)), giving credence to radiative line driving as a viable model.

To support bulge-black hole co-evolution via feedback, current models (Hopkins

& Elvis (2010)) require $0.5-5\%$ kinetic energy luminosity as a fraction of bolometric luminosity. The kinetic energy luminosity is related to the outflow column density, which can itself be difficult to constrain. Most BALQSOs are identified via C IV absorption; however, because both C^{+3} is a common ion and the C IV $\lambda\lambda 1548, 1551$Å doublet transition has a high opacity, C IV is easily saturated. Once a line becomes saturated, a substantial increase in column density will lead to little if any change in the line profile and therefore only a lower limit can be measured. One solution to the saturation problem is the use of rare ions, such as P^{+4}, which has a resonant UV doublet transition at P V $\lambda\lambda 1118, 1128$Å. Phosphorous has an abundance $\sim 1,000\times$ lower than carbon (Anders & Grevesse (1989)) and is therefore much less likely to saturate, even for high column density outflows.

We study a sample of 66 HST Faint Object Spectrograph (FOS), Space Telescope Imaging Spectrograph (STIS), and COS observed AGN from the Barbara A. Mikulski Archive for Space Telescopes (MAST) for P V absorption and outflow properties. This is the first study of its kind because no such large quantitative study of P V has yet been performed. Although Filiz Ak et al. (2014) and Hamann et al. (2012) comment on the incidence of P V absorption in SDSS observed quasars. By utilizing HST observations, we probe a lower redshift and lower luminosity sample than the SDSS, as evidenced by comparison with Gibson et al. (2009) and Filiz Ak et al. (2014) in figures 2.15 and 2.16. Both to facilitate our search for P V absorption and to measure the upper limit on how much absorption could hide within the noise and not be detected, we require nearby Si IV $\lambda\lambda 1394, 1403$Å, C IV $\lambda\lambda 1548, 1551$Å or O VI $\lambda\lambda 1032, 1038$Å to fall within the observed bandpass and show evidence

for absorption. Where absorption occurs in these ions, we derive an optical depth profile from the respective ion and apply it to the P V region in order to measure the potential absorption present.

2.2 The Data

OU graduate student Aaron Morris started narrowing the possible data selection on this project by downloading the entire HST catalog of FOS, STIS and COS observations, observed as of May 2013, and removing any objects not qualifying as an AGN. The next cut removed any targets where the observed frame wavelengths did not include rest frame coverage of the P V ($\lambda\lambda 1118, 1128$Å) doublet and at least one of Si IV ($\lambda\lambda 1394, 1403$), C IV ($\lambda\lambda 1548, 1551$), or O VI ($\lambda\lambda 1032, 1038$). For a target to be included in our sample, it had to meet one of the following criteria: 1) visible Si IV, C IV, or O VI absorption in the MAST archive preview spectrum, 2) multiple observations so that absorption in one of these ions might be possible if combined to improve the signal-to-noise ratio (SNR), or 3) independent confirmation of absorption in the literature. Our final sample contains 66 targets with redshifts $\sim 0.1 - 1.3$. Target information is given in table B.2.6. Some targets have been removed from our sample for various reasons, described in Appendix D. Three undergraduate students have been involved in the data processing and spectral modeling of this project: Kenya Davis (REU Summer 2013), Tarryn Kahre (REU Summer 2014, UGRA Fall 2013 - Fall 2015), and Adam Marrs.

Table 2.1: Target Information

TARGET[a]	NED Primary Name[b]	RA	DEC	z	RL/RQ[c]	ion[d]
SDSSJ001224.01-102226.5	FBQS J0012-1022	00 12 24.01	−10 22 26.5	0.229	RL	Si IV
HS-0033+4300	GALEXASC J003623.07+431640.8	00 36 22.980	+43 16 40.30	0.12	RQ	C IV
IOandQSO0045+3926	IO And	00 48 18.986	+39 41 11.64	0.134	RQ	C IV
CT344	LBQS 0103-2753	01 05 34.77	−27 36 58.40	0.834	RQ	Si IV
0110+0019	SDSS J011056.89+001912.0	01 10 56.938	+00 19 11.21	0.805986	RQ	C IV
NGC520.40	GALEXASC J211427.71+035305.8	01 24 57.585	+03 53 48.18	1.202	RQ	Si IV
SDSSJ015530.02-085704.0	SDSS J015530.01-085704.0	01 55 30.0	−08 57 04	0.164427	RQ	C IV
3C57	3C 057	02 01 57.2	−11 32 33	0.6705	RL	Si IV
SDSSJ080359.23+433258.4	2MASSi J0803592+433258	02 03 59.23	+43 32 58.4	0.4487	RQ	O VI
FIRST-J020930.7-043826	FBQS J0209-0438	02 09 30.743	−04 38 26.27	1.128	RL	O VI
HE0238-1904	2MASSi J0240325-185151	02 40 32.5	−18 51 51	0.631	RQ	O VI
HE0409-5004	GALEXASC J041100.92-495656.2	04 11 00.8	−49 56 56.00	0.817	RQ	C IV
RBS542	GALEXASC J042600.66-571200.9	04 26 00.777	−57 12 01.13	0.104	RL	Si IV
HE0436-2614	2MASSi J0438101-260837	04 38 10.1	−26 08 37	0.69	RQ	Si IV
RXJ0439.6-5311	6dF J0439387-531131	04 39 38.7	−53 11 31	0.243	RQ	O VI
PKS0454-22	[HB89] 0454-220	04 56 08.9	−21 59 09	0.5335	RL	Si IV
3C186	FBQS J074417.4+375317	07 44 17.4	+37 53 17	1.067	RL	C IV
SDSSJ075620.08+304535.3	SDSS J075620.07+304535.4	07 56 20.08	+30 45 35.3	0.2361	RQ	C IV
PG0804+761	PG 0804+761	08 10 58.6	+76 02 43	0.1	RL	C IV
3C196.0	3C 196	08 13 36.0	+48 13 03.00	0.871	RL	O VI
3C207	3C 207	08 40 47.6	+13 12 24	0.6808	RL	Si IV
SDSSJ092837.98+602521.0	SBS 0924+606B	09 28 37.98	+60 25 21.0	0.2954	RL	Si IV

Continued on next page

[a] target name from the HST MAST Archive
[b] target primary as resolved in NED
[c] identifies whether the target has ever been classified as any type of radio galaxy in NED (RL, radio loud for yes; RQ, radio quiet for no)
[d] the ion from which we derived an optical depth profile to apply to the P V region

Table 2.1 – *Continued from previous page*

TARGET[a]	NED Primary Name[b]	RA	DEC	z	RL/RQ[c]	ion[d]
SDSSJ093653.84+533126.8	SDSS J093653.84+533126.8	09 36 53.86	+53 31 26.87	0.2277	RQ	Si IV
SDSSJ094733.21+100508.7	2MASX J09473320+1005093	09 47 33.216	+10 05 08.88	0.13954	RQ	O VI
4C40-24	FBQS J094855.3+403944	09 48 55.330	+40 39 45.00	1.249964	RL	O VI
PG0946+301	PG 0946+301	09 49 41.106	+29 55 19.12	1.223448	RQ	Si IV
SDSSJ095000.73+483129.3	SDSS J095000.73+483129.3	09 50 00.73	+48 31 29.3	0.5887	RQ	O VI
PG1001+054	PG 1001+054	10 04 20.1	+05 13 00	0.161076	RQ	C IV
PKS1004+130	PG 1004+130	10 07 26.090	+12 48 56.20	0.2408	RQ	O VI
SDSSJ100902.06+071343.8	SDSS J1009+0713	10 09 02.06	+07 13 43.8	0.4556	RQ	O VI
SDSSJ110312.93+414154.9	2MASS J11031293+4141549	11 03 12.93	+41 41 54.9	0.4019	RQ	O VI
PG1114+445	PG 1114+445	11 17 06.390	+44 13 33	0.143862	RQ	C IV
SDSSJ111754.31+263416.6	TON 0576	11 17 54.31	+26 34 16.6	0.4205	RQ	O VI
PG1115+407	PG 1115+407	11 18 30.3	+40 25 54	0.154338	RL	C IV
MC1118+12	[HB89] 1118+128	11 21 29.7	+12 36 17	0.6836	RL	C IV
MC1146+111	[HB89] 1146+111E	11 48 47.894	+10 54 59.44	0.861	RL	C IV
SDSSJ115758.72-002220.8	SDSS J115758.72-002220.7	11 57 58.72	−00 22 20.8	0.2602	RQ	C IV
IRAS11598-0112	2MASX J12022678-0129155	12 02 26.750	−01 29 15	0.150694	RL	O VI
SDSSJ120944.81+023212.7	SDSS J120944.81+023212.6	12 09 44.81	+02 32 12.7	0.2384	RQ	O VI
SDSSJ121037.56+315706.0	SDSS J121037.56+315706.0	12 10 37.56	+31 57 06.0	0.389	RQ	O VI
SDSSJ122534.79-024757.1	SDSS J122534.79-024757.0	12 25 34.8	−02 47 57	0.1952	RQ	C IV
1225-0052	SDSS J122558.44-005226.1	12 25 58.4	−00 52 27.05	0.9631	RQ	C IV
RXJ1230.8+0115	SDSS J123050.03+011522.6	12 30 50.040	+01 15 21.70	0.117	RQ	C IV
Q1239+0028	LBQS 1239+0028	12 42 02.660	+00 12 28.50	1.217243	RQ	Si IV

Continued on next page

[a] target name from the HST MAST Archive
[b] target primary as resolved in NED
[c] identifies whether the target has ever been classified as any type of radio galaxy in NED (RL, radio loud for yes; RQ, radio quiet for no)
[d] the ion from which we derived an optical depth profile to apply to the P V region

Table 2.1 – *Continued from previous page*

TARGET[a]	NED Primary Name[b]	RA	DEC	z	RL/RQ[c]	ion[d]
PG 1254+047	PG 1254+047	12 56 59.9	+04 27 34	1.025584	RQ	Si IV
1306+3021	[HB89] 1306+303	13 08 29.69	+30 05 39.00	0.8077	RQ	C IV
PG1309+355	FBQS J131217.7+351521	13 12 17.8	+35 15 21	0.1829	RL	C IV
SDSSJ13205941+295728.1	2MASX J02001261+0300114	13 20 59.41	+29 57 28.1	0.2064	RQ	Si IV
PG1322+659	PG 1322+659	13 23 49.5	+65 41 48	0.168	RQ	O VI
SDSSJ133053.27+311930.5	[HB89] 1328+315	13 30 53.27	+31 19 30.5	0.2422	RQ	O VI
IRAS13349+2438	[HB89] 1334+246	13 37 18.718	+24 23 02.95	0.107641	RL	C IV
SDSSJ134206.56+050523.8	[HB89] 1339+053	13 42 06.56	+05 05 23.8	0.266	RL	O VI
3C288.1	SBS 1340+606	13 42 13.24	+60 21 42.8	0.9645	RL	C IV
PG1404+226	PG 1404+226	14 06 21.900	+22 23 46.90	0.098	RL	C IV
QSO-1431+3952	FBQS J143120.5+395241	14 31 20.420	+39 52 40.07	1.217032	RL	O VI
SDSSJ143511.53+360437.2	SDSS J1435+3604	14 35 11.53	+36 04 37.2	0.4286	RQ	O VI
4C63.22	4C +63.22	15 23 45.9	+63 39 24	0.204	RL	O VI
SDSSJ161916.54+334238.4	SDSS J1619+3342	16 19 16.54	+33 42 38.4	0.4709	RQ	O VI
1631+3930	FBQS J163302.0+392427	16 33 02.19	+39 24 27.20	1.024575	RL	C IV
PG1700+518	[HB89] 1700+518	17 01 24.8	+51 49 20	0.292	RL	Si IV
3C351.0	SBS 1704+608	17 04 41.4	+60 44 31	0.3719	RL	C IV
1714+5757	SDSS J171413.39+575711.0	17 14 13.409	+57 57 11.16	1.252755	RQ	O VI
PG2112+059	[HB89] 2112+059 NED01	21 14 52.6	+06 07 42	0.466	RQ	C IV
Q2208-1720	LBQS 2208-1720	22 11 15.415	−17 05 25.84	1.21	RQ	Si IV
IRAS-F22456-5125	2MASX J22484165-5109338	22 48 41.204	−51 09 53.15	0.1016	RQ	Si IV
PKS2251+11	[HB89] 2251+113	22 54 10.4	+11 36 38	0.3255	RL	Si IV
PG2302+029	[HB89] 2302+029	23 04 45.0	+03 11 46	1.044	RQ	C IV

[a] target name from the HST MAST Archive
[b] target primary as resolved in NED
[c] identifies whether the target has ever been classified as any type of radio galaxy in NED (RL, radio loud for yes; RQ, radio quiet for no)
[d] the ion from which we derived an optical depth profile to apply to the P V region

2.3 Processing

2.3.1 Downloading

The first task in processing the data is to obtain the target spectra from the MAST archive. This is done by querying the archive database and submitting a request for the relevant data and reference files. All requested STIS and COS observations were re-calibrated on the fly through the most up-to-date version of the relevant pipeline, CALSTIS and CALCOS, respectively, with the most up-to-date reference files by the archive prior to being made available for download following a request. The FOS instrument was removed from HST in 1997 and all archived observations were re-calibrated with the improved FOS pipeline, POA_CALFOS, by the Post-Operational Archives (POA) branch of the Space Telescope - European Coordinating Facility (ST-ECF) and placed in the HST archive in 2004. Once the request is fulfilled, the files were downloaded from the FTP server at Space Telescope Science Institute (STScI), `stdatu.stsci.edu`.

2.3.2 Extracting and Combining

Although all of the calibrated 1D spectra are stored in Flexible Image Transport System (FITS) files, the method of extracting the data from those files and combining them into one spectrum depends on the instrument from which the observations originate. A number of our objects have a Higher Level Science Product (HLSP), i.e. a combined spectrum, in the MAST Archive. We use these HLSP files in place of our own processed spectra whenever possible.

Information in FOS observed spectra are stored in separate FITS image files for wavelength, flux, and statistical error, each containing a matrix of values where each row is a separate time interval. FOS has two observing modes, ACCUM and RAPID. The time intervals of ACCUM mode observations are cumulative and so the final spectrum is simply the last row of the matrix. The vast majority of FOS targets are observed in ACCUM mode. Some objects were observed in RAPID mode. The time intervals of RAPID mode observations are independent and each row must be combined to produce the final spectrum. Because the time intervals are short, the individual observations making up a RAPID mode spectrum are photon limited. All 5 targets to which this situation applies have a HLSP available from MAST, and we use those pre-combined spectra. If a FOS target has multiple observations we add them, weighting by SNR^2, and propagate the errors accordingly. For observations with a sufficient number of photons weighting by SNR^2 is akin to weighting by the exposure time, since the noise scales with $\sqrt{\mathrm{exposure\,time}}$.

Spectral information in STIS files are stored as FITS tables. For most of these targets, the spectra were extracted and combined in the same way as described for FOS multiple observation targets, weighting by SNR and propagating the errors accordingly. A few of our STIS observed targets have echelle spectra, which must be handled separately using the prescription outlined in the STIS Data Handbook and Python-based interface to the Image Reduction and Analysis Facility (IRAF) (PyRAF). The images are first flagged with a 10-pixel border (PyRAF utility `imcalc`) to compensate for vignetting at the edge of the detector and a new 1D extraction (PyRAF utility `x1d`) is performed. The new 1D extracted spectra were combined

using the PyRAF utility `splice`.

COS observed spectra are also stored as FITS tables. The COS instrument has two detectors, one for Near UltraViolet (NUV) and one for Far UltraViolet (FUV), each with a variety of dispersion gratings. Each grating has a variety of central wavelength positions, which move the slit image across the detector in the dispersion direction in order to extend the wavelength coverage of an observation. At any of these settings, the instrument has four nod positions which shifts the slit image slightly to 1) compensate for fixed patterned noise in the detector and 2) reduce the long term damaging effects of exposing the detector to geocoronal $Ly\alpha$. The combining of COS spectra for the same configuration using different nod positions is done by the calibration pipeline. The combining of any other observation configurations must be done in post-processing. We use the same method as described for FOS multi-observation targets and STIS multi-observation, non-echelle targets. The COS FUV data are separated into two segments (two separate images) and the NUV data are separated into three stripes (in a single image). To avoid gaps in the combined spectrum during processing, we combine COS data in wavelength order starting with 1) different central wavelengths of the same grating, segment/stripe and detector, 2) different gratings of the same segment/stripe and detector, 3) different segments/stripes of the same detector, and 4) different detectors.

Many targets have observations from multiple instruments, but we were unable to combine the data into one final spectrum for a variety of reasons. First, observations from multiple instruments are unlikely to be simultaneous and if the target is variable over the time between observations, the spectra are likely to be different. Second,

not all of the multi-instrument observations will have the same wavelength coverage. For some objects we will use data from different instruments for different ions, due to the constraints of the wavelength coverage. Finally for some multi-instrument observations, the combination of the spectra may significantly compromise the SNR.

2.3.3 Wavelength Calibration

Once the data have been combined, we need to evaluate the overall wavelength calibration. To do this, we first plot the individual spectra that make up the combined spectrum for the regions that narrowly cover our catalog of Interstellar Medium (ISM) absorption lines as well as their rest wavelengths from the National Institutes of Standards and Technology (NIST) database. If an individual spectrum varies significantly from the rest wavelength in all its ISM lines, then a shift is made to correct it. So far, no targets have required shifts in an individual observation. If all the individual spectra, and hence the combined spectrum, differs significantly in the same direction in all its ISM lines from the NIST rest wavelength, we measure the observed wavelengths of the ISM lines, then compute and apply an appropriate shift. We use the general rule of thumb that if the spectrum deviates by more than ~ 0.1Å, a shift should be applied. This has been the case for a few spectra.

Should a shift be required, we use the Chandra Interactive Analysis of Observations (CIAO) spectral modeling and fitting application Sherpa to measure the position, velocity width, and optical depth of the individual ISM lines in the spectrum to be shifted. We use the ISM line measurements to evaluate whether a linear or constant shift is more appropriate and shift the data accordingly.

2.3.4 Binning

COS spectra are over sampled and require binning to bring the spectra to the standard two bins per resolution element. We use the median bin size of the data compared to the size of the resolution element for the configuration to determine how many bins should be combined to produce the required spectrum. For most COS spectra, three bins are combined to produce the required resolution.

2.3.5 Finalizing Spectra - De-redden & De-redshift

The final steps in processing data for analysis are to correct for reddening due to extinction along the line of sight in our own galaxy and to correct for cosmological redshift to bring the spectrum into its rest frame. We obtain the target redshifts and E(B-V) reddening parameters from the NASA/IPAC Extragalactic Database (NED) (`https://ned.ipac.caltech.edu`) and correct for galactic reddening using the Cardelli et al. (1989) reddening curve (the `ccm_unred` utility in Interactive Data Language (IDL)).

2.4 Continuum and Emission Modeling

In order to analyze the absorption, we must first remove the contribution of the continuum and line emission flux. In most targets we can readily identify the level of the continuum and line emission. However, for a handful of targets the absorption is so extensive we can only set the level of the continuum with the aid of a template or composite spectrum. Because it is derived from HST FOS quasars, we choose to

use the FOS Quasar Composite Spectrum of Zheng et al. (1997).

2.4.1 Direct Modeling: CIAO Sherpa

For most targets in our sample we can readily see the level of the continuum and line emission. We use the CIAO modeling and fitting application, Sherpa (CIAO 4.5 Sherpa v1). To model the continuum, we fit a power law to line-free regions of the spectrum and add gaussian components to fit the line emission regions, ignoring the absorption contaminated regions. The final fit is achieved when the change in fit statistic (`chi2gehrels`) reaches zero between iterations. We propagate the 1σ confidence intervals (results of the Sherpa functions `conf` or `covar`) through the model in IDL to generate the error spectrum of the final fit.

2.4.2 Composite Modeling: FOS Quasar Composite

Targets in our sample with a considerable amount of absorption pose a challenge to modeling the continuum directly and require a different approach. For these targets, we use the FOS Quasar Composite of Zheng et al. (1997) to aid continuum placement. As with the other targets, we model the continuum and line emission of the FOS Composite in CIAO Sherpa. When applying the composite, we scale the emission peak to the emission peak of the data in the region, e.g. in the vicinity of Si IV, C IV, or O VI, and tilt the power law continuum, by stepping through new values of the power law index, to best fit the continuum of the data. We determine the best fit, lower and upper bounds, on the new power law index using a minimum χ^2 method for regions appearing to be free of absorption. As with the direct modeling

approach, we propagate the estimated uncertainties to generate the error spectrum of the final fit. The estimated uncertainties arise from the uncertainty associated with scaling the template to the data and determining the new tilt. We assume that there are no statistical or systematic errors in the FOS Composite, and therefore exclude the uncertainties associated with the 1σ confidence intervals from fitting the FOS Composite in Sherpa.

Because the estimated error in the FOS Composite arise from the real variations of actual quasar spectra, we exclude the uncertainties associated with the 1σ confidence intervals from fitting the FOS Composite in Sherpa. For some targets we were able to scale the size of the emission line model fit to the data for a more appropriate fit.

2.4.3 Intervening Geocoronal Lyα Damping Wings

Short-ward of intrinsic Lyα (1215Å), spectra are plagued with the narrow, but intense, peak of geocoronal Lyα arising from hydrogen emission in our own atmosphere as well as the Lyα damping wings associated with hydrogen absorption in our own galaxy. In one object where the potential P V velocities overlapped the side of an otherwise clean Lyα damping wing, we were able to model the wing using a Voigt absorption profile in Python to generate the intrinsic flux profile.

Note: To do this we had to run Sherpa inside the Python environment rather than inside CIAO, which allowed us the use of both numpy and scipy to create a Voigt profile. While Sherpa does have a built in `absorptionvoigt` profile, we found it not to work as intended.

2.5 Absorption Modelling

From the data and emission + continuum model, we generate the normalized flux (I/I_0), which is defined as the ratio of the data to the model. In doing this, we remove the effects the emission lines have on the absorbed spectrum. This method assumes the outflow absorbs both the emission region and the continuum, i.e. that the observed spectrum has the form

$$I = observed\,flux = (continuum + emission) * absorption$$

and not

$$I = observed\,flux = continuum * absorption + emission$$

so that with this assumption, the normalized flux is

$$\frac{I}{I_0} = \frac{observed\,flux}{continuum + emission} = absorption$$

2.5.1 Derive Absorption Profile from Ion

To determine the properties of the potential absorption feature in P V, we first derive a profile from another ion in preferential order of Si IV, C IV, or O VI, depending on availability of data and existence of absorption in the region. We chose Si IV preferentially first not only because, like P V, due to its comparative rarity, Si IV requires a thick outflow to produce observable absorption, but also because Junkkarinen et al. (2001) has shown P V profiles tend to resemble Si IV

more than they do C IV. Furthermore, Si IV tends to suffer less from the effects of saturation than C IV, which itself tends to suffer less than O VI. Atomic physics predicts that for these resonant doublet pairs, the ratio of their optical depths should be 2:1, short:long. The observed ratio can be reduced to 1:1, because as the blue line saturates, the red line will grow correspondingly stronger until it also saturates, and the observed ratio will be some intermediate value. Partial covering effects can become important, since it will cause saturation to happen at non-zero intensity. We start by deriving the optical depth in the region that is one doublet's separation from the edge of the trough. For example, we could choose the high velocity end, where the contribution is solely from the blue line of the doublet. At those wavelengths, the optical depth derived for the blue line is

$$\tau_{\rm b}(\lambda) = -\ln\frac{\rm I(\lambda)}{\rm I_0(\lambda)}$$

Moving to the next set of wavelengths, one doublet's separation away, we force the red line optical depth to be half the strength of the blue line optical depth at the previous wavelengths

$$\tau_{\rm r}(\lambda + \Delta\lambda) = 0.5 * \tau_{\rm b}(\lambda) = -0.5 * \ln\frac{\rm I(\lambda)}{\rm I_0(\lambda)}$$

And we can then derive the next piece of the blue line optical depth as follows

$$\tau_{\rm b}(\lambda + \Delta\lambda) = \tau(\lambda + \Delta\lambda) - \tau_{\rm r}(\lambda + \Delta\lambda) = -\ln\frac{\rm I(\lambda + \Delta\lambda)}{\rm I_0(\lambda + \Delta\lambda)} + 0.5 * \ln\frac{\rm I(\lambda)}{\rm I_0(\lambda)}$$

and on across the profile. Note that $\Delta\lambda$ must be exactly the wavelength separation of the doublet and not some other arbitrary width, because $\lambda + \Delta\lambda$ is the set of wavelengths corresponding to the same velocities as the blue set of wavelengths, λ. We also choose to derive a profile starting from the low velocity end of the trough, where only the red line optical depth contributes to those wavelengths

$$\tau_{\rm r}(\lambda) = -\ln\frac{\rm I(\lambda)}{\rm I_0(\lambda)}$$

and derive the blue line optical depth a doublet's separation away

$$\tau_{\rm b}(\lambda - \Delta\lambda) = 2 * \tau_{\rm r}(\lambda) = -2 * \ln\frac{\rm I(\lambda)}{\rm I_0(\lambda)}$$

The next piece of the red line optical depth is analogous to the method above. Once we have all the derived profiles (blue derived from blue edge, red derived from blue edge, red derived from red edge, blue derived from red edge), we take a weighted average based on how well the profiles come together to recreate the normalized flux. The estimated errors are propagated accordingly, and derived in Appendix E. An example of the profile derivation for PG 1254+047 is given in figure 2.1.

2.5.2 Apply Absorption Profile to Pv

Armed with the derived absorption profiles, we can apply them to the normalized flux in the P V region and compute the estimated $\tau_{\rm PV}$ and its limits. We resample the optical depth profile onto the appropriate wavelengths and increase its magnitude to find the best fit according to two methods: (1) minimizing the sum of the distances

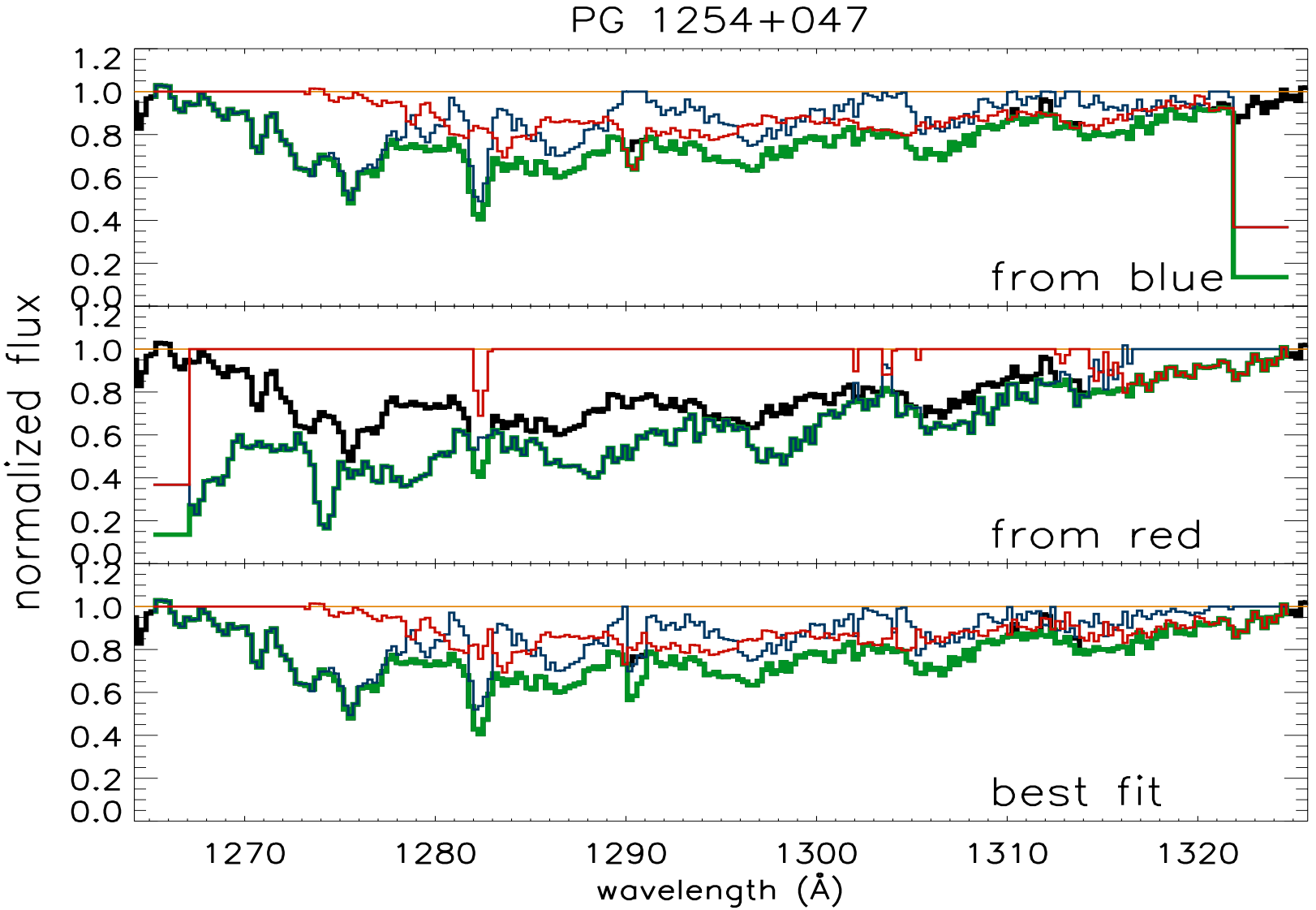

Figure 2.1: Derivation of τ profile: PG 1254+047 from Si IV (1393, 1402Å). The top panel shows the derivation from the blue side, forcing a 2:1, blue:red ratio. The middle panel starts the derivation from the red side. The bottom panel shows the best fitting average of the two results.

between the upper error bars on the normalized flux spectrum generated from the profile and the lower error bars on the data normalized flux spectrum and (2) minimizing χ^2 between the normalized flux spectrum generated from the profile and the data normalized flux spectrum, where χ^2 is:

$$\chi^2 = \sum \frac{\frac{\mathrm{I}}{\mathrm{I_0}} - \mathrm{e}^{-\mathrm{f}*(\tau_\mathrm{b}+\frac{1}{2}\tau_\mathrm{r})}}{\sigma^2_{\frac{\mathrm{I}}{\mathrm{I_0}}}},$$

where τ_b is the derived optical depth profile resampled onto the corresponding wavelengths for the blue line of P V and $\frac{1}{2}\tau_r$ is its red line analog, but at half the strength. We also compute the upper and lower limits on method (2) by increasing χ^2 by 6.635 to include the 99% error bars, as was done in Grupe et al. (2013).

A detailed description of the algorithm used to derive the best fit and estimated errors in the multiplicative factor applied to the optical depth profile in the P V region is given in Appendix E, along with the error propagation associated with computing $\bar{\tau}$, $\tau_{\bar{\mathrm{PV}}}$, and $\mathrm{depth}_{\mathrm{PV}}$.

2.5.3 Levels of Detection

While many of our results indicate non-zero lower limits on the P V optical depth, a second look reveals that many of them are spurious, preferentially fitting strong features such that the blue and red P V troughs do not quite align. To quantitatively evaluate the strength of those detections, we compute how far from zero the estimated absorption lies from zero, in units of standard deviation, i.e. the ratio of the multiplicative factor to its lower limit. Of the 17 targets having non-zero lower limits, 7 targets have strong, obvious, and believable P V absorption troughs with a ratio

> 9, a natural break in the sample. An additional target, 1714+5757, also has a ratio > 9 has a strong, obvious, and believable P V absorption trough, but only occurs at the very highest velocity end and not over the entire range of velocities covered by the O VI derived profile, bringing our total number of P V detections to 8. Others of the initial 7 detections have P V absorption matching only portions of the derived profile troughs, but the discrepancy is considerably less obvious. A further 9 targets have a ratio > 1, indicating a nonzero lower limit.

2.6 Results & Discussion

2.6.1 Sample Characteristics

We have measured a number of parameters to describe the targets and their absorption profiles: luminosity at 1121Å, maximum velocity, width, depth, average optical depth ($\bar{\tau}$), as well as the corresponding $\mathrm{depth_{PV}}$ and $\bar{\tau}_{\mathrm{PV}}$ estimates of the applied P V trough profiles. How we compute these quantities and their corresponding uncertainties is described in appendix B. We have applied a linear regression tool using the IDL utility `linmix_err.pro` of Kelly (2007). The tool is a Bayesian approach that computes the likelihood function and returns 5,000 draws of the slope and intercept from the posterior probability distribution. We chose `linmix` for its ability to handle censored data, which will be required to deal with the P V derived quantities, discussed later in this section. In the figures, the fit mean is the line described by the average values of those draws and the 1σ, 2σ, and 3σ bounds are found by sorting the deviations of each line from the mean and computing the values that include 68.3%, 95.4%,

and 99.7% of the distribution, respectively. With the described parameters and the results of `linmix`, we explore expected trends as well as new and possibly interesting relationships in the examples below.

WIDTH VS. v_{max}

Figure 2.2 shows a plot of trough width versus maximum velocity. We would expect larger widths to translate to higher maximum velocities, however, narrow width troughs can also have high maximum velocities. For example, in a trough having a minimum velocity of zero, the width is equal to the maximum velocity, whereas a very narrow trough might have a substantially higher maximum velocity than the width would indicate. Targets having a wider trough than their maximum velocity would dictate correspond to troughs having a positive minimum velocity. This could be due either to the uncertainty in redshift or to the troughs or parts of troughs corresponding to inflowing material rather than outflows. Overall the parameters are very closely related, as expected.

v_{max} AND WIDTH VS. DEPTH

The relationship between v_{max} and trough depth, shown in figure 2.3, exhibits considerable scatter. A slight negative relationship is observed at the 1σ level, though at 2σ and 3σ, the results are consistent with no relationship. When studying variability in BAL troughs, Filiz Ak et al. (2012a) found that shallower, higher-velocity portions of troughs tended to disappear more often than their deeper or lower velocity counterparts, possibly indicating the link where higher velocity troughs tend to be shallower. This trend makes physical sense given that deep, thick outflows should be difficult to drive to higher maximum velocities. However, the depth

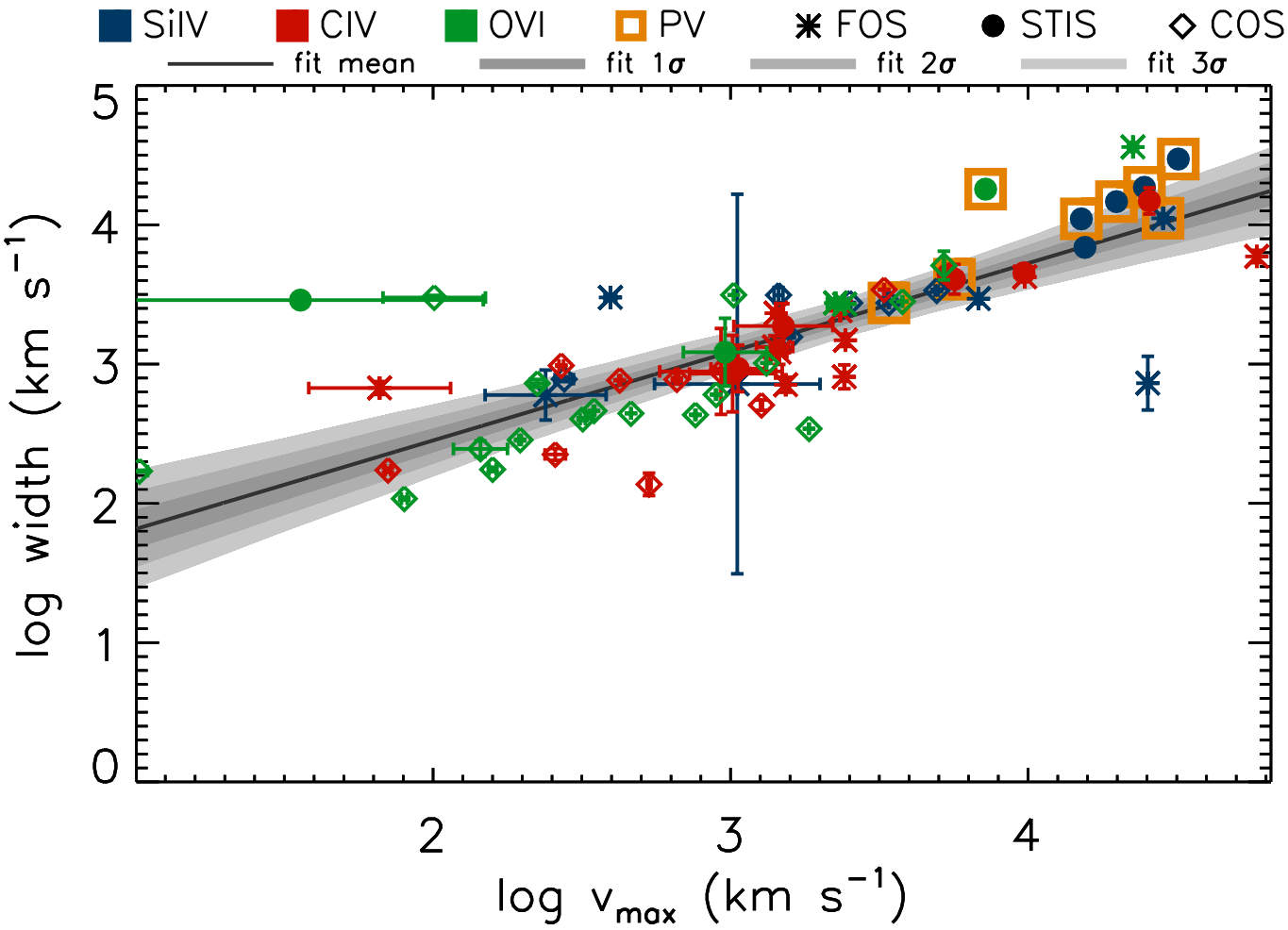

Figure 2.2: Log Width vs. Log v_{max}. Log Width correlates with Log v_{max} except for very narrow troughs or troughs with portions corresponding to inflows.

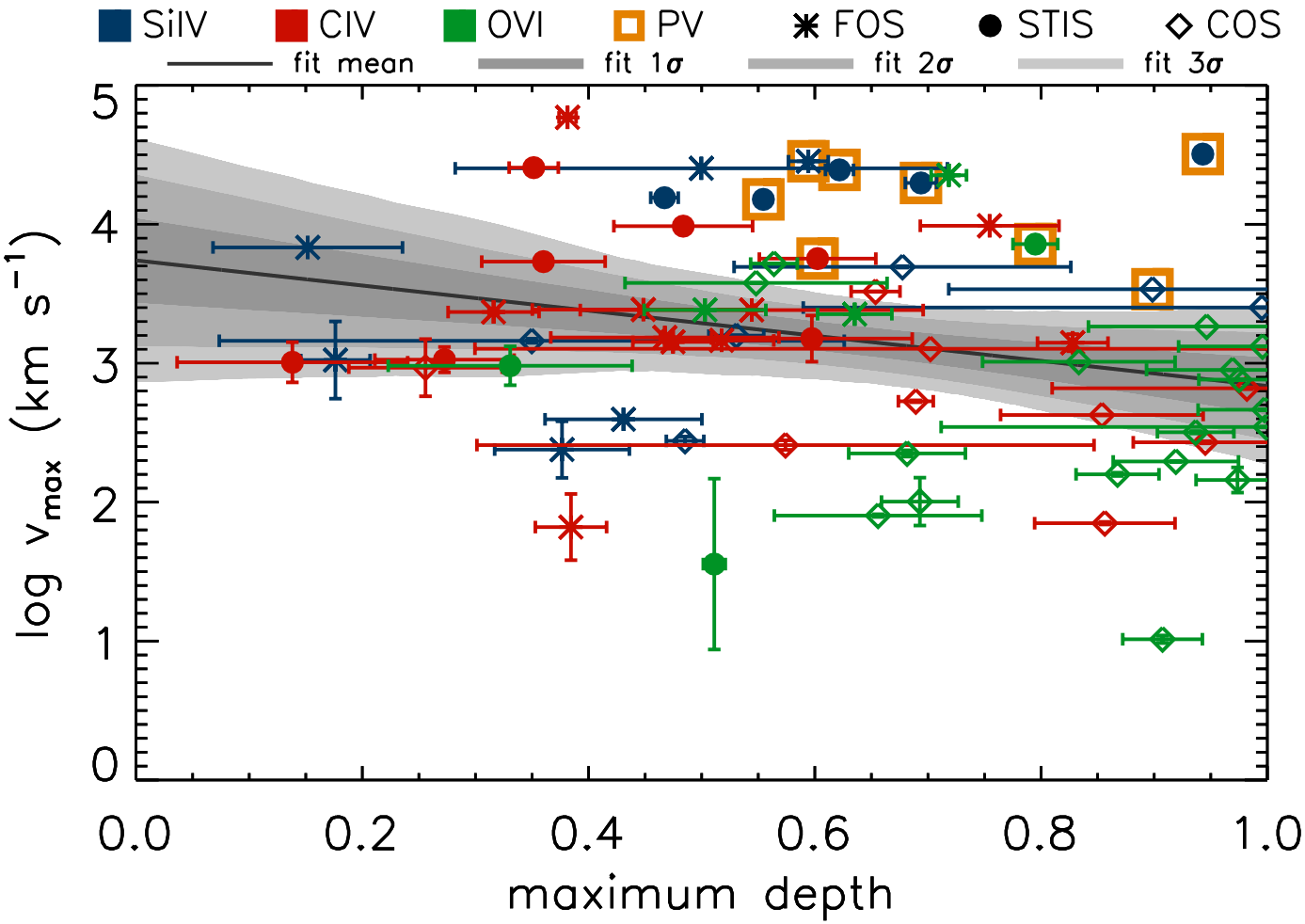

Figure 2.3: Log v_{max} vs. Maximum Depth. Considerable scatter and overall negative trend consistent with no trend at 2 and 3σ, but possibly links high velocities to shallow troughs as might be indicated by variability study of Filiz Ak et al. (2012b).

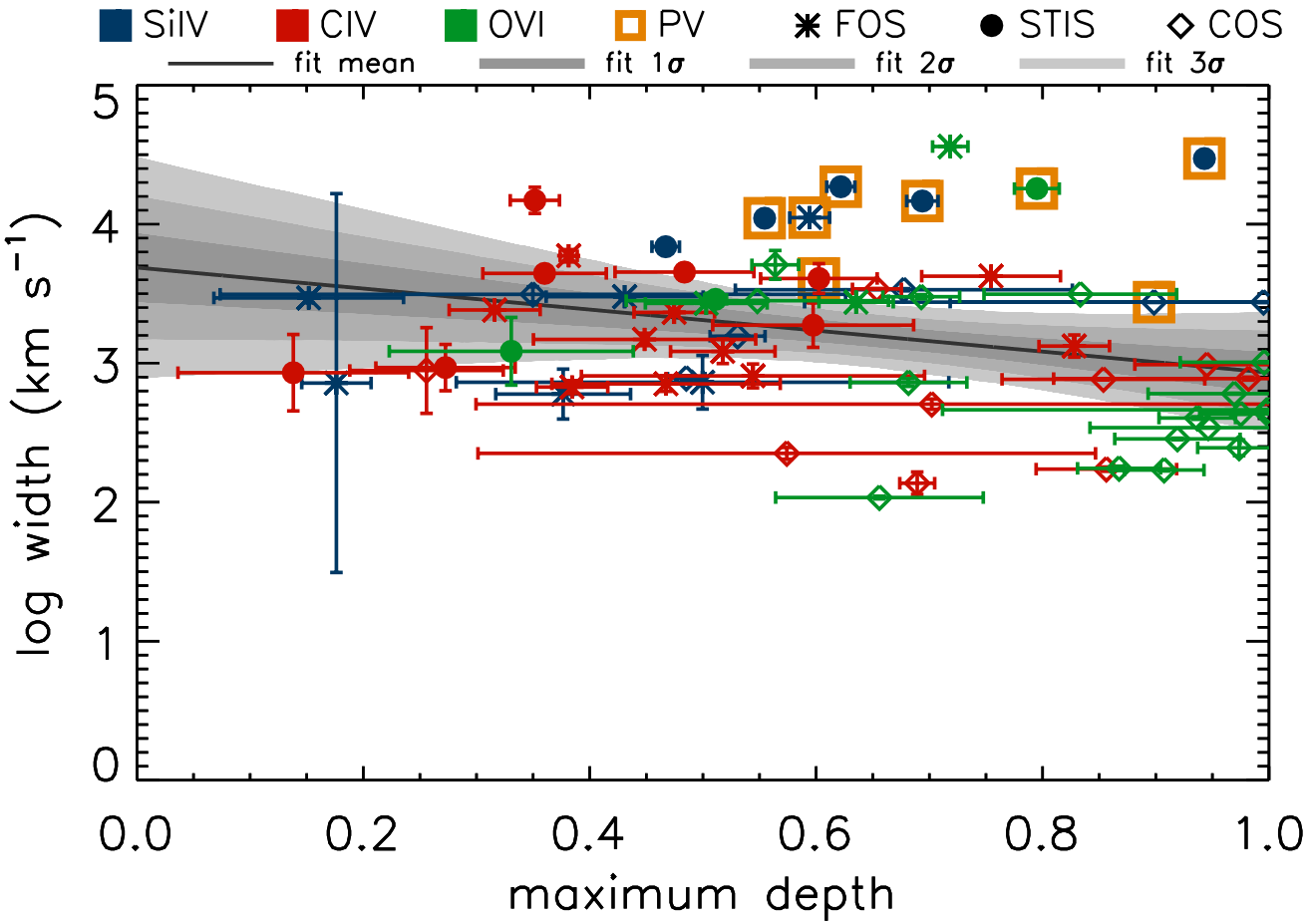

Figure 2.4: Log Width vs. Maximum Depth. Considerable scatter and overall negative trend consistent with no trend, but at widths $> 10^4\,\mathrm{km\,s^{-1}}$, tentative positive trend. Broader troughs tend to be shallower, but the broadest troughs tend to be the deepest.

measurement here is indicative of the deepest part of the trough and does not necessarily lie close to the high velocity end. If we consider the relationship between trough width and depth, shown in Figure 2.4, we still observe an overall negative trend as expected given the correlation of v_{max} with width, though if we consider only the largest widths ($\gtrsim 10,000\,\mathrm{km\,s^{-1}}$), we see a tentative positive trend.

$\bar{\tau}$ VS. DEPTH

Due to the nature of optical depth, we should expect optical depth to correlate with trough depth and the relationship to be exponential. A positive relationship is observed in Figure 2.5 and is clearly non-linear. For some targets, the highest depths translate to considerably higher optical depths, indicating possible saturation. Note that those such targets are dominated by profiles derived from O VI and no such targets are derived from Si IV. As discussed in section 2.6.2, O VI derived troughs are more likely to be observed with COS, which has higher resolution and is therefore able to resolve intrinsically narrower troughs that would otherwise be smeared into wider, shallower troughs. None of our P V detected targets appear to have $\bar{\tau}$s near of saturation, and therefore allowing a measurement of only a lower limit, but it could be that they have a smaller covering fraction.

$\bar{\tau}$ VS. v_{max}

We show the relationship between $\bar{\tau}$ and v_{max} in Figure 2.6. We observe a negative relationship between the two parameters, but more than that, we see very large optical depths require moderate velocities. Very thick (potentially saturated) outflows may be difficult to drive to higher velocities due to the enormous amounts of energy required.

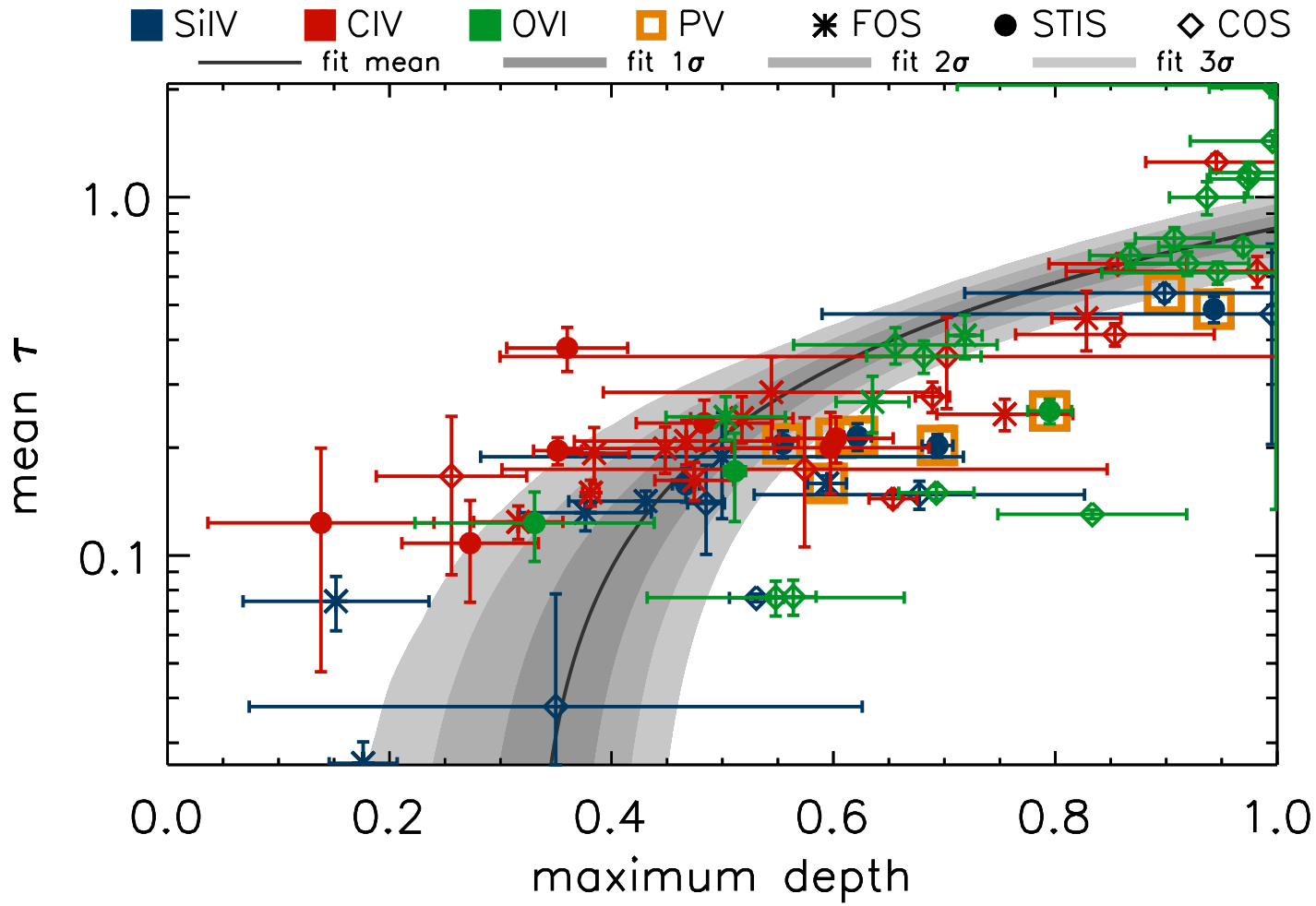

Figure 2.5: $\bar{\tau}$ vs. Maximum Depth. Logarithmic relationship, as expected. Some COS observed O VI potentially near saturation, but not for P V detections.

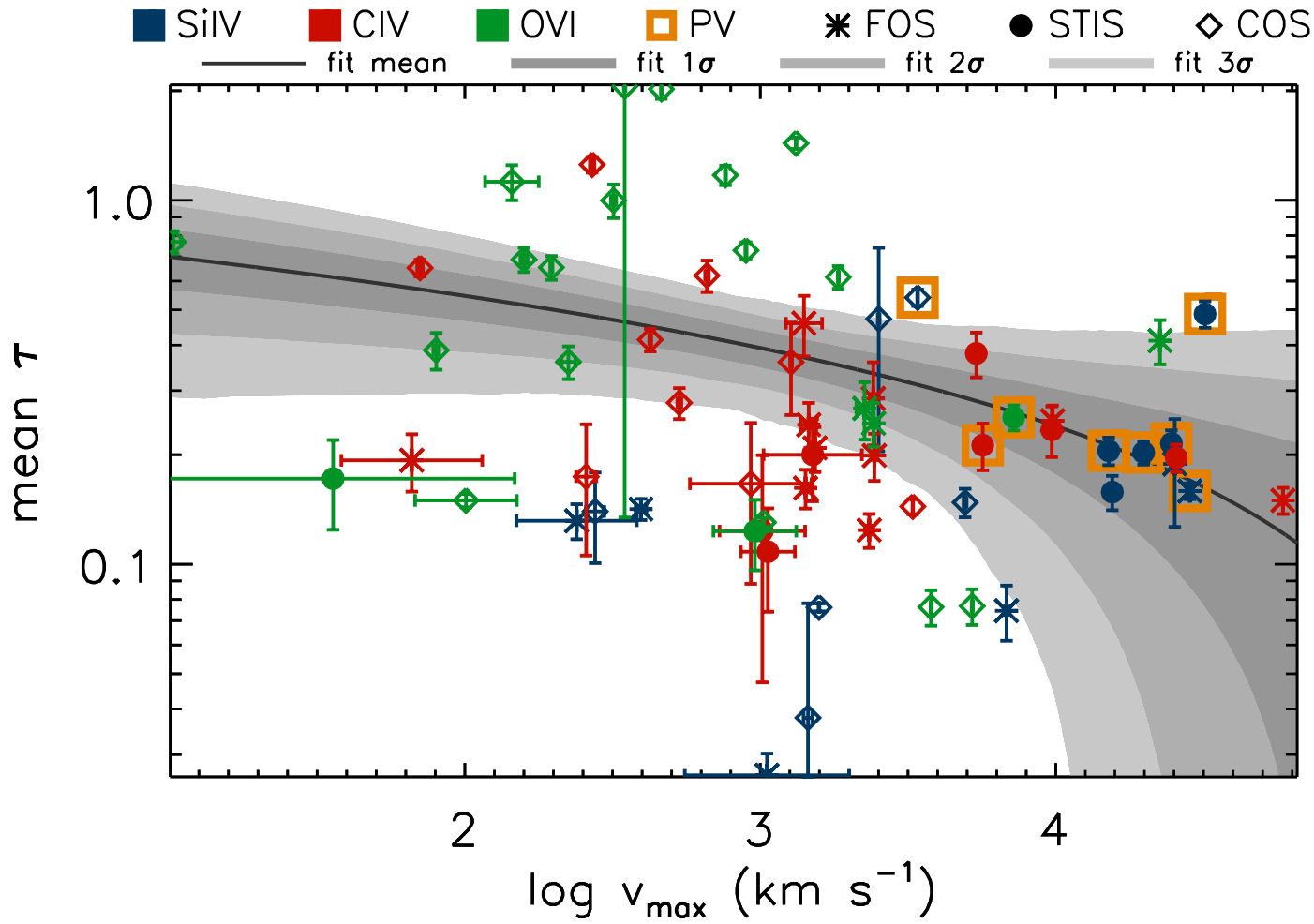

Figure 2.6: $\bar{\tau}$ vs. v_{max}. Overall negative relationship. The highest average optical depths require moderate maximum velocities. Very thick outflows may be difficult to drive to higher velocities.

Below, we describe how these parameters relate to the targets' luminosity.

LUMINOSITY VS. v_{max}, DEPTH, AND $\bar{\tau}$

Based on the previous works of Laor & Brandt (2002), Ganguly et al. (2007), and Ganguly & Brotherton (2008), we know absorption troughs exhibit an envelope relationship between maximum velocity and luminosity, where only the most luminous objects can drive the highest velocity troughs. Figure 2.7 shows an example of this for our sample. Here the P V detected targets appear to form the upper part of the envelope and we have fit a linear regression to those points using the IDL utility `linmix_err.pro` of Kelly (2007).

Ganguly et al. (2007) equation 5 gives the functional form and fit parameters of the envelope they fit in their figure 7:

$$v = v_0 \Big(\frac{L}{L_0} \Big)^{\alpha}$$

$$log\, v_0 = 3.96 \pm 0.29$$

$$log\, L_0 = 45.0$$

$$\alpha = 0.662 \pm 0.004$$

In order to reproduce their figure 7 using our data, we first estimate the 3000Å luminosity from our 1121Å luminosities. Leighly et al. (2016) states that quasars have a UV continuum similar to $F_\nu \propto \nu^{-0.5}$. In order to estimate the 3000Å luminosities, we apply

$$\nu F_\nu = \lambda F_\lambda$$

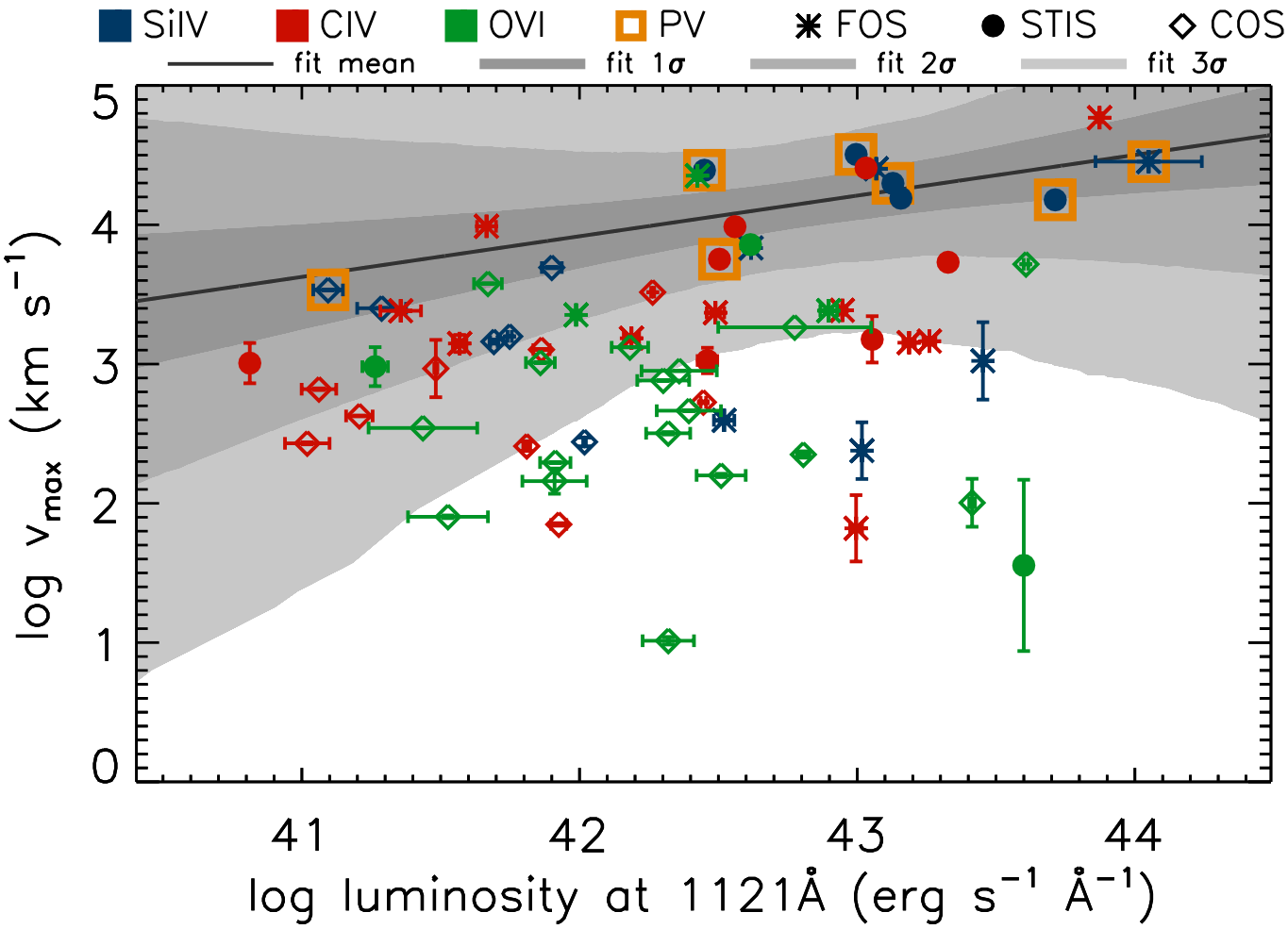

Figure 2.7: Log v_{max} vs. Log Luminosity at 1121Å. Similar qualitative envelope behavior as in Laor & Brandt (2002), where here P V detections form the upper part of the envelope.

and dim our 1121Å luminosities by a factor of $(3000/1121)^{-1.5}$, which amounts to a shift of ~ 0.2 in log space. We plot our data with Ganguly et al. (2007)'s fit in figure 2.8. The highest v_{max} target in our sample, PG 2302+029, also appears in Ganguly & Brotherton (2008) figure 1, an update of Ganguly et al. (2007) figure 7. In that figure PG 2302+029 has a log λ L(3000Å) of ~ 46.8 and our estimate of PG 2302+029's 3000Å luminosity is ~ 46.7, suggesting our estimates of the 3000Å are reasonable. If our P V detections form the upper envelope as they appear in 2.7, then we find a shallower envelope than Ganguly et al. (2007).

This envelope relationship suggests that an object's luminosity limits the maximum velocity its outflow can achieve. That more luminous objects can drive massive outflows to higher maximum velocities makes sense, however, why can lesser outflows not seem to exceed the maximum velocity for their given luminosities? Narrow outflows do not necessarily contain as much material unless they are also very thick, so it should be possible for narrow outflows to exceed that maximum velocity, but it is not observed.

The relationship between depth and luminosity is slightly negative similar to the relationship between v_{max} and depth, although with considerably more scatter. This is shown in figure 2.9. More luminous objects tend to drive shallower outflows, but the trend is not highly convincing, due to scatter.

The relationship between $\bar{\tau}$ and luminosity is potentially more interesting, shown in figure 2.10. We might expect only higher luminosity targets to be able to drive thicker outflows due to the energy requirements, but, as is seen in figure 2.10, this is simply not the case. Without compensating for partial covering effects, these $\bar{\tau}$s

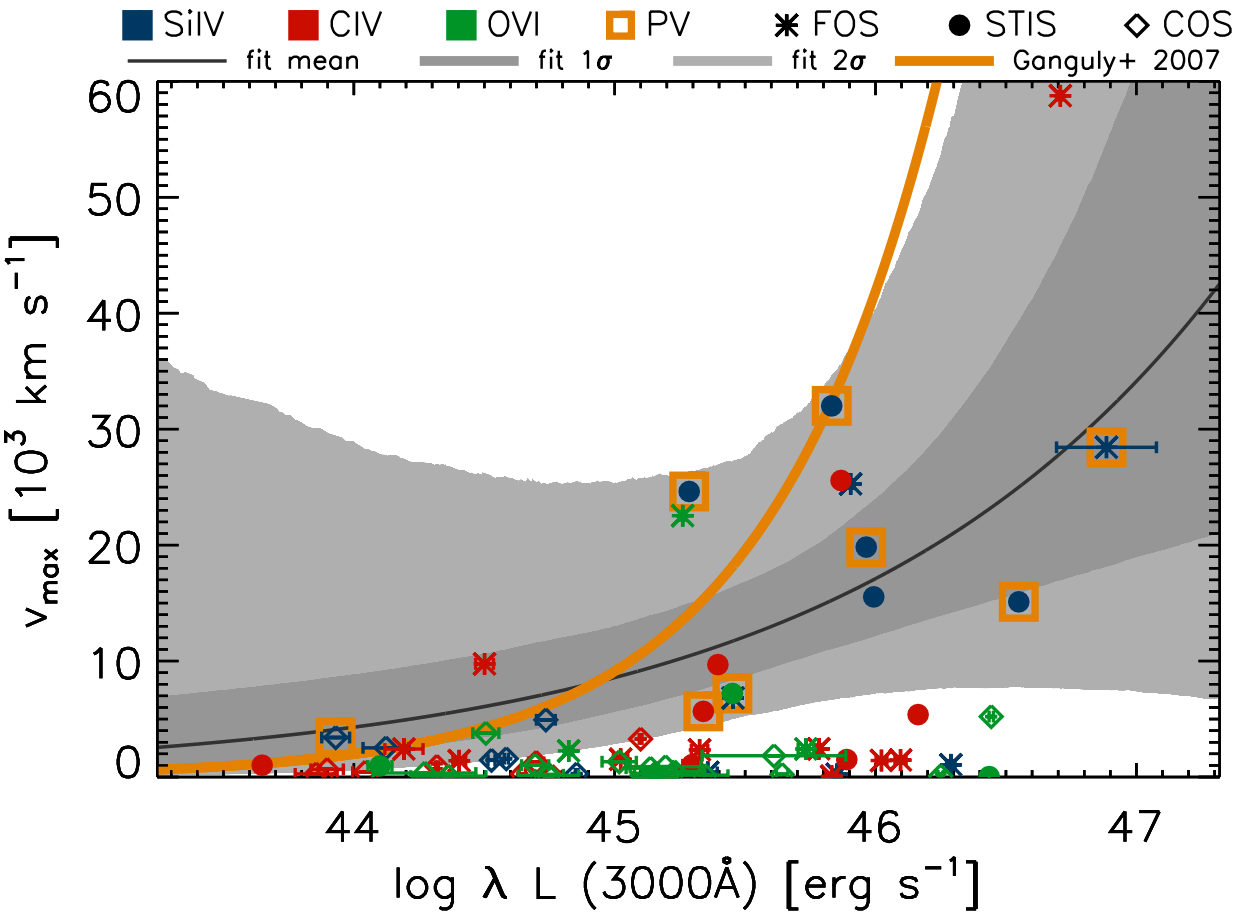

Figure 2.8: v_{max} vs. Log λ Luminosity at 1121Å. Updated version of Ganguly & Brotherton (2008) figure 1, with our data and Ganguly et al. (2007) fit. If our P V detections form the upper envelope as they appear in 2.7, then we find a shallower envelope than Ganguly et al. (2007).

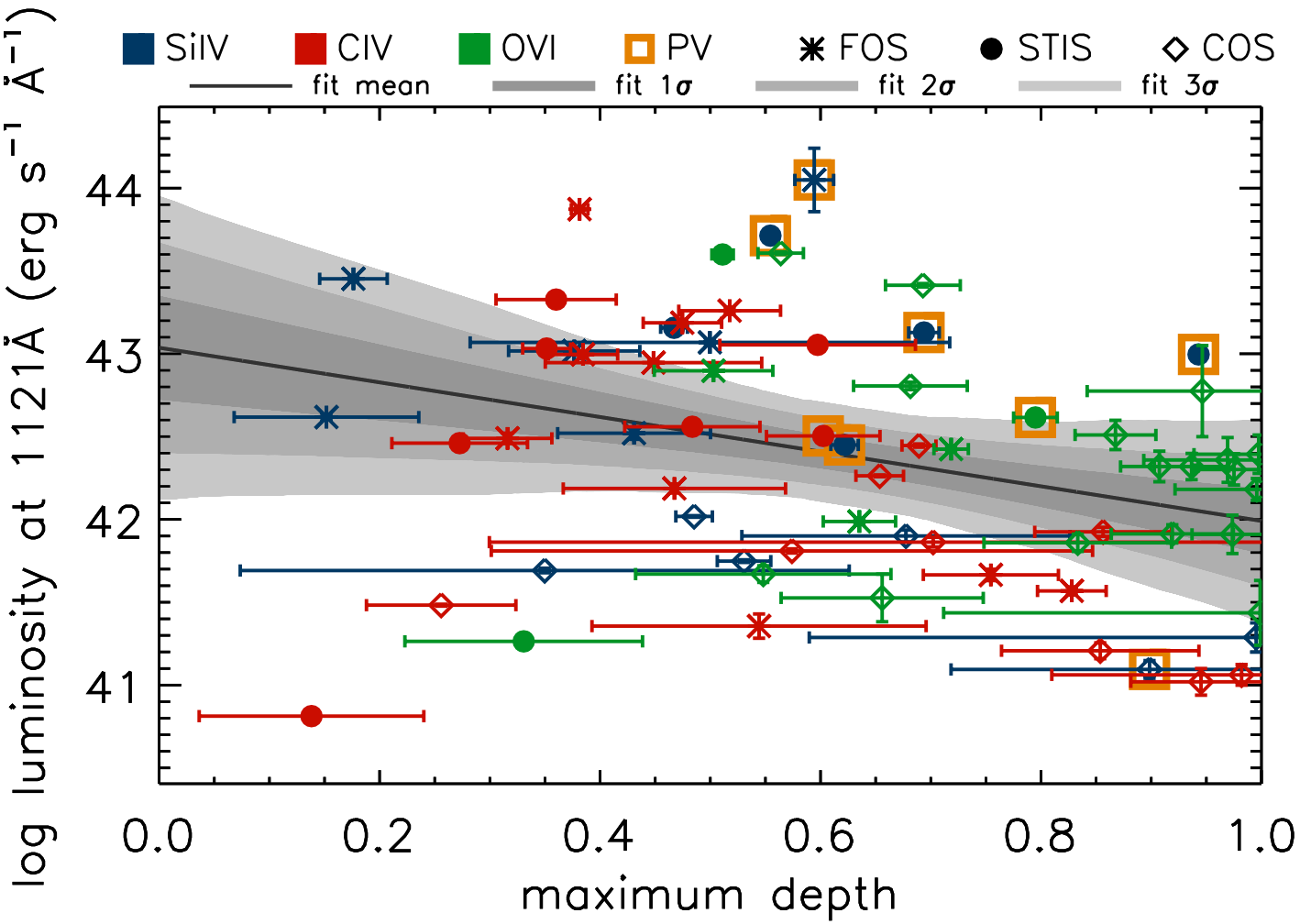

Figure 2.9: Log Luminosity at 1121Å vs. Maximum Depth. Slight negative relationship, but lots of scatter. The highest luminosity targets do not drive the deepest troughs.

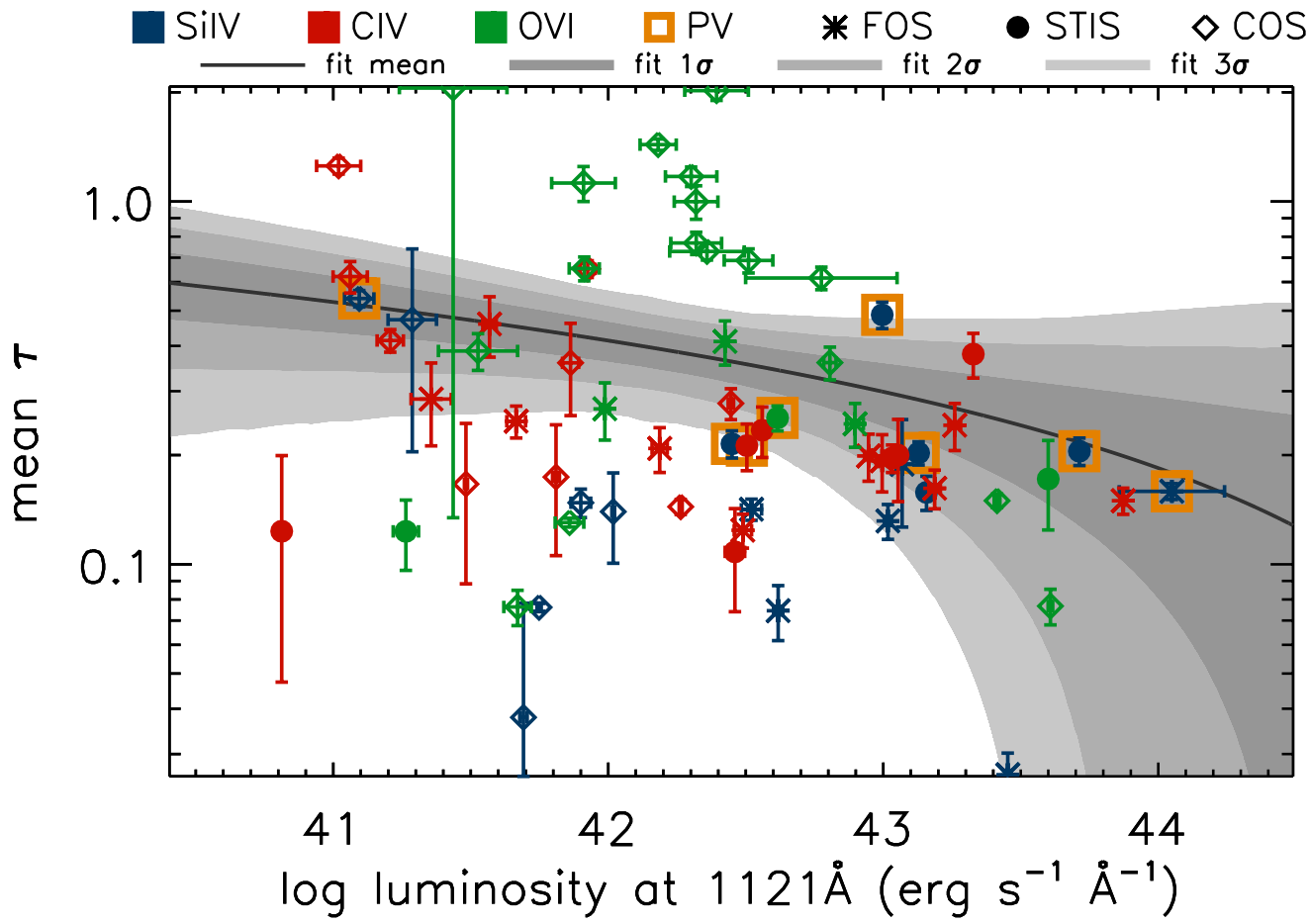

Figure 2.10: $\bar{\tau}$ vs. Log Luminosity at 1121Å. Higher luminosity targets do not drive the thickest outflows, but this might be hampered by resolution effects, whereby deeper, narrower lines get smeared into wider shallower ones. In comparison, the thickest outflows shown derive from the highest resolution detector, COS.

are only apparent optical depths and may be only lower limits as much more gas could reside in the outflow if the outflow only partially covers the emission source. Additionally, almost all of the higher optical depth targets are observed with COS and derived from O VI. The resolution of COS is higher than either COS or STIS and may allow us to see narrower, deeper lines that might have otherwise been smeared into wider, shallower ones by another lower resolution detector.

P V DERIVED QUANTITIES

Because our sample of P V derived quantities is dominated by upper limits, we chose the IDL utility `linmix` of Kelly (2007), which handles censored data. The quantity $\mathrm{depth_{PV}}$ derives directly from the applied τ_{PV} profile, we should expect a correlation between $\mathrm{depth_{PV}}$ and $\bar{\tau}_{\mathrm{PV}}$. Figure 2.11 shows such a correlation. The relationship between the P V derived quantities and all of the other variables is consistent with zero at the 3σ level. The relationships in figure 2.12 appear significant within 2σ, though by eye not exactly convincing. The upper left portion of each plot is devoid of data, supporting a possible positive relationship with each set of variables, $\bar{\tau}_{\mathrm{PV}}$ and $\mathrm{depth_{PV}}$ with $\mathrm{v_{max}}$ and width, indicating wider, higher velocity outflows, contrary to that shown in figures 2.6, 2.5, 2.4 and 2.3. However, the upper right portion of the plots are also sparsely populated, making any relationship considerably less convincing.

2.6.2 Validation Check to Combine Ions and Detector Subsamples

In our sample, we have derived absorption profiles from ions and detectors based on availability in the bandpass and the presence of absorption in the spectrum,

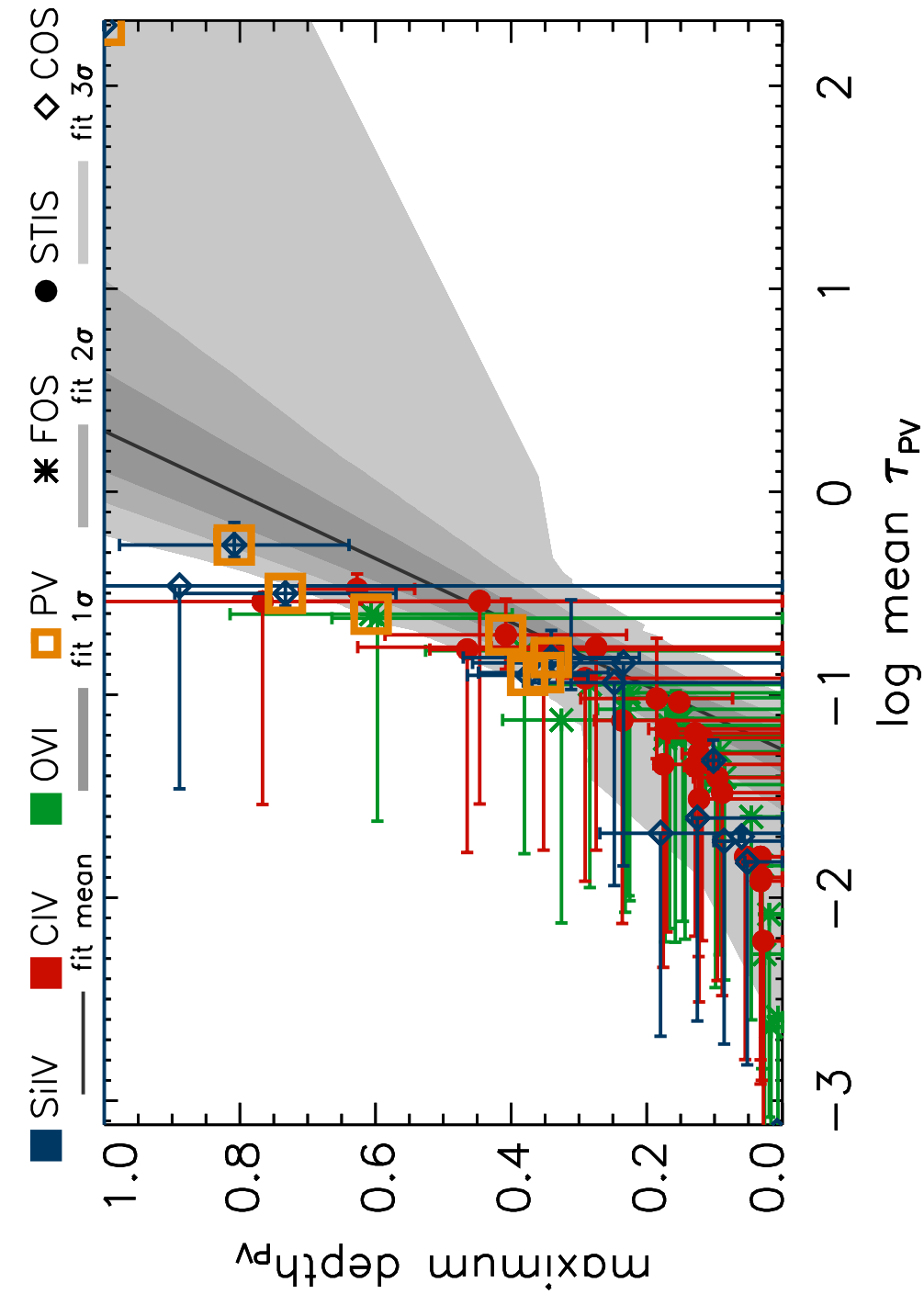

Figure 2.11: depth$_{\rm PV}$ vs. Log $\bar{\tau}_{\rm PV}$. Dominated by upper limits, but depth$_{\rm PV}$ correlates width Log $\bar{\tau}_{\rm PV}$, as expected.

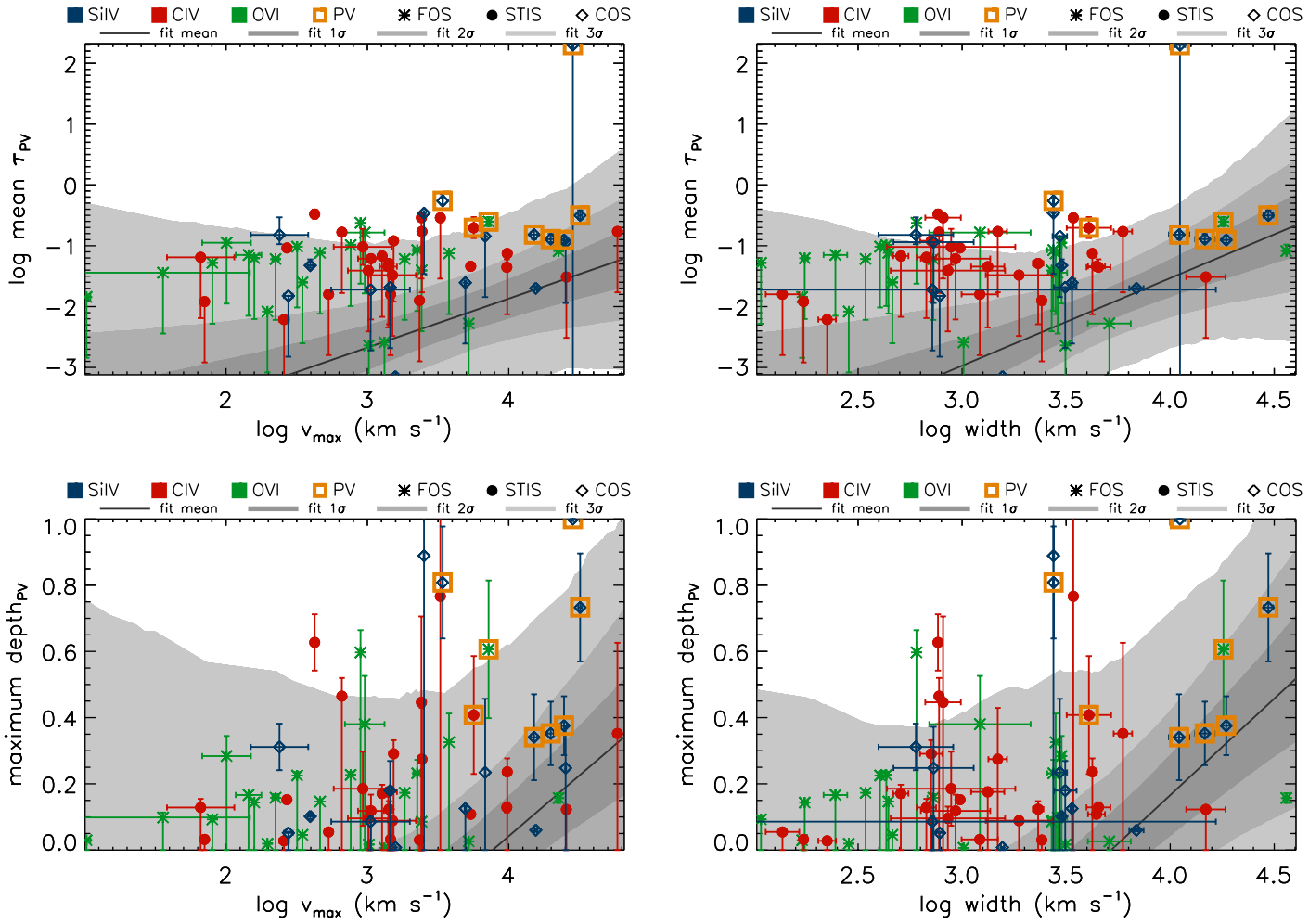

Figure 2.12: $\mathrm{depth_{PV}}$ and $\bar{\tau}_{\mathrm{PV}}$ vs. $\mathrm{v_{max}}$ and width

now we test the validity of combining these subsamples. Either they uniformly sample the whole range of the properties we investigate, or it could be that some ion or detector subsample occupies a distinct region of parameter space. We test to what level of significance we would reject the null hypothesis that the subsamples derive from distinct distributions and not the same parent sample. We performed Kolomogorov-Smirnov (KS) Tests (specifically `scipy.stats.ks_2samp()` in Python) on the parameters of interest, in combinations of our three ion subsamples and our three detector subsamples. If the p-values are > 0.05, then we can reject the null hypothesis that the targets derive from different parent samples. The results are in Tables 2.2 and 2.3, respectively.

	Si IV & C IV	C IV & O VI	O VI & Si IV
Redshift (z)	0.374	0.257	0.488
Log Luminosity	0.803	0.860	0.542
$\text{Depth}_{\text{ION}}$	0.868	0.052	0.014
$\pm$ Log v_{max}	0.344	0.633	0.157
Log Width	0.143	0.438	0.231
$\bar{\tau}_{\text{ION}}$	0.014	0.197	0.066

Table 2.2: KS test p-value results for the sample absorption properties by ion.

	FOS & STIS	STIS & COS	COS & FOS
Redshift (z)	0.667	0.004	0.010
Log Luminosity	0.888	0.007	0.005
$\text{Depth}_{\text{ION}}$	0.134	0.001	0.002
$\pm$ Log v_{max}	0.667	0.017	0.072
Log Width	0.134	0.030	0.111
$\bar{\tau}_{\text{ION}}$	0.991	0.018	0.013

Table 2.3: KS test p-value results for the sample absorption properties by detector.

A more visual representation of the sample characteristics is shown in Figures 2.13 and 2.14 in the form of cumulative histograms. COS probes statistically significantly lower redshifts and luminosities, but the ions are otherwise well mixed in redshift. COS also probes significantly deeper depths and larger average τs. O VI also probes significantly deeper depths and larger average τs, but a large sample of O VI derived profiles comes from COS. STIS probes significantly larger widths than COS, but the ions are well mixed. STIS does have a lower resolution than COS, which will result in a comparatively wider and shallower profile if observed with STIS for the same absorption. STIS probes only higher velocities, but the difference between FOS & STIS is not significant. COS & FOS look very similar, but have a marginally significant difference according to the KS test.

Overall, most of the tested parameters are well mixed among both ion and detector. Our detections are made almost exclusively from Si IV derived profiles, which might indicate P V occupies a more similar region of parameter space to Si IV than O VI. This would be in line with the discovery of Junkkarinen et al. (2001) that P V troughs more resemble the shape of Si IV troughs than they do other ions. Like P V, Si IV is rarer than either C IV or O VI and a thicker outflow is required to observe the ion in absorption.

2.6.3 Comparison with Other Samples

We compare our work to previous citations of P V BAL incidence from the literature, namely the works of Filiz Ak et al. (2014) and Hamann et al. (2012).

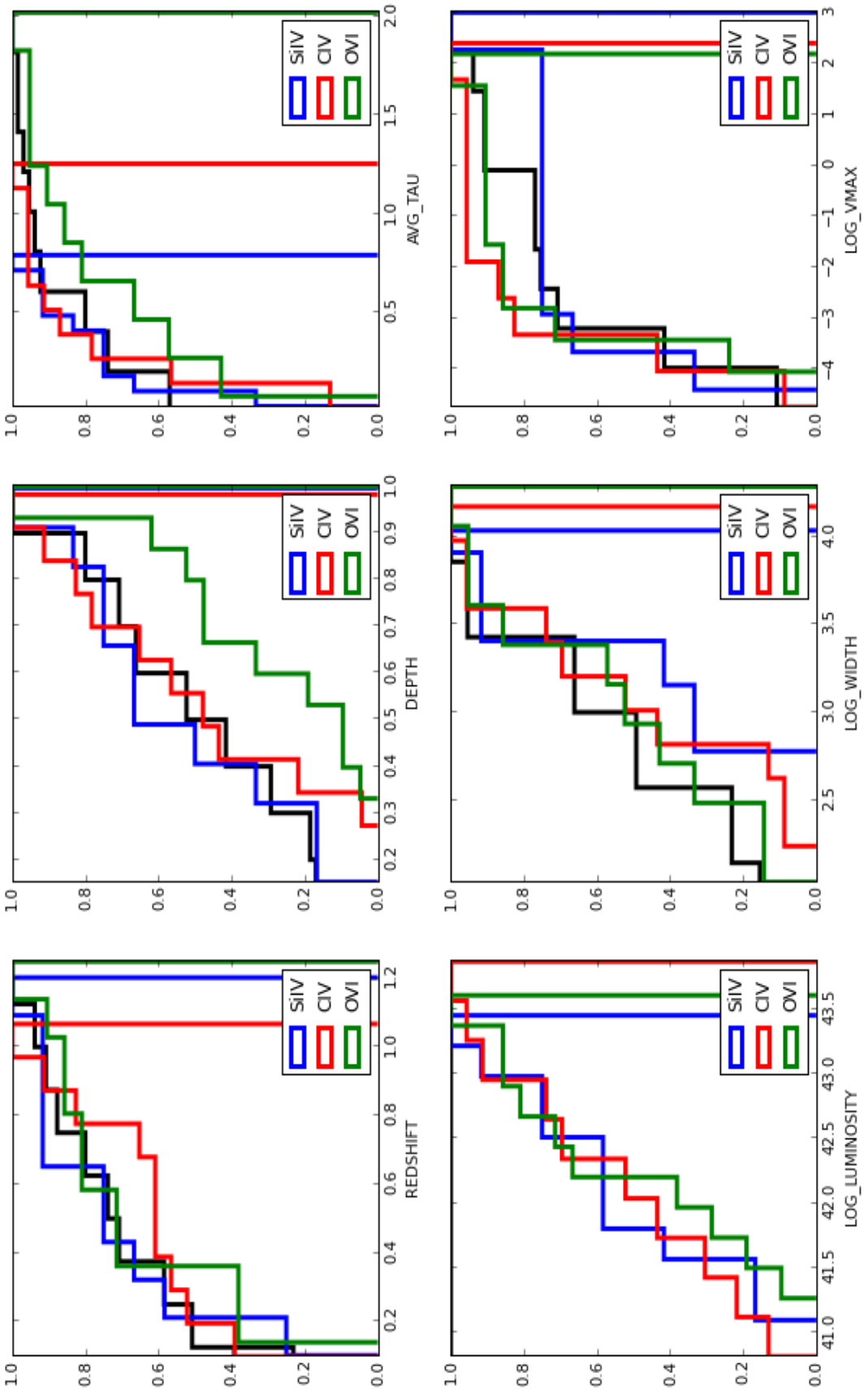

Figure 2.13: Cumulative histograms of subsample properties by ion.

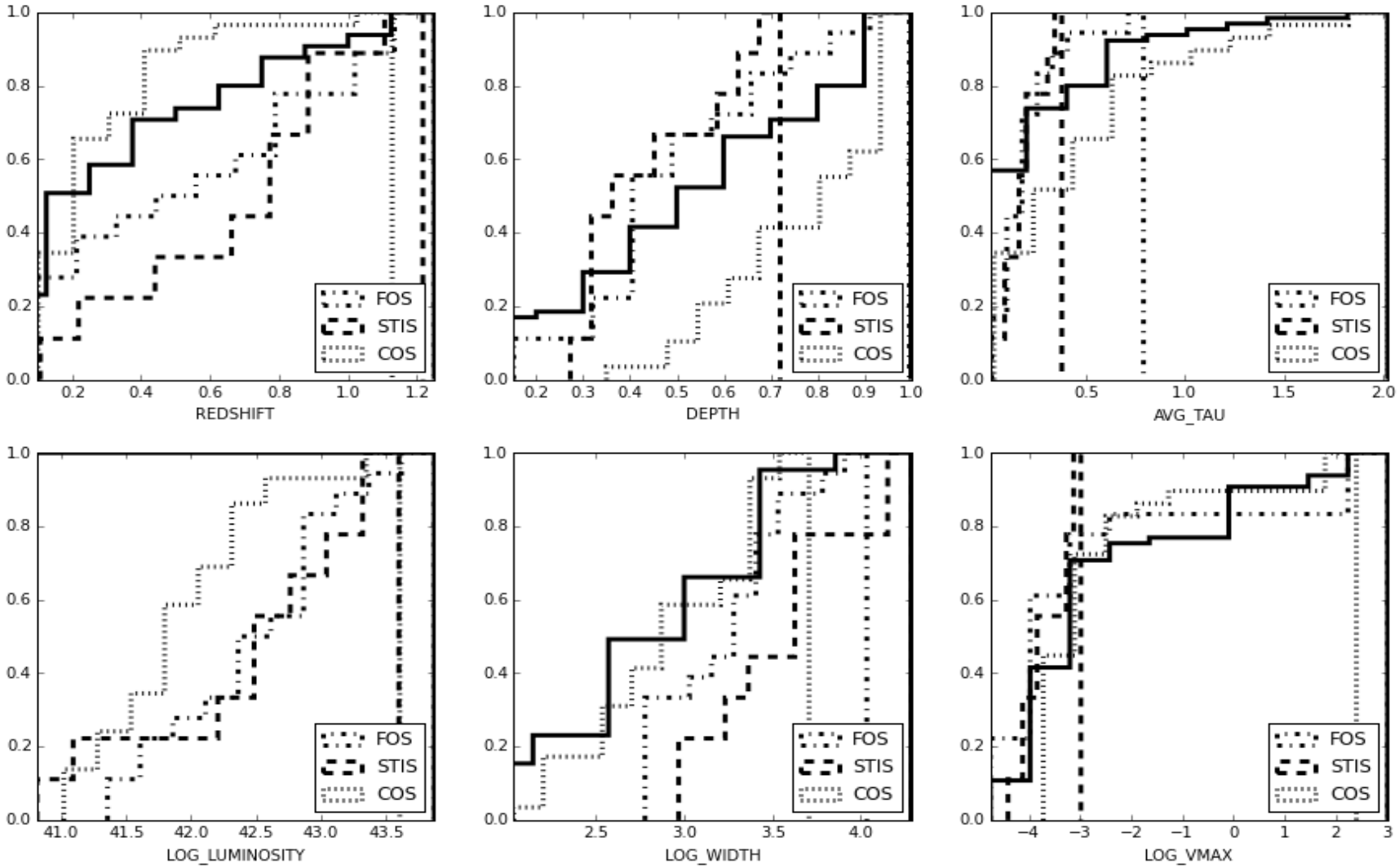

Figure 2.14: Cumulative histograms of subsample properties by detector.

Filiz Ak et al. (2014) is a variability study and a subsample of Gibson et al. (2009), requiring at least one observation each in the SDSS-I/II and Baryon Oscillation Spectroscopic Survey (BOSS) of SDSS-III. Filiz Ak et al. (2014) requires presence of a moderately strong C IV BAL, with $\mathrm{BI}_0 > 100\,(\mathrm{km\,s^{-1}})$, and subdivide their sample by accompaniment (or lack thereof) of other broad absorption line species. The C IV_{00} subsample has no accompanying BAL from either Si IV or Al III in the same velocities as the C IV BAL. C $\mathrm{IV}_{\mathrm{S0}}$ has a Si IV BAL, but no Al III BAL, and C $\mathrm{IV}_{\mathrm{SA}}$ has BALs in both Si IV and Al III at the same velocities as the C IV BAL. To comment on the incidence of P V absorption, they further restricted their sample to targets that would cover a P V BAL and visually investigated that region in the velocity locations of the C IV BAL troughs. Filiz Ak et al. (2014) report only the approximate percentages of their subsamples that appear to have detectable or moderate to strong P V absorption. Because we are interested in comparing the total incidence of P V absorption, we calculate the total percentage of targets appearing to have either at least detectable or moderate to strong P V absorption from their total number of targets in which P V would fall within the bandpass. The results are summarized in Table 2.4.

subsample	# targets	detectable		moderate+	
		(%)	(#)	(%)	(#)
C IV_{00}	40	$\sim 12\%$	5	$\sim 0\%$	0
C $\mathrm{IV}_{\mathrm{S0}}$	113	$\sim 50\%$	57	$\sim 10\%$	11
C $\mathrm{IV}_{\mathrm{SA}}$	47	$\sim 88\%$	41	$\sim 70\%$	33
TOTAL	200	$\sim 52\%$	103	$\sim 22\%$	44

Table 2.4: Summary of P V incidence in Filiz Ak et al. (2014).

Although Filiz Ak et al. (2014) do not exactly define the boundaries of detectable versus moderate to strong P V absorption, all 8 of our detections should fall into the moderate to strong category as they all exhibit clear presence of P V absorption. Of those 8 detections, 6 were made using profiles derived from Si IV, the 7th and 8th from C IV and O VI, respectively, for total incidence of $\sim 12\%$. Without knowledge of Al III absorption, our $\sim$ 12% moderate to strong P V absorption is in good agreement with the Filiz Ak et al. (2014) comments on C $\mathrm{IV}_{\mathrm{S0}}$ BALs, but a factor of ~ 2 lower than the figure for their total P V sample. So, despite the luminosity differences in the sample, we find a similar incidence of P V absorption.

Hamann et al. (2012) visually inspected ~ 3000 BAL quasars in SDSS DR9 with $z > 2.3$ (requiring P V to fall in the SDSS bandpass). While the work is ongoing, they report finding > 50 quasars with 'definite strong' P V BALs and 'many more' where P V BALs are 'probably present'. Details are to follow in Capellupo et al. (2013, in prep.).

We also compare sample properties to show our sample probes significantly lower luminosities and redshifts. These are shown in figures 2.15 and 2.16, respectively. Due to the vast differences in sample size and therefore scale, we use non-uniform bin sizes among the samples. Notably these figures show that our targets occupy the low end of both the flux and redshift ranges, indicating our sample probes nearer, fainter objects. The pileup of velocities in the comparison samples near $-25,000\mathrm{km\,s^{-1}}$ and $3,000\mathrm{km\,s^{-1}}$ are indicative of the requirements imposed by balnicity (see appendix G). We do not impose such velocity requirements and our troughs can probe different velocity troughs than the comparison sample.

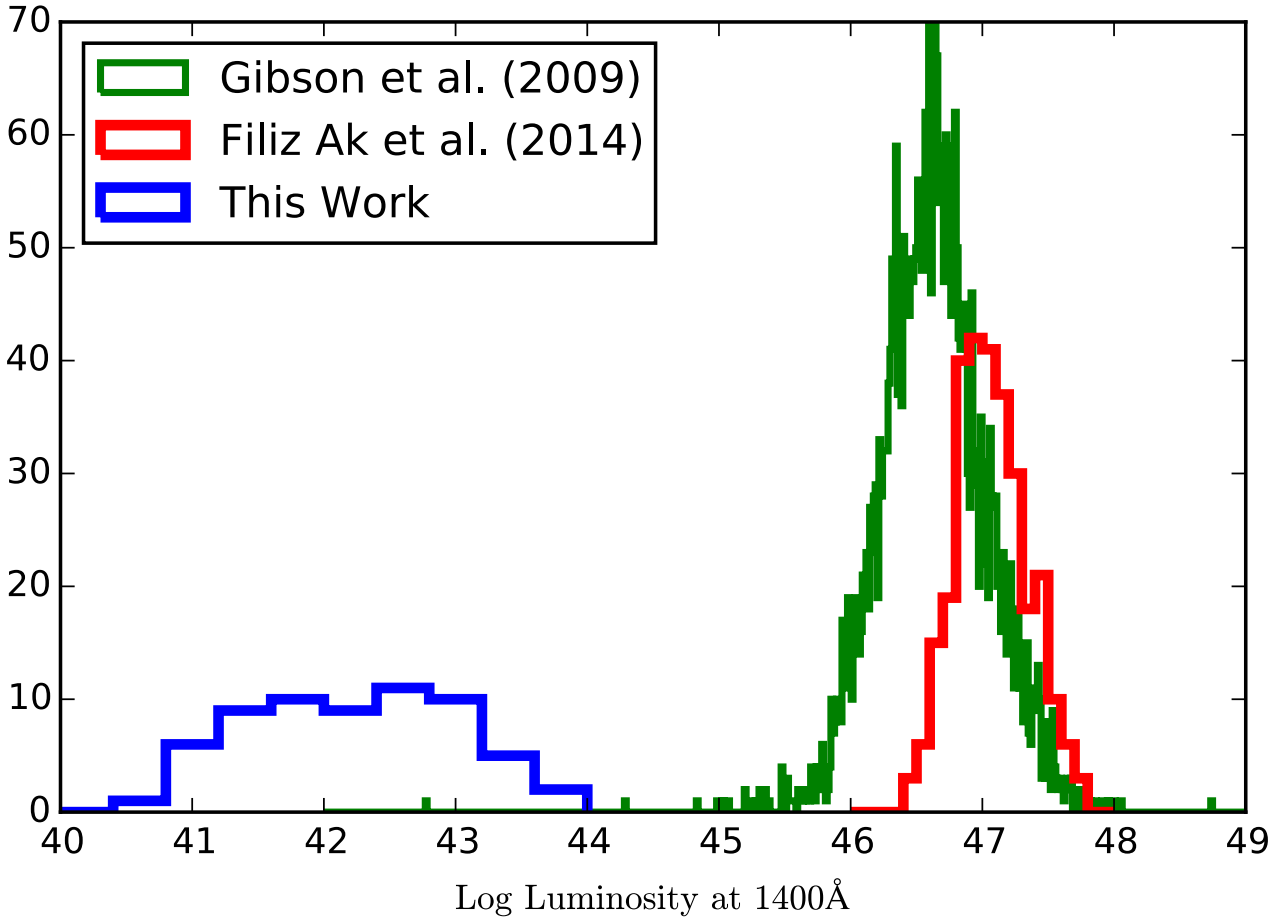

Figure 2.15: Histogram of monochromatic luminosities in comparison to other samples.

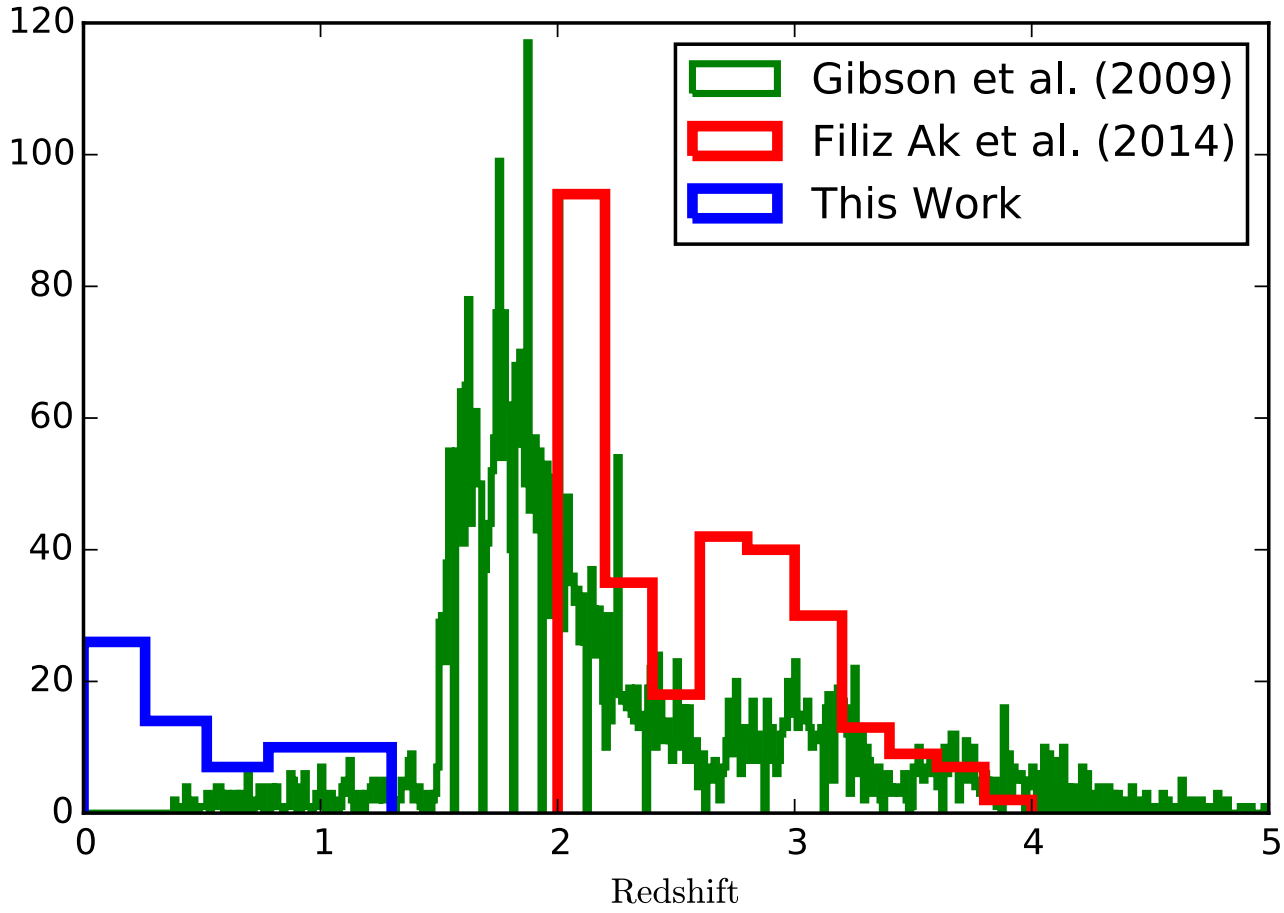

Figure 2.16: Histogram of redshifts in comparison to other samples.

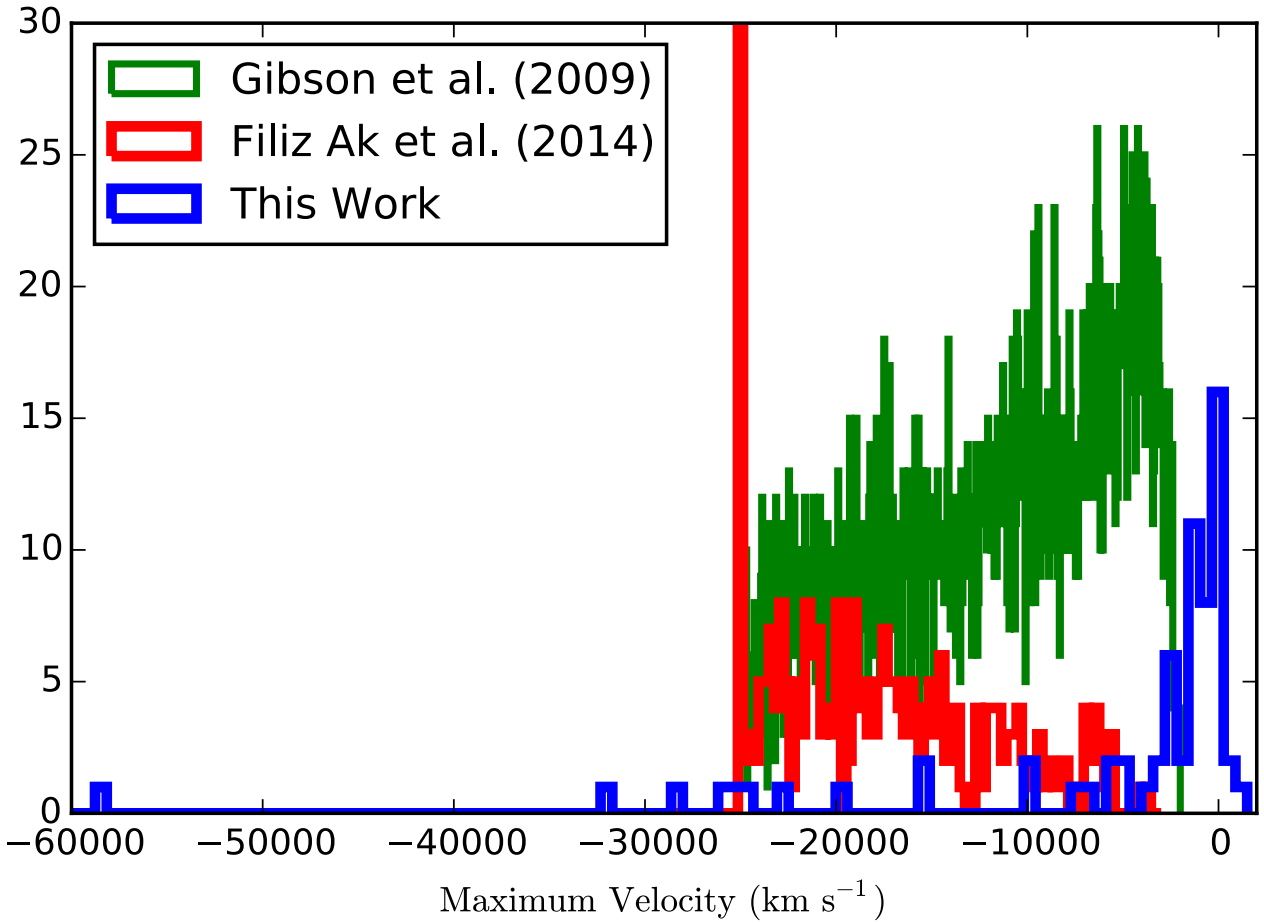

Figure 2.17: Histogram of maximum velocities in comparison to other samples. Note the pileup at -25,000 km s^{-1} for the Filiz Ak et al. (2014) and Gibson et al. (2009) samples as this is the maximum velocity cutoff for their C IV troughs.

2.7 Summary & Conclusions

We have analyzed a sample of 66 HST observed quasars for possible P V absorption by applying optical depth profiles derived from Si IV, C IV, and O VI and our results indicate the following:

(1) We detect P V absorption in 8 of our targets, for an incidence of $\sim$ 12%, consistent with the $\sim$ 10% figure from Filiz Ak et al. (2014) quoted for C IV_{S0} BALs.

(2) We only detect P V absorption in targets with broad absorption line troughs. Due to phosphorus' lower abundance, a fairly thick column is required to observe P V in absorption and therefore P V is often found in thicker outflows. However, that P V is only observed in broad outflows and never in narrow ones was not previously known.

(3) We observe the behavior of an envelope relationship between v_{max} and luminosity as described in Laor & Brandt (2002) and Ganguly & Brotherton (2008), indicating only the brightest targets can drive the highest velocity troughs and that the maximum velocity of the wind is limited by its luminosity.

(4) We find that the brightest targets do not drive the thickest or deepest outflows, though this observation is heavily biased by detector.

(5) Our detections are made almost exclusively from Si IV derived profiles, which might indicate P V occupies a more similar region of parameter space to Si IV than O VI. This would be in line with the discovery of Junkkarinen et al. (2001)

that P V troughs more resemble the shape of Si IV troughs than they do other ions.

Chapter 3

WPVS007: BAL Variability in a NLS1 Galaxy

3.1 Introduction

That a central black hole's mass correlates with physical properties of its host galaxy, bulge stellar velocity dispersion and luminosity (Ferrarese & Merritt (2000)) indicates the black hole exerts influence on its host galaxy's evolution. However, the stellar bulge lies outside of the black hole's gravitational influence and how these components communicate is still not well understood. One possible mechanism of black holes influencing host galaxy evolution is via feedback from accretion disk winds. Outflowing winds can infuse the host galaxy with chemically enriched material, mass and energy. Viable AGN feedback models (Hopkins & Elvis (2010)) require a kinetic energy luminosity of $0.5 - 5\%$ of the bolometric luminosity to exert influence on its host galaxy. One method of testing feedback models is by observing variability in AGN outflows. WPVS007, with its Seyfert level luminosity yet high velocity outflows, presents promise in achieving the 0.5-5% required for feedback.

Observed variability in AGN is driven by three primary physical properties: (1) variation in the ionization state of the outflowing material, (2) changes in the geometry of that material along the line of sight, and (3) shifts in velocity structure.

The ionization state of the gas varies in response to either the fluctuations of the ionizing source itself or variation in the shielding gas, if it exists, theorized to keep the outflow from becoming overly ionized. Changes in ionization shift the population

of the favored ionic species, increasing or decreasing the number of ions capable of making the observed transition. Such variability would be seen as variation in the depth of the absorption trough, which is largely the kind of variability we observe (Capellupo et al. (2013), Hall et al. (2011), Lundgren et al. (2007), Miller et al. (2012), Barlow (1993), Voit et al. (1987), and Smith & Penston (1988)). Smith & Penston (1988), Barlow et al. (1992), Chen & Qin (2015), Kraemer et al. (2002), and Grier et al. (2015) all attribute the trough depth variation observed in their samples to changes in ionization. Additionally the depth of trough segments are observed to vary in concert within the same ion at different velocities (Capellupo et al. (2012) and Filiz Ak et al. (2012a)) and for Si IV and C IV at the same velocity (Capellupo et al. (2012) and Gibson et al. (2010)), with Si IV more likely to vary (Capellupo et al. (2012)). Because the troughs at widely separated velocities should arise from physically widely separated parts of the outflow, such coordinated variability may be due to changes in the ionization state of the gas, which is capable of acting over a wide range of radii. That the fractional change in absorption varies inversely with BAL strength, i.e. shallower troughs vary more strongly than deeper ones (Capellupo et al. (2011) and Filiz Ak et al. (2012a)) also supports variability due to changing ionization, as saturated troughs would show little change in response to even large changes in ionization. No link has yet been found between the variability of the absorption trough and the continuum radiation.

A variation in covering fraction changes how we see the outflow oriented to the source along the line of sight, i.e. its geometry. Like the response to variable ionizing radiation, changes in covering fraction would appear as a variation of trough depths,

i.e. deeper troughs when more of the outflow covers the line of site. However, a change in covering fraction might also alter the ratio of optical depths in the doublet lines of species such as C IV, Si IV, N V, and O VI. Variable saturated troughs are more readily attributable to changes in outflow geometry since saturated troughs respond only weakly to variable ionization. That only small, discrete segments of troughs tend to vary (Capellupo et al. (2013), Filiz Ak et al. (2012a), Gibson et al. (2008), Miller et al. (2012), Kraemer et al. (2002), Joshi et al. (2014), and Vivek et al. (2012)) tends to support variation due to changes in covering fraction as ionization changes should cause more coordinated variability.

We know acceleration of the outflowing gas has to occur, as gas velocities have been observed to reach high speeds (~ 0.1c), whether by radiation pressure, magnetic pressure, or some other mechanism. Although a shift in the velocity profile would be the unmistakeable signature of acceleration, none has yet been definitively observed. We can see acceleration via radiative line driving in the form of line locked doublets, in which the short wavelength trough of the lower velocity parcel overlaps the long wavelength trough of the higher velocity parcel. This occurs when one parcel shadows the other, moderating the radiation and requiring both parcels to have the same acceleration. Some line locked candidates have been observed (e.g. Hall et al. (2007), Ganguly et al. (2003), and Srianand et al. (2002)), but tend to be quite rare.

Some BAL troughs have been observed to wholly appear or wholly disappear (Filiz Ak et al. (2012a)), sometimes converting such objects from a non-BAL to a BAL or vice versa. Are such occurrences extremes of the variability spectrum or a whole other beast entirely? Filiz Ak et al. (2013) found that the distribution of

BAL equivalent width variability indicates trough disappearance is only an extreme example of general variability rather than a qualitatively distinct phenomenon.

WPVS007 is unusual in that its trough depth variations are not coordinated, nor is the variability limited to changes in trough depth. The BALs lose strength at higher velocities and simultaneously gain strength at lower ones. The miniBALs appear constant over the observations. We will investigate the causes of variability in WPVS007 with the current HST and Swift UVOT observations described in §3.2. In §3.3, we discuss the size scales and probable origin of the outflow as being from the torus rather than the accretion disk, as is commonly thought.

3.2 Observations

3.2.1 HST COS Observations

In Leighly et al. (2015) we presented new WPVS007 data from the *Hubble Space Telescope Cosmic Origins Spectrograph* (HST COS) in addition to the archival FOS spectrum taken in 1996. The new observations were taken June 11, 2010, June 4, 2013, December 12, 2013, and March 30, 2015. For all observations, the instrument was configured with the FUV detector, Primary Science Aperature (PSA) and G140L grating. The 2010 exposures were configured at a central wavelength of 1230Å in each of three nod positions for a total exposure time of 5060.576s. In Cycle 20, two new central wavelength configurations became available and the June and December 2013 data sets were configured at central wavelength positions of 1280Å and 1105Å in each of two nod positions for total exposure times of 4606.688s and 4606.720s,

respectively. The March 2015 data set was configured in the 1105Å position only, for a total exposure time of 5322.752s. Details are in Table 3.1.

Table 3.1: Observation Log

Date	Central Wavelength	Exposure Time (s)	Wavelength Range (Å)[a]
2010-06-11	1230 (Å)	5060.576	1087-1986[b]
2013-06-04	1105 (Å)	2590.336	1108-1833
	1280 (Å)	2016.352	
2013-12-12	1105 (Å)	2590.336	1110-1840
	1280 (Å)	2016.384	
2015-03-30	1105 (Å)	5322.752	1110-1717[c]

(a) where the signal to noise ratio > 10, observed frame
(b) gap in coverage at 1172Å-1265Å, observed frame
(c) the flux in 2015 is much lower than in previous observations, so wavelength range given is for where the signal to noise ratio > 2, observed frame

Based on measurements of the interstellar medium absorption lines in Segment A of each of the spectra, we determined slight shifts (< 1Å) were necessary for the June 2010, December 2013 and March 2015 data. The detailed measurements are given in Appendix E. Data for a single central wavelength position and several nod positions are combined by the CalCOS pipeline (Massa et al. (2013)). For the 2013 datasets, we utilize two central wavelength positions and combine the data in the overlapping regions choosing to weight by the square of the signal to noise ratio (which is similar to weighting by the exposure for Poisson statistics). We bin the data by combining sets of three adjacent data points to adjust for over sampling, a factor of three for all sets. For all data, we smooth with a three point scheme where the center point is weighted by 3/5 and the adjacent points 1/5 each. We correct for galactic reddening using the Cardelli et al. (1989) reddening curve and

$E(B-V) = 0.012$ mag for WPVS007 from Schegel et al. (1998). Finally we shift the spectra into the rest frame using the same redshift value of Leighly et al. (2009), $z = 0.02882$.

The resulting data are shown in figure 3.1, along with appropriate line identifications. The progression of observations is towards lower luminosity, lower velocity, and shallower troughs.

3.2.2 Swift UVOT Observations

The Swift UVOT has also monitored WPVS007 since 2005, (Grupe et al. (2007, 2008, 2013), Leighly et al. (2015)), most recently published through August 2015. Near weekly observations in all filters have continued to the present time and figure 3.2 shows the updated UVM2 fluxes (upper) and $E(B-V)$ intrinsic reddening (lower), computed, as in Leighly et al. (2015), by simultaneous fitting of a constant indexed power law + SMC reddening (Pei (1992)).

Figure 3.3 shows the corresponding updated version of the color-magnitude plot that is the right-hand panel of figure 1 in Leighly et al. (2015). As with the previous plot, the lines indicate the best fits to SMC reddening (Pei (1992)) and intrinsic variability (Kokubo et al. (2014)). Leighly et al. (2015) find that both (1) the data favor the SMC reddening model, and (2) the UVM2 trough around March 2015 is characteristic of occultation. The dynamic timescale for this occultation is 60 days. Since the latest observations reported in Leighly et al. (2015), WPVS007 has largely occupied the same region of color-magnitude space, though with considerable scatter.

Figure 3.4 shows a more visual representation of the reddening between observa-

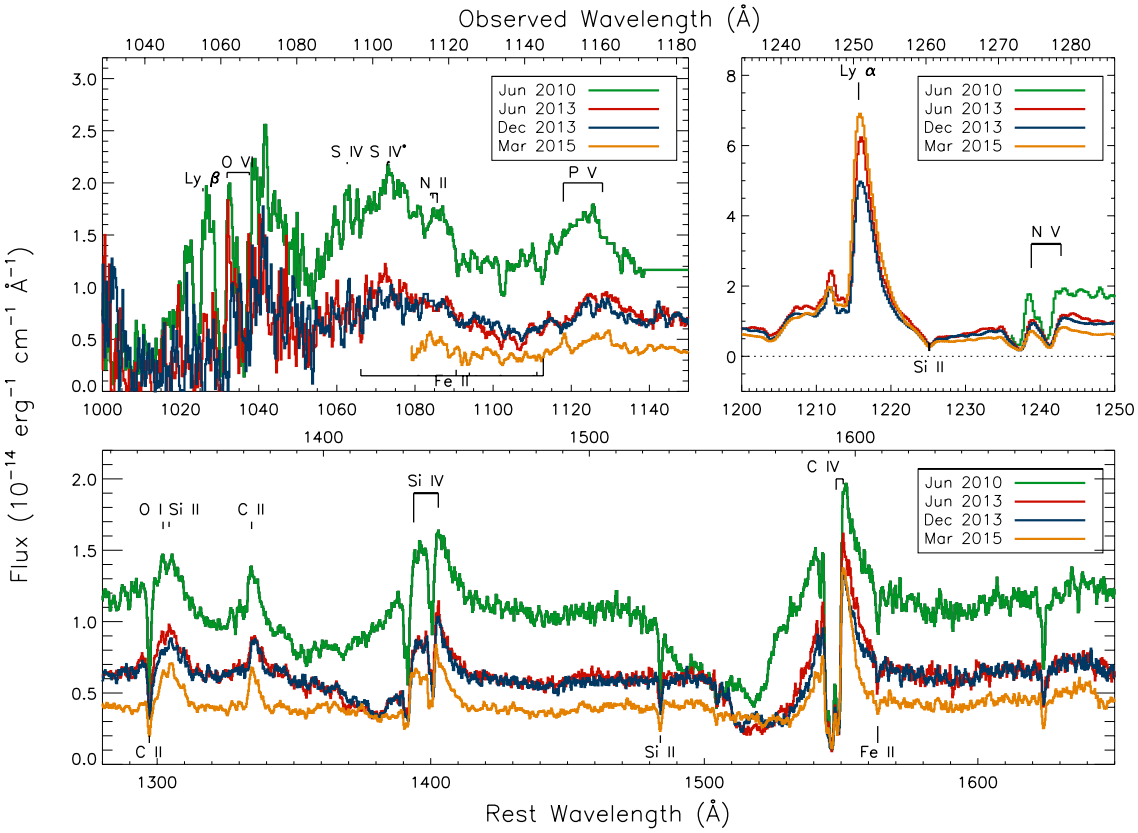

Figure 3.1: HST COS Observations. The data are plotted as-is, with no scaling. The progression of observations is towards lower luminosity, lower velocity, and shallower troughs. For the 2010 data, the detector configuration requires Lyα to fall in the gap between segments resulting in a gap in coverage between P V and N V. Line identifications above the data are possible emission and absorption troughs intrinsic to WPVS007, while identifications below the data are possible interstellar absorption lines from our own galaxy.

tions. The HST spectra are plotted alongside the Swift photometry in their respective bands. The Swift photometric curve for March and April 2015 appears intrinsically and more dramatically redder than the previous observations complementing the near secular decrease in flux since 2010.

3.3 Analysis

Leighly et al. (2015) argue Swift variability in WPVS007 (decrease in flux accompanying an increase in intrinsic reddening) points to the first observed UV AGN occultation and that the corresponding BAL velocity and BEL width variability point to an origin in the torus.

3.3.1 Size Scales

Figure 3.6 shows the relevant size scales relative to the range of possible black hole masses for WPVS007. Leighly et al. (2009) estimated a black hole mass of $4.1 \times 10^6\,\mathrm{M}_\odot$. The spread in $\mathrm{M_{BH}}$ arises from the 0.43 dex uncertainty estimated by Vestergaard & Peterson (2006) with regard to the scaling relation derived masses.

WPVS007 is a low-luminosity object, and based on the 5500Å luminosity density and the relationship between UV luminosity and α_{ox} Steffen et al. (2006), the predicted value of α_{ox} for this object is -1.22. Grupe et al. (2008) reported the first hard X-ray spectrum of WPVS 007, obtained during a long observation using *Swift*. The X-ray spectrum showed clear evidence for partial covering, and when that had been taken into account, the spectral energy distribution was found to be X-ray weak, with $\alpha_{ox} = -1.9$. Leighly et al. (2009) showed that an X-ray weak

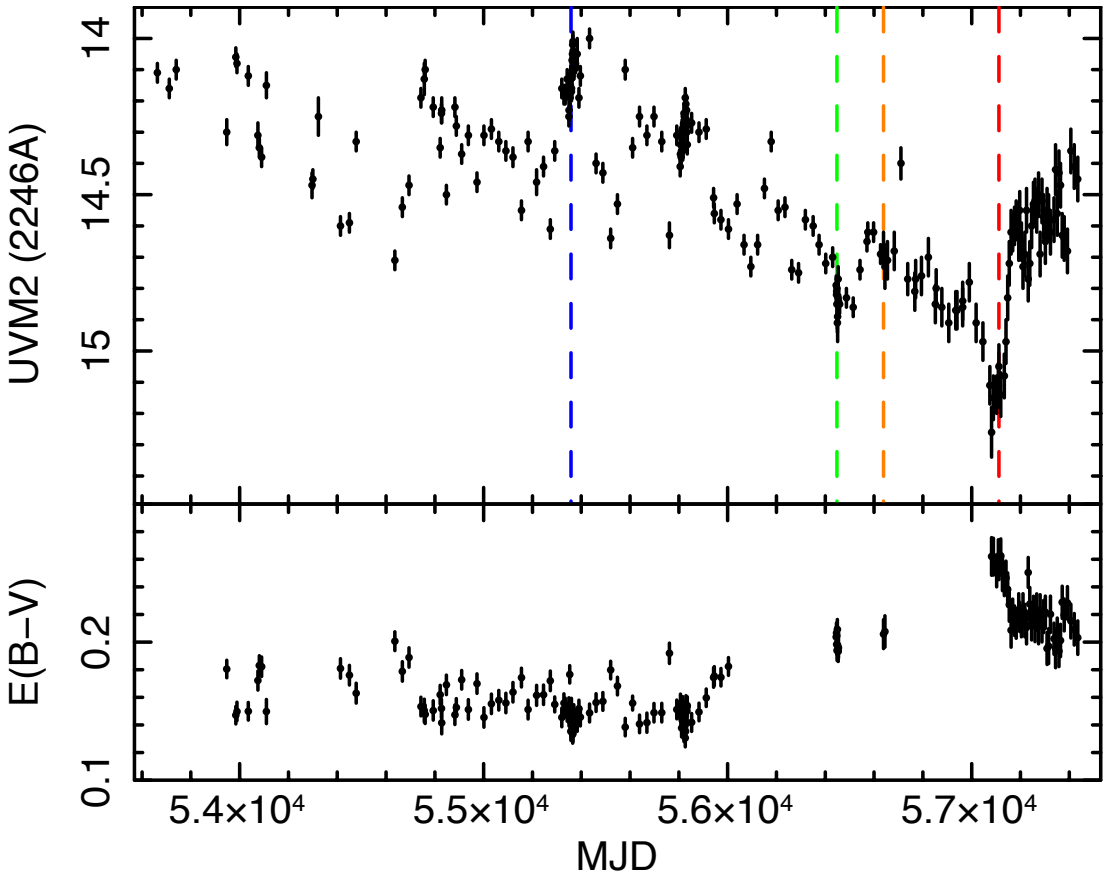

Figure 3.2: Swift UVOT Observations: UVM2 and E(B−V). This plot is the updated version of the left panel of Figure 1 in Leighly et al. (2015), to show additional data collected since that time. The times of HST observations are plotted as vertical dashed lines. Between the 2010 and 2015 HST observations, WPVS007 experienced a near secular decrease in UVM2 flux coupled with a rise in the computed E(B − V) intrinsic reddening. Since Leighly et al. (2015), we observe a rise in UVM2 flux accompanied by a decrease in E(B − V) intrinsic reddening.

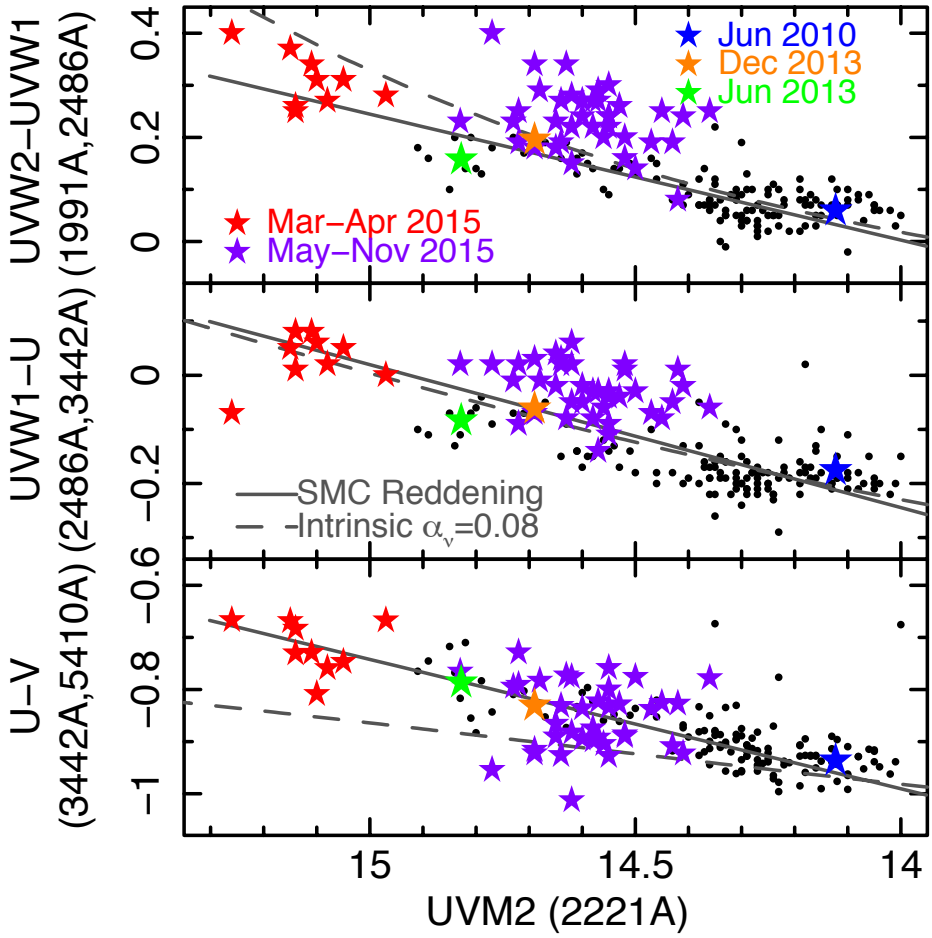

Figure 3.3: Swift UVOT Observations: color-magnitude plots. This plot is the updated version of the right panel of figure 1 in Leighly et al. (2015), to show additional data collected since that time. The times of HST observations are plotted as their own colored stars. The lines indicate the best fits to SMC reddening vs intrinsic spectral variability, solid and dashed, respectively. Since the latest observations in Leighly et al. (2015), WPVS007 has largely occupied the same region of color-magnitude space, though with considerable scatter.

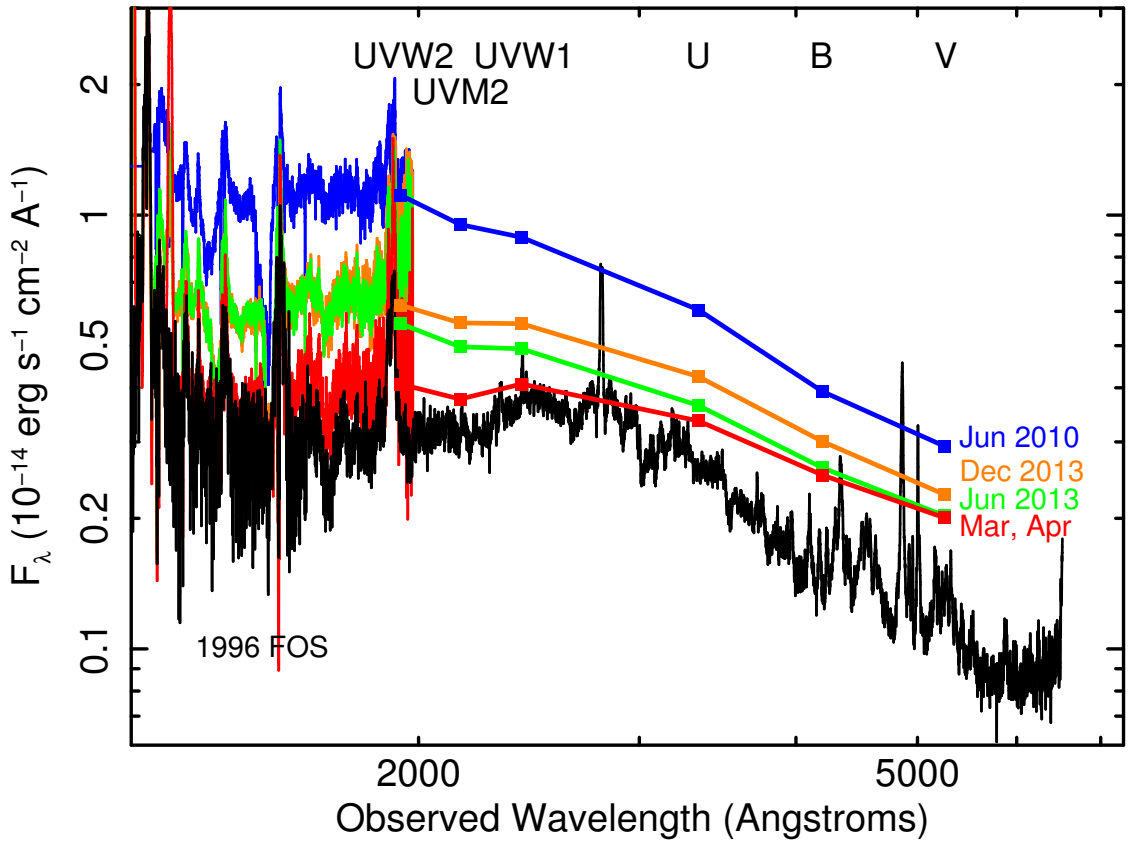

Figure 3.4: Combined HST spectra and Swift photometry: Note how the Swift photometric curve for March and April 2015 appears intrinsically and more dramatically redder than the previous observations.

SED explained the absorption lines better than an SED with $\alpha_{ox} = -1.28$, close to the value expected based on the UV luminosity. Normalizing this SED to the 1996 HST FOS optical spectrum yields the photoionizing flux at earth for this SED, for a luminosity distance of 1.245 Mpc, of 0.154 photons s^{-1} cm^{-2}. This normalized flux density yields a bolometric luminosity of 5.0×10^{43} erg s^{-1}. Using that estimated bolometric luminosity and an $\eta = 0.1$ sum of blackbodies accretion disk, Leighly et al. (2015) estimated three characteristic continuum radii: (1) R_{1550}, the emission at 1550Å, under C IV, (2) R_{2150}, the emission at 2150Å, the Swift UVM2 filter rest frame effective wavelength, and (3) R_{3350}, the emission at 3350Å, the Swift U filter rest frame effective wavelength.

Leighly et al. (2015) estimated the location of the BLR from Hβ and C IV. The Hβ estimation is bracketed by the Leighly et al. (2009) $R_{H\beta} = 9.7 \times 10^{-3}$ pc and somewhat smaller value, $R_{H\beta} = 4.2 \times 10^{-3}$ pc of Grupe et al. (2013). Emission line fitting of C IV, shown in figure **??**, reproduced from Leighly et al. (2015), Figure 3, gives a C IV broad component width of 4170 km s^{-1}. Scaled with the Hβ line width, 1190 km s^{-1}, from Leighly et al. (2009) and assuming virialization, Leighly et al. (2015) estimate 3.4×10^{-4} pc $< R_{CIV} < 7.9 \times 10^{-4}$ pc.

The torus distance estimates are bracketed by the dust sublimation radius, approximated by the K-band reverberation radius R_{TK}, and the $12\mu m$ peak emission radius. From Kishimoto et al. (2011), and the HST FOS 5500Å flux density, Leighly et al. (2015) estimate the inner edge of the torus to be 0.036 pc. Leighly et al. (2015) estimate the peak $12\mu m$ emission by comparing WPVS007's bolometric luminosity with Burtscher et al. (2013) Table 6, and find values ranging $0.3\,pc < R_{12\mu m} < 2\,pc$.

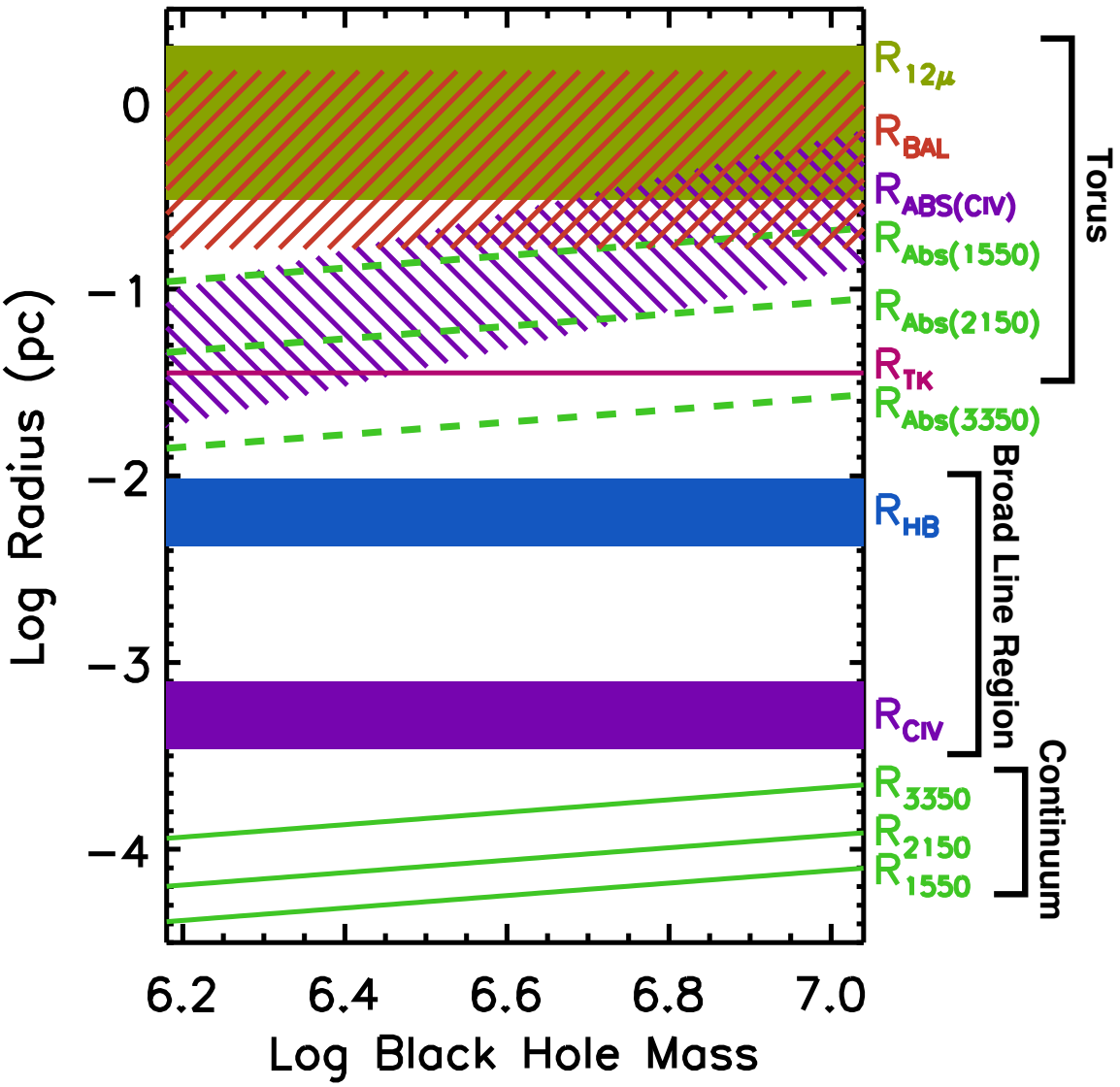

Figure 3.5: Leighly et al. (2015) Figure 4. Relevant size scales in WPVS007 for plausible black hole masses. The dynamical properties of the BAL absorber indicate a possible origin in the torus.

The distance to the absorber is related to the electron density and ionization parameter by

$$U = \frac{Q}{4\pi R^2 n_e c}.$$

Leighly et al. (2015) estimate the electron density from the 2009 *FUSE* S IV trough and the ionization parameter *Cloudy* modeling in the presence of P V absorption lines.

The 2003 *FUSE* spectrum revealed absorption from S IV, from both the ground state at 1063Å, and from the fine-structure excited state at 1073Å Leighly et al. (2009). These lines can be used to measure the density of the absorbing gas (e.g., Dunn et al., 2012; Borguet et al., 2013), because for increasing density, toward and past the critical density, the excited state is increasingly populated up to a ratio of $n(excited)/n(ground) = g_{ik}(excited)/g_{ik}(ground) = 2.02$. So, the measured ratio of the excited state and ground state column densities can be used to estimate the density. Then, using the photoionization parameter estimated from *Cloudy* analysis of the absorption lines Leighly et al. (2009), we can estimate the distance of the absorber from the continuum emission region.

The apparent column densities of S IVλ1062 and S IV*λ1073 measured from the *FUSE* spectrum were $1.47 \pm 0.065 \times 10^{15}\,\mathrm{cm}^{-2}$, and $1.88 \pm 0.042 \times 10^{15}\,\mathrm{cm}^{-2}$, respectively (Table 2, Leighly et al. (2009)). These combine to yield a ratio of excited state column density to ground state column density of 1.28 ± 0.05.

However, this spectrum suffers from partial covering. We know this because the ratio of the optical depths of the P V absorption lines is not 2 but is rather 1.38. Moreover, it is also clear that the partial covering is inhomogeneous; that is, the

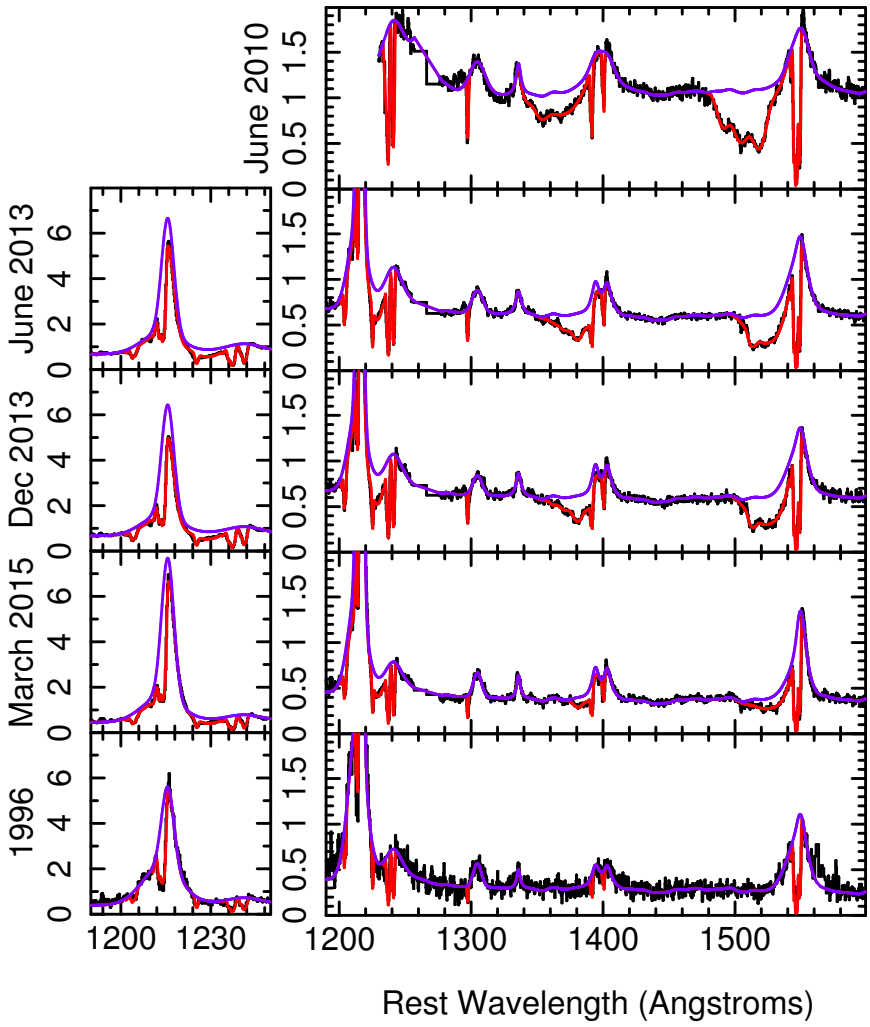

Figure 3.6: Leighly et al. (2015) Figure 3, right panel. Simultaneous continuum fitting, power law + emission line lorentzians.

different lines have different covering fractions, depending, most likely, on the line opacity (e.g., Hamann et al., 2001; Lucy et al., 2014). This can be seen in Fig. 9 in Leighly et al. (2009), where the O VI absorption is nearly black; the residual intensity at the bottom of the trough is about $\sim$ 10% of the continuum (i.e., a covering fraction of about 90%), while analysis of the P V troughs yields a maximum covering fraction of about 55%. So, to investigate this situation, 0.45 was subtracted from the I/I_0 spectrum, the P V optical depth template was re-derived (following the method described in Leighly et al. (2009)), and the column densities of the P V and S IV lines were re-derived. It is noteworthy that the P^+ column densities estimated from each of the doublet lines are now consistent with one another, implying that partial covering has been accounted for. For the S IV lines, the resulting column densities were $3.37 \pm 0.26 \times 10^{15}\,\mathrm{cm}^{-2}$ and $4.04 \pm 0.20 \times 10^{15}\,\mathrm{cm}^{-2}$ for the ground and excited states, respectively, yielding a ratio of 1.20 ± 0.09.

Combining the two ratio estimates and their statistical errors yields a conservative range of ratios between 1.11 and 1.33. Lucy et al. (2014) (Fig. 14) computed the expected ratio of the excited state to ground state column densities. Using that information, we find a range of densities between 7.3×10^4 and $1.34 \times 10^5\,\mathrm{cm}^{-2}$.

Leighly et al. (2009) showed that that the photoionization parameter required to explain the observed absorption lines (in particular, the P V lines, which require both a high column density and a high ionization parameter, was $\log U \geq 0$. We re-evaluated that number with higher sampling of the ionization parameter to yield a revised value of $\log U \geq -0.3$.

Leighly et al. (2015) roughly estimate the upper limit from the standard global

covering fraction, $\Omega = 0.2$, and an implausibly large ($> 20\%$) kinetic energy fraction to give $0.17\,pc < R_{\rm BAL} < 1.47\,pc$, consistent with the previous estimate for the location of the torus.

3.3.2 Absorber Location

Assuming the coordinated variability of the BAL velocities, C IV emission widths, and intrinsic reddening implies a common origin, the variability time scale can be used to estimate the location to the C IV absorber. For a rough estimate, the timescale is naturally bracketed by 190 d < T < 473 d, since not much variation is observed between the 2013 observations (190d apart), and serious variability is observed between the December 2013 and March 2015 observations (473d apart). The resulting location, plotted in 3.6, is consistent with an origin in the torus.

3.3.3 Occulter Location

Photoionization, S IV density, variability timescale dynamical arguments put WPVS007's BAL in the location of the torus, but what about the dynamical argument for the location of the occulter? Assuming a Keplerian velocity, $V = R_\lambda/T$ with an occultation timescale of 60 days, and an occulting cloud size equivalent to the size of the continuum emitting region, Leighly et al. (2015) estimate distances to the occulter for gas absorbing at the continuum wavelengths listed previously, 1550Å, 2150Å, and 3350Å. As previously mentioned, an increase in reddening accompanies the occultation, indicating the presence of dust and implying a location beyond the dust sublimation radius, previously approximated by the K-band reverberation radius,

$R_{\rm TK}$. This scenario is consistent for the inner clouds, absorbing at 1550Å and 2150Å, but not the outer cloud absorbing at 3350Å.

3.3.4 The Bigger Picture

So if the absorber and the occulter have locations consistent with the dusty torus, what does the spectral variability we observe in WPVS007 imply? As previously stated, WPVS007 is unusual in that its trough depth variations are not coordinated, nor is the variability limited to changes in trough depth; its BALs lose strength at higher velocities and simultaneously gain strength at lower ones. The emission line width and reddening variability is also unlike that seen in other AGN.

Leighly et al. (2015) propose a scenario of for the variability in WPVS007 described in figure 3.7, reproduced from their figure 5. If WPVS007 has a variable scale height torus, the observed variability is naturally explained by the variation in height rotating into and out of our line of sight. Deep, high velocity troughs and low reddening (like that observed in 2010), are observed when the scale height of the torus is low. If the torus is also the origin of the BAL gas, then the BAL gas has moved quite far from the torus and is nearly unobscured. When a higher scale height piece of the torus rotates into our line of sight, we're looking through mostly dust, and the BAL very near the torus boundary and is nearly completely obscured (as seen in 2015), hence the enhanced reddening. The 2013 BAL troughs are observed when an intermediate scale height piece of torus lies in our line of sight.

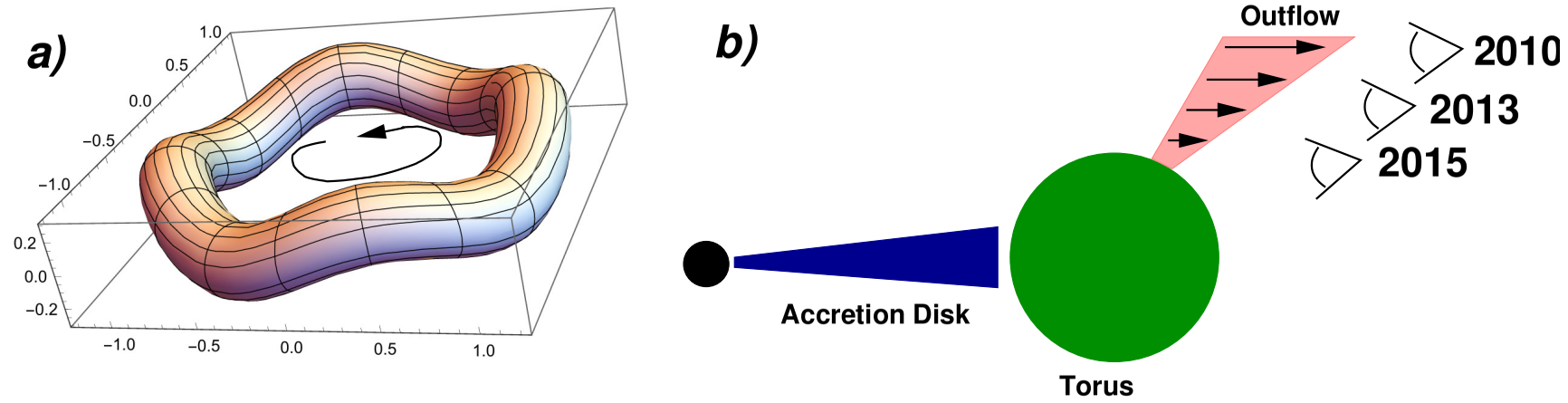

Figure 3.7: Leighly et al. (2015) Figure 5. Cartoon of the variability implied by WPVS007. If WPVS007 has a variable scale height torus, the observed variability is naturally explained by the variation in height rotating into and out of our line of sight. Deep, high velocity, low reddening troughs (like that observed in 2010), are observed when the scale height of the torus is low, and the absorber has emerged higher off the torus. When a higher scale height piece of the torus rotates into our line of sight, we're looking through mostly dust, and the BAL is nearly completely obscured (as seen in 2015).

3.4 Summary

WPVS007 is the first ever observed UV occultation event. Its BAL and reddening variability support the broad absorption line gas natural origin in the dusty, gas-rich torus. But what about WPVS007 is otherwise so unique? WPVS007's low luminosity and small black hole mass allow for a shorter variability timescale, possible on human timescales. Indeed Leighly et al. (2009) compared WPVS007 and 100× more luminous LBQS1212+1445 and found the difference in time scales to favor WPVS007 by a factor of 10. While the emergence of BAL gas from the dusty torus seems a natural explination, further monitoring is needed to fully test the prediction that as WPVS007 emerges from the occultation (as it has been since March 2015), we would observe an increase in the BAL maximum velocity, deepening of the trough, and a broadening of the C IV emission line. Further testing is also needed to see whether the explanation is extendible to other objects, though for most objects the time scales necessary are probably prohibitive.

Chapter 4

Ultraviolet Iron Emission in Strong Iron Emitting AGN in the SDSS

Fe II emission poses a long-standing yet important problem in studies of quasar broad emission lines. Fe II emission is a primary coolant of the broad-line region, a primary player in the set of emission line correlations known as Eigenvector 1, and can potentially yield information about metallicities in the early Universe. While it is generally thought that UV Fe II emission has the same general shape in quasars, varying only in equivalent width, Leighly et al. (2007) identified two characteristic shapes. Typical strong iron emitting quasars exhibit somewhat rounded Fe II emission in the $\sim$ $2250 - 2650$Å region while PHL 1811-like strong iron emitting quasars exhibit additional Fe II emission in the $\sim$ $2250 - 2650$Å region and excess emission in the regions $\sim 2050 - 2150$Å and $\sim 1900 - 2000$Å. These regions are highlighted in Figure 4.1. Leighly et al. hypothesized the difference in shape arises from differences in Fe excitation and ionization in these strong Fe emitters: that the emission in typical strong iron emitters arises from less excited levels of Fe II, and in PHL 1811-like spectra the emission arises from more highly excited levels Fe II and also some Fe III.

Here we probe the near UV Fe emission in quasars by modeling strong Fe emitters with templates generated using the atomic data in the Kurucz database. We populate the levels as in a thermal gas, and allow them to depart from equiliibrium in groups of upper level energy. We emphasize that this is an empirical model, intended as a

tool to investigate and quantify differences in Fe emission among strong Fe emitting AGN.

4.1 "Normal" vs. "PHL 1811-like" Emission: The Puzzle

When analyzing the UV emission in PHL 1811 with the I Zw 1 Fe II template of Vestergaard & Wilkes (2001), Leighly et al. (2007) found that while the template fit quite well near the Mg II $\lambda\lambda 2798, 2803$Å doublet, it fell short at shorter wavelengths (particularly the region $2300 - 2500$Å). Their Figure 5 demonstrates that other objects share PHL 1811's unusual Fe emission shape. Visual inspection of 81 strong iron emitting quasars in the SDSS reveals a total of 26 objects ($\sim 32\%$) sharing PHL 1811's unusual shape, 44 objects ($\sim 54\%$) having the more typical rounded shape of I Zw 1, and the remaining 11 objects ($\sim 14\%$) having a third, possibly intermediate shape. Note that these objects do not form a complete sample, so the fractional occurrance is merely illustrative. We choose a sample of 6 each of typical and PHL 1811-like shape to model with our empirical Fe templates. Details of the sample are given in Table 4.1

To investigate the unusual Fe emission in PHL 1811, Leighly et al. (2007) plot, in Figure 6, the spectrum of PHL 1811 along with the Fe II and Fe III atomic transition upper level energies, differentiated by the strength of the transition probability, A_{ij}. Fe has an especially rich spectrum of line transitions in the UV and the locations of particularly strong transitions in the vicinity of PHL 1811's emission excess suggests the emission may arise from both Fe III and more highly excited transitions of Fe II.

Target	RA	DEC	z
Typical Fe Shape			
J124244.37+624659.1	190.68486	62.783	1.2953
J105023.68-010555.5	162.60000	−1.0850	1.536421
J172314.14+654746	260.80893	65.7961	1.4409
J092332.32+574557.3	140.88472	57.76595	1.3784
J091301.03+525928.9	138.25424	52.99138	1.3785
J120702.40+492853.2	181.76002	59.48145	1.3745
PHL 1811-like Fe Shape			
PHL 1811	328.7583	−9.3733	0.192
J094257.808-004705.2	145.7417	−0.7847	1.362837
J014940.12+0.001718.0	27.41718	0.28834	1.4641
J143613.18+045400.0	219.05495	4.90002	1.4224
J231253.05+144453.3	348.22102	14.74817	1.5261
J094021.12+033144.7	145.08802	3.52911	1.294

Table 4.1: Sample Information.

In order to contrast the shapes of the typical strong iron emitting quasar with those like PHL 1811, Figure 4.1 reproduces the essence of their Figure 6, but includes a typical Fe shaped spectrum, J091301.03+525928.9, and shades the interesting regions to highlight the Fe II bump (light grey) and Fe III excess flux regions (darker grey).

4.2 A Thermal Model

Our current aim is to investigate whether Fe III and highly excited Fe II explain the excess emission observed in objects like PHL 1811. We cannot simply use the popular photoionization code Cloudy (Ferland et al. (2013)) to simulate the Fe emission as it does not have sufficient atomic data available to generate the specific spectra we need. Bruhweiler & Verner (2008) produced and inserted into Cloudy an 830 level Fe II atom up to 14.06 eV, nearly the upper level energy we employ

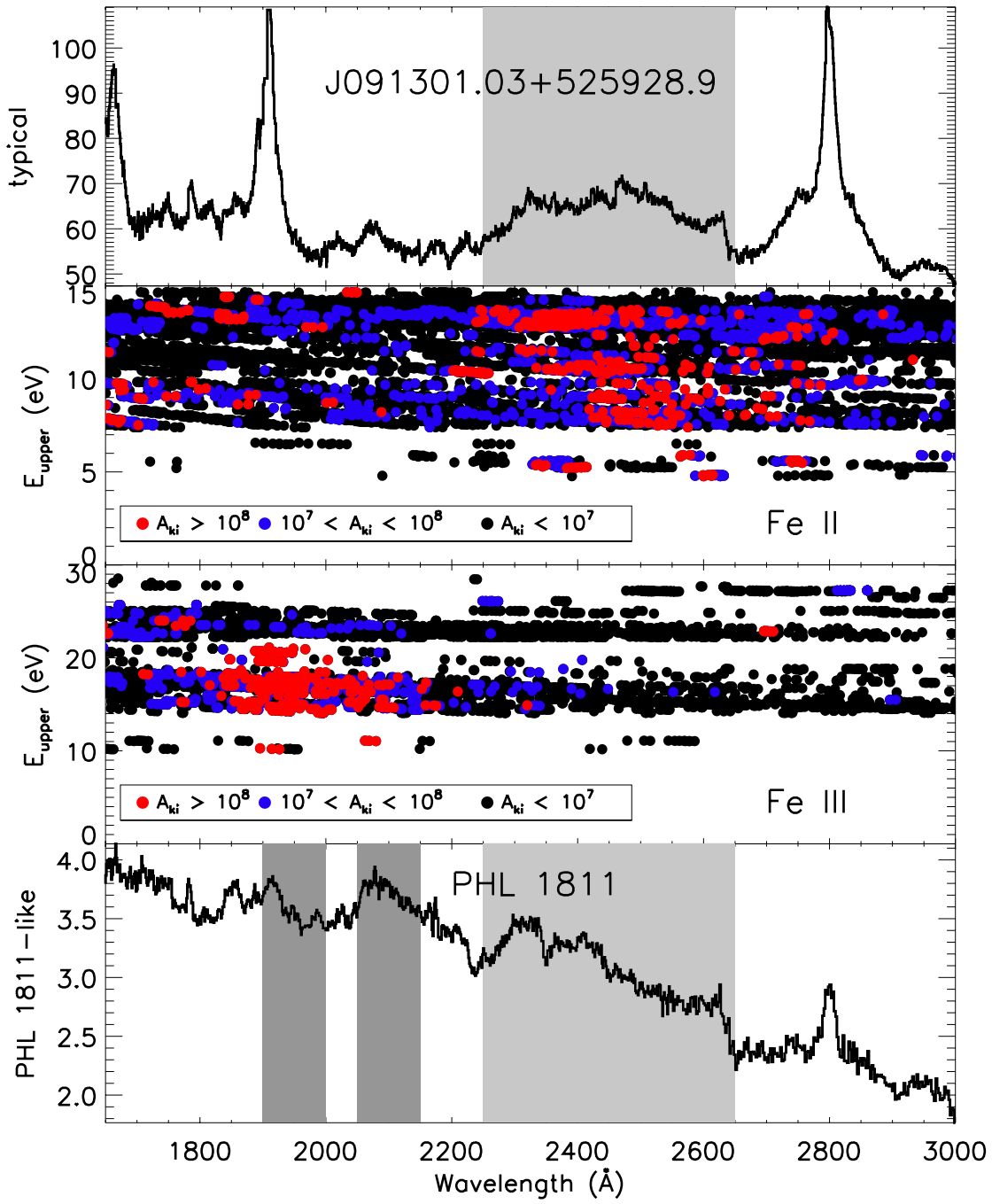

Figure 4.1: Fe Shape Examples: Typical vs. PHL 18111-like, with A_{ki}s for each ion plotted in upper level energy for reference.

here, but did not make it publicly available. The most up to date Fe II atom in Cloudy is the 371 level model of Verner et al. (1999), which includes levels up to 11.6eV while the ionization potential of Fe^{+} is 16.18eV. Regardless, the available Fe III data in Cloudy is completely insufficient for our purposes as no model atom for Fe^{+2} currently exists in the code. Lykins et al. (2015) cite two sources for the Fe III atomic data in Cloudy: Zhang (1996), up to 1.127 Ry = 15.327 eV, and Kurucz (2009), which makes no mention of Fe III. As a result, we use the more uncertain data in the Kurucz database (Kurucz & Bell (1995)).

Additionaly, Joly et al. (2007) and Joly et al. (2008), when investigating the optical spectrum of strong Fe II emitter IRAS 07598+6508, concluded that photoionization was unable to explain the observed line ratios and that a small, dense, cloud shielded from the central engine produced the best results. In such conditions the excitation and ionization are driven by collisions rather than photons. This collisional requirement motivates our thermal model.

We start with all the transitions available in the Kurucz database for each ion and group them by upper level energy. These ranges are shown in Table 4.2. We use a zeroth order approach and generate a set of templates of added gaussian lines whose amplitudes and widths are assigned as follows. We populate the levels as in a thermal gas and allow all radiation to exit the gas. For a thermal gas, the levels are populated according to the Boltzmann equation, relative to ground:

$$\frac{N_k}{N_{ground}} = \frac{g_k}{g_{ground}} e^{-\frac{E_k}{kT}}$$

If k is the upper level of the transition and i is the lower, the power radiated in each line as given by Drake (2006) Eq. 10.11:

$$\epsilon_{line} = \frac{hc}{4\pi\lambda_0} A_{ki} N_k$$

and the total emitted line intensity is related to the line profile, $I(\lambda)$ by:

$$I_{line} = \int \epsilon_{line} dV = \int I(\lambda) d\lambda$$

We assign amplitudes according to ϵ_{line} relative to N_{ground}:

$$Amplitude = \frac{\epsilon_{line}}{N_{ground}} = \frac{h\,c\,A_{ki}}{4\pi\lambda_0}(2J_k + 1)e^{-\frac{E_k}{kT}}$$

Within each group the distribution of energy levels is thermal. We produce a template for each group of upper level energies for each ion and allow them to depart from equilibrium in those groups. The departure coefficients of the groups of upper levels are related to the template amplitudes in the fits, but because the amplitudes depend on the ground state population, N_{ground}, we will compute departures relative to the lowest upper level energy bin.

Osterbrock & Ferland (2006) suggest a good approximate estimate of the temperature in Broad Line Region (BLR) to be $\sim 10^4$ K, since T > 35,000 K would ionize almost all of the Fe II to Fe III. We adopt their suggested value here. We also assign a full width at half maximum velocity width of 1,000 $\mathrm{km\,s^{-1}}$ to each line in the template, based on the measurements of the relatively isolated Fe II UV 191

template designation	Upper Level Energy Ranges (eV) Fe II	Fe III	Ni II	Ni III
a	4-7	10-12	6-10	13-16
b	7-10	12-22	10-14	16-19
c	10-12	22-29	14-18	19-24
d	12-15			24-31

Table 4.2: Upper Level Energy Ranges for Template Partitions.

multiplet in each spectrum.

Figures 4.2 and 4.3 show the Fe II and Fe III templates, respectively, along with their transitions, differentiated in color by their transition probability.

When fitting our sample spectra, we discovered our templates cannot fit the characteristic bump that straddles 2200Å, as no significantly strong Fe lines exist there. To remedy this problem, we looked at transitions and generated templates for other Fe peak elements, metals with sufficient lines to be effective coolants and significant abundance so as to be plausible. Ni fits those requirements and Ni II's lower level transitions reproduce the characteristic 2200Å bump, so we include those templates in our spectral fitting also.

4.3 Spectral Fitting

We fit our sample of strong Fe emitting quasar spectra using the CIAO modeling and fitting application, Sherpa (4.7.1), inside an iPython notebook. First we fit a power law and gaussian lines to the Mg II doublet ($\lambda\lambda 2798, 2803$Å), C III] ($\lambda 1909$Å),

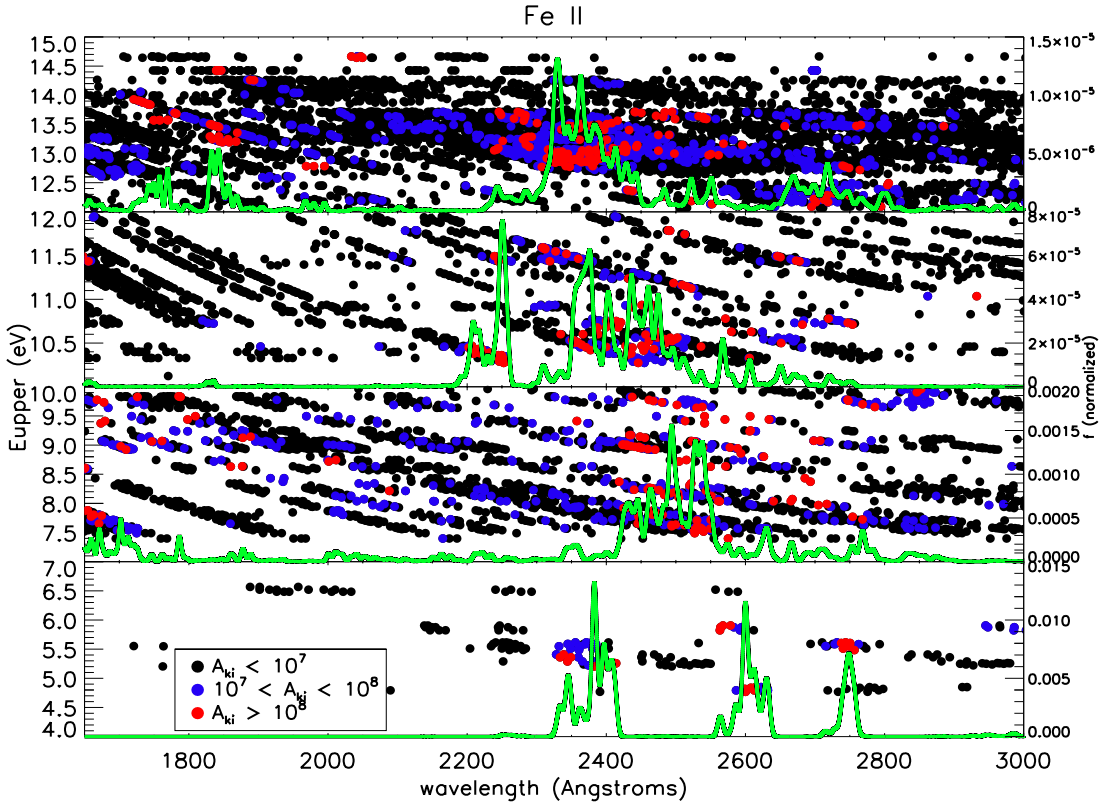

Figure 4.2: Fe II Models and A_{ki}s separated by upper level energy of transition.

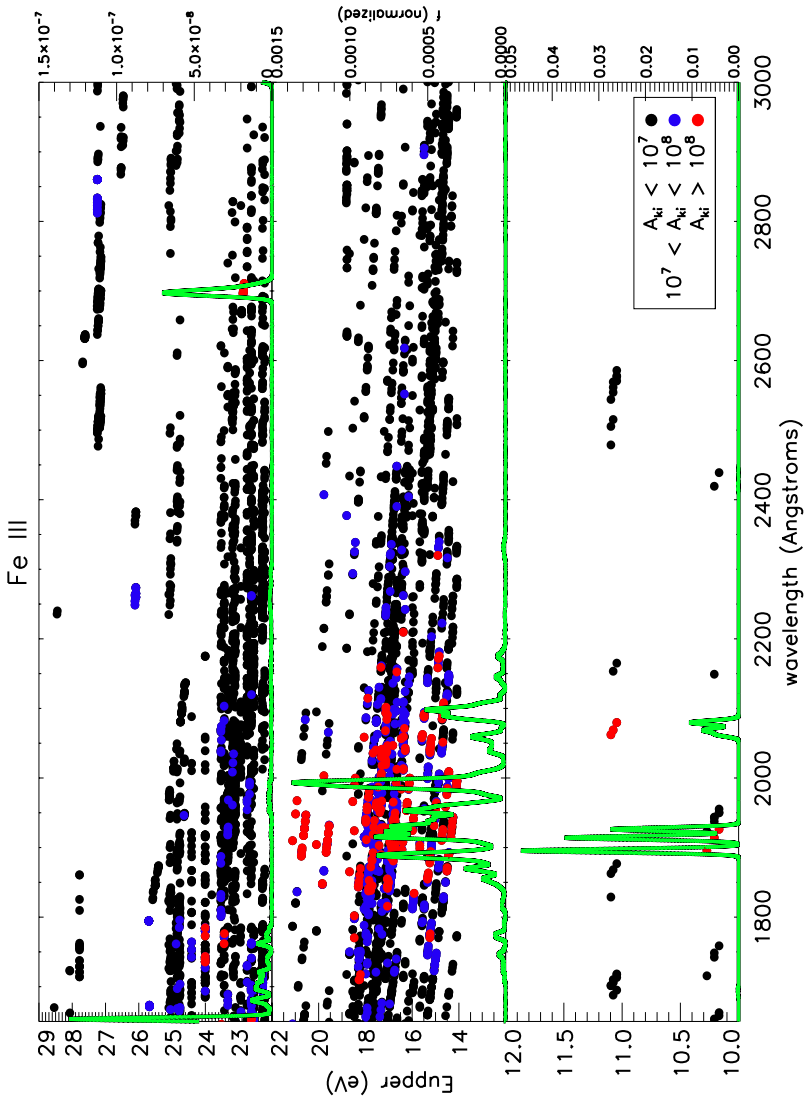

Figure 4.3: Fe III Models and A_{ki}s separated by upper level energy of transition.

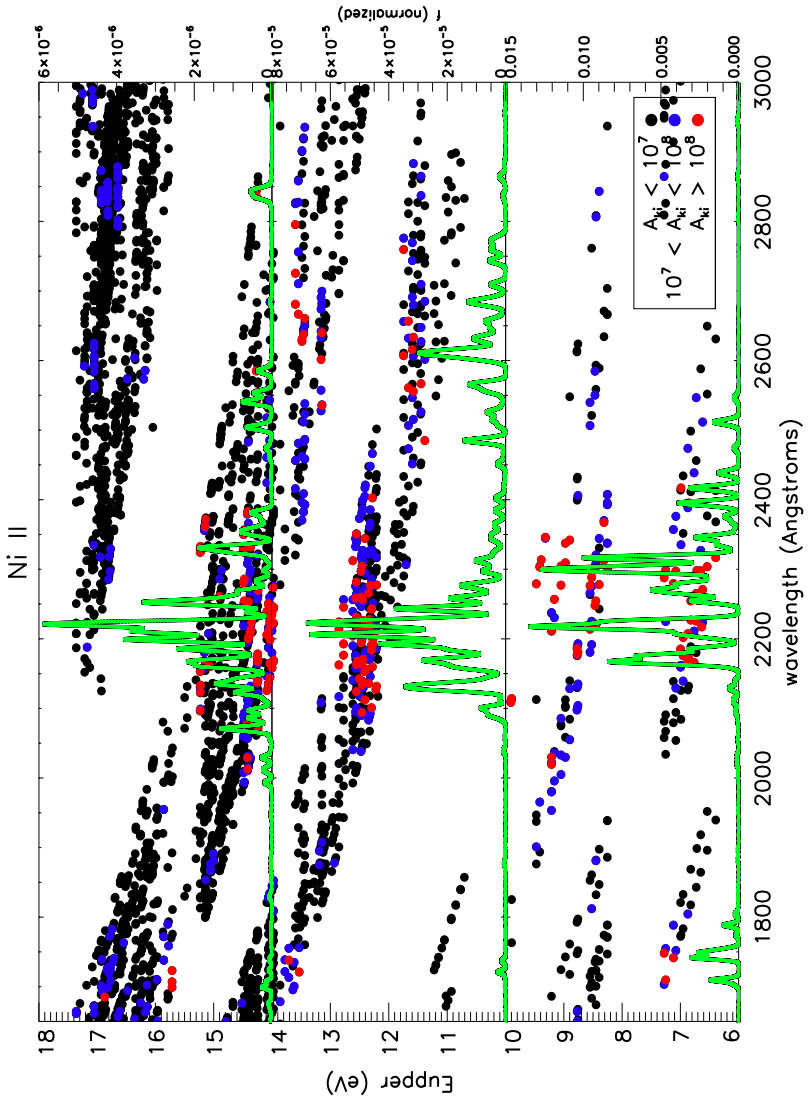

Figure 4.4: Ni II Models and A_{ki}s separated by upper level energy of transition.

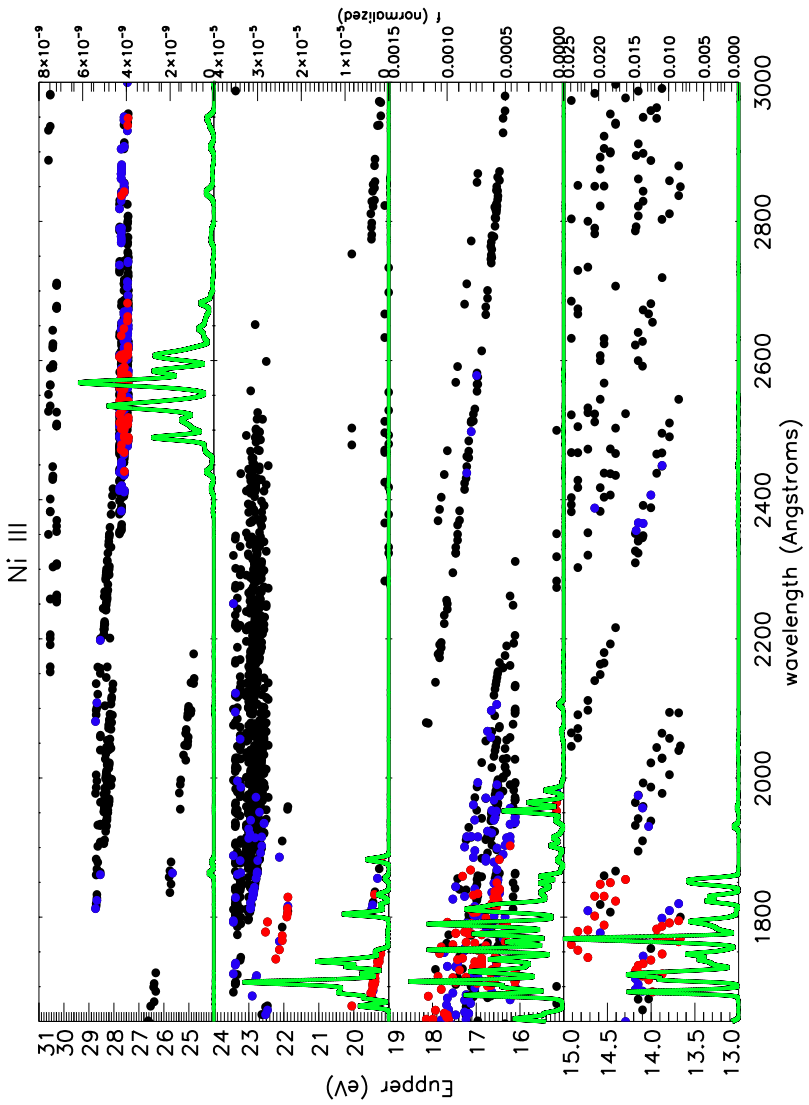

Figure 4.5: Ni III Models and A_{ki}s separated by upper level energy of transition.

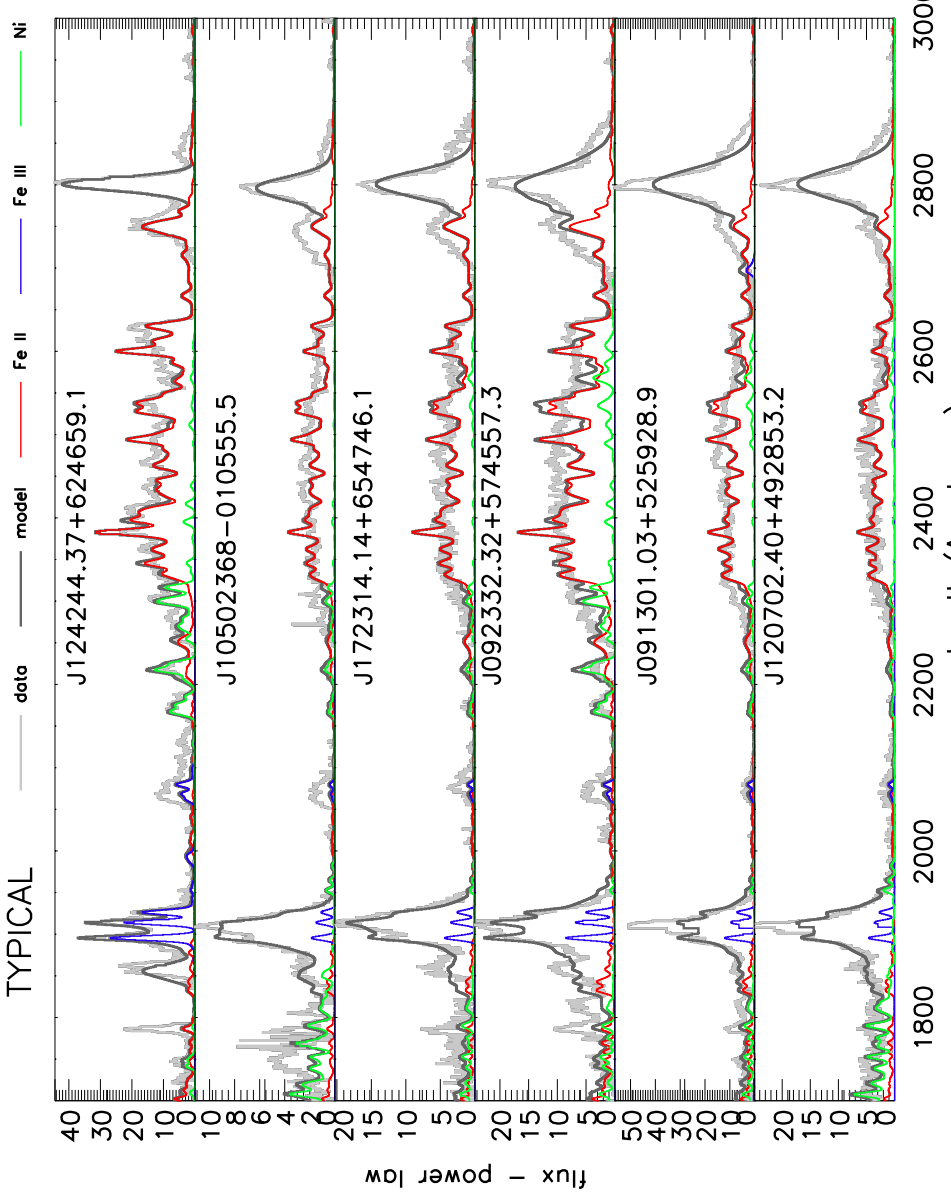

Figure 4.6: Spectral Fits: Typical Fe Shape

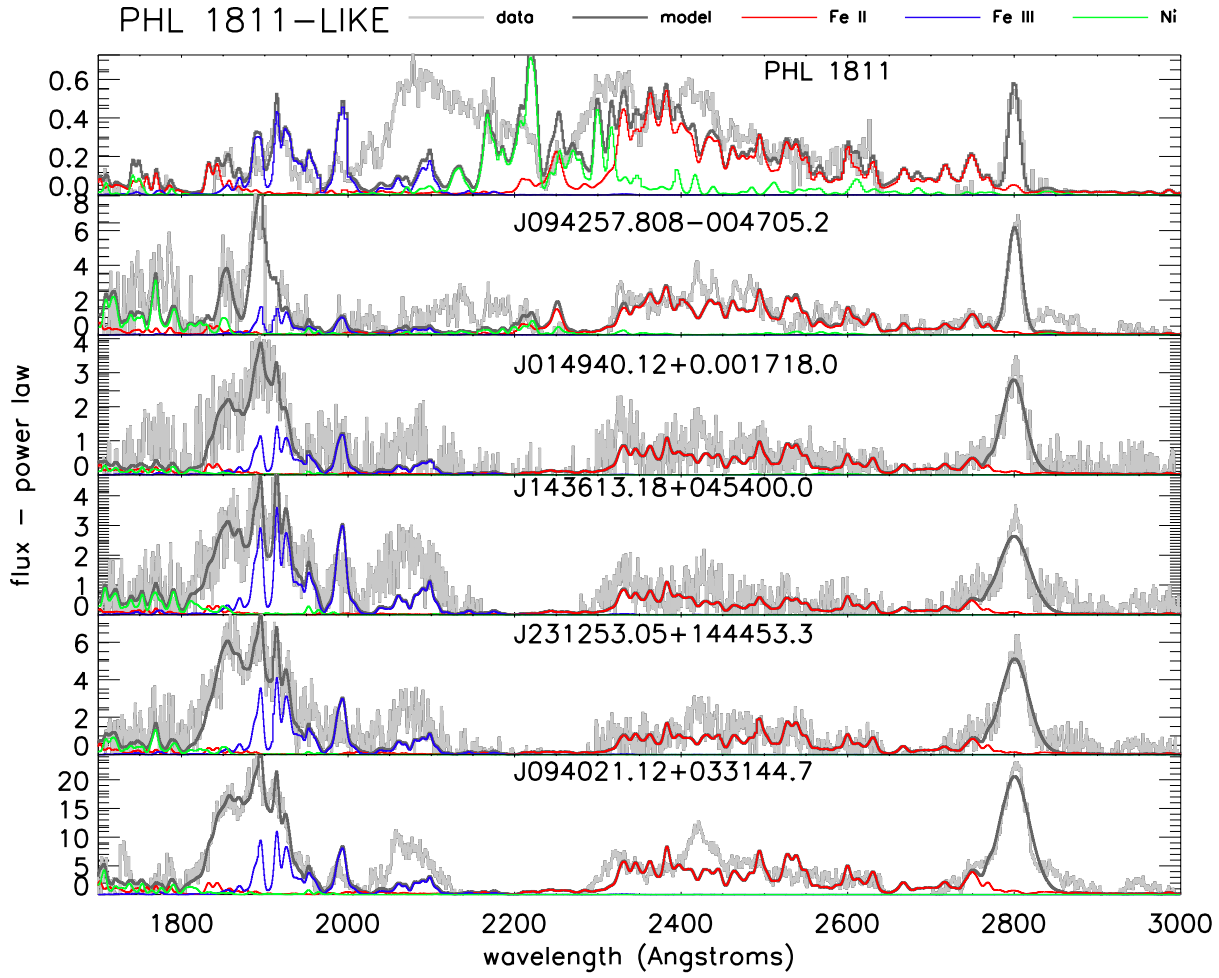

Figure 4.7: Spectral Fits: PHL 1811-like Fe Shape

Si III] (λ1892Å), and Al III (λ1855Å), while ignoring the Fe pseudo-continuum. Their widths and positions are constrained relative to the red line of the Mg II doublet. Finally we add in the templates, loaded as table models whose only tunable parameter is the amplitude, and fit to convergence.

4.4 Results

The resulting fits are shown in figures 4.6 and 4.7 for the Typical and PHL1811-like spectra, respectively. The fitted power law has been subtracted from each spectrum to highlight the fit to the emission.

The breakdown of the Fe II template fits to the Fe II bump in each target is shown in Figure 4.8. Visually we can see the relative strength of higher ionization Fe II shift in PHL 1811-like targets compared to Typical Strong Fe Emitting targets. In typical targets, the 12-15 eV template is weak relative to the 7-10 eV one, whereas in PHL 1811-like targets the amplitudes of both templates are comparable. This shows that PHL 1811-like targets require higher excitation Fe II, as predicted.

Table 4.3 also shows the breakdown of Fe II fit by the templates as a fraction of the total Fe II emission fit. Although all targets show the highest fraction of Fe II fit in the most highly excited bin, $E_{up} = 12 - 15$eV, the PHL 1811-like targets show a higher fraction in that bin relative to the to the more typical targets, which was predicted. Table 4.4 shows the fractions of Fe fit by each ion, Fe II and Fe III. As predicted, the PHL 1811-like targets mostly show a stronger fraction of Fe fit by Fe III, although there is some overlap of J094257.808-004705.2 with the more typical

targets. This is also true of the FeIId/FeII fraction for J094257.808-004705.2. That target also has a higher fraction of FeIIc/FeII, $E_{up} = 10 - 12$eV, relative to the other PHL 1811-like targets, possibly placing it as an intermediate target.

Some obvious inadequacies stand out in the final fits. The Fe II bump edge near ~ 2600Å is fit particularly poorly, as is the width of the Fe II clump just to the blue of the Mg II doublet. Our final fit of the prototypical PHL 1811 is particularly poor across the spectrum and continues to have excess emission in the $\sim 2050 - 2150$Å region. The final fit of J094257.808-004705.2 is better, but still has excess emission in the $\sim 2050 - 2150$Å region. The rest of the so-called PHL 1811-like targets are fit considerably better across the spectrum, with the exception of a spike of excess emission around ~ 2450Å, which appears in all PHL 1811-like targets.

Selective pumping may be important for some transitions, particularly the Fe II UV 191 1787Å triplet, which is poorly fit by the templates in most objects. Baldwin et al. (1996) suggest UV 191 may be pumped from UV9 1265Å or from a chance overlap with Si II 1263Å, which itself must be pumped to reproduce their observed Si II lines. Sigut & Pradhan (1998) demonstrate Lyα's significance in powering the near-IR Fe II 9200$\mathring{A}$ bump. The subsequent cascade powers several UV transitions, including those near the Mg II doublet.

4.4.1 Departure Coefficients

We started with a simple, thermal model, but just how far do our results depart from equilibrium? As mentioned previously, that the fit coefficients depend on the ground state population means we need to normalize relative to the lowest upper

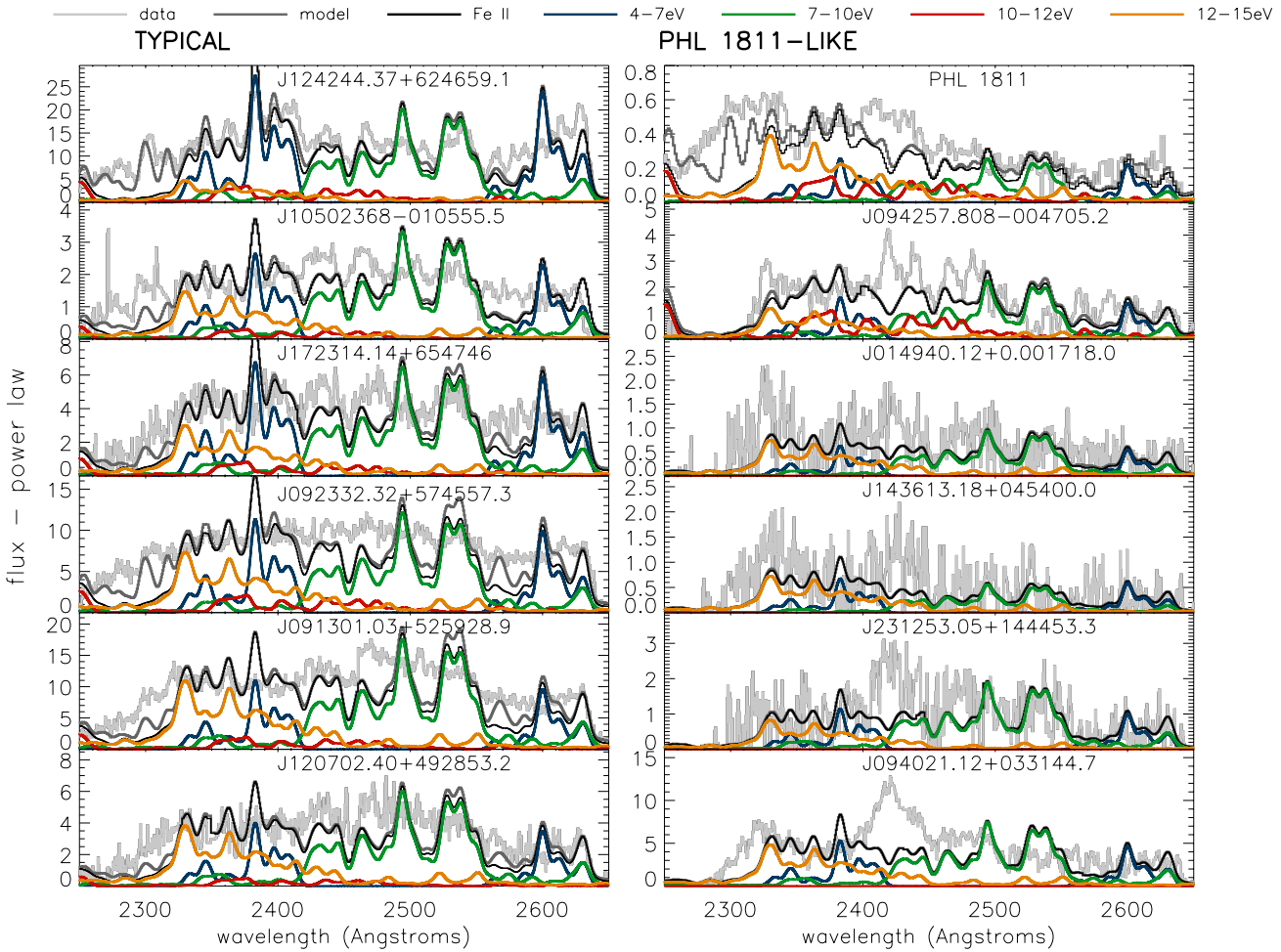

Figure 4.8: Spectral Fits: Fe II Breakdown

Target	FeIIa/FeII	FeIIb/FeII	FeIIc/FeII	FeIId/FeII
Typical Fe Shape				
J124244.37+624659.1	0.309	0.459	0.091	0.140
J10502368-010555.5	0.191	0.481	0.049	0.279
J172314.14+654746	0.229	0.441	0.063	0.267
J092332.32+574557.3	0.190	0.409	0.080	0.321
J091301.03+525928.9	0.139	0.445	0.054	0.363
J120702.40+492853.2	0.147	0.445	0.041	0.368
PHL 1811-like Fe Shape				
PHL 1811	0.120	0.240	0.159	0.481
J094257.808-004705.2	0.137	0.385	0.212	0.266
J014940.12+0.001718.0	0.140	0.421	0.000	0.439
J143613.18+045400.0	0.181	0.303	0.000	0.517
J231253.05+144453.3	0.161	0.535	0.000	0.305
J094021.12+033144.7	0.161	0.453	0.000	0.386
Thermal Equilibrium, $10^4\,K$	**0.789**	**0.200**	**0.009**	**0.002**

Table 4.3: Fe II Results: Fraction of the fitted Fe II flux from each upper level energy bin.

level energy bin to excise its influence. Table 4.5 gives the departure coefficients relative to that lowest bin. As might be expected, the upper levels depart are significantly overpopulated relative to equilibrium, departing by a few to several orders of magnitude. The uppermost levels of the PHL1811-like targets appear to depart more than the typical ones, though there is significant overlap.

4.5 Comparison to Other Templates

4.5.1 Vestergaard & Wilkes: 1Zw1

This investigation began with the inability of the Vestergaard & Wilkes (2001) 1Zw1 template to fit the Fe pseudo-continuum in PHL 1811 and other like objects. So how well do our models fit the 1Zw1 template? Figure 4.9 shows the results, with the

Target	FeII/Fe	FeIII/Fe
Typical Fe Shape		
J124244.37+624659.1	0.891	0.109
J10502368-010555.5	0.944	0.056
J172314.14+654746	0.957	0.043
J092332.32+574557.3	0.958	0.042
J091301.03+525928.9	0.739	0.261
J120702.40+492853.2	0.950	0.050
PHL 1811-like Fe Shape		
PHL 1811	0.797	0.203
J094257.808-004705.2	0.888	0.112
J014940.12+0.001718.0	0.749	0.251
J143613.18+045400.0	0.498	0.502
J231253.05+144453.3	0.645	0.355
J094021.12+033144.7	0.757	0.243

Table 4.4: Total Fe Results: Fraction of the fitted Fe flux from each ion, Fe II and Fe III.

templates of Fe II in the upper panel and those of Fe II in the lower. Our models are unable to satisfactorily fit the blue edge of the Fe II bump, though fits to all our targets suggest Ni may do well here and with the double bump surrounding $\sim$ 2200Å. The width of the Fe II clump to the blue of the Mg II doublet, as in the other targets, and the red side of the Mg II doublet is woefully underfit. Both suggest selective pumping may be important.

Target	FeIIa/FeII	FeIIb/FeII	FeIIc/FeII	FeIId/FeII
Typical Fe Shape				
J124244.37+624659.1	1.00	5.85	25.74	162.36
J10502368-010555.5	1.00	9.95	22.51	524.75
J172314.14+654746	1.00	7.59	23.93	418.83
J092332.32+574557.3	1.00	8.50	36.75	608.26
J091301.03+525928.9	1.00	12.63	33.88	938.66
J120702.40+492853.2	1.00	11.92	24.14	897.48
PHL 1811-like Fe Shape				
PHL 1811	1.00	7.89	115.05	1437.34
J094257.808-004705.2	1.00	11.11	135.35	699.26
J014940.12+0.001718.0	1.00	11.81	0.00	1121.34
J143613.18+045400.0	1.00	6.59	0.00	1026.21
J231253.05+144453.3	1.00	13.12	0.00	681.18
J094021.12+033144.7	1.00	11.07	0.00	859.74

Table 4.5: Fe II level contribution compared to Thermal Equilibrium, relative to the lowest upper energy level bin.

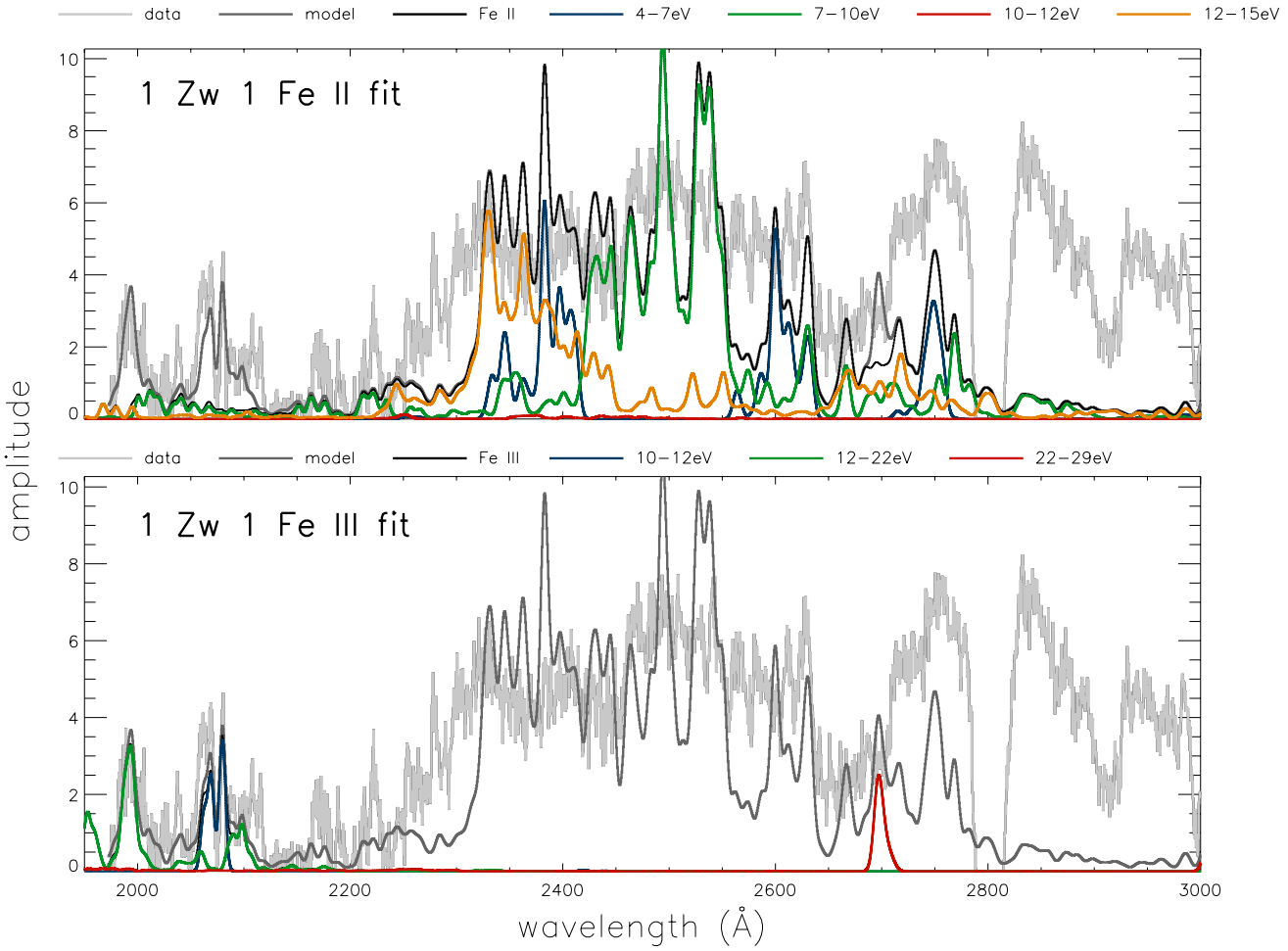

Figure 4.9: Spectral Fits: 1Zw1 Fe II and Fe III Breakdown

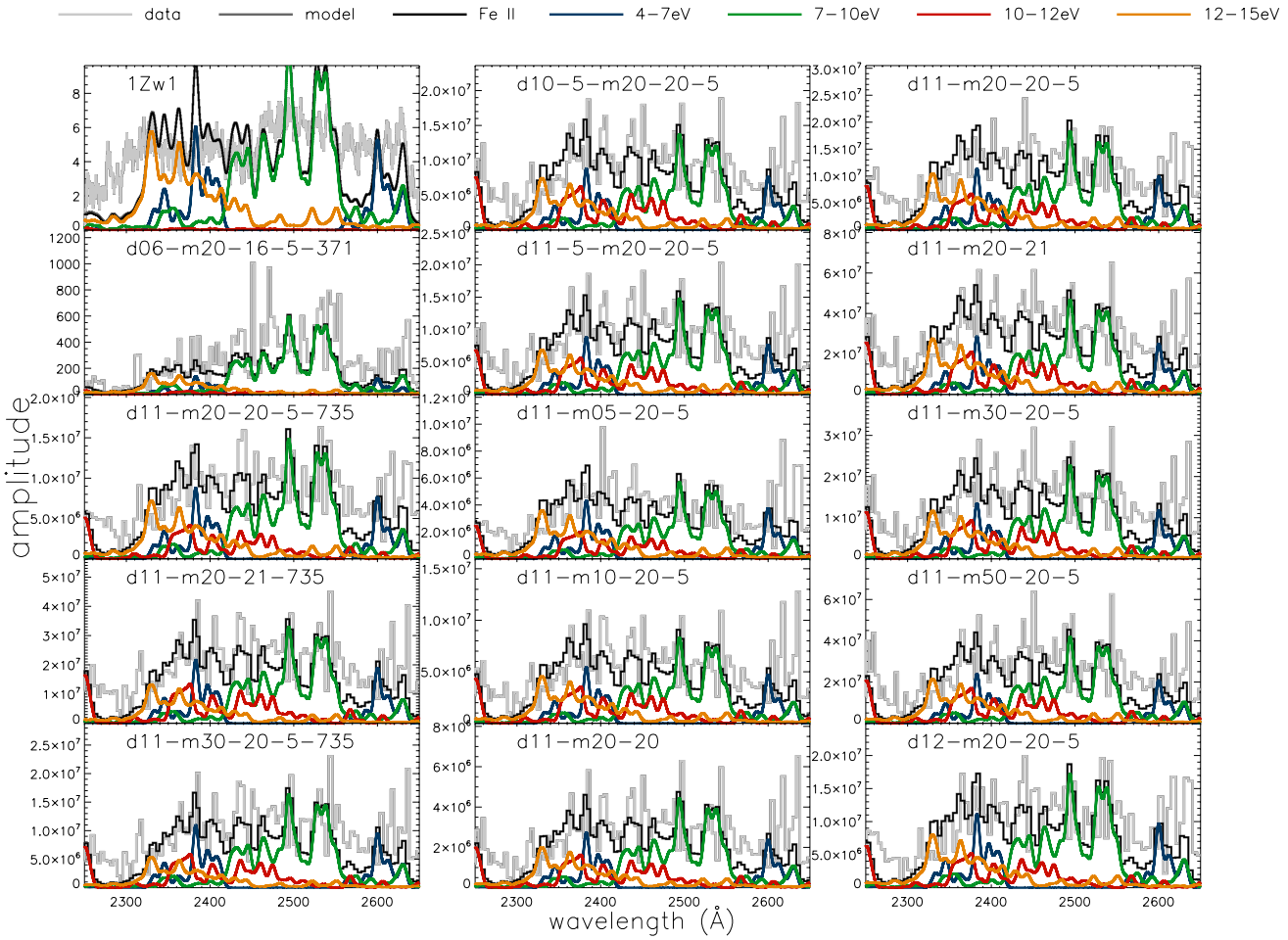

Figure 4.10: Spectral Fits: Comparison Models Fe II Breakdown

4.5.2 Bruhweiler & Verner

While Bruhweiler & Verner (2008) do not make their atomic data publicly available, they do post several template models online (available at: `http://iacs.cua.edu/personnel/personal-verner-feii.cfm`). Figure 4.10 shows the 14 available models in addition to a close up of the fit to 1Zw1. The far left panels show the fits to 1Zw1, followed by their 371 level atom model, and three models for their 735 level atom. The remaining 10 plots show fits to models for their 830 level atom. Overall, our fits are reasonable, with the exception of the bump leading off to the blue from $\sim$ 2300Å, which is consistently under fit. The Bruhweiler & Verner (2008) models would also appear to inadequately fit the blue edge of the Fe II bump in 1Zw1, as ours do.

Visual inspection of our fits to the Bruhweiler models show weak 12-15 eV Fe II relative to the 7-10 eV Fe II, as was seen in the fits of our typical targets and for 1Zw1. This coupled with a lack of Fe III indicates these models would also be a poor fit for our PHL1811-like targets. The biggest factor in achieving comparable 12-15 eV and 7-10 eV Fe II seems to be the inclusion of more levels, 371 to 735 to 870. This should not be surprising since the inclusion of more energy levels contributes to the highest excitation bin, but no trend with density, ionization or microtubulance parameter is observed.

4.6 Conclusions

Although our model is simple, with levels populated thermally and the gas transparent to radiation, we are able to demonstrate that the Fe II bump in PHL 1811-like objects appears to need a larger contribution from the more highly excited levels as well as a larger contribution from Fe III.

Chapter 5

Conclusions

So what have we learned?

P V absorption is only observed in thick broad absorption line outflows and $\sim 10\%$ of the targets studied, consistent with the moderate to strong figure from Filiz Ak et al. (2014) for C IV$_{\rm S0}$ BALs. The maximum velocity of a trough is limited by its luminosity and only the most luminous targets can drive the highest velocity troughs, consistent with the envelope relationship of Laor & Brandt (2002) and Ganguly & Brotherton (2008).

The observed variability in the low luminosity, narrow line Seyfert 1 galaxy WPVS007 is consistent with arising from a variable scale height torus rotating into the line of sight. The decreased brightness, shallower, lower velocity troughs, and increased reddening point to a dusty occultation, while measures of the location of the absorbing gas put it in a location consistent with the torus. This is the first UV occultation observed.

Modeling of UV Fe II and Fe III emission in PHL1811-like AGN is consistent with a higher contribution from more highly excited levels of Fe II and additional Fe III compared with more typical strong Fe emitting AGN, as put forth by Leighly et al. (2007).

References

Anders, E., & Grevesse, N. 1989, GeCoA, 53, 197

Baldwin, J. A., Ferland, G. J., Korista, K. T., et al. 1996, ApJ, 461, 664

Barlow, T. A. 1993, PhD thesis, California University

Barlow, T. A., Junkkarinen, V. T., Burbidge, E. M., et al. 1992, ApJ, 397, 81

Bennett, C. L., Larson, D., Weiland, J. L., et al. 2013, ApJS, 208, 20

Borguet, B. C. J., Arav, N., Edmonds, D., Chamberlain, C., & Benn, C. 2013, ApJ, 762, 49

Boroson, T. A., & Green, R. F. 1992, ApJS, 80

Bostroem, K., & Proffitt, C. 2011, "STIS Data Handbook", Version 6.0, (Baltimore: STScI)

Bruhweiler, F., & Verner, E. 2008, ApJ, 675, 83

Burtscher, L., Meisenheimer, K., Tristram, K. R. W., et al. 2013, AAP, 558, A149

Capellupo, D., et al. 2013, in prep.

Capellupo, D. M., Hamann, F., Shields, J. C., Halpern, J. P., & Barlow, T. A. 2013, MNRAS, 429, 1872

Capellupo, D. M., Hamann, F., Shields, J. C., Rodríguez Hidalgo, P., & Barlow, T. A. 2011, MNRAS, 413, 908

—. 2012, MNRAS, 422, 3249

Cardelli, J. A., Clayton, G. C., & Mathis, J. S. 1989, ApJ, 345, 245

Cavaliere, A., Lapi, A., & Menci, N. 2002, ApJL, 581, L1

Chen, Z.-F., & Qin, Y.-P. 2015, ApJ, 799, 63

Dai, X., Shankar, F., & Sivakoff, G. R. 2008, ApJ, 672, 108

Drake, G. W. F. 2006, Springer Handbook of Atomic, Molecular, and Optical Physics, doi:10.1007/978-0-387-26308-3

Dunn, J. P., Arav, N., Aoki, K., et al. 2012, ApJ, 750, 143

Ferland, G. J., Porter, R. L., van Hoof, P. A. M., et al. 2013, Revista Mexicana de

Astronomia y Astrofisica, 49, 1

Ferrarese, L., & Merritt, D. 2000, ApJL, 539, L9

Filiz Ak, N., Brandt, W. N., Hall, P. B., et al. 2012a, ApJ, 757, 114

—. 2012b, ApJ, 757, 114

—. 2013, ApJ, 777, 168

—. 2014, ApJ, 791, 88

Ganguly, R., & Brotherton, M. S. 2008, ApJ, 672, 102

Ganguly, R., Brotherton, M. S., Cales, S., et al. 2007, ApJ, 665, 990

Ganguly, R., Masiero, J., Charlton, J. C., & Sembach, K. R. 2003, ApJ, 598, 922

Gibson, R. R., Brandt, W. N., Gallagher, S. C., Hewett, P. C., & Schneider, D. P. 2010, ApJ, 713, 220

Gibson, R. R., Brandt, W. N., Schneider, D. P., & Gallagher, S. C. 2008, ApJ, 675, 985

Gibson, R. R., Jiang, L., Brandt, W. N., et al. 2009, ApJ, 692, 758

Grier, C. J., Hall, P. B., Brandt, W. N., et al. 2015, ApJ, 806, 111

Grupe, D., Komossa, S., Scharwächter, J., et al. 2013, AJ, 146, 78

Grupe, D., Leighly, K. M., & Komossa, S. 2008, AJ, 136, 2343

Grupe, D., Schady, P., Leighly, K. M., et al. 2007, AJ, 133, 1988

Hall, et al. 2002, ApJS, 141, 267

Hall, P. B., Anosov, K., & White, R. L. 2011, MNRAS, 411, 2653

Hall, P. B., Sadavoy, S. I., Hutsemekers, D., Everett, J. E., & Rafiee, A. 2007, ApJ, 665, 174

Hamann, F., Capellupo, D., Chartas, G., et al. 2012, in "Nuclei of Seyfert galaxies and QSOs - Central engine conditions of star formation"

Hamann, F. W., Barlow, T. A., Chaffee, F. C., Foltz, C. B., & Weymann, R. J. 2001, ApJ, 550, 142

Hopkins, P. F., & Elvis, M. 2010, MNRAS, 401, 7

Joly, M., Véron-Cetty, M., & Véron, P. 2007, in Astronomical Society of the Pacific Conference Series, Vol. 373, The Central Engine of Active Galactic Nuclei, ed. L. C. Ho & J.-W. Wang, 376

Joly, M., Véron-Cetty, M., & Véron, P. 2008, in Revista Mexicana de Astronomia y Astrofisica Conference Series, Vol. 32, Revista Mexicana de Astronomia y Astrofisica Conference Series, 59

Joshi, R., Chand, H., Srianand, R., & Majumdar, J. 2014, MNRAS, 442, 862

Junkkarinen, V. T., Cohen, R. D., Hamann, F., & Shields, G. A. 2001, in Bulletin of the American Astronomical Society, Vol. 33, American Astronomical Society Meeting Abstracts #198, 897

Kelly, B. C. 2007, ApJ, 665, 1489

Kishimoto, M., Hönig, S. F., Antonucci, R., et al. 2011, AAP, 536, A78

Kokubo, M., Morokuma, T., Minezaki, T., et al. 2014, ApJ, 783, 46

Kraemer, S. B., Crenshaw, D. M., George, I. M., et al. 2002, ApJ, 577, 98

Kurucz, R. L. 2009, in American Institute of Physics Conference Series, Vol. 1171, American Institute of Physics Conference Series, ed. I. Hubeny, J. M. Stone, K. MacGregor, & K. Werner, 43–51

Kurucz, R. L., & Bell, B. 1995, 1995 Atomic Line Data, Kurucz [CD-ROM] No. 23. Cambridge, Mass: Smithsonian Astrophysical Observatory

Laor, A., & Brandt, W. N. 2002, ApJ, 569, 641

Leighly, K. M., Cooper, E., Grupe, D., Terndrup, D. M., & Komossa, S. 2015, 809, L13

Leighly, K. M., Halpern, J. P., Jenkins, E. B., & Casebeer, D. 2007, ApJS, 173, 1

Leighly, K. M., Hamann, F., Casebeer, D. A., & Grupe, D. 2009, ApJ, 701, 176

Leighly, K. M., Terndrup, D. M., Gallagher, S. C., & Lucy, A. B. 2016, ArXiv e-prints, arXiv:1604.03456

Lucy, A. B., Leighly, K. M., Terndrup, D. M., Dietrich, M., & Gallagher, S. C. 2014, ApJ, 783, 58

Lundgren, B. F., Wilhite, B. C., Brunner, R. J., et al. 2007, ApJ, 656, 73

Lykins, M. L., Ferland, G. J., Kisielius, R., et al. 2015, ApJ, 807, 118

Massa, D., York, B., et al. 2013, "COS Data Handbook", Version 2.0, (Baltimore: STScI)

Miller, B. P., Welling, C. A., Brandt, W. N., & Gibson, R. R. 2012, in "AGN Winds in Charleston", Vol. 460, 118

Osterbrock, D. E., & Ferland, G. J. 2006, Astrophysics of gaseous nebulae and active galactic nuclei

Pâris, I., Petitjean, P., Aubourg, E., et al. 2012, A&A, 548, A66

Pâris, I., Petitjean, P., Aubourg, É., et al. 2014, A&A, 563, A54

Pei, Y. C. 1992, ApJ, 395, 130

Scannapieco, E., & Oh, S. P. 2004, ApJ, 608, 62

Schegel, D. J., Finkbeiner, D. P., & Davis, M. 1998, ApJ, 500, 525

Shankar, F., Dai, X., & Sivakoff, G. R. 2008, ApJ, 687, 859

Sigut, T. A. A., & Pradhan, A. K. 1998, ApJL, 499, L139

Smith, L. J., & Penston, M. V. 1988, MNRAS, 235, 551

Srianand, R., Petitjean, P., Ledoux, C., & Hazard, C. 2002, MNRAS, 336, 753

Steffen, A. T., Strateva, I., Brandt, W. N., et al. 2006, AJ, 131, 2826

Verner, E. M., Verner, D. A., Korista, K. T., et al. 1999, ApJS, 120, 101

Vestergaard, M., & Peterson, B. M. 2006, ApJ, 641, 689

Vestergaard, M., & Wilkes, B. J. 2001, ApJS, 134, 1

Vivek, M., Srianand, R., Mahabal, A., & Kuriakose, V. C. 2012, MNRAS, 421, L107

Voit, G. M., Shull, J. M., & Begelman, M. C. 1987, ApJ, 316, 573

Weymann, R. J., Morris, S. L., Foltz, C. B., & Hewett, P. C. 1991, ApJ, 373, 23

Zhang, H. 1996, AAS, 119, 523

Zheng, W., Kriss, G. A., Telfer, R. C., & Grimes, J. P. 1997, ApJ, 475, 469

Appendix A

Acronyms

AGN Active Galactic Nucleus

BAL Broad Absorption Line

BALQSO Broad Absorption Line Quasi-Stellar Object

BLR Broad Line Region

BOSS Baryon Oscillation Spectroscopic Survey

CIAO Chandra Interactive Analysis of Observations

COS Cosmic Origins Spectrograph

FITS Flexible Image Transport System

FOS Faint Object Spectrograph

FUV Far UltraViolet

HLSP Higher Level Science Product

HST Hubble Space Telescope

IDL Interactive Data Language

ISM Interstellar Medium

MAST Barbara A. Mikulski Archive for Space Telescopes

NED NASA/IPAC Extragalactic Database

NIST National Institutes of Standards and Technology

NUV Near UltraViolet

POA Post-Operational Archives

PyRAF Python-based interface to the Image Reduction and Analysis Facility (IRAF)

SDSS Sloan Digital Sky Survey

SNR signal-to-noise ratio

ST-ECF Space Telescope - European Coordinating Facility

STIS Space Telescope Imaging Spectrograph

STScI Space Telescope Science Institute

Swift UVOT Swift UV-optical Telescope

Appendix B

P v Project: Parameters of Interest and Their Estimated Errors

This appendix explains the origin and shows the derivation of the quantities measured in the P V Project, described in Chapter 2.

B.1 Direct Parameters

The following parameters are gathered directly from the data or normalized flux without depending on the derivation of the optical depth profile.

B.1.1 log luminosity

The only spectral region common to all of the targets in our sample is that covered by P V $\lambda\lambda 1118\text{Å}, 1128\text{Å}$. For that reason we choose to define our luminosity based on the flux at the oscillator strength weighted average of the P V doublet line, 1121Å. Because any given spectrum may have absorption in the immediate vicinity, we take the flux at this wavelength from the modeled flux, I_0, instead of directly from the data.

The flux measured at Earth is related to the intrinsic luminosity of the AGN by the geometric dilution factor:

$$L = 4\pi\, D_L^2\, F \tag{B.1}$$

where L is the luminosity in question, F is the flux taken at the wavelength described above, and D_L is the luminosity distance, which is related to the comoving transverse

distance, D_M, by:

$$D_L = (1+z)\, D_M \tag{B.2}$$

D_M is related by the comoving radial distance, D_C, by

$$D_M = \begin{cases} \frac{D_H}{\sqrt{\Omega_k}} \sinh(\sqrt{\Omega_k}\frac{D_C}{D_H}) & \Omega_k > 0 \\ D_C & \Omega_k = 0 \\ \frac{D_H}{\sqrt{|\Omega_k|}} \sin(\sqrt{|\Omega_k|}\frac{D_C}{D_H}) & \Omega_k < 0 \end{cases} \tag{B.3}$$

D_H is the Hubble distance and $D_H = c/H_0$, the speed of light divided by the present day value of the Hubble constant. The density parameter Ω_k is the curvature of the universe and together with Ω_M, the matter density, and Ω_Λ, the dark energy density, sum to 1:

$$\Omega_M + \Omega_\Lambda + \Omega_k = 1 \tag{B.4}$$

For the cosmological parameters, we choose the final results from *WMAP*, in Bennett et al. (2013), presented here in Table B.1. From the values in Table B.1 and Equation

parameter	value	units
Ω_M	0.2865	
Ω_Λ	0.7135	
H_0	69.32	$\mathrm{km\,s^{-1}\,Mpc^{-1}}$

Table B.1: Cosmological Parameters from *WMAP* Final Results, Bennett et al. (2013).

B.4, we see $\Omega_k = 0$, consistent with a flat universe. Equation B.3 and $\Omega_k = 0$ tell us

$D_M = D_C$. The comoving radial distance, D_C, is:

$$D_C = D_H \int_0^z \frac{dz'}{E(z')} \tag{B.5}$$

where z is the redshift of the AGN and $E(z)$ is the Hubble parameter:

$$E(z) = \sqrt{\Omega_M (1+z)^3 + \Omega_k (1+z)^2 + \Omega_\Lambda} \tag{B.6}$$

Putting Equations B.1, B.2, B.5, and B.6 together, we get

$$L = 4\pi \, (1+z)^2 \left(\frac{c}{H_0}\right)^2 \Big[\int_0^z \frac{dz'}{\sqrt{\Omega_M (1+z)^3 + \Omega_k (1+z)^2 + \Omega_\Lambda}} \Big]^2 F \tag{B.7}$$

Performing dimensional analysis on Equation B.7:

$$\left(\frac{[\mathrm{km\,s^{-1}}]}{[\mathrm{km\,s^{-1}\,Mpc^{-1}}]}\right)^2 [\mathrm{erg\,s^{-1}\,cm^{-2}\,\AA^{-1}}\,10^{-14}] = [\mathrm{erg\,s^{-1}\,\AA^{-1}}] \left(\frac{\mathrm{Mpc}}{\mathrm{cm}}\right)^2 10^{-14} \tag{B.8}$$

shows us we need to multiply the results of Equation B.7 by a conversion factor

$$\left(\frac{\mathrm{Mpc}}{\mathrm{cm}}\right)^2 10^{-14} = (3.08567758\mathrm{E}24)^2 \, 10^{-14} \tag{B.9}$$

to get the luminosity in $[\mathrm{erg\,s^{-1}\,\AA^{-1}}]$. We propagate the flux errors through the luminosity by calculating

$$\sigma_L = \frac{L(F+\sigma_F) - L(F-\sigma_F)}{2}. \tag{B.10}$$

For the flux errors, σ_F, we take an average of the flux errors in the vicinity of 1121Å directly from the data. Because the luminosities can span several orders of magnitude, we prefer to use the log luminosity, so we calculate $\log \mathrm{L}$ and propagate the errors accordingly:

$$(\sigma_{\log L})^2 = \left(\frac{\partial \log L}{\partial L}\sigma_L\right)^2 = \left(\frac{\sigma_L}{L \log 10}\right)^2 \tag{B.11}$$

So the error in $\log L$ is $\sigma_{\log L} = \sigma_L/(L \log 10)$.

B.1.2 $\mathrm{v_{min,ION}}$, $\mathrm{v_{max,ION}}$, and $\mathrm{width_{ION}}$

The minimum velocity, $\mathrm{v_{min,ION}}$, derives from the maximum wavelength transformed to a velocity space where zero velocity corresponds to the longer (red) wavelength of the doublet and $\mathrm{v_{max,ION}}$ derives from the minimum wavelength transformed to a velocity space where zero velocity corresponds to the shorter (blue) wavelength of the doublet. To derive the minimum and maximum velocities and the width of the absorption trough from which the profile was derived, we consider the points where the normalized flux in the trough falls (1) just below 1 and (2) to 10% below 1. Our choice of 10% below the continuum reflects the original balnicity definition of Weymann et al. (1991), where the trough was required to be 10% below the continuum with a width of $2,000\,\mathrm{km\,s^{-1}}$, excluding the first $3,000\,\mathrm{km\,s^{-1}}$ blue-ward of the emission peak. For $\mathrm{v_{max}}$ we call these $\mathrm{v_{max,<1}}$ and $\mathrm{v_{max,10\%}}$, respectively. We define $\mathrm{v_{max}}$ as the average of these two values and the error in $\mathrm{v_{max}}$, $\sigma_{\mathrm{v_{max}}}$, as half

the difference:

$$\mathrm{v_{max}} = \frac{\mathrm{v_{max,<1}} + \mathrm{v_{max,10\%}}}{2} \tag{B.12}$$

$$\sigma_{\mathrm{v_{max}}} = \frac{\left|\mathrm{v_{max,10\%}} - \mathrm{v_{max,<1}}\right|}{2} \tag{B.13}$$

and similarly for $\mathrm{v_{min}}$ and $\sigma_{\mathrm{v_{min}}}$:

$$\mathrm{v_{min}} = \frac{\mathrm{v_{min,<1}} + \mathrm{v_{min,10\%}}}{2} \tag{B.14}$$

$$\sigma_{\mathrm{v_{min}}} = \frac{\left|\mathrm{v_{min,<1}} - \mathrm{v_{min,10\%}}\right|}{2} \tag{B.15}$$

From these quantities we calculate the width in the usual way:

$$\mathrm{width} = \mathrm{v_{min}} - \mathrm{v_{max}} \tag{B.16}$$

and propagate the errors accordingly

$$\sigma_{\mathrm{width}} = \sqrt{\left(\frac{\partial \mathrm{width}}{\partial \mathrm{v_{min}}}\sigma_{\mathrm{v_{min}}}\right)^2 + \left(\frac{\partial \mathrm{width}}{\partial \mathrm{v_{max}}}\sigma_{\mathrm{v_{max}}}\right)^2} = \sqrt{\sigma^2_{\mathrm{v_{min}}} + \sigma^2_{\mathrm{v_{max}}}} \tag{B.17}$$

Each of these quantities can span several orders of magnitude, so we choose to use the logarithm instead. No target has a $|v_{min}|$ or $|v_{max}| < 1$, so we choose to preserve the negative sign as an indicator of a blue-shifted velocity rather than a negative power of ten. We define the pseudo $\log \mathrm{v_{min}}$ in the following way:

$$\log \mathrm{v_{min}} = \log_{10}(\mathrm{v_{min}})\frac{\mathrm{v_{min}}}{|\mathrm{v_{min}}|} \tag{B.18}$$

and propagate the error bars accordingly:

$$\sigma_{\log \mathrm{v}_{\min}} = \sqrt{\Big(\frac{\partial \log \mathrm{v}_{\min}}{\partial \mathrm{v}_{\min}} \sigma_{\mathrm{v}_{\min}}\Big)^2} = \frac{\sigma_{\mathrm{v}_{\min}}}{|\mathrm{v}_{\min}| \ln 10} \tag{B.19}$$

The definitions for $\log \mathrm{v}_{\max}$ and its corresponding error bars are similar:

$$\log \mathrm{v}_{\max} = \log_{10}(\mathrm{v}_{\max}) \frac{\mathrm{v}_{\max}}{|\mathrm{v}_{\max}|} \tag{B.20}$$

$$\sigma_{\log \mathrm{v}_{\max}} = \sqrt{\Big(\frac{\partial \log \mathrm{v}_{\max}}{\partial \mathrm{v}_{\max}} \sigma_{\mathrm{v}_{\max}}\Big)^2} = \frac{\sigma_{\mathrm{v}_{\max}}}{|\mathrm{v}_{\max}| \ln 10} \tag{B.21}$$

The width of the ion profile is always a positive quantity, so log width is defined in the normal way:

$$\log \mathrm{width} = \log_{10}(\mathrm{width}) \tag{B.22}$$

$$\sigma_{\log \mathrm{width}} = \sqrt{\Big(\frac{\partial \log \mathrm{width}}{\partial \mathrm{width}} \sigma_{\mathrm{width}}\Big)^2} = \frac{\sigma_{\mathrm{width}}}{\mathrm{width} \ln 10} \tag{B.23}$$

B.1.3 $\mathrm{depth}_{\mathrm{ION}}$

The depth of the ion trough occurs where the normalized flux is a minimum:

$$\mathrm{depth}_{\mathrm{ION}} = 1 - \min\Big(\frac{\mathrm{I}}{\mathrm{I}_0}\Big) \tag{B.24}$$

The errors in the depth are the same as the errors in the normalized flux at that minimum point:

$$\sigma_{\mathrm{depth}_{\mathrm{ION}}} = \sqrt{\Big(\frac{\partial \mathrm{depth}_{\mathrm{ION}}}{\partial \frac{\mathrm{I}}{\mathrm{I}_0}} \sigma_{\frac{\mathrm{I}}{\mathrm{I}_0}}\Big)^2} = \sigma_{\frac{\mathrm{I}}{\mathrm{I}_0}}\Big|_{\min(\frac{\mathrm{I}}{\mathrm{I}_0})} \tag{B.25}$$

Table B.2: Direct Parameters. Measurements not relying on derived optical depth profile.

TARGET[a]	Log Luminosity[b] ($\mathrm{erg\,s^{-1}\,\AA^{-1}}$)	depth[c]	v_{min}[d] ($\mathrm{km\,s^{-1}}$)	v_{max}[e] ($\mathrm{km\,s^{-1}}$)	width[f] ($\mathrm{km\,s^{-1}}$)
SDSSJ001224.01-102226.5	41.69 ± 0.01	0.3 ± 0.3	1700 ± 300	−1450 ± 50	3100 ± 400
HS-0033+4300	41.02 ± 0.08	0.95 ± 0.06	707 ± 5	−270 ± 5	976 ± 10
IOandQSO0045+3926	41.81 ± 0.01	0.6 ± 0.3	482 ± 2	260 ± 20	220 ± 20
CT344	42.45 ± 0.02	0.62 ± 0.01	−6000 ± 600	−25000 ± 1000	19000 ± 2000
0110+0019	42.56 ± 0.02	0.48 ± 0.06	−5200 ± 100	−9700 ± 500	4500 ± 600
NGC520.40	43.02 ± 0.01	0.38 ± 0.06	800 ± 100	200 ± 100	600 ± 200
SDSSJ015530.02-085704.0	41.482 ± 0.006	0.26 ± 0.07	0 ± 200	−900 ± 400	900 ± 600
3C57	43.453 ± 0.008	0.18 ± 0.03	2000 ± 2000	1100 ± 700	1000 ± 2000
SDSSJ080359.23+433258.4	42.32 ± 0.08	0.94 ± 0.03	85 ± 2	−319 ± 6	403 ± 9
FIRST-J020930.7-043826	43.41 ± 0.01	0.69 ± 0.03	3110 ± 70	100 ± 40	3000 ± 100
HE0238-1904	43.608 ± 0.008	0.56 ± 0.02	0 ± 1000	−5210 ± 20	5000 ± 1000
HE0409-5004	43.33 ± 0.01	0.36 ± 0.05	−1000 ± 300	−5400 ± 100	4400 ± 400
RBS542	42.018 ± 0.005	0.49 ± 0.02	500 ± 10	−280 ± 20	780 ± 30
HE0436-2614	43. ± 0.02	0.943 ± 0.006	−2400 ± 500	−32000 ± 1000	30000 ± 2000
RXJ0439.6-5311	41.91 ± 0.05	0.92 ± 0.06	89 ± 2	−196 ± 2	285 ± 3
PKS0454-22	43.07 ± 0.01	0.5 ± 0.2	−24500 ± 100	−25300 ± 200	700 ± 300
3C186	43. ± 0.02	0.38 ± 0.03	610 ± 40	−70 ± 40	670 ± 70
SDSSJ075620.08+304535.3	41.06 ± 0.06	1. ± 0.2	115 ± 9	−660 ± 9	770 ± 20

Continued on next page

[a] target name from the HST MAST Archive
[b] monochromatic log luminosity at 1121Å ($\mathrm{erg\,s^{-1}\,\AA^{-1}}$)
[c] $1 -$ trough minimum
[d] minimum velocity of trough, ($\mathrm{km\,s^{-1}}$)
[e] maximum velocity of trough, ($\mathrm{km\,s^{-1}}$)
[f] width of trough, ($\mathrm{km\,s^{-1}}$)

Table B.2 – *Continued from previous page*

TARGET[a]	Log Luminosity[b] ($\mathrm{erg\,s^{-1}\,\AA^{-1}}$)	depth[c]	v_{min}[d] ($\mathrm{km\,s^{-1}}$)	v_{max}[e] ($\mathrm{km\,s^{-1}}$)	width[f] ($\mathrm{km\,s^{-1}}$)
PG0804+761	42.446 ± 0.01	0.69 ± 0.02	670 ± 20	532 ± 8	140 ± 30
3C196.0	42.425 ± 0.01	0.72 ± 0.02	13700 ± 1000	−22500 ± 200	36000 ± 1000
3C207	42.52 ± 0.04	0.43 ± 0.07	3400 ± 50	390 ± 20	3010 ± 70
SDSSJ092837.98+602521.0	41.9 ± 0.04	0.7 ± 0.1	−1559 ± 3	−4930 ± 60	3370 ± 60
SDSSJ093653.84+533126.8	41.29 ± 0.09	1. ± 0.4	231 ± 3	−2520 ± 20	2750 ± 20
SDSSJ094733.21+100508.7	41.67 ± 0.05	0.5 ± 0.1	−967 ± 6	−3782 ± 2	2816 ± 8
4C40-24	42.9 ± 0.03	0.5 ± 0.05	270 ± 20	−2420 ± 20	2690 ± 30
PG0946+301	43.713 ± 0.001	0.555 ± 0.003	−4100 ± 400	−15100 ± 800	11000 ± 1000
SDSSJ095000.73+483129.3	42.8 ± 0.3	0.9 ± 0.1	−1493 ± 2	−1836 ± 1	344 ± 2
PG1001+054	41.67 ± 0.03	0.75 ± 0.06	−5530 ± 50	−9750 ± 80	4200 ± 100
PKS1004+130	42.18 ± 0.07	1. ± 0.07	−305 ± 3	−1321 ± 2	1016 ± 5
SDSSJ100902.06+071343.8	42.4 ± 0.1	0.97 ± 0.08	−291 ± 1	−894 ± 4	603 ± 5
SDSSJ110312.93+414154.9	42.3 ± 0.09	0.98 ± 0.04	−330 ± 1	−762 ± 3	432 ± 4
PG1114+445	41.57 ± 0.02	0.83 ± 0.03	−80 ± 50	−1400 ± 200	1300 ± 200
SDSSJ111754.31+263416.6	42.51 ± 0.09	0.87 ± 0.04	334 ± 2	159 ± 4	175 ± 6
PG1115+407	41.93 ± 0.03	0.86 ± 0.06	102 ± 5	−71 ± 2	173 ± 6
MC1118+12	42.46 ± 0.04	0.27 ± 0.06	−100 ± 100	−1100 ± 200	900 ± 400
MC1146+111	42.49 ± 0.03	0.32 ± 0.04	80 ± 10	−2340 ± 70	2410 ± 90
SDSSJ115758.72-002220.8	41.86 ± 0.03	0.7 ± 0.4	−760 ± 30	−1270 ± 9	510 ± 40
IRAS11598-0112	41.4 ± 0.2	1. ± 0.3	115 ± 1	−347 ± 2	462 ± 3

Continued on next page

[a] target name from the HST MAST Archive
[b] monochromatic log luminosity at 1121Å ($\mathrm{erg\,s^{-1}\,\AA^{-1}}$)
[c] $1 -$ trough minimum
[d] minimum velocity of trough, ($\mathrm{km\,s^{-1}}$)
[e] maximum velocity of trough, ($\mathrm{km\,s^{-1}}$)
[f] width of trough, ($\mathrm{km\,s^{-1}}$)

Table B.2 – *Continued from previous page*

TARGET[a]	Log Luminosity[b] ($\mathrm{erg\,s^{-1}\,\AA^{-1}}$)	depth[c]	v_{min}[d] ($\mathrm{km\,s^{-1}}$)	v_{max}[e] ($\mathrm{km\,s^{-1}}$)	width[f] ($\mathrm{km\,s^{-1}}$)
SDSSJ120944.81+023212.7	41.26 ± 0.05	0.3 ± 0.1	300 ± 400	−1000 ± 300	1200 ± 700
SDSSJ121037.56+315706.0	42.32 ± 0.09	0.91 ± 0.04	160 ± 2	−10 ± 1	170 ± 3
SDSSJ122534.79-024757.1	41.21 ± 0.05	0.85 ± 0.09	341 ± 3	−424 ± 3	765 ± 6
1225-0052	42.5 ± 0.01	0.6 ± 0.05	−1600 ± 800	−5700 ± 200	4000 ± 1000
RXJ1230.8+0115	42.263 ± 0.005	0.65 ± 0.02	140 ± 10	−3281 ± 8	3420 ± 20
Q1239+0028	43.157 ± 0.005	0.47 ± 0.01	−8600 ± 300	−15500 ± 300	6900 ± 500
PG 1254+047	44. ± 0.2	0.59 ± 0.02	−17300 ± 300	−28400 ± 300	11100 ± 600
1306+3021	43.19 ± 0.02	0.47 ± 0.04	900 ± 100	−1420 ± 40	2300 ± 100
PG1309+355	42.19 ± 0.03	0.5 ± 0.1	−820 ± 40	−1530 ± 40	710 ± 90
SDSSJ13205941+295728.1	41.09 ± 0.05	0.9 ± 0.2	−658 ± 4	−3410 ± 10	2750 ± 10
PG1322+659	41.99 ± 0.02	0.64 ± 0.03	490 ± 50	−2300 ± 100	2700 ± 200
SDSSJ133053.27+311930.5	41.86 ± 0.05	0.83 ± 0.09	2113 ± 3	−1025 ± 2	3138 ± 5
IRAS13349+2438	40.81 ± 0.01	0.1 ± 0.1	−200 ± 200	−1000 ± 300	900 ± 500
SDSSJ134206.56+050523.8	41.9 ± 0.1	0.97 ± 0.04	390 ± 2	140 ± 30	250 ± 30
3C288.1	43.054 ± 0.005	0.6 ± 0.09	400 ± 100	−1500 ± 600	1900 ± 700
PG1404+226	41.36 ± 0.07	0.5 ± 0.2	−1600 ± 100	−2410 ± 50	800 ± 200
QSO-1431+3952	43.6 ± 0.005	0.511 ± 0.01	2800 ± 200	−40 ± 50	2900 ± 300
SDSSJ143511.53+360437.2	42.4 ± 0.1	1. ± 0.06	−20 ± 2	−463 ± 1	442 ± 2
4C63.22	41.5 ± 0.1	0.66 ± 0.09	188 ± 1	80 ± 2	108 ± 2
SDSSJ161916.54+334238.4	42.81 ± 0.02	0.68 ± 0.05	500 ± 40	−220 ± 10	730 ± 50

Continued on next page

[a] target name from the HST MAST Archive
[b] monochromatic log luminosity at 1121Å ($\mathrm{erg\,s^{-1}\,\AA^{-1}}$)
[c] $1 -$ trough minimum
[d] minimum velocity of trough, ($\mathrm{km\,s^{-1}}$)
[e] maximum velocity of trough, ($\mathrm{km\,s^{-1}}$)
[f] width of trough, ($\mathrm{km\,s^{-1}}$)

Table B.2 – *Continued from previous page*

TARGET[a]	Log Luminosity[b] ($\mathrm{erg\,s^{-1}\,\AA^{-1}}$)	depth[c]	v_{min}[d] ($\mathrm{km\,s^{-1}}$)	v_{max}[e] ($\mathrm{km\,s^{-1}}$)	width[f] ($\mathrm{km\,s^{-1}}$)
1631+3930	43.26 ± 0.02	0.52 ± 0.05	−200 ± 200	−1460 ± 90	1200 ± 200
3C351.0	42.95 ± 0.01	0.45 ± 0.1	−900 ± 100	−2430 ± 40	1500 ± 200
1714+5757	42.62 ± 0.02	0.79 ± 0.02	10800 ± 400	−7200 ± 50	18000 ± 500
PG2112+059	43.03 ± 0.02	0.35 ± 0.02	−11000 ± 2000	−26000 ± 1000	15000 ± 3000
Q2208-1720	43.128 ± 0.005	0.69 ± 0.01	−5200 ± 500	−20000 ± 1000	15000 ± 2000
IRAS-F22456-5125	41.748 ± 0.008	0.53 ± 0.02	−20 ± 20	−1580 ± 5	1560 ± 20
PKS2251+11	42.62 ± 0.02	0.15 ± 0.08	−3900 ± 200	−6810 ± 40	2900 ± 200
PG2302+029	43.873 ± 0.006	0.381 ± 0.008	−52800 ± 400	−58700 ± 200	5900 ± 600

[a] target name from the HST MAST Archive
[b] monochromatic log luminosity at 1121Å ($\mathrm{erg\,s^{-1}\,\AA^{-1}}$)
[c] $1 -$ trough minimum
[d] minimum velocity of trough, ($\mathrm{km\,s^{-1}}$)
[e] maximum velocity of trough, ($\mathrm{km\,s^{-1}}$)
[f] width of trough, ($\mathrm{km\,s^{-1}}$)

B.1.4 Measured Values

The measured values for the direct quantities, log luminosity, depth, v_{min}, v_{max}, and width, are presented in table B.2.

B.2 Derived Parameters

Because the definition of the following parameters requires the deconvolution of the optical depth profile, $\tau_{\rm ION}$, from the absorption trough of the ion of choice, they cannot be computed directly from the data.

B.2.1 $\bar{\tau}_{\rm ION}$

The average optical depth for the derived profile of the ion of choice is just:

$$\bar{\tau}_{\rm ION} = \frac{1}{\rm N}\sum_{\rm i=1}^{\rm N}\tau_{\rm ION,i} \tag{B.26}$$

where i is the index of each point (wavelength or velocity bin) and N is the total number of such points in the derived profile trough. The error in the average optical depth is as follows:

$$\sigma_{\bar{\tau}_{\rm ION}} = \sqrt{\left(\frac{\partial\bar{\tau}_{\rm ION}}{\partial\tau_{\rm ION,1}}\sigma_{\tau_{\rm ION,1}}\right)^2 + ... + \left(\frac{\partial\bar{\tau}_{\rm ION}}{\partial\tau_{\rm ION,N}}\sigma_{\tau_{\rm ION,N}}\right)^2} = \frac{1}{\rm N}\sqrt{\sum_{\rm i=1}^{\rm N}\sigma^2_{\tau_{\rm ION,i}}} \tag{B.27}$$

B.2.2 f, $(\tau_{PV} = f * \tau_{ION})$

We multiply $\tau_{\rm ION}$ by a factor f to get the P V optical depth, $\tau_{\rm PV}$. We use two figures of merit to evaluate values of f and combine the results to get the upper limits and

best values with upper and lower error bars on f. One figure of merit minimizes the sum of the distances between the lower error bar on the data normalized flux and the upper error bar on the calculated normalized flux, given f, to find the best f value, $f_{\min}$. This minimizing distance figure of merit should be appropriate for upper limits, where we are looking for the maximum amount of absorption that can be present but still hidden within the noise. The other figure of merit is a traditional minimum χ^2 approach where the upper and lower bounds occur where $\Delta\chi^2 = 6.635$ and correspond to the 99% confidence interval. Our choice of the 99% confidence interval really makes our determination of the error bars at the level of 3σ rather than 1σ.

We combine the results as follows. If either the minimizing distance figure of merit f, $f_{\min}$, or the χ^2 figure of merit f lower bound, $f_{\chi^2,\mathrm{lo}}$, are 0 (consistent with no absorption), then the resulting f is an upper limit whose value is either f_{min} or the $f\chi^2$ upper bound, $f_{\chi^2,\mathrm{hi}}$, whichever is greater. To summarize, for an upper limit, f takes on the values:

$$f = \begin{cases} f_{\min} & \text{if } f_{\chi^2,\mathrm{lo}} = 0 \text{ and } f_{\min} > f_{\chi^2,\mathrm{hi}} \\ f_{\chi^2,\mathrm{hi}} & \text{if } f_{\chi^2,\mathrm{lo}} = 0 \text{ and } f_{\min} < f_{\chi^2,\mathrm{hi}} \\ f_{\chi^2,\mathrm{hi}} & \text{if } f_{\min} = 0 \end{cases} \tag{B.28}$$

The error bars for an upper limit measurement are as follows:

$$\begin{aligned} \sigma_{f,\text{lower}} &= f, \text{so that } f - \sigma_{f,\text{lower}} = 0 \\ \sigma_{f,\text{upper}} &= 0, \text{because } f + \sigma_{f,\text{upper}} = f \end{aligned} \tag{B.29}$$

If neither the minimizing distance nor the χ^2 lower bound fs are zero, then f is assigned the value of the χ^2 best fit f. The lower error bar derives naturally from $f_{\chi^2,\text{lo}}$ and the upper error bar derives from either $f_{\chi^2,\text{hi}}$ or f_{min}, whichever is greater. Recall f_{min} is an indicator of the maximum amount of absorption we can fit in the P V region and still be within the noise, so it would be an appropriate upper limit whenever it is greater than $f_{\chi^2,\text{hi}}$. For a non-upper limit measurement:

$$f = f_{\chi^2,\text{best}} \tag{B.30}$$

$$\sigma_{f,\text{lower}} = f - f_{\chi^2,\text{lo}} \tag{B.31}$$

$$\sigma_{f,\text{upper}} = \begin{cases} f_{\text{min}} - f & \text{if } f_{\text{min}} > f_{\chi^2,\text{hi}} \\ f_{\chi^2,\text{hi}} - f & \text{if } f_{\text{min}} < f_{\chi^2,\text{hi}} \end{cases} \tag{B.32}$$

B.2.3 τ_{PV}

Once we have a measurement for $f^{\sigma_{f,\text{upper}}}_{\sigma_{f,\text{lower}}}$, we can construct the optical depth for P V, τ_{PV}, and its corresponding upper and lower error bars in order to compute the average optical depth, $\bar{\tau}_{\text{PV}}$, and depth, depth_{PV}.

The profile $\tau_{\rm PV}$ is reconstructed as follows:

$$\tau_{\rm PV} = f(\tau_{\rm ION,b} + \frac{1}{2}\tau_{\rm ION,r}) \tag{B.33}$$

based on the assumption that P V fully covers the source and is not saturated. For that assumption, atomic physics tells us the ratio of the optical depth profiles for each line of the doublet should be 2:1, blue:red. $\tau_{\rm ION,b}$ is the contribution from the blue line of the doublet, shifted to the corresponding wavelengths for the blue line of the PV Doublet and $\tau_{\rm ION,r}$ is the contribution from the red line of the doublet. The profiles have the same shape, $\tau_{\rm ION}$, just separately shifted to their corresponding wavelengths. Because the error bars on f are asymmetric, the error bars on $\tau_{\rm PV}$ are also asymmetric. The error bars at each point have the form:

$$\begin{aligned}\sigma_{\tau_{\rm PV}} &= \sqrt{\Big(\frac{\partial\tau_{\rm PV}}{\partial f}\sigma_f\Big)^2 + \Big(\frac{\partial\tau_{\rm PV}}{\partial\tau_{\rm ION,b}}\sigma_{\tau_{\rm ION,b}}\Big)^2 + \Big(\frac{\partial\tau_{\rm PV}}{\partial\tau_{\rm ION,r}}\sigma_{\tau_{\rm ION,r}}\Big)^2} \\ &= \sqrt{(\tau_{\rm ION,b} + \frac{1}{2}\tau_{\rm ION,r})^2\sigma_f^2 + f^2\tau_{\rm ION,b}^2 + \frac{1}{4}f^2\tau_{\rm ION,r}^2}\end{aligned} \tag{B.34}$$

B.2.4 $\bar{\tau}_{\rm PV}$

With the re-constructed $\tau_{\rm PV}$ profile and errors, the definition of $\bar{\tau}_{\rm PV}$ follows naturally in the same way as $\bar{\tau}_{\rm ION}$:

$$\bar{\tau}_{\rm PV} = \frac{1}{\rm N}\sum_{\rm i=1}^{\rm N}\tau_{\rm PV,i} \tag{B.35}$$

where i denotes the individual wavelength points. Again, the asymmetric error bars on $\tau_{\rm PV}$ imply asymmetric errors for $\bar{\tau}_{\rm PV}$. They otherwise have the same form as

$\sigma_{\bar{\tau}_{ION}}$:

$$\sigma_{\bar{\tau}_{\mathrm{PV}}} = \sqrt{\Big(\frac{\partial\bar{\tau}_{\mathrm{PV}}}{\partial\tau_{\mathrm{PV,1}}}\sigma_{\tau_{\mathrm{PV,1}}}\Big)^2 + ... + \Big(\frac{\partial\bar{\tau}_{\mathrm{PV}}}{\partial\tau_{\mathrm{PV,N}}}\sigma_{\tau_{\mathrm{PV,N}}}\Big)^2} = \frac{1}{\mathrm{N}}\sqrt{\sum_{\mathrm{i=1}}^{\mathrm{N}}\sigma^2_{\tau_{\mathrm{PV,i}}}} \tag{B.36}$$

B.2.5 $\mathrm{depth}_{\mathbf{PV}}$

To compute $\mathrm{depth}_{\mathrm{PV}}$, we first convert τ_{PV} to a normalized flux, $(\frac{I}{I_0})_{PV}$:

$$\Big(\frac{\mathrm{I}}{\mathrm{I_0}}\Big)_{\mathrm{PV}} = \mathrm{e}^{-\tau_{\mathrm{PV}}} \tag{B.37}$$

with asymmetric errors of the form:

$$\sigma_{(\frac{\mathrm{I}}{\mathrm{I_0}})_{\mathrm{PV}}} = \sqrt{\Big(\frac{\partial(\frac{\mathrm{I}}{\mathrm{I_0}})_{\mathrm{PV}}}{\partial\tau_{\mathrm{PV}}}\sigma_{\tau_{\mathrm{PV}}}\Big)^2} = \Big(\frac{\mathrm{I}}{\mathrm{I_0}}\Big)_{\mathrm{PV}}\sigma_{\tau_{\mathrm{PV}}} \tag{B.38}$$

The calculation of $\mathrm{depth}_{\mathrm{PV}}$ and its error bars then follow the $\mathrm{depth}_{\mathrm{ION}}$ formulation:

$$\mathrm{depth}_{\mathrm{PV}} = 1 - \min\Big(\frac{\mathrm{I}}{\mathrm{I_0}}\Big)_{\mathrm{PV}} \tag{B.39}$$

The errors are asymmetric and are the errors in the normalized flux at that minimum point:

$$\sigma_{\mathrm{depth}_{\mathrm{PV}}} = \sqrt{\Big(\frac{\partial\mathrm{depth}_{\mathrm{PV}}}{\partial(\frac{\mathrm{I}}{\mathrm{I_0}})_{\mathrm{PV}}}\sigma_{(\frac{\mathrm{I}}{\mathrm{I_0}})_{\mathrm{PV}}}\Big)^2} = \sigma_{(\frac{\mathrm{I}}{\mathrm{I_0}})_{\mathrm{PV}}}\Big|_{\min((\frac{\mathrm{I}}{\mathrm{I_0}})_{\mathrm{PV}})} \tag{B.40}$$

B.2.6 Measured Values

The measured values for the derived quantities, $\bar{\tau}$, $\bar{\tau}_{\mathrm{PV}}$, and $\mathrm{depth}_{\mathrm{PV}}$, are presented in table B.3.

Table B.3: Indirect Parameters. Measurements requiring derived optical depth profile.

TARGET [a]	$\bar{\tau}$ [b]	$\bar{\tau}_{\rm PV}$ [c]	depth$_{\rm PV}$ [d]
SDSSJ001224.01-102226.5	0.04 ± 0.04	$0.02^{+0.}_{-0.02}$	$0.18^{+0.09}_{-0.09}$
HS-0033+4300	1.25 ± 0.06	$0.119^{+0.003}_{-0.0008}$	$0.192^{+0.005}_{-0.005}$
IOandQSO0045+3926	0.17 ± 0.07	$0.006^{+0.}_{-0.006}$	$0.0279^{+0.0006}_{-0.0006}$
CT344	0.21 ± 0.02	$0.125^{+0.008}_{-0.006}$	$0.38^{+0.09}_{-0.09}$
0110+0019	0.23 ± 0.04	$0.044^{+0.006}_{-0.002}$	$0.13^{+0.02}_{-0.02}$
NGC520.40	0.13 ± 0.01	$0.15^{+0.05}_{-0.02}$	$0.31^{+0.07}_{-0.07}$
SDSSJ015530.02-085704.0	0.17 ± 0.08	$0.1^{+0.03}_{-0.03}$	$0.2^{+0.1}_{-0.1}$
3C57	0.026 ± 0.004	$0.02^{+0.}_{-0.02}$	$0.09^{+0.02}_{-0.02}$
SDSSJ080359.23+433258.4	1. ± 0.1	$0.1^{+0.}_{-0.1}$	$0.23^{+0.01}_{-0.01}$
FIRST-J020930.7-043826	0.15 ± 0.006	$0.1^{+0.}_{-0.1}$	$0.28^{+0.06}_{-0.06}$
HE0238-1904	0.077 ± 0.009	$0.005^{+0.}_{-0.005}$	$0.0263^{+0.0008}_{-0.0008}$
HE0409-5004	0.38 ± 0.05	$0.046^{+0.001}_{-0.001}$	$0.108^{+0.006}_{-0.006}$
RBS542	0.14 ± 0.04	$0.02^{+0.}_{-0.02}$	$0.052^{+0.004}_{-0.004}$
HE0436-2614	0.49 ± 0.04	$0.32^{+0.03}_{-0.02}$	$0.7^{+0.2}_{-0.2}$
RXJ0439.6-5311	0.65 ± 0.05	$0.008^{+0.}_{-0.008}$	$0.0194^{+0.0002}_{-0.0002}$
PKS0454-22	0.19 ± 0.06	$0.1^{+0.}_{-0.1}$	$0.2^{+0.1}_{-0.1}$
3C186	0.19 ± 0.03	$0.06^{+0.}_{-0.06}$	$0.13^{+0.03}_{-0.03}$
SDSSJ075620.08+304535.3	0.62 ± 0.06	$0.2^{+0.}_{-0.2}$	$0.46^{+0.06}_{-0.06}$
PG0804+761	0.28 ± 0.03	$0.02^{+0.}_{-0.02}$	$0.055^{+0.002}_{-0.002}$
3C196.0	0.41 ± 0.06	$0.082^{+0.009}_{-0.003}$	$0.16^{+0.01}_{-0.01}$
3C207	0.142 ± 0.01	$0.047^{+0.005}_{-0.002}$	$0.102^{+0.008}_{-0.008}$
SDSSJ092837.98+602521.0	0.15 ± 0.01	$0.02^{+0.}_{-0.02}$	$0.125^{+0.008}_{-0.008}$

Continued on next page

[a] target name from the HST MAST Archive
[b] average optical depth of derived profile
[c] average optical depth of estimated P V profile
[d] depth of estimated P V trough

Table B.3 – *Continued from previous page*

TARGET [a]	$\bar{\tau}$ [b]	$\bar{\tau}_{\rm PV}$ [c]	depth$_{\rm PV}$ [d]
SDSSJ093653.84+533126.8	0.5 ± 0.3	$0.3^{+0.}_{-0.3}$	$1.^{+2.}_{-2.}$
SDSSJ094733.21+100508.7	0.076 ± 0.009	$0.1^{+0.}_{-0.1}$	$0.5^{+0.2}_{-0.2}$
4C40-24	0.24 ± 0.03	$0.04^{+0.}_{-0.04}$	$0.086^{+0.008}_{-0.008}$
PG0946+301	0.21 ± 0.02	$0.15^{+0.02}_{-0.01}$	$0.3^{+0.1}_{-0.1}$
SDSSJ095000.73+483129.3	0.62 ± 0.04	$0.00007^{+0.}_{-0.00007}$	$0.000213^{+0.}_{-0.}$
PG1001+054	0.25 ± 0.03	$0.07^{+0.}_{-0.07}$	$0.24^{+0.04}_{-0.04}$
PKS1004+130	1.43 ± 0.05	$0.001^{+0.}_{-0.001}$	$0.002576^{+0.000003}_{-0.000003}$
SDSSJ100902.06+071343.8	0.73 ± 0.04	$0.2^{+0.}_{-0.2}$	$0.6^{+0.07}_{-0.07}$
SDSSJ110312.93+414154.9	1.17 ± 0.07	$0.0005^{+0.}_{-0.0005}$	$0.001266^{+0.}_{-0.}$
PG1114+445	0.46 ± 0.09	$0.05^{+0.}_{-0.05}$	$0.18^{+0.01}_{-0.01}$
SDSSJ111754.31+263416.6	0.69 ± 0.05	$0.06^{+0.}_{-0.06}$	$0.144^{+0.006}_{-0.006}$
PG1115+407	0.65 ± 0.03	$0.01^{+0.}_{-0.01}$	$0.03222^{+0.0001}_{-0.0001}$
MC1118+12	0.11 ± 0.03	$0.06^{+0.}_{-0.06}$	$0.12^{+0.05}_{-0.05}$
MC1146+111	0.12 ± 0.01	$0.01^{+0.}_{-0.01}$	$0.03^{+0.002}_{-0.002}$
SDSSJ115758.72-002220.8	0.4 ± 0.1	$0.07^{+0.}_{-0.07}$	$0.17^{+0.03}_{-0.03}$
IRAS11598-0112	2. ± 2.	$0.02^{+0.}_{-0.02}$	$0.046^{+0.004}_{-0.004}$
SDSSJ120944.81+023212.7	0.12 ± 0.03	$0.2^{+0.}_{-0.2}$	$0.4^{+0.1}_{-0.1}$
SDSSJ121037.56+315706.0	0.77 ± 0.05	$0.01^{+0.}_{-0.01}$	$0.0299^{+0.0003}_{-0.0003}$
SDSSJ122534.79-024757.1	0.41 ± 0.03	$0.33^{+0.02}_{-0.02}$	$0.63^{+0.09}_{-0.09}$
1225-0052	0.21 ± 0.03	$0.2^{+0.04}_{-0.03}$	$0.4^{+0.2}_{-0.2}$
RXJ1230.8+0115	0.144 ± 0.007	$0.5^{+0.}_{-0.5}$	$0.9^{+0.5}_{-0.5}$
Q1239+0028	0.16 ± 0.02	$0.02^{+0.0007}_{-0.0004}$	$0.06^{+0.004}_{-0.004}$

Continued on next page

[a] target name from the HST MAST Archive
[b] average optical depth of derived profile
[c] average optical depth of estimated P V profile
[d] depth of estimated P V trough

Table B.3 – *Continued from previous page*

TARGET [a]	$\bar{\tau}$ [b]	$\bar{\tau}_{\rm PV}$ [c]	depth$_{\rm PV}$ [d]
PG 1254+047	0.159 ± 0.008	$0.119^{+0.006}_{-0.004}$	$0.3^{+0.1}_{-0.1}$
1306+3021	0.16 ± 0.02	$0.05^{+0.}_{-0.05}$	$0.12^{+0.02}_{-0.02}$
PG1309+355	0.21 ± 0.03	$0.1^{+0.}_{-0.1}$	$0.29^{+0.04}_{-0.04}$
SDSSJ13205941+295728.1	0.54 ± 0.03	$0.55^{+0.08}_{-0.03}$	$0.8^{+0.2}_{-0.2}$
PG1322+659	0.27 ± 0.05	$0.08^{+0.}_{-0.08}$	$0.23^{+0.04}_{-0.04}$
SDSSJ133053.27+311930.5	0.13 ± 0.004	$0.002^{+0.}_{-0.002}$	$0.01673^{+0.00006}_{-0.00006}$
IRAS13349+2438	0.12 ± 0.08	$0.04^{+0.}_{-0.04}$	$0.1^{+0.04}_{-0.04}$
SDSSJ134206.56+050523.8	1.1 ± 0.1	$0.07^{+0.}_{-0.07}$	$0.166^{+0.006}_{-0.006}$
3C288.1	0.2 ± 0.05	$0.03^{+0.}_{-0.03}$	$0.089^{+0.009}_{-0.009}$
PG1404+226	0.29 ± 0.07	$0.3^{+0.}_{-0.3}$	$0.4^{+0.3}_{-0.3}$
QSO-1431+3952	0.17 ± 0.05	$0.04^{+0.}_{-0.04}$	$0.1^{+0.01}_{-0.01}$
SDSSJ143511.53+360437.2	2. ± 0.1	$0.08^{+0.}_{-0.08}$	$0.147^{+0.007}_{-0.007}$
4C63.22	0.39 ± 0.04	$0.05^{+0.}_{-0.05}$	$0.093^{+0.009}_{-0.009}$
SDSSJ161916.54+334238.4	0.36 ± 0.04	$0.06^{+0.}_{-0.06}$	$0.16^{+0.01}_{-0.01}$
1631+3930	0.24 ± 0.04	$0.02^{+0.}_{-0.02}$	$0.032^{+0.001}_{-0.001}$
3C351.0	0.2 ± 0.03	$0.2^{+0.}_{-0.2}$	$0.3^{+0.2}_{-0.2}$
1714+5757	0.25 ± 0.02	$0.00981^{+0.0002}_{-0.00006}$	$0.036^{+0.0008}_{-0.0008}$
PG2112+059	0.2 ± 0.02	$0.03^{+0.}_{-0.03}$	$0.123^{+0.007}_{-0.007}$
Q2208-1720	0.2 ± 0.01	$0.128^{+0.01}_{-0.007}$	$0.35^{+0.1}_{-0.1}$
IRAS-F22456-5125	0.076 ± 0.002	$0.0007^{+0.}_{-0.0007}$	$0.00793^{+0.00005}_{-0.00005}$
PKS2251+11	0.07 ± 0.01	$0.02^{+0.}_{-0.02}$	$0.04^{+0.006}_{-0.006}$
PG2302+029	0.15 ± 0.01	$0.07^{+0.}_{-0.07}$	$0.16^{+0.06}_{-0.06}$

[a] target name from the HST MAST Archive
[b] average optical depth of derived profile
[c] average optical depth of estimated P V profile
[d] depth of estimated P V trough

Appendix C

P v Project: Spectral and τ Profile Data

The following plots are the data and results for the individual targets in our HST archival sample. The upper panel in each plot is the spectrum shifted to the AGN's rest-frame. The continuum+emission models for the ion from which we derive an optical depth profile (Si IV, C IV, or O VI) and for P V are over-plotted in red. The left middle and lower panels are the region of the spectrum for the ion from which we derived an optical depth profile and for P V, respectively. Again, the continuum+emission models are over-plotted in red. The middle right panel is the optical depth profile for the ion from which we chose to derive one. Based no availability of data and existence of absorption we chose to derive profiles first from Si IV, next from C IV or lastly from O VI.

The lower right panel is the derived optical depth profile applied to the normalized flux in the P V region. The τ profile is applied to each line of the P V doublet, blue for 1117.98Å and red for 1128.01Å. A green line shows the contribution from both where they overlap. If the best fit factor from the χ^2 method is not zero, the factor used to plot the applied profile is the best fit factor and the plot is labelled with 'best fit'. If the best fit factor from the χ^2 method is zero, then the factor used to plot the applied profile is the upper limit and the plot is labelled with 'upper limit'. These factors and upper limits are for the case where the profile was derived by forcing full covering. They are applied assuming full covering also.

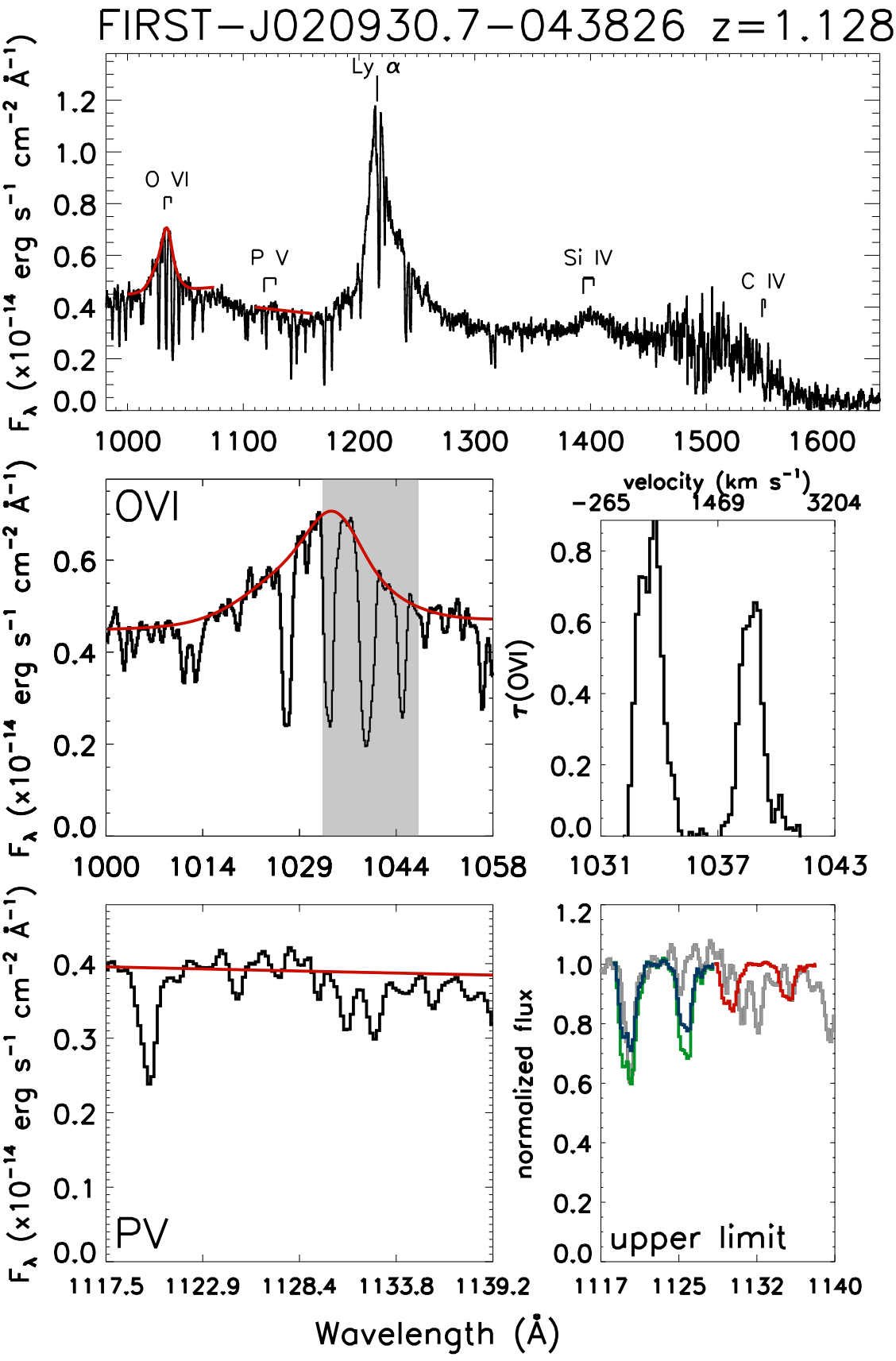
FIRST−J020930.7−043826 z=1.128
Ly α
O VI
P V
Si IV
C IV
OVI
velocity (km s−1)
−265
1469
3204
τ(OVI)
PV
normalized flux
upper limit
Wavelength (Å)

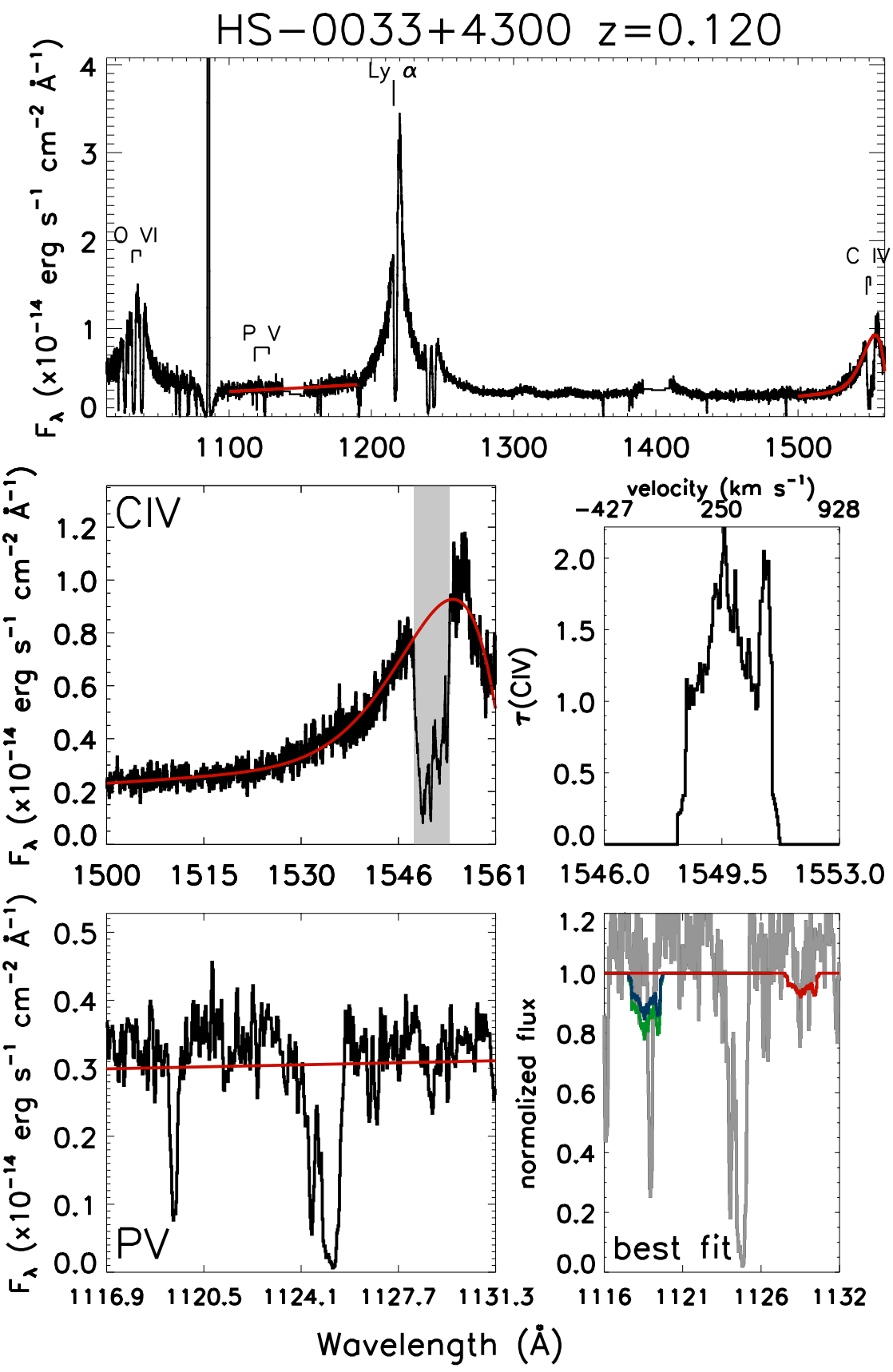
HS−0033+4300 z=0.120
Ly α
O VI
P V
C IV
F_λ (x10^{-14} erg s^{-1} cm^{-2} Å^{-1})
1100
1200
1300
1400
1500
CIV
velocity (km s^{-1})
−427
250
928
τ(CIV)
1500
1515
1530
1546
1561
1546.0
1549.5
1553.0
PV
normalized flux
best fit
1116.9
1120.5
1124.1
1127.7
1131.3
1116
1121
1126
1132
Wavelength (Å)

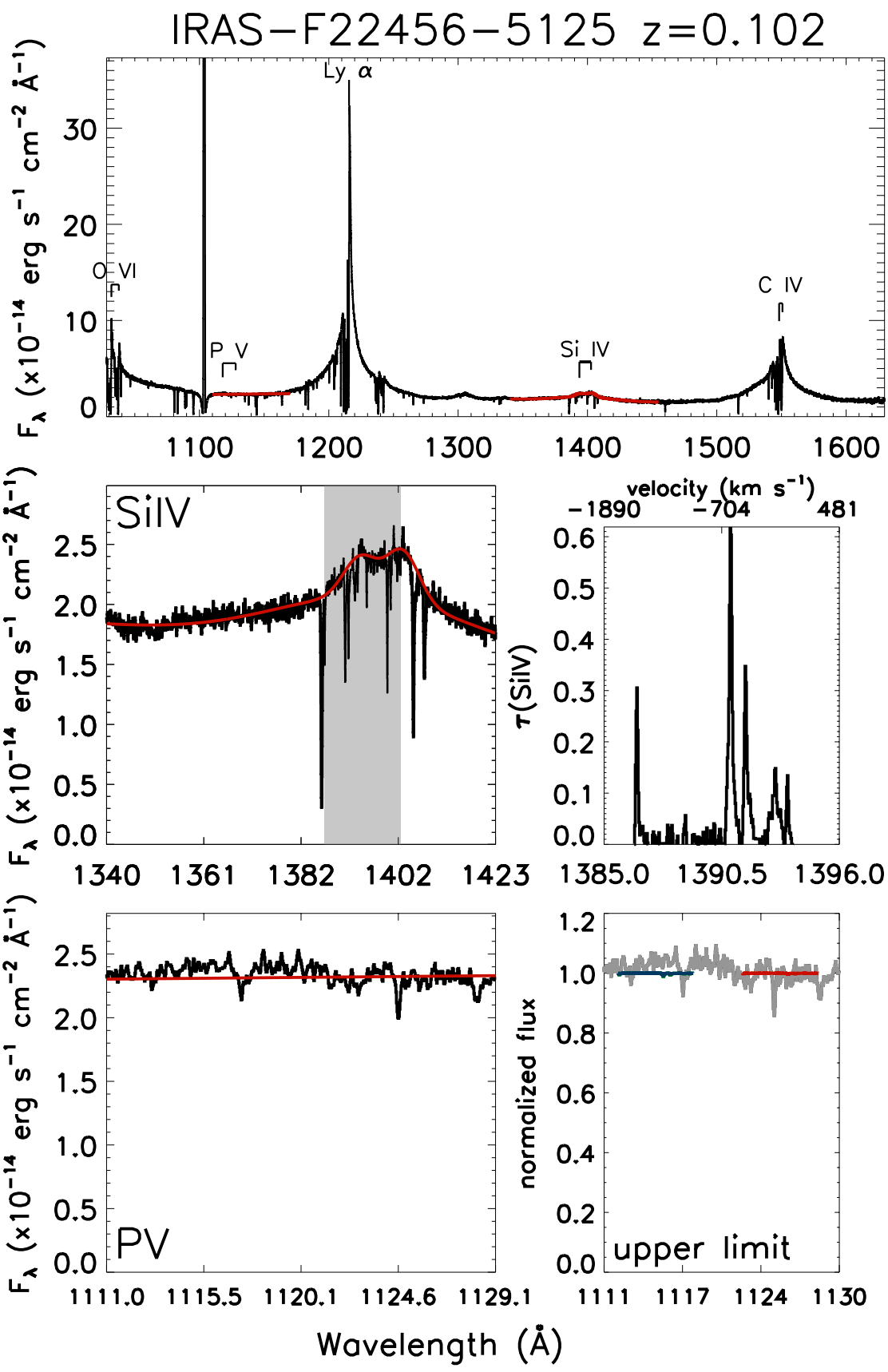
IRAS−F22456−5125 z=0.102
Ly α
O VI
P V
Si IV
C IV
SiIV
PV
velocity (km s⁻¹)
−1890
−704
481
τ(SiV)
normalized flux
upper limit
Wavelength (Å)

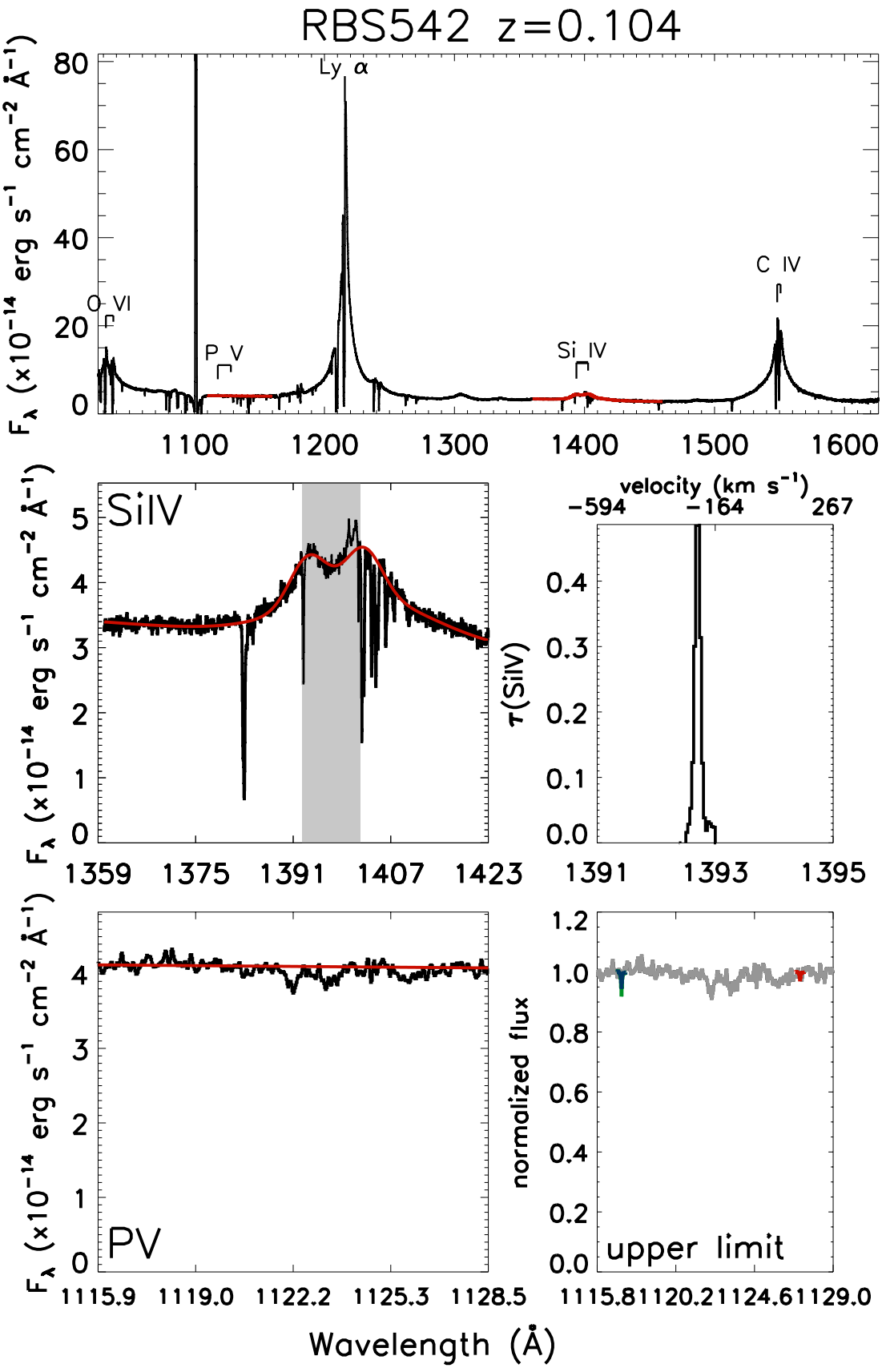
RBS542 z=0.104
Ly α
O VI
P V
Si IV
C IV
F_λ (x10^-14 erg s^-1 cm^-2 Å^-1)
SiIV
velocity (km s^-1)
τ(SiIV)
PV
normalized flux
upper limit
Wavelength (Å)

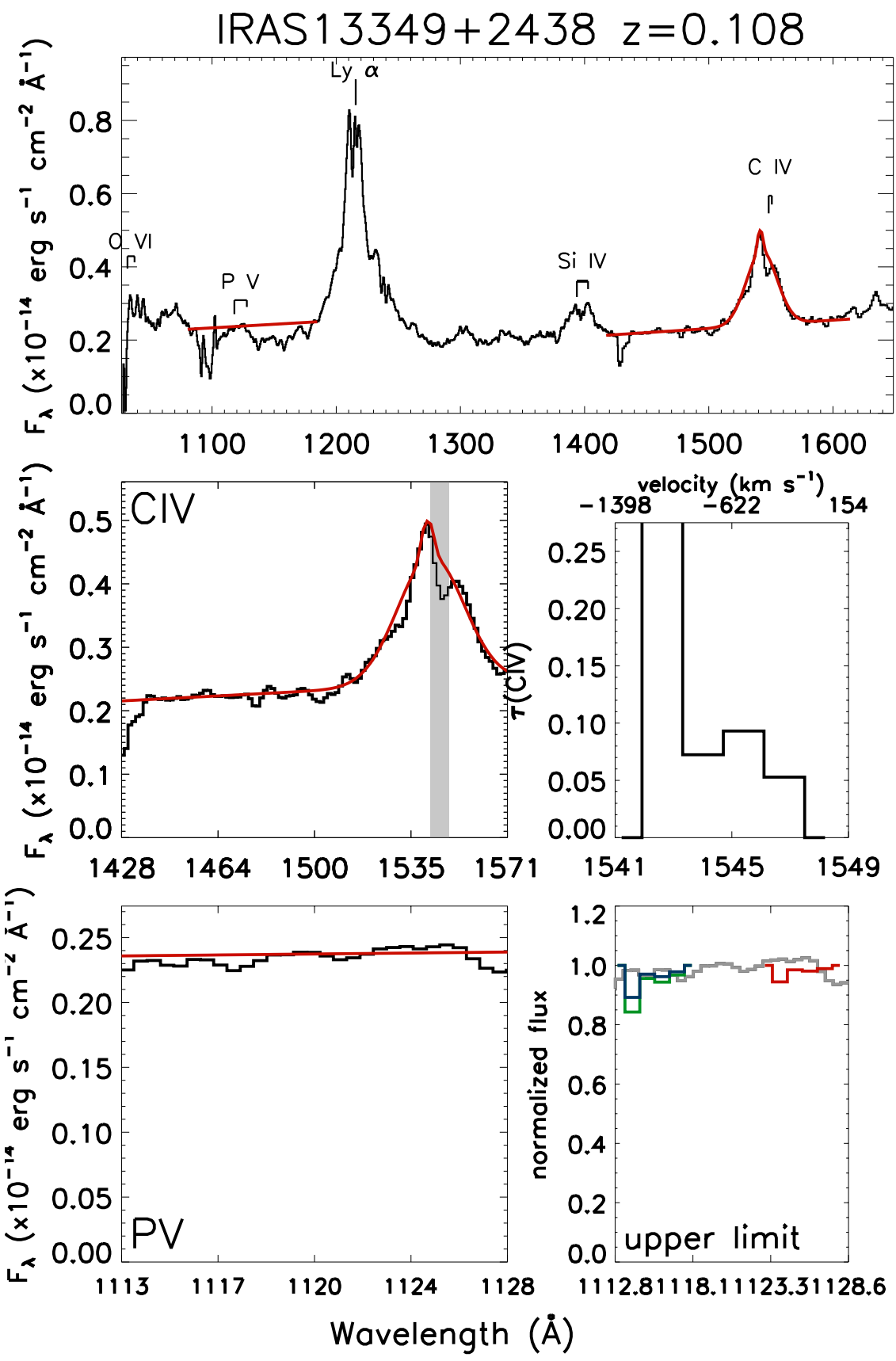
IRAS13349+2438 z=0.108
Ly α
C IV
O VI
P V
Si IV
CIV
PV
velocity (km s⁻¹)
−1398
−622
154
τ(CIV)
normalized flux
upper limit
Wavelength (Å)

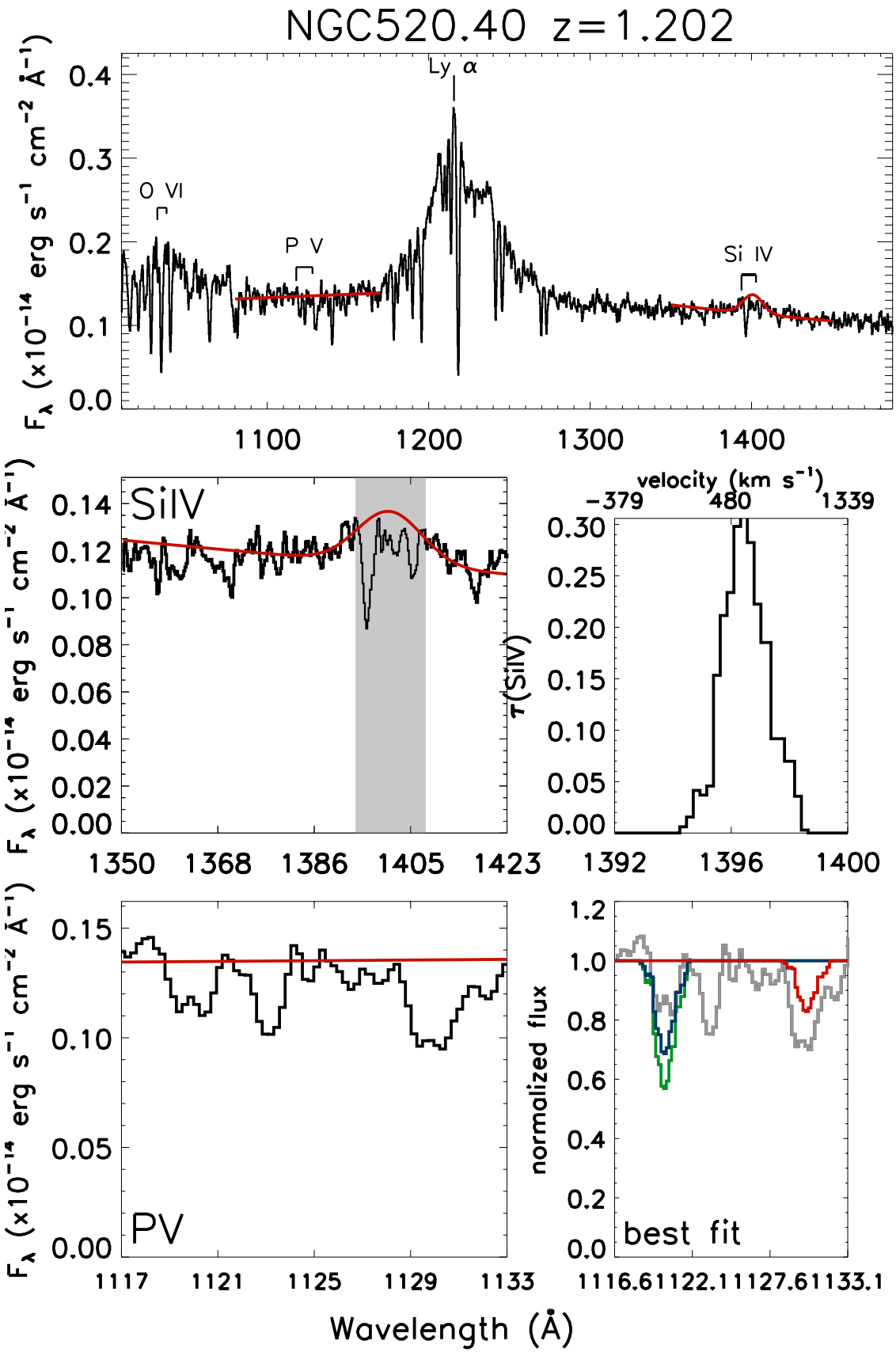
NGC520.40 z=1.202
Ly α
O VI
P V
Si IV
SiIV
PV
velocity (km s⁻¹)
τ(SiIV)
normalized flux
best fit
Wavelength (Å)

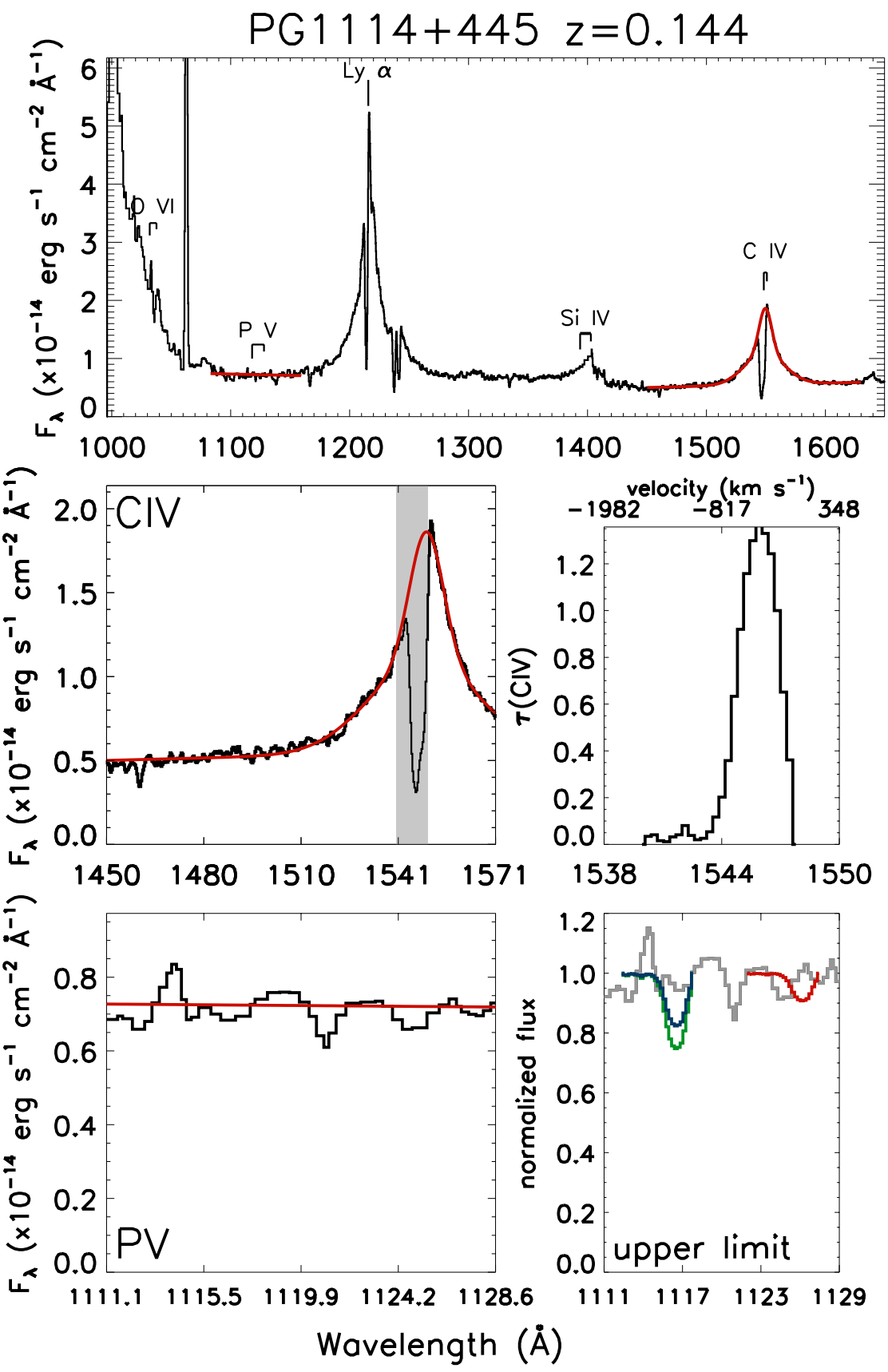
PG1114+445 z=0.144
Ly α
O VI
P V
Si IV
C IV
F_λ (x10^{-14} erg s^{-1} cm^{-2} Å^{-1})
1000
1100
1200
1300
1400
1500
1600
CIV
velocity (km s^{-1})
−1982
−817
348
τ(CIV)
1450
1480
1510
1541
1571
1538
1544
1550
PV
normalized flux
upper limit
1111.1
1115.5
1119.9
1124.2
1128.6
1111
1117
1123
1129
Wavelength (Å)

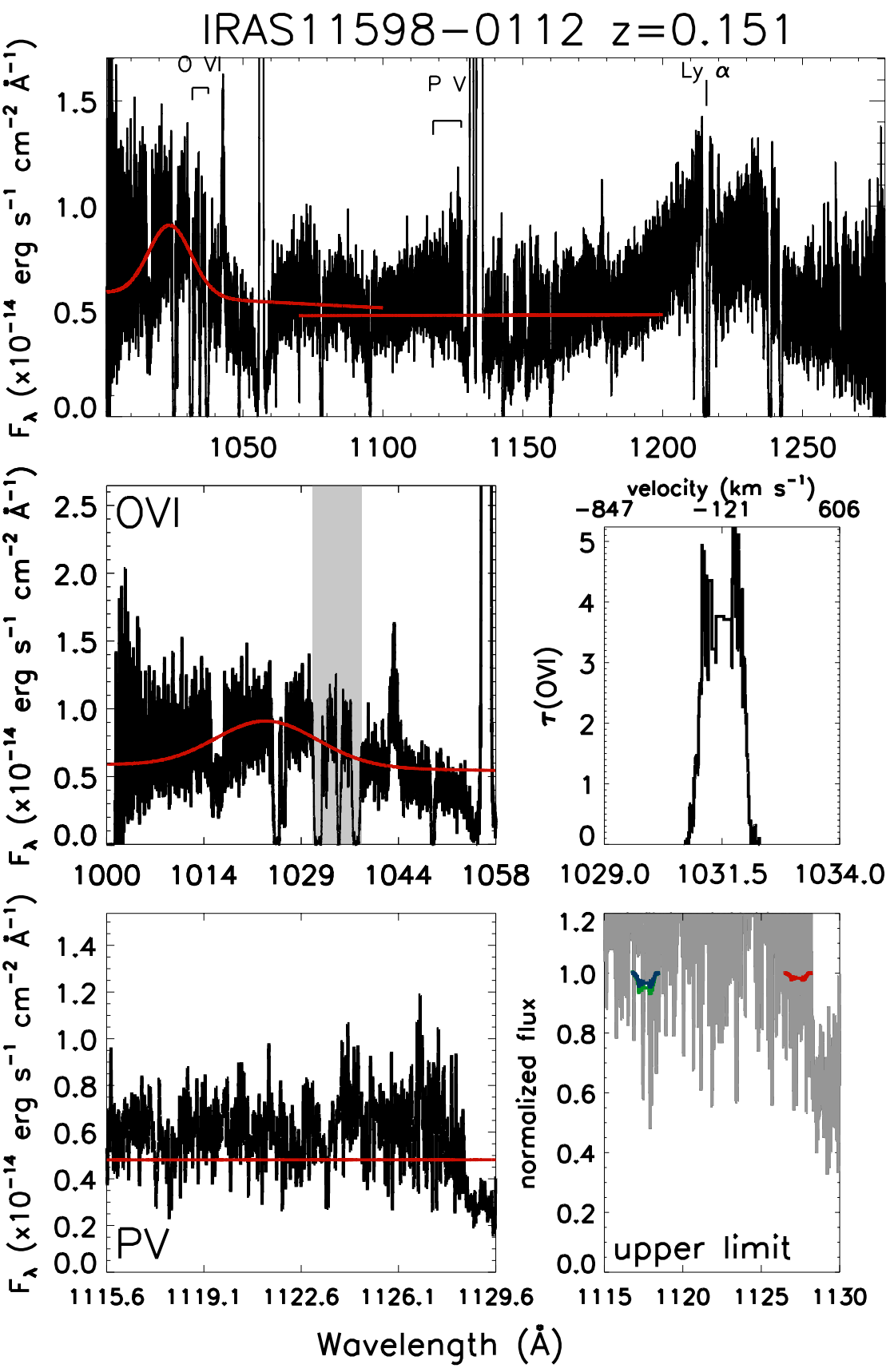
IRAS11598−0112 z=0.151
O VI
P V
Ly α
OVI
PV
velocity (km s⁻¹)
−847
−121
606
τ(OVI)
normalized flux
upper limit
Wavelength (Å)

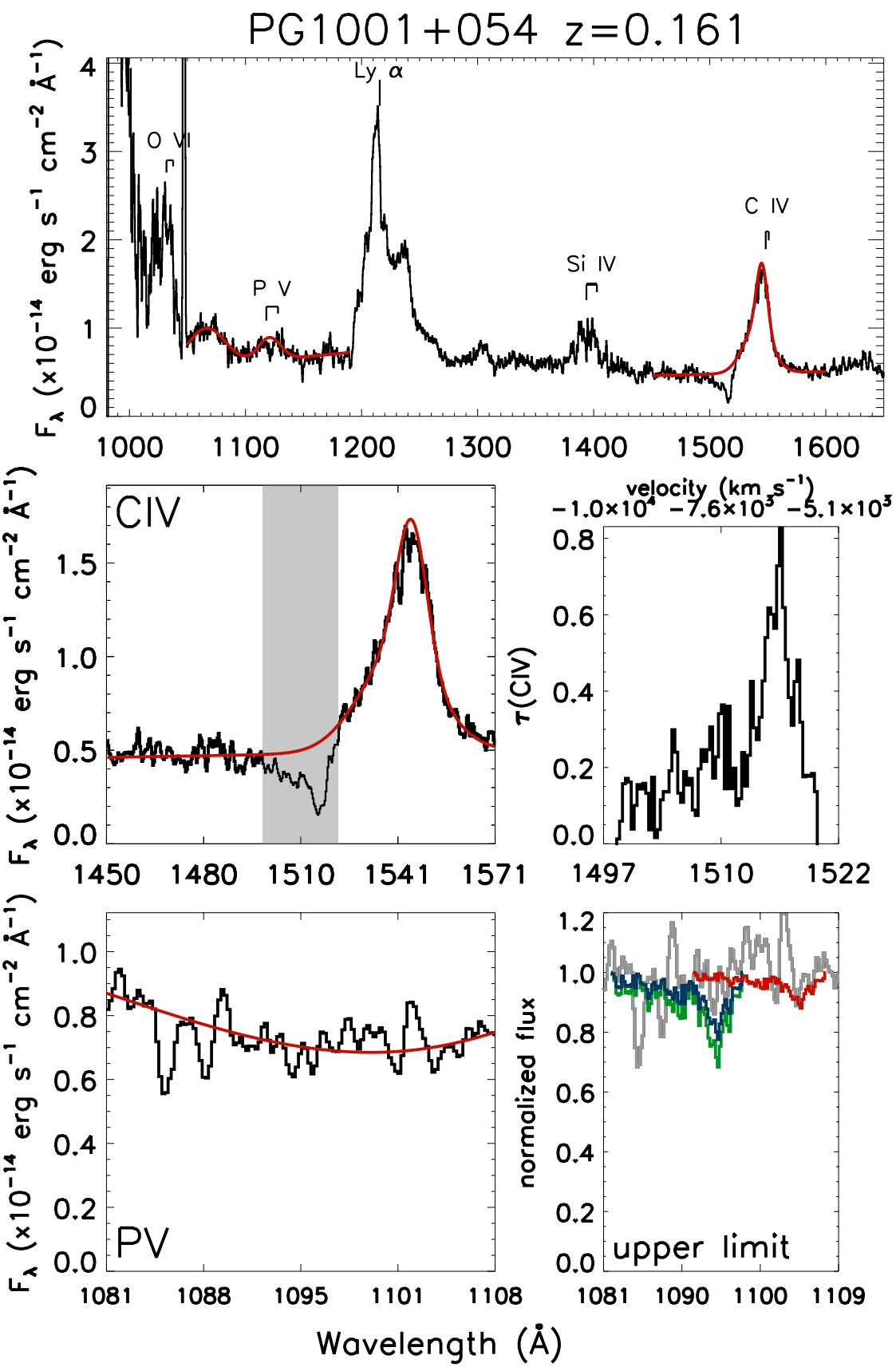
PG1001+054 z=0.161
Ly α
O VI
P V
Si IV
C IV
F_λ (x10^-14 erg s^-1 cm^-2 Å^-1)
CIV
velocity (km s^-1)
−1.0×10^4 −7.6×10^3 −5.1×10^3
τ(CIV)
PV
upper limit
normalized flux
Wavelength (Å)

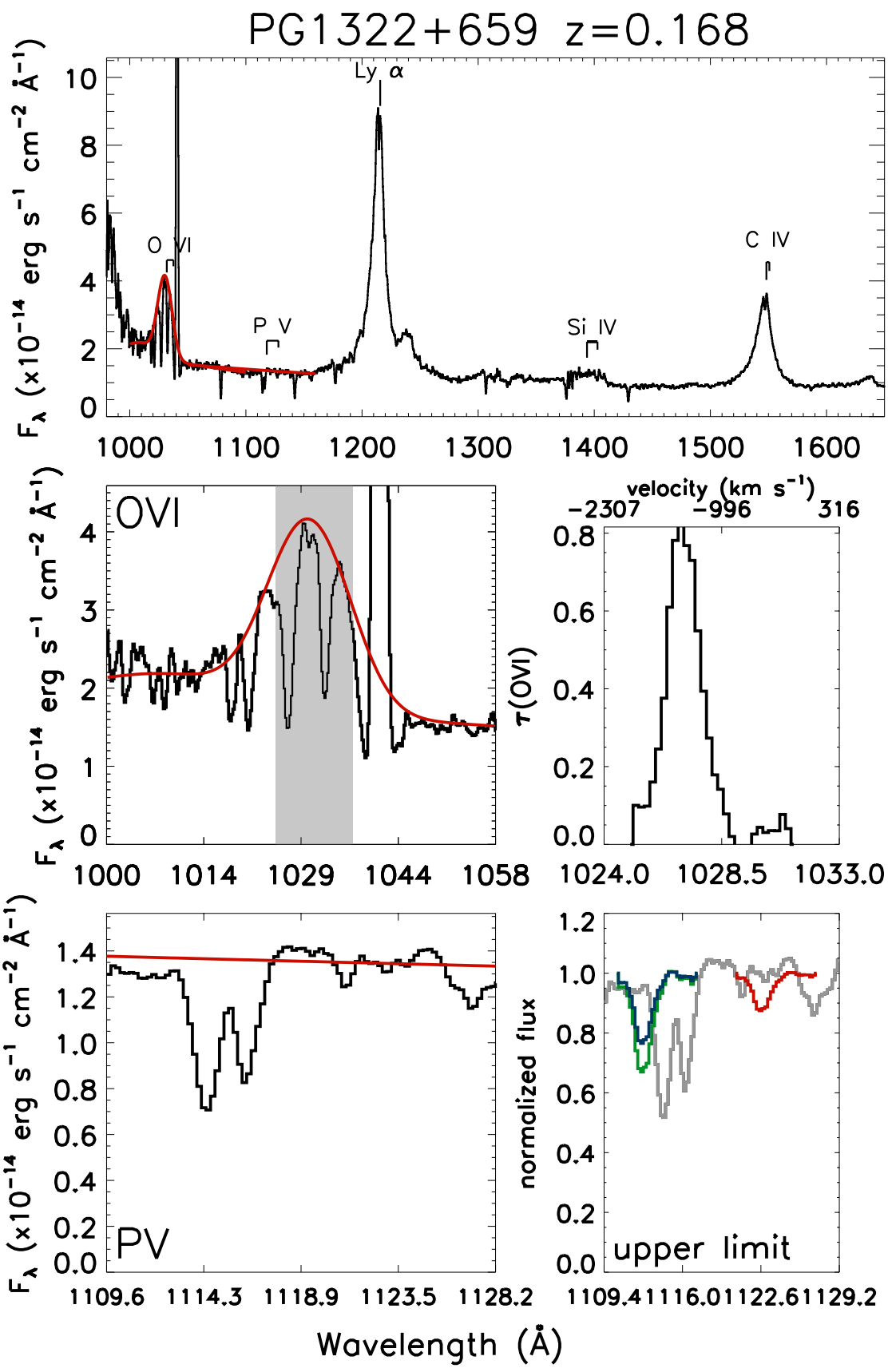
PG1322+659 z=0.168
Ly α
O VI
P V
Si IV
C IV
F_λ (x10^-14 erg s^-1 cm^-2 Å^-1)
OVI
velocity (km s^-1)
−2307
−996
316
τ(OVI)
PV
normalized flux
upper limit
Wavelength (Å)

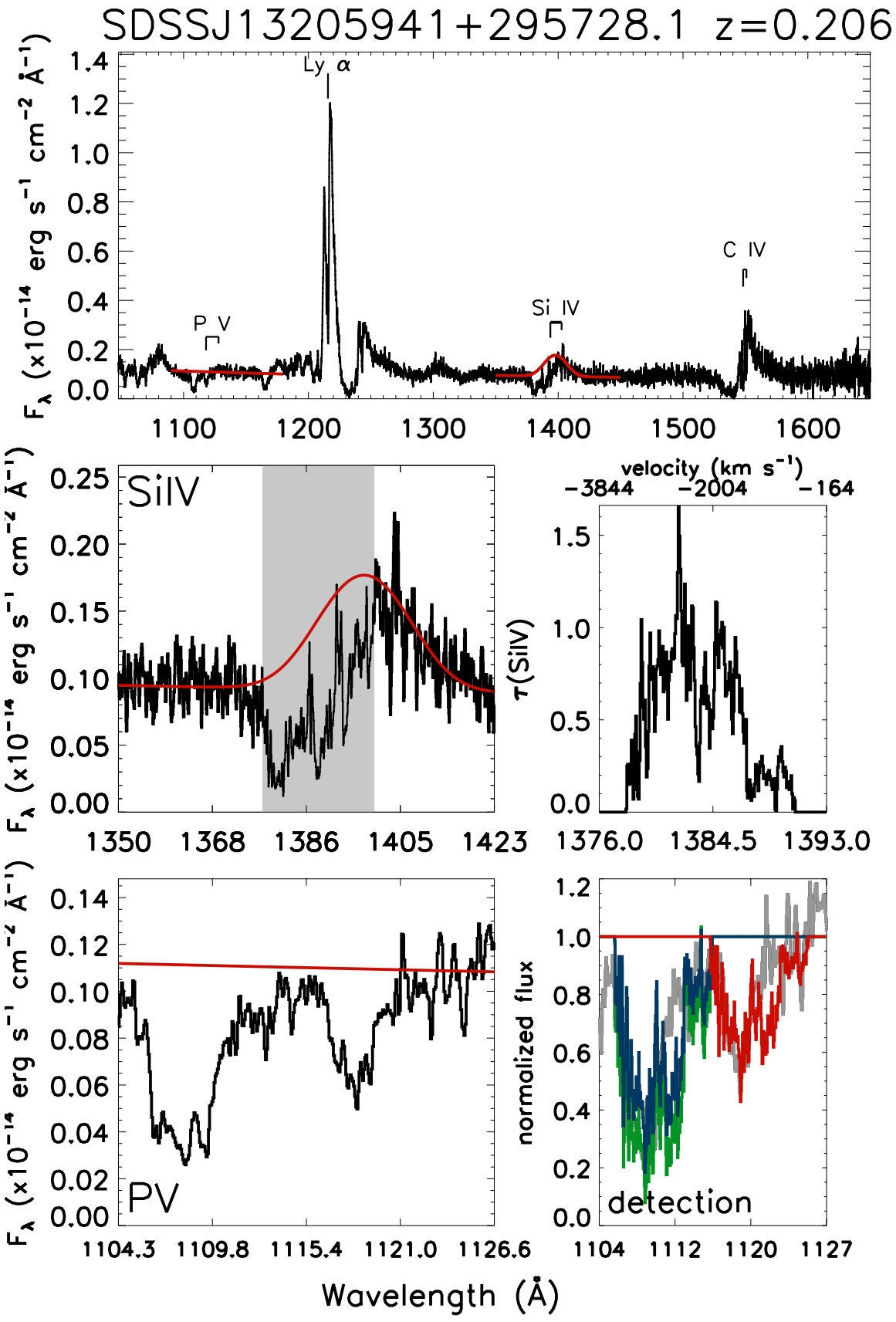
SDSSJ13205941+295728.1 z=0.206
Ly α
P V
Si IV
C IV
SiIV
PV
velocity (km s⁻¹)
−3844
−2004
−164
τ(SiIV)
normalized flux
detection
Wavelength (Å)

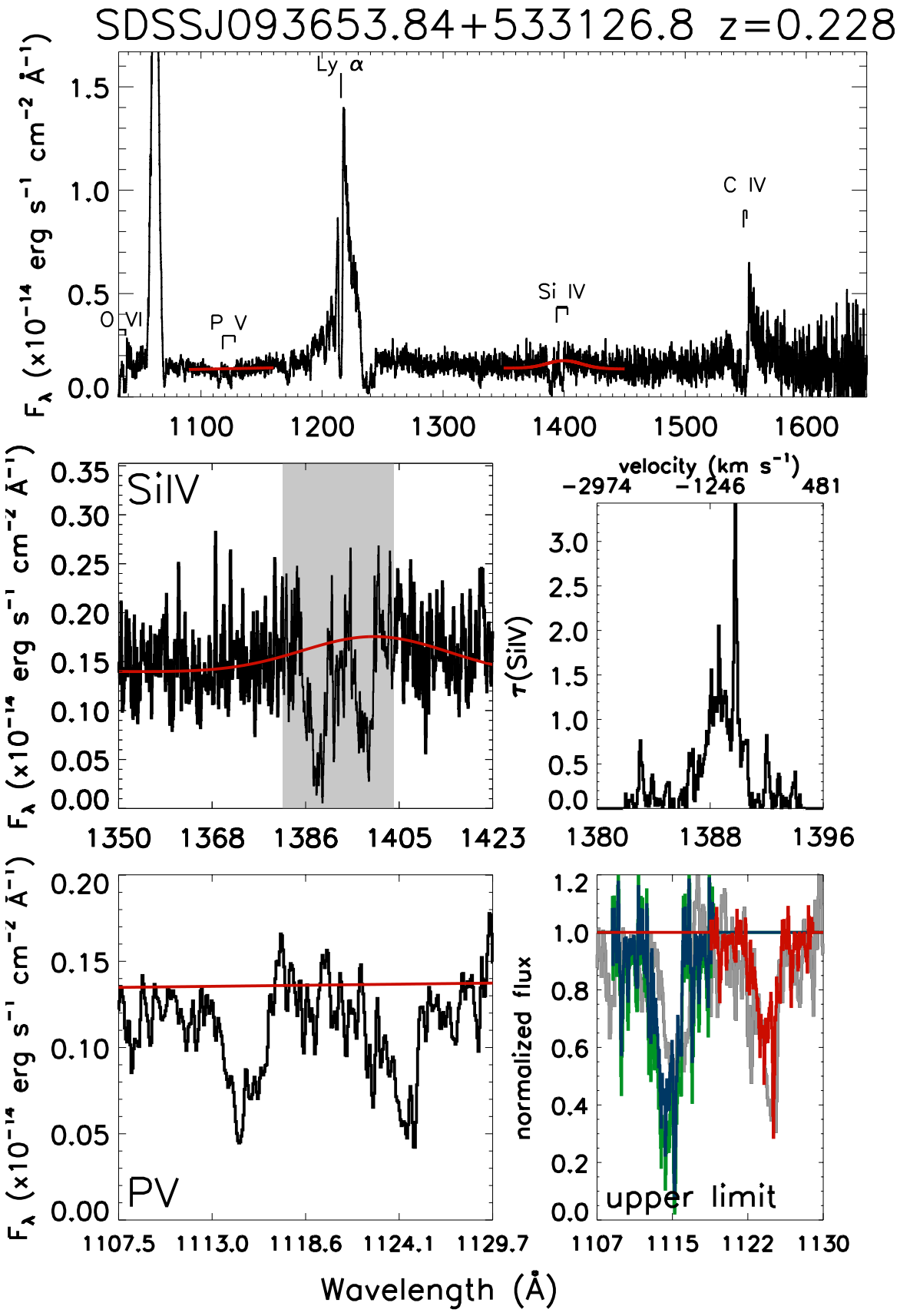
SDSSJ093653.84+533126.8 z=0.228
Ly α
C IV
Si IV
O VI
P V
F_λ (x10^-14 erg s^-1 cm^-2 Å^-1)
1100
1200
1300
1400
1500
1600
SiIV
PV
velocity (km s^-1)
−2974
−1246
481
τ(SiIV)
normalized flux
upper limit
Wavelength (Å)

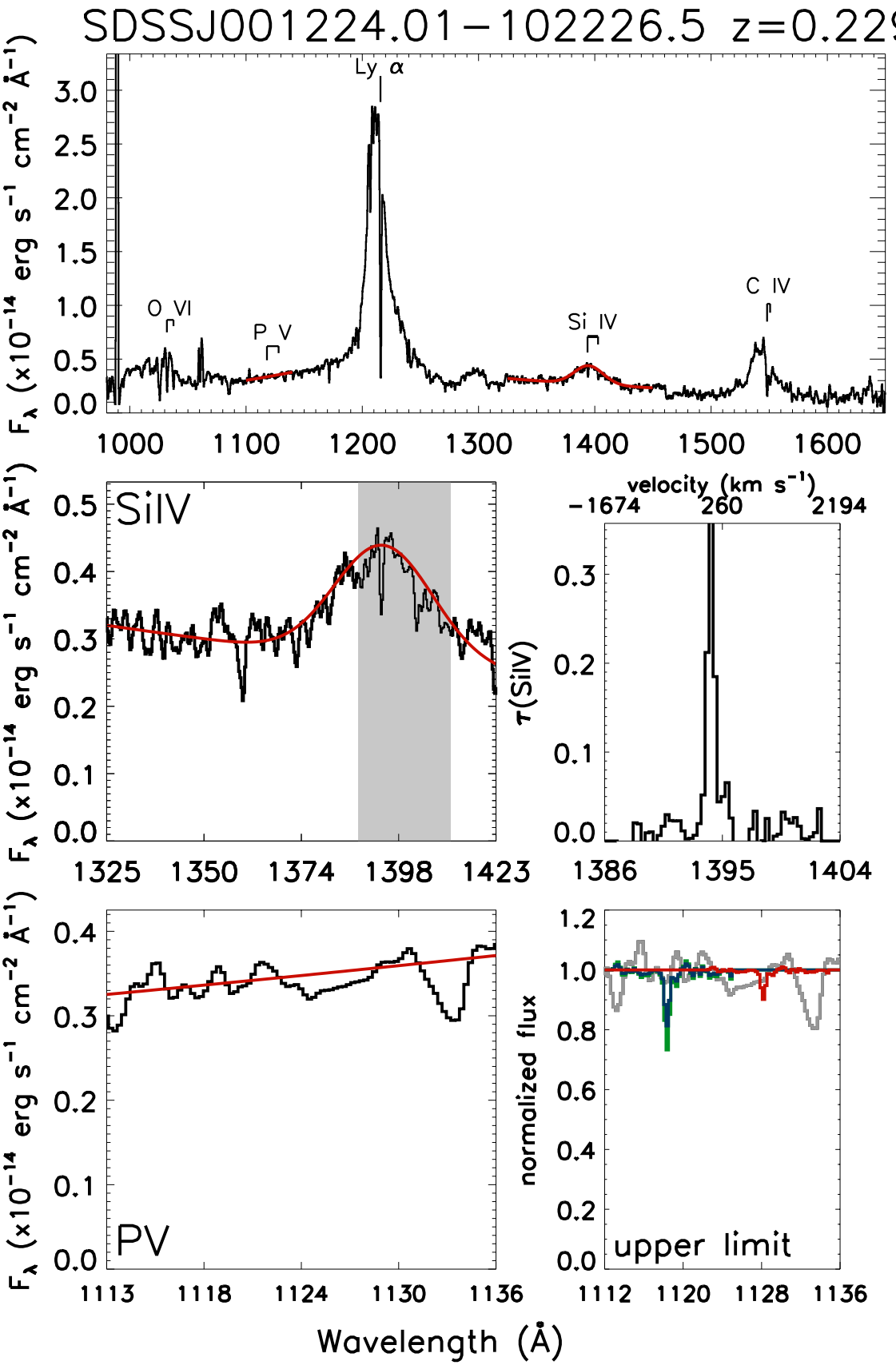
SDSSJ001224.01−102226.5 z=0.229
Ly α
O VI
P V
Si IV
C IV
SiIV
PV
velocity (km s⁻¹)
−1674
260
2194
τ(SiV)
normalized flux
upper limit
Wavelength (Å)

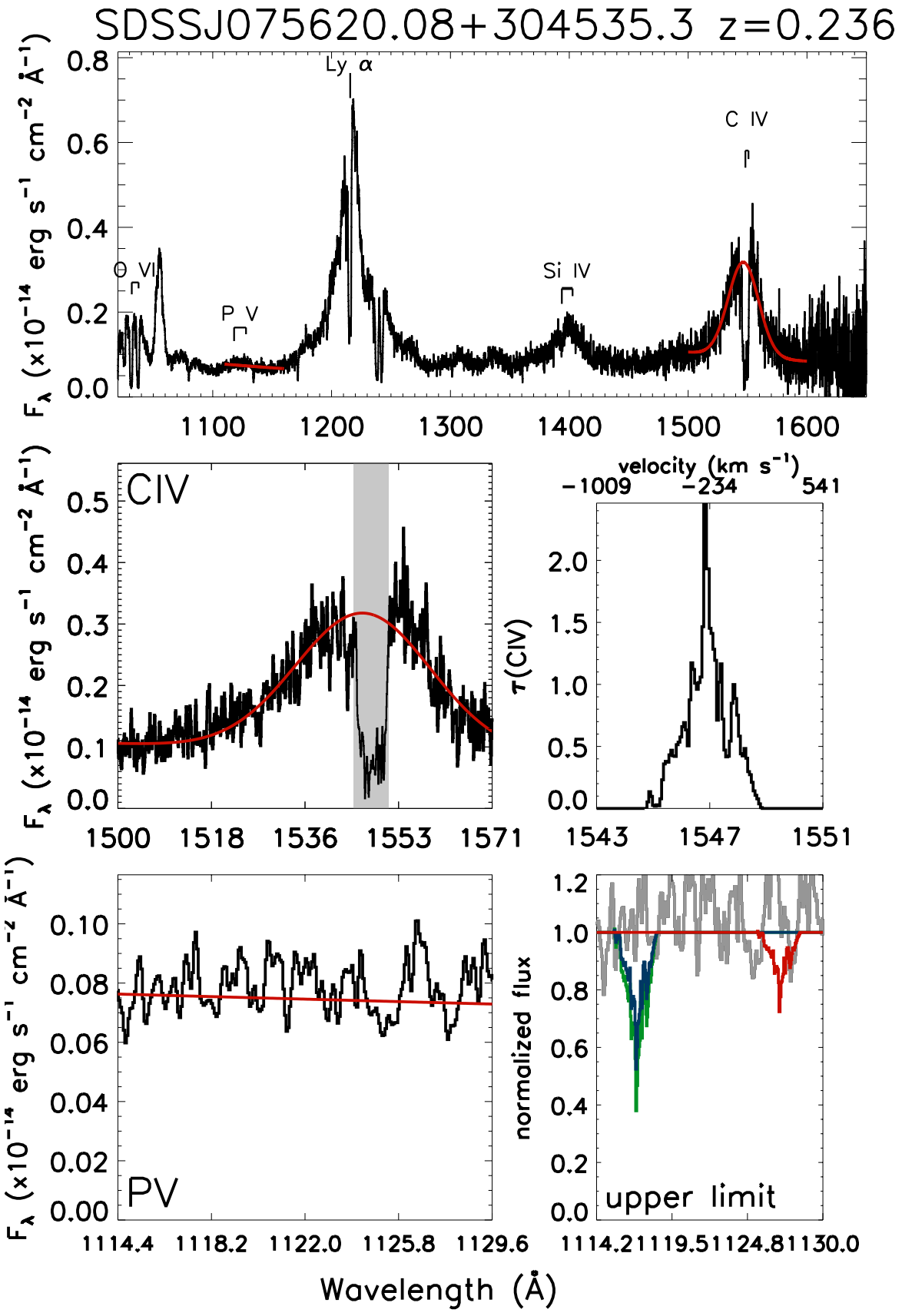
SDSSJ075620.08+304535.3 z=0.236
Ly α
C IV
O VI
P V
Si IV
F_λ (x10^{-14} erg s^{-1} cm^{-2} Å^{-1})
CIV
velocity (km s^{-1})
−1009
−234
541
τ(CIV)
PV
normalized flux
upper limit
Wavelength (Å)

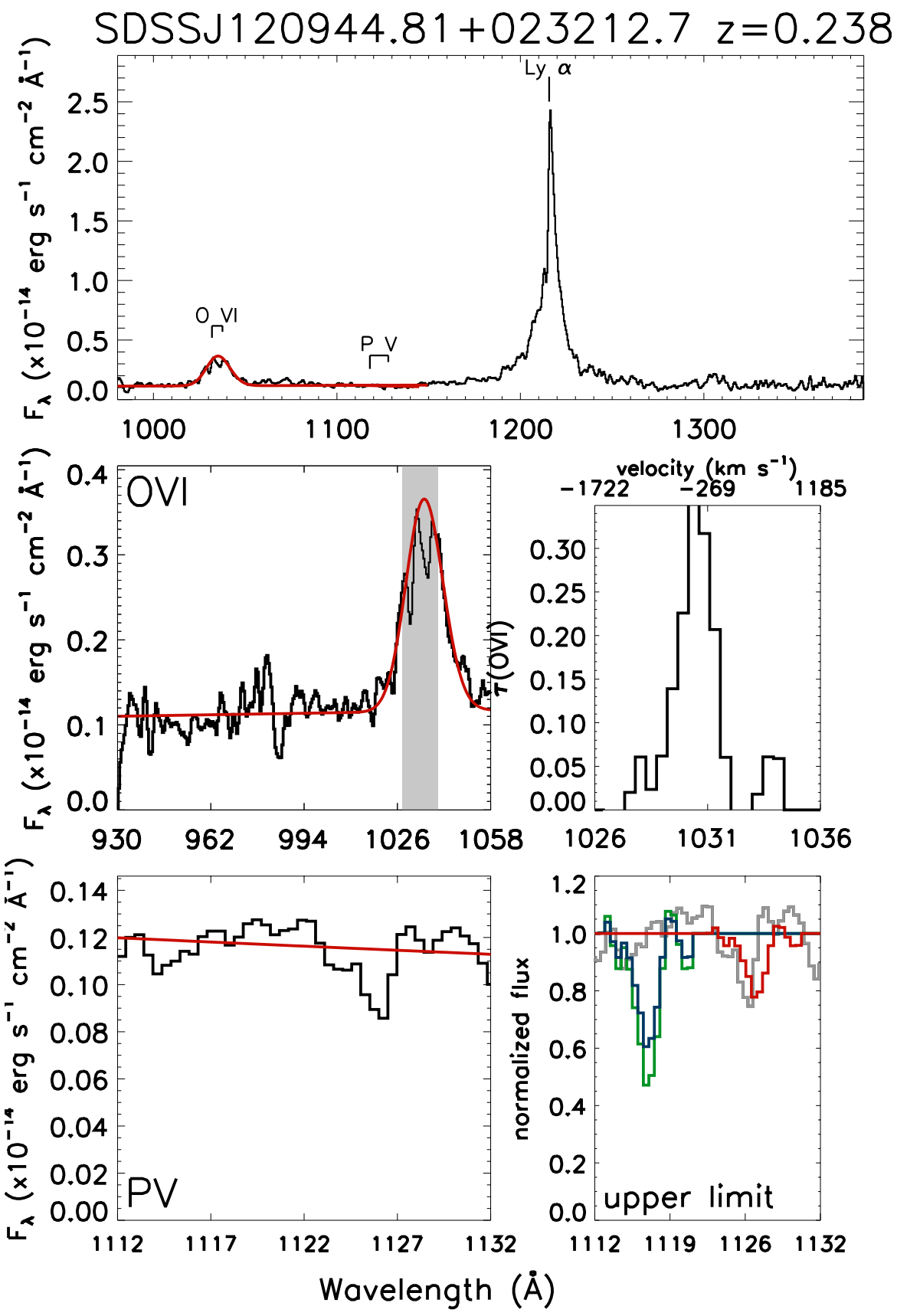
SDSSJ120944.81+023212.7 z=0.238
Ly α
O VI
P V
OVI
PV
velocity (km s⁻¹)
−1722
−269
1185
τ(OVI)
normalized flux
upper limit
Wavelength (Å)

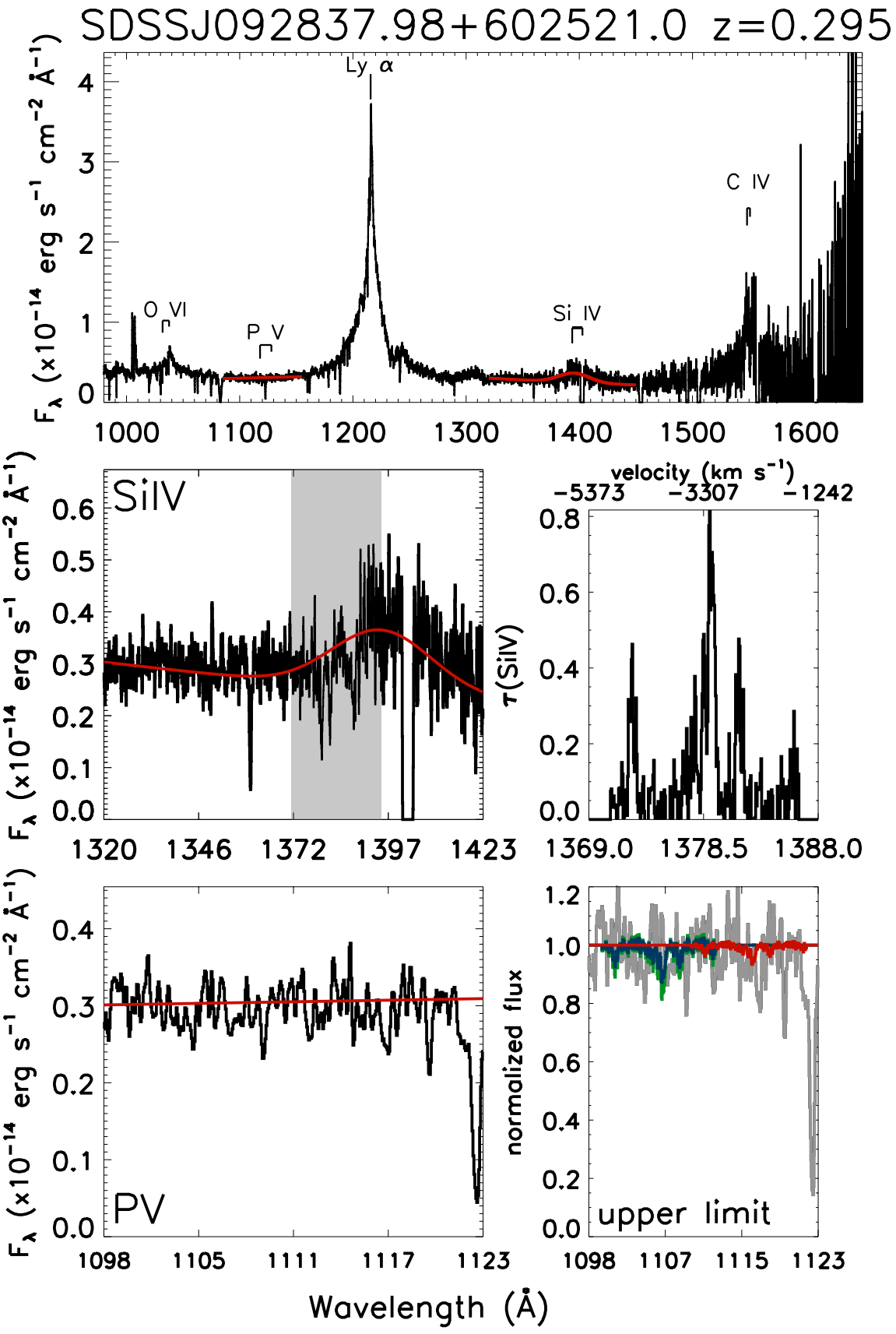
SDSSJ092837.98+602521.0 z=0.295
Ly α
O VI
P V
Si IV
C IV
F_λ (x10^-14 erg s^-1 cm^-2 Å^-1)
1000
1100
1200
1300
1400
1500
1600
SiIV
PV
velocity (km s^-1)
−5373
−3307
−1242
τ(SiIV)
normalized flux
upper limit
1320
1346
1372
1397
1423
1369.0
1378.5
1388.0
1098
1105
1111
1117
1123
1107
1115
Wavelength (Å)

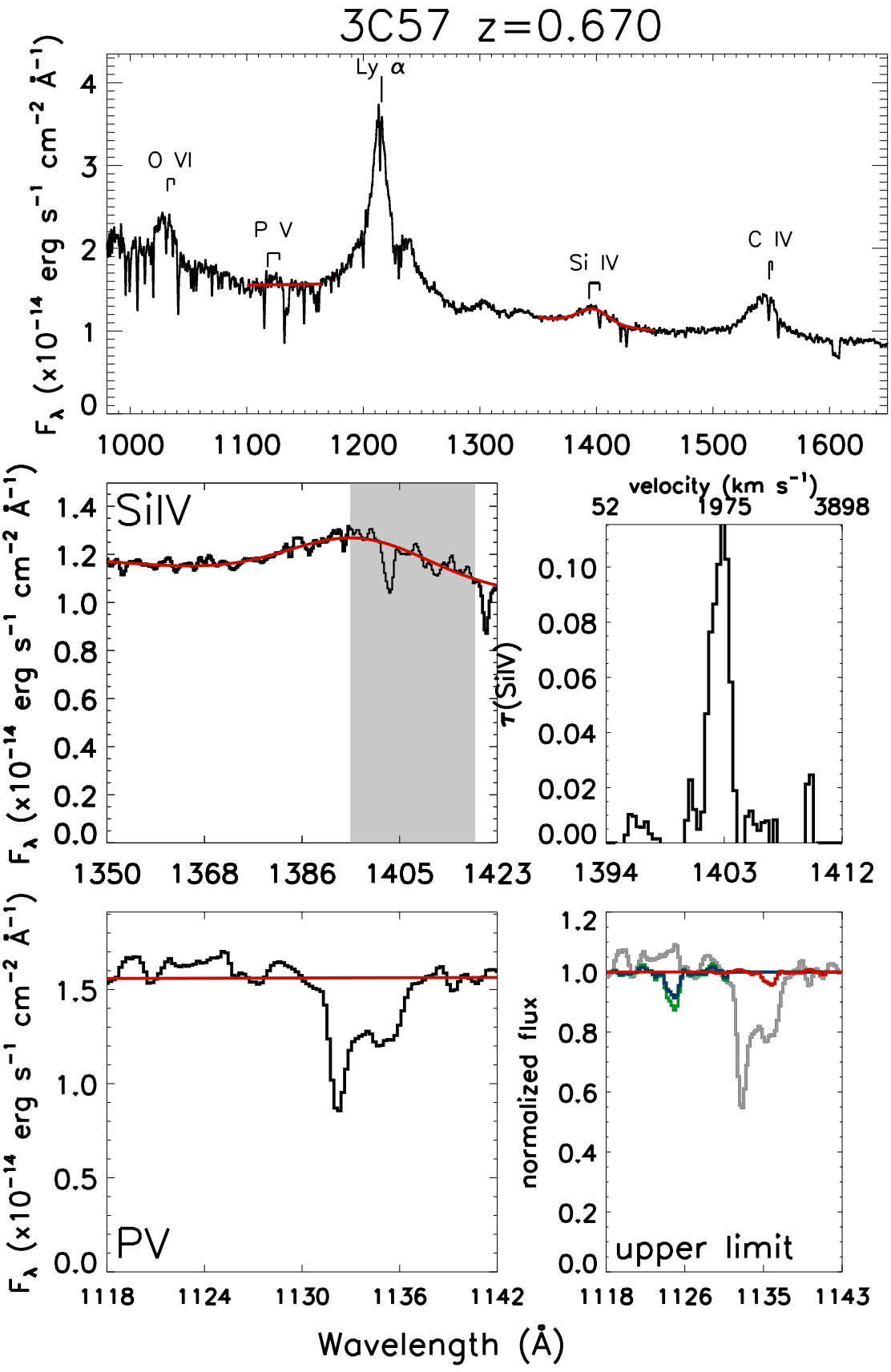
3C57 z=0.670
Ly α
O VI
P V
Si IV
C IV
F_λ (x10^{-14} erg s^{-1} cm^{-2} Å^{-1})
SiIV
PV
τ(SiIV)
velocity (km s^{-1})
52
1975
3898
normalized flux
upper limit
Wavelength (Å)

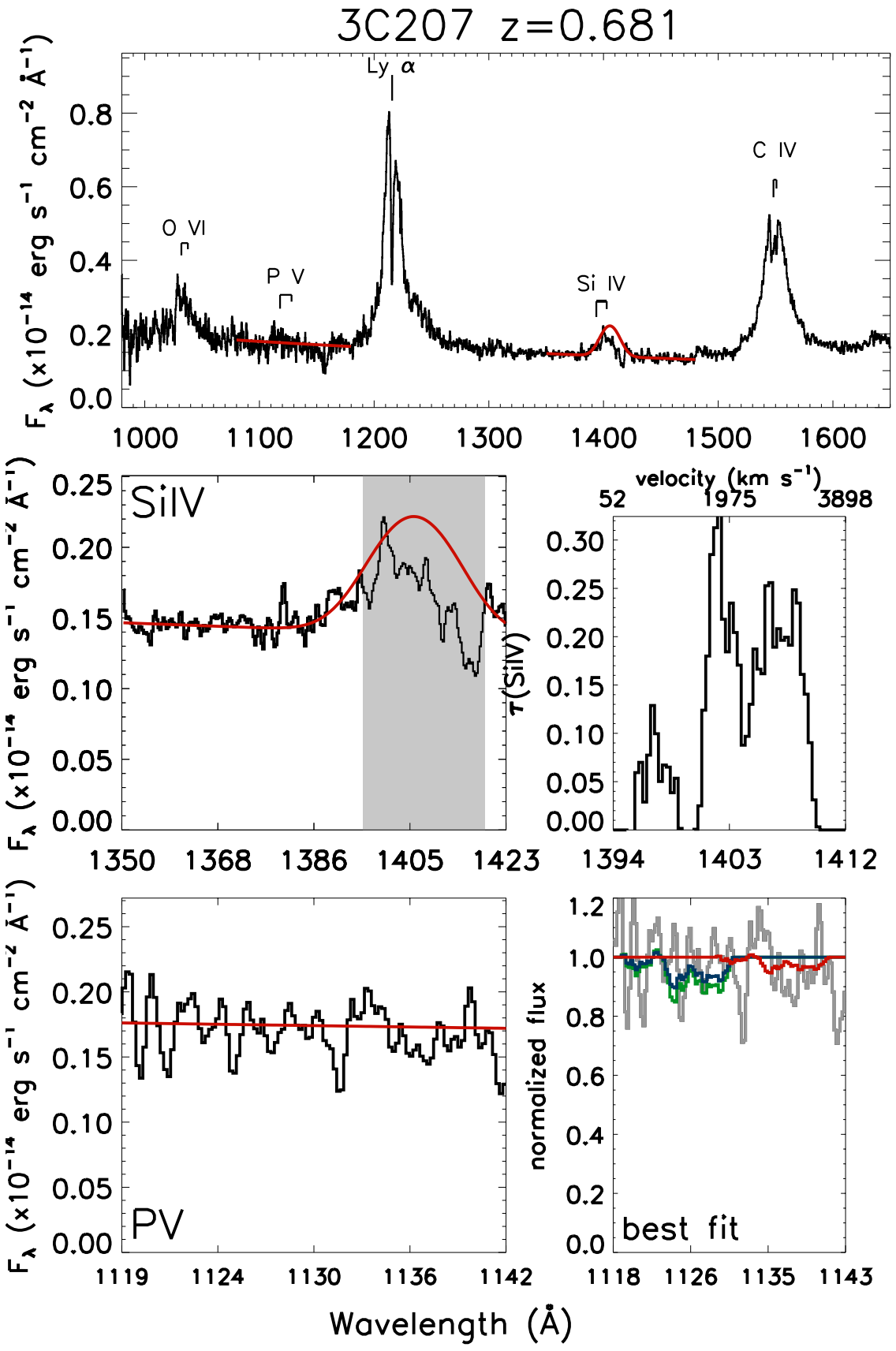
3C207 z=0.681
Ly α
O VI
P V
Si IV
C IV
F_λ (x10^{-14} erg s^{-1} cm^{-2} Å^{-1})
SiIV
velocity (km s^{-1})
τ(SiIV)
PV
normalized flux
best fit
Wavelength (Å)

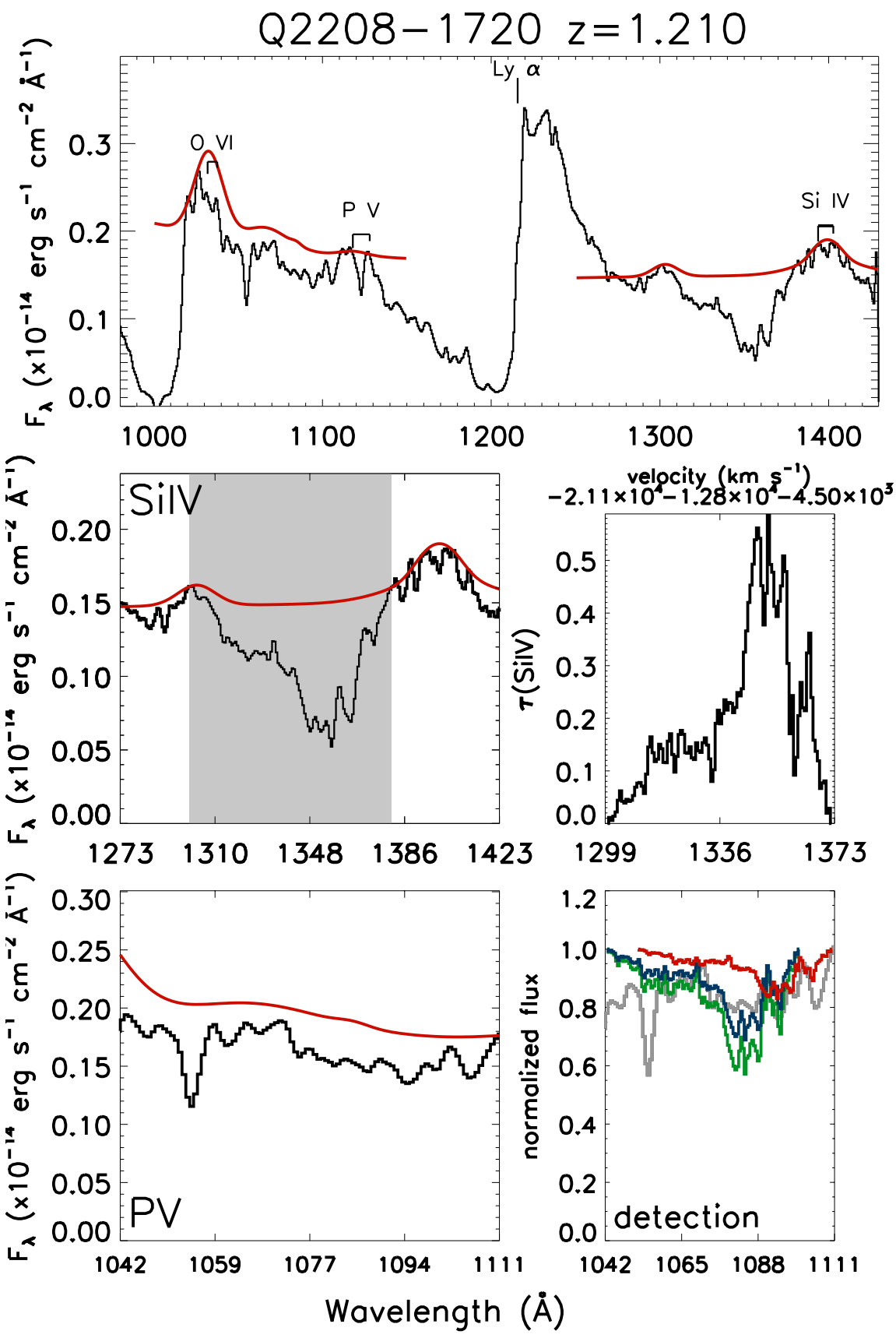
Q2208−1720 z=1.210
Ly α
O VI
P V
Si IV
F_λ (x10^{-14} erg s^{-1} cm^{-2} Å^{-1})
1000
1100
1200
1300
1400
SiIV
F_λ (x10^{-14} erg s^{-1} cm^{-2} Å^{-1})
1273
1310
1348
1386
1423
velocity (km s^{-1})
−2.11×10^4 −1.28×10^4 −4.50×10^3
τ(SiIV)
1299
1336
1373
PV
F_λ (x10^{-14} erg s^{-1} cm^{-2} Å^{-1})
1042
1059
1077
1094
1111
normalized flux
detection
1042
1065
1088
1111
Wavelength (Å)

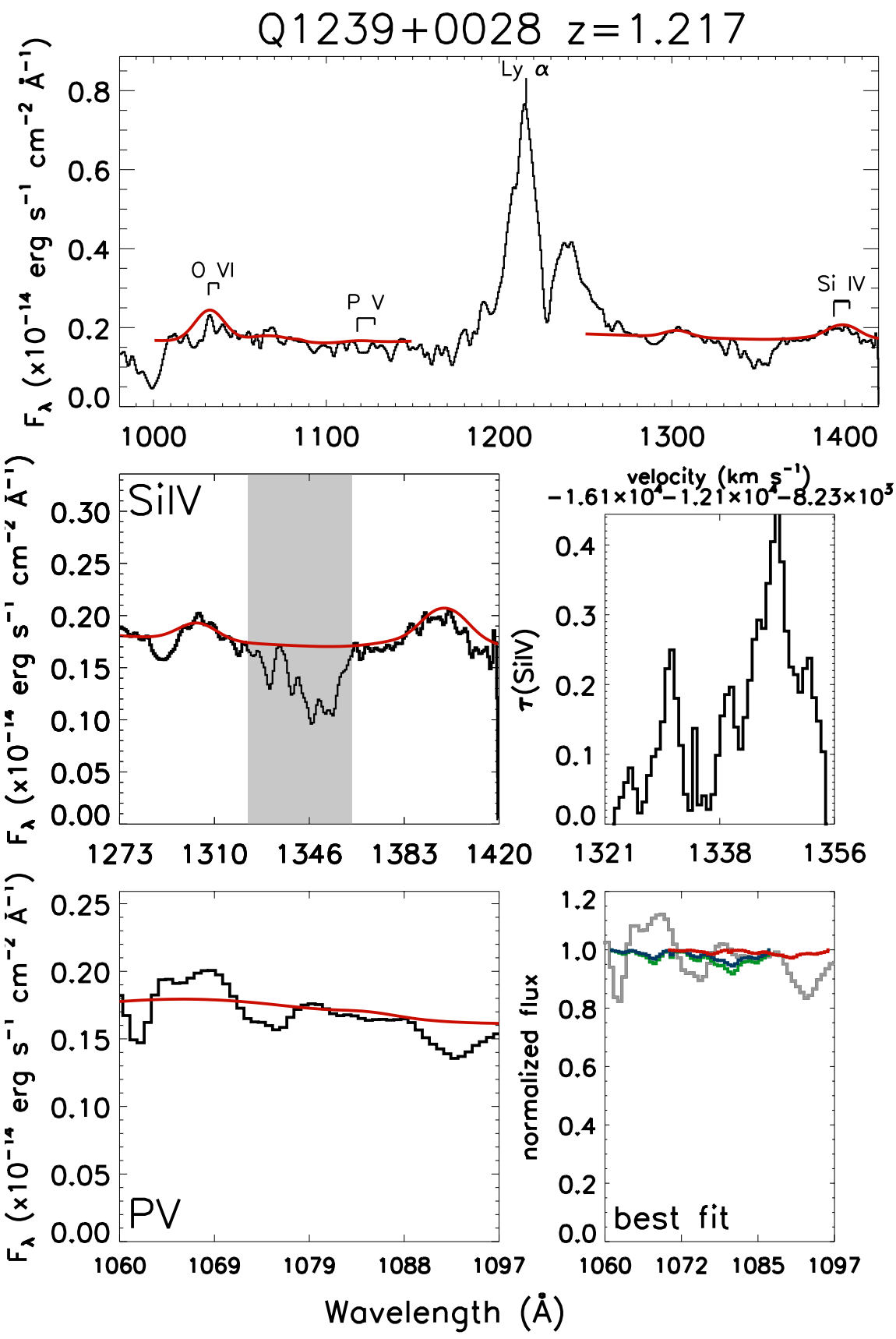
Q1239+0028 z=1.217
Ly α
O VI
P V
Si IV
F_λ ($\times 10^{-14}$ erg s^{-1} cm^{-2} Å^{-1})
SiIV
PV
velocity (km s^{-1})
−1.61×10^4 −1.21×10^4 −8.23×10^3
τ(SiIV)
normalized flux
best fit
Wavelength (Å)

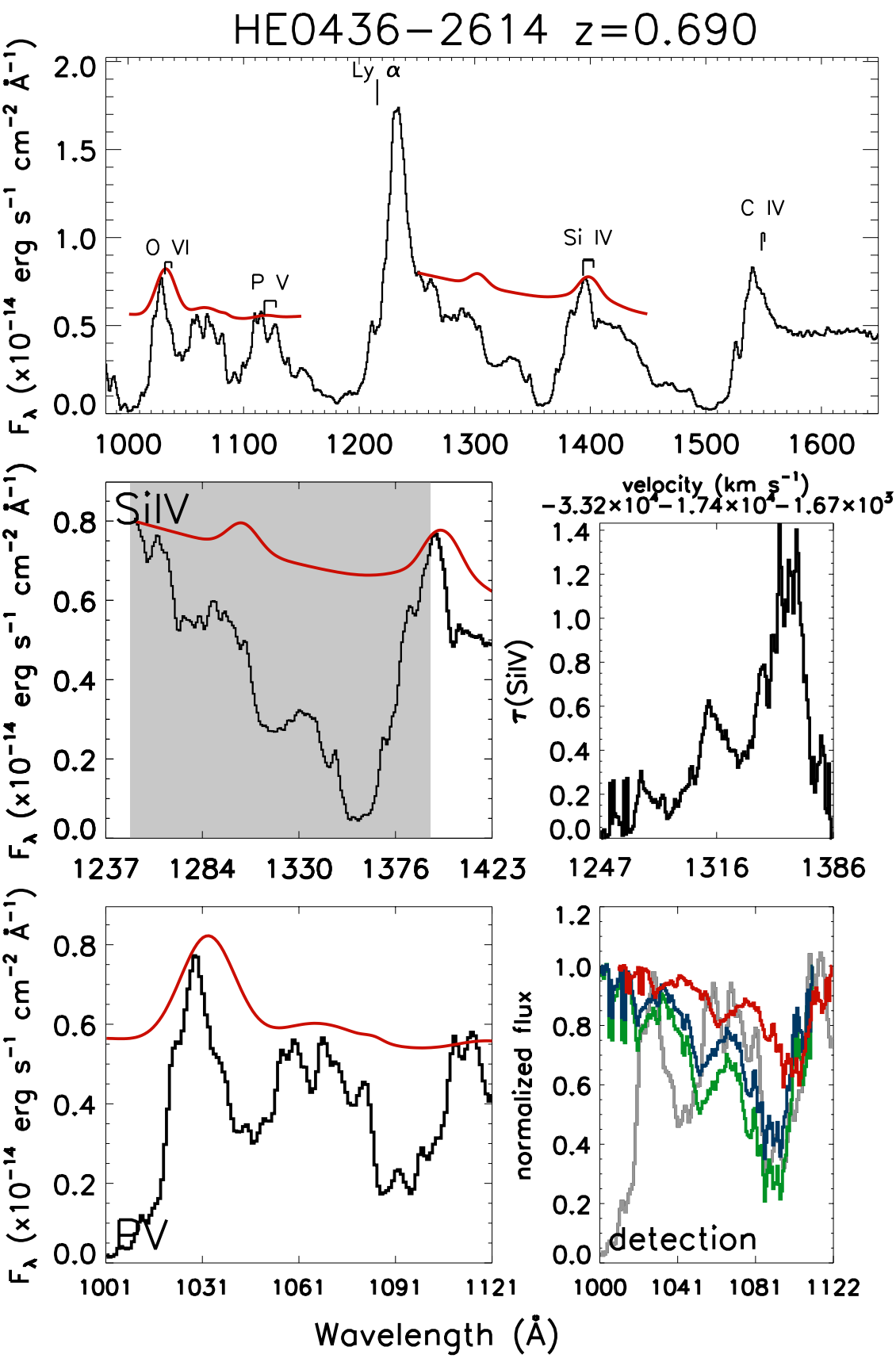
HE0436−2614 z=0.690
Ly α
O VI
P V
Si IV
C IV
SiIV
PV
velocity (km s⁻¹)
−3.32×10⁴ −1.74×10⁴ −1.67×10³
τ(SiIV)
normalized flux
detection
Wavelength (Å)

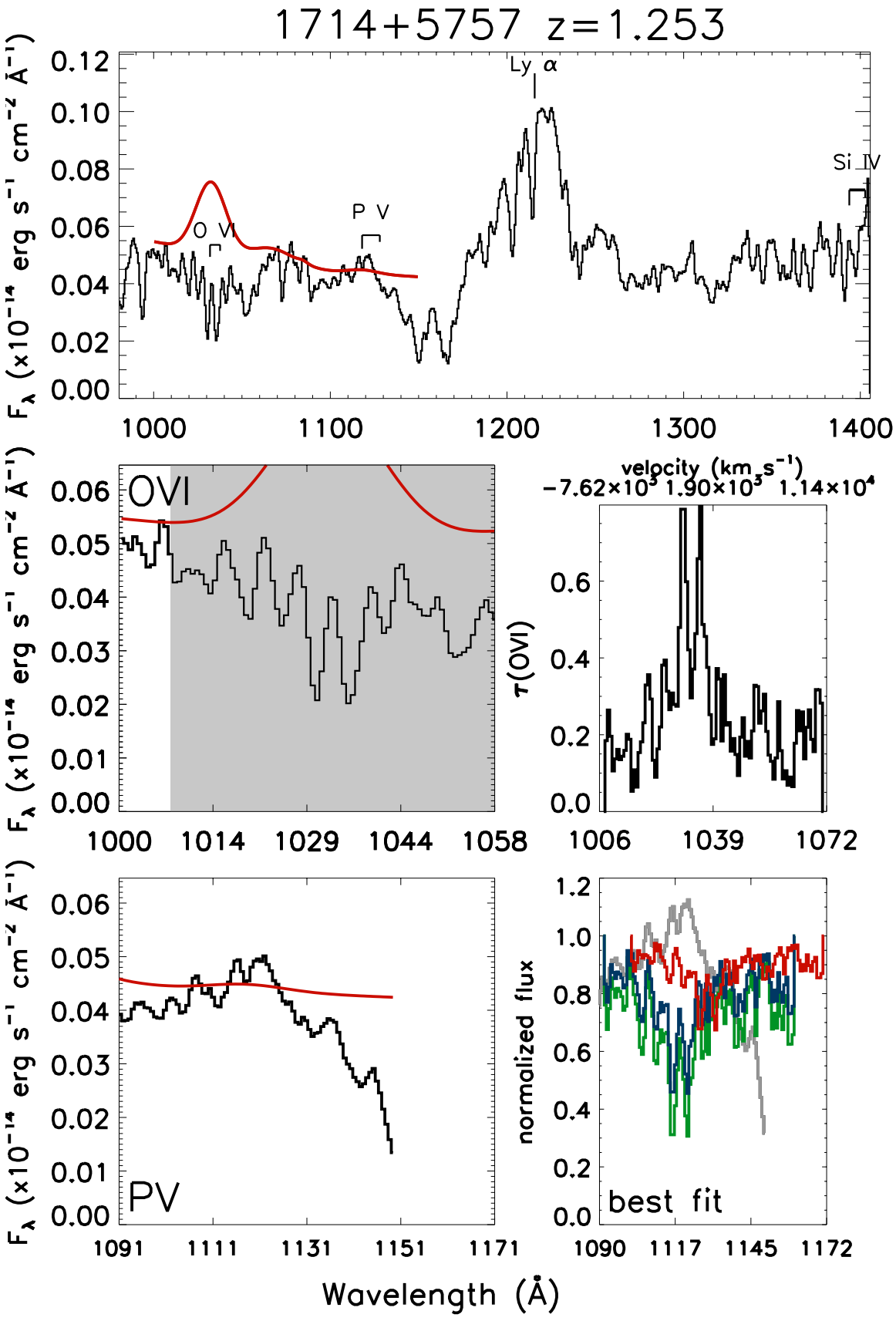
1714+5757 z=1.253
Ly α
Si IV
P V
O VI
OVI
PV
velocity (km s⁻¹)
−7.62×10³ 1.90×10³ 1.14×10⁴
τ(OVI)
normalized flux
best fit
Wavelength (Å)

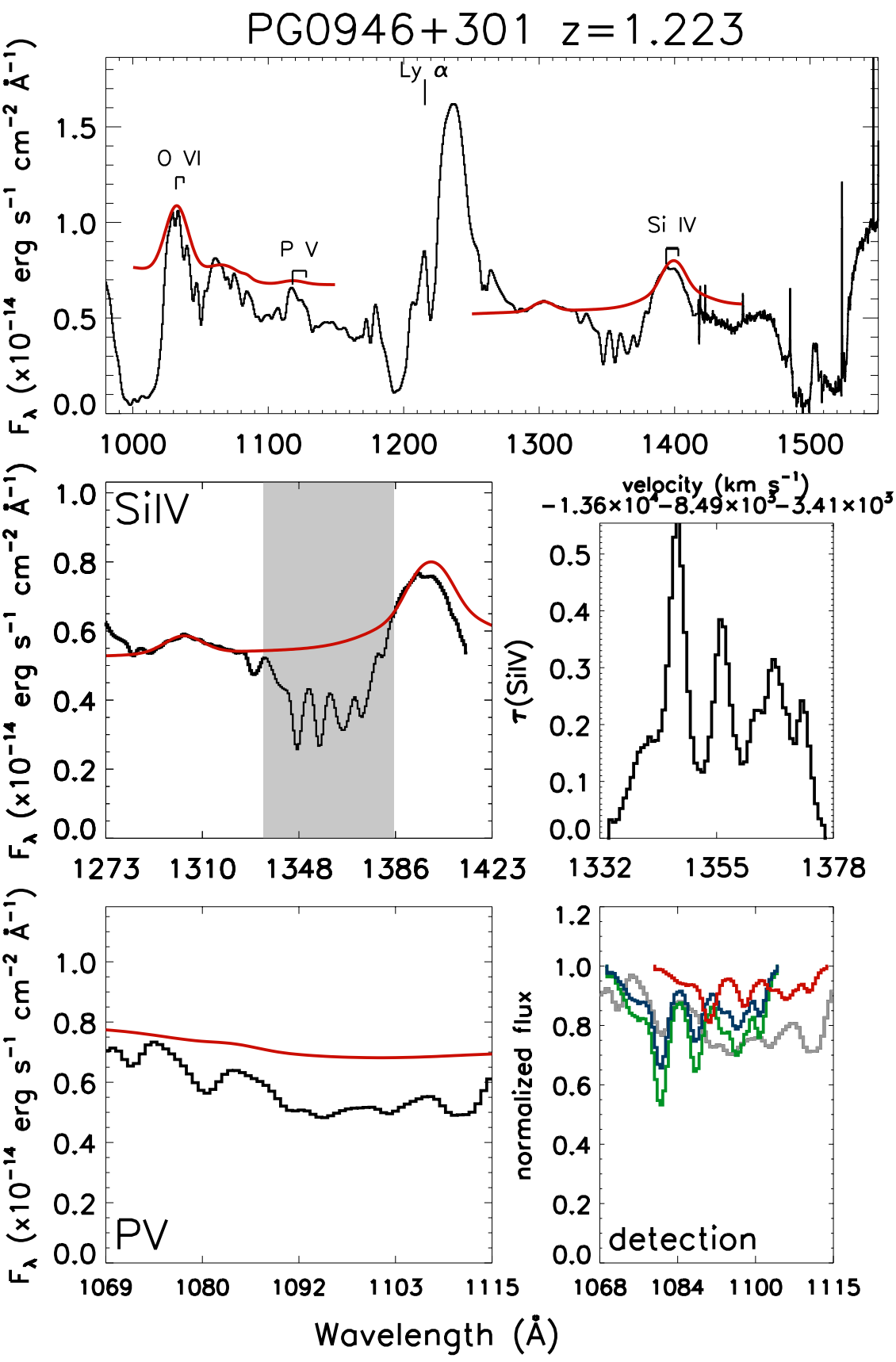
PG0946+301 z=1.223
Ly α
O VI
P V
Si IV
SiIV
PV
velocity (km s⁻¹)
−1.36×10⁴ −8.49×10³ −3.41×10³
τ(SiIV)
normalized flux
detection
Wavelength (Å)

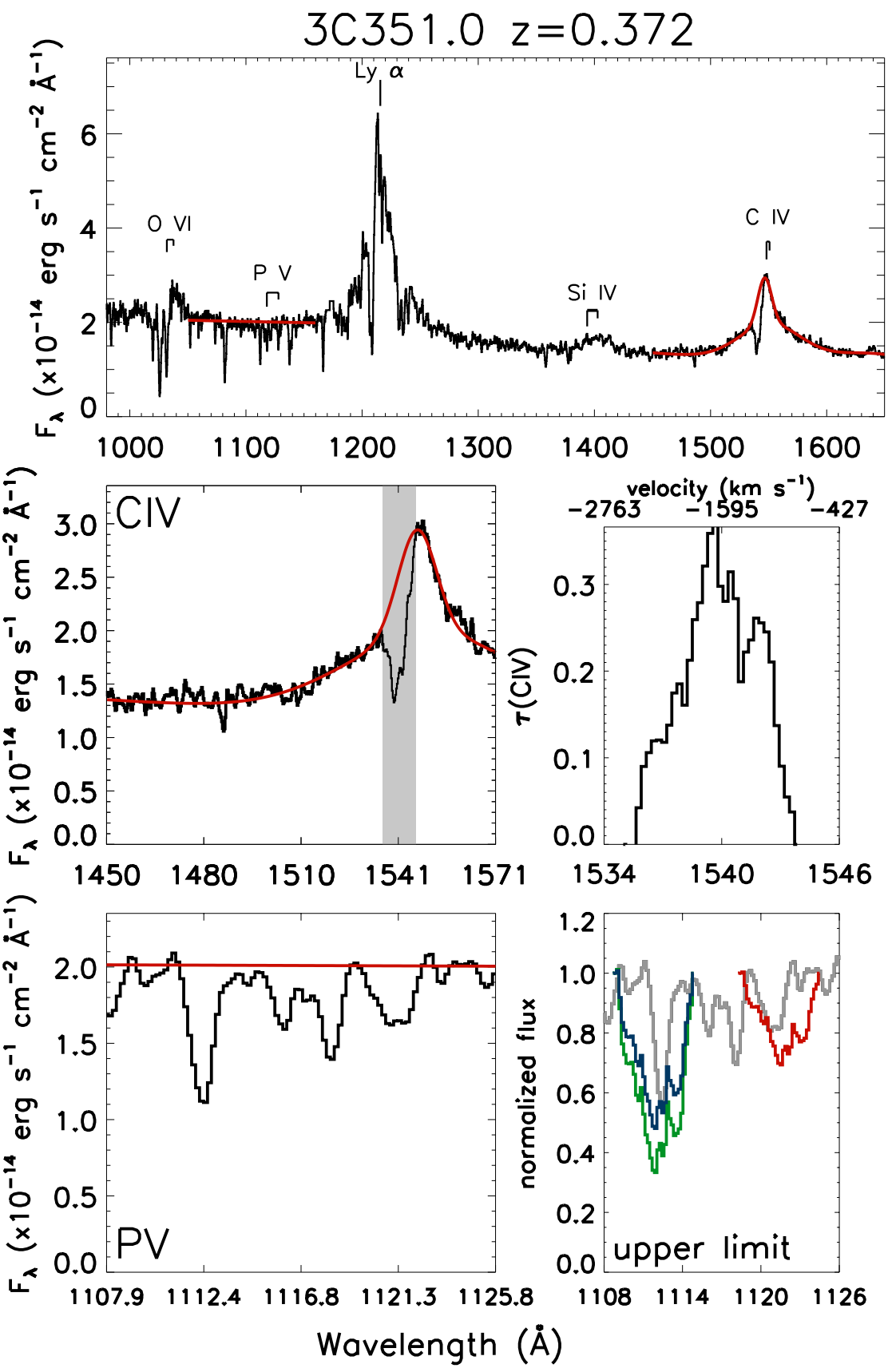
3C351.0 z=0.372
Ly α
O VI
P V
Si IV
C IV
F_λ (x10^{-14} erg s^{-1} cm^{-2} Å^{-1})
1000
1100
1200
1300
1400
1500
1600
CIV
PV
velocity (km s^{-1})
−2763
−1595
−427
τ(CIV)
normalized flux
upper limit
1450
1480
1510
1541
1571
1534
1540
1546
1107.9
1112.4
1116.8
1121.3
1125.8
1108
1114
1120
1126
Wavelength (Å)

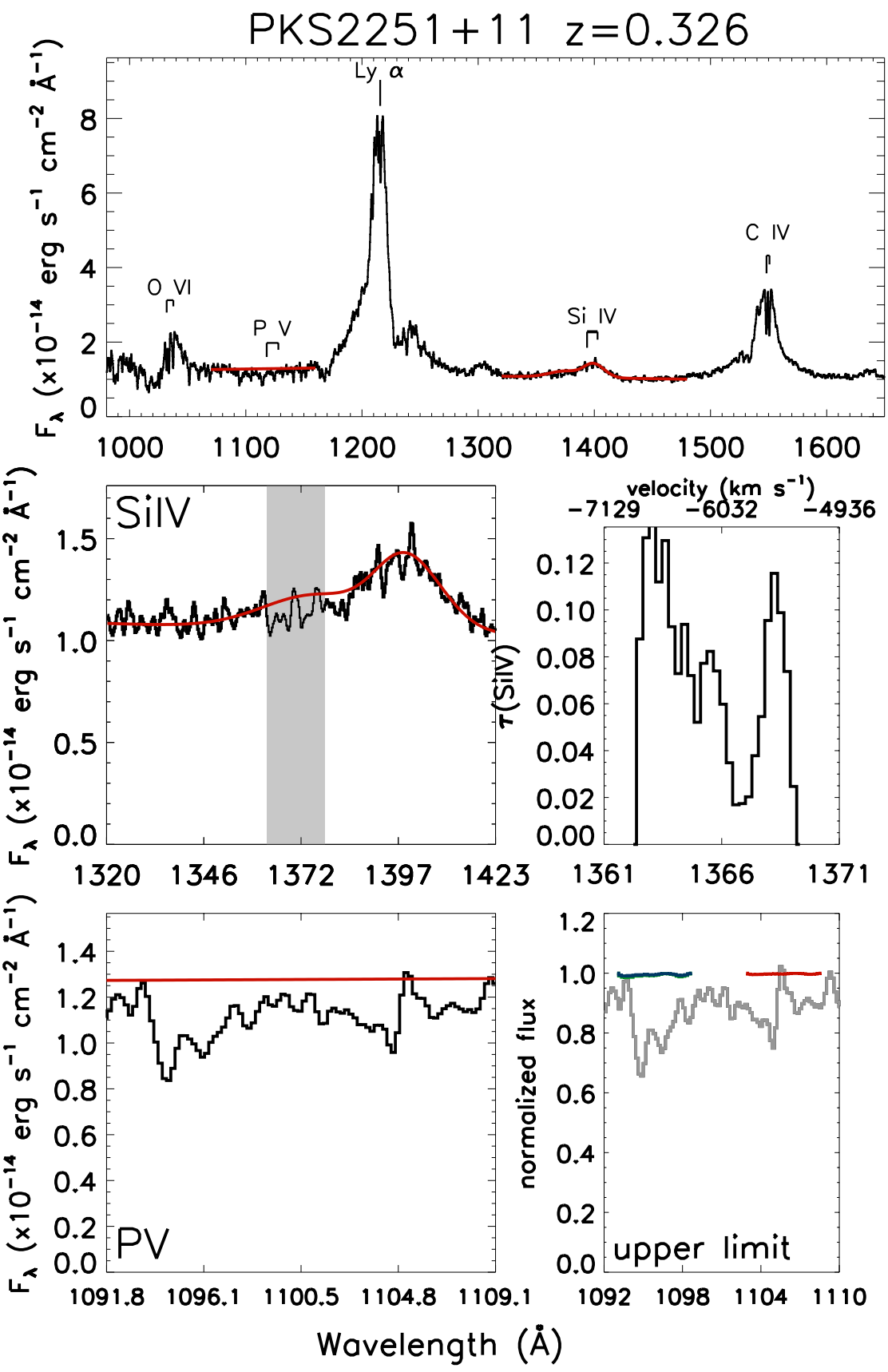
PKS2251+11 z=0.326
Ly α
O VI
P V
Si IV
C IV
F_λ (x10^{-14} erg s^{-1} cm^{-2} Å^{-1})
SiIV
velocity (km s^{-1})
−7129
−6032
−4936
τ(SiIV)
PV
normalized flux
upper limit
Wavelength (Å)

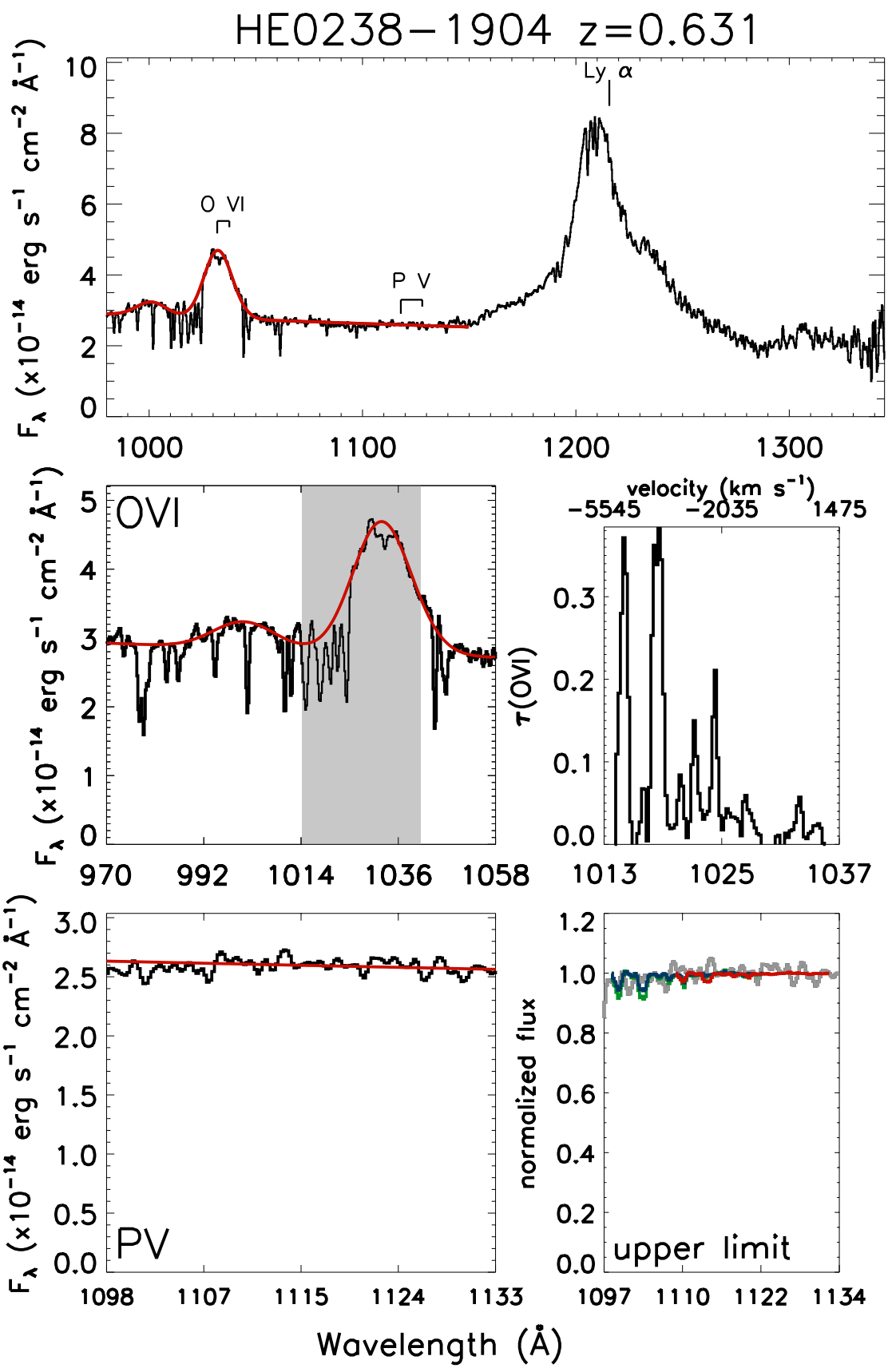
HE0238−1904 z=0.631
O VI
P V
Ly α
OVI
PV
upper limit
velocity (km s⁻¹)
−5545
−2035
1475
τ(OVI)
normalized flux
Wavelength (Å)

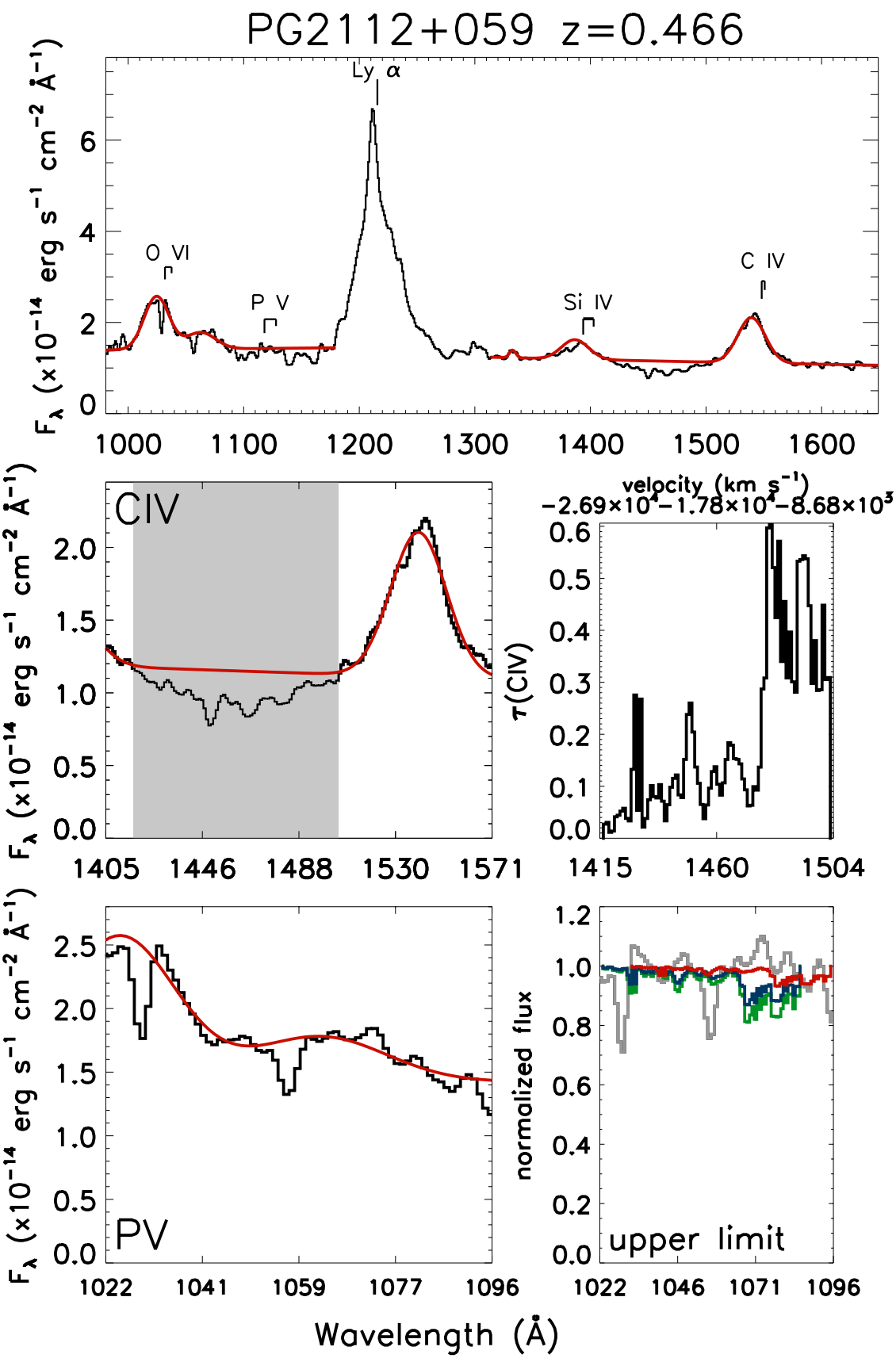
PG2112+059 z=0.466
Ly α
O VI
P V
Si IV
C IV
F_λ (x10^{-14} erg s^{-1} cm^{-2} Å^{-1})
1000
1100
1200
1300
1400
1500
1600
CIV
PV
velocity (km s^{-1})
−2.69×10^4 −1.78×10^4 −8.68×10^3
τ(CIV)
normalized flux
upper limit
1405
1446
1488
1530
1571
1415
1460
1504
1022
1041
1059
1077
1096
1046
1071
Wavelength (Å)

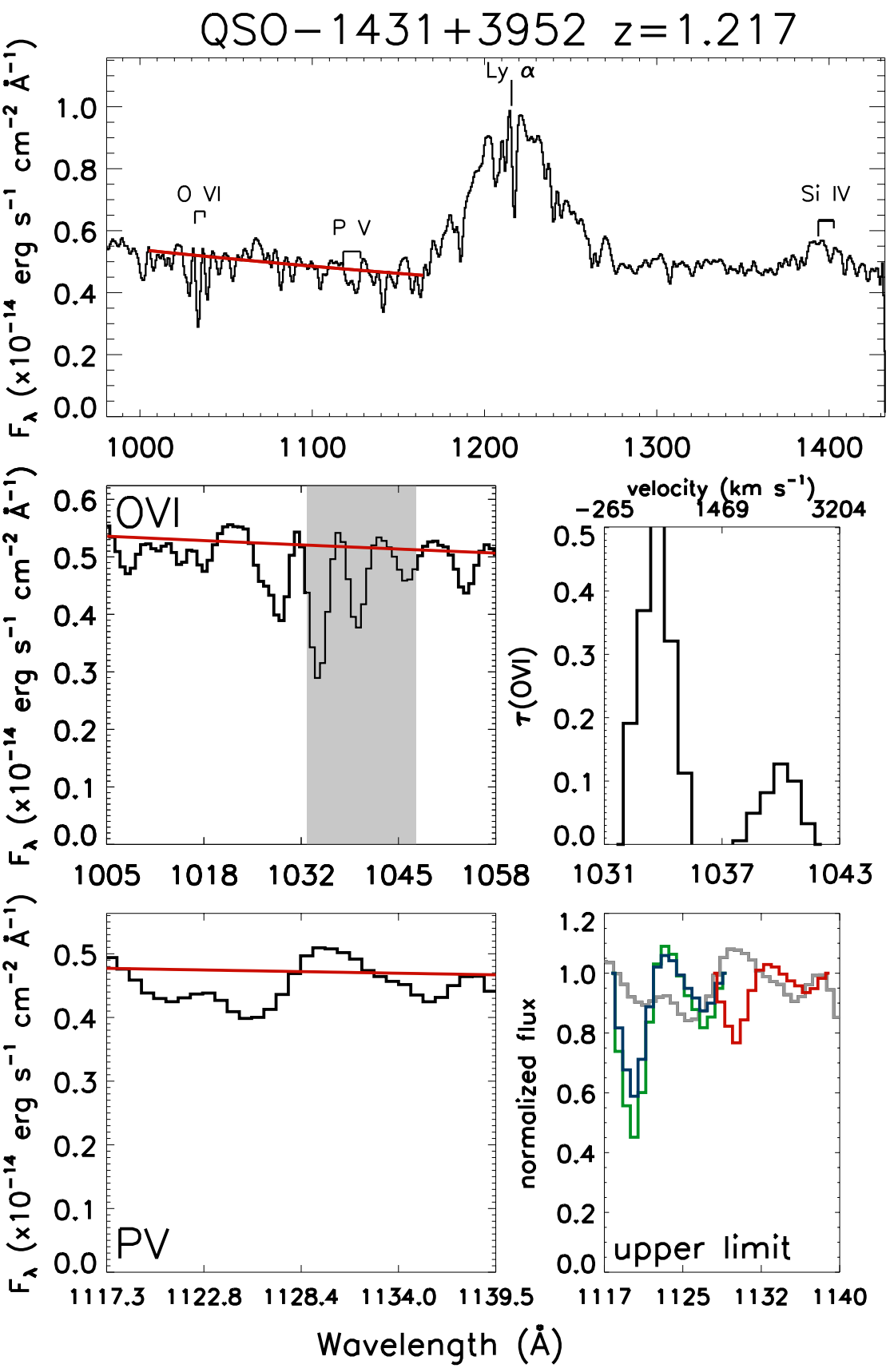
QSO−1431+3952 z=1.217
Ly α
O VI
P V
Si IV
OVI
velocity (km s⁻¹)
−265
1469
3204
τ(OVI)
PV
normalized flux
upper limit
Wavelength (Å)

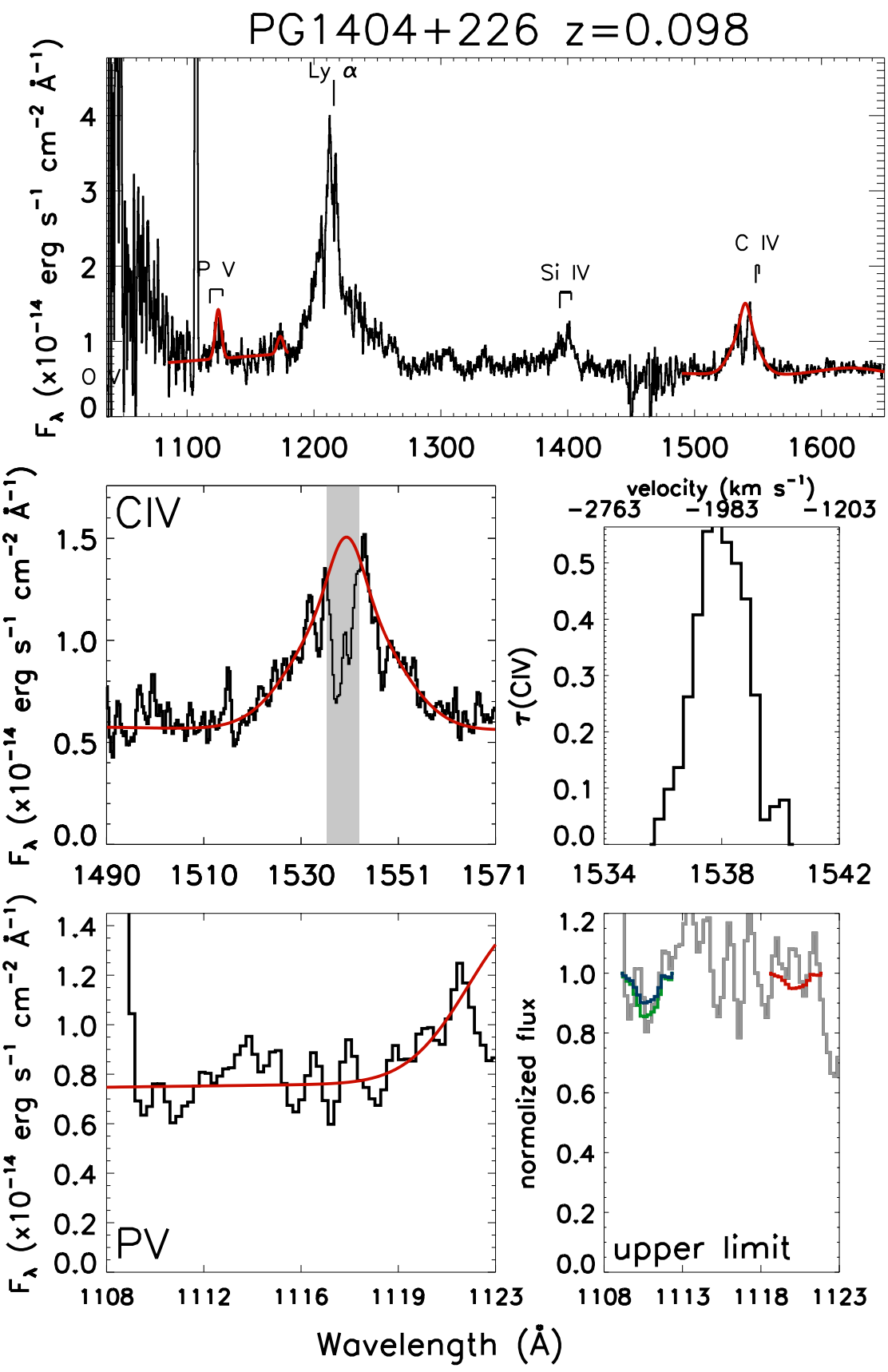
PG1404+226 z=0.098
Ly α
P V
Si IV
C IV
F_λ (x10^{-14} erg s^{-1} cm^{-2} Å^{-1})
1100
1200
1300
1400
1500
1600
CIV
PV
velocity (km s^{-1})
−2763
−1983
−1203
τ(CIV)
normalized flux
upper limit
1490
1510
1530
1551
1571
1534
1538
1542
1108
1112
1116
1119
1123
1113
1118
Wavelength (Å)

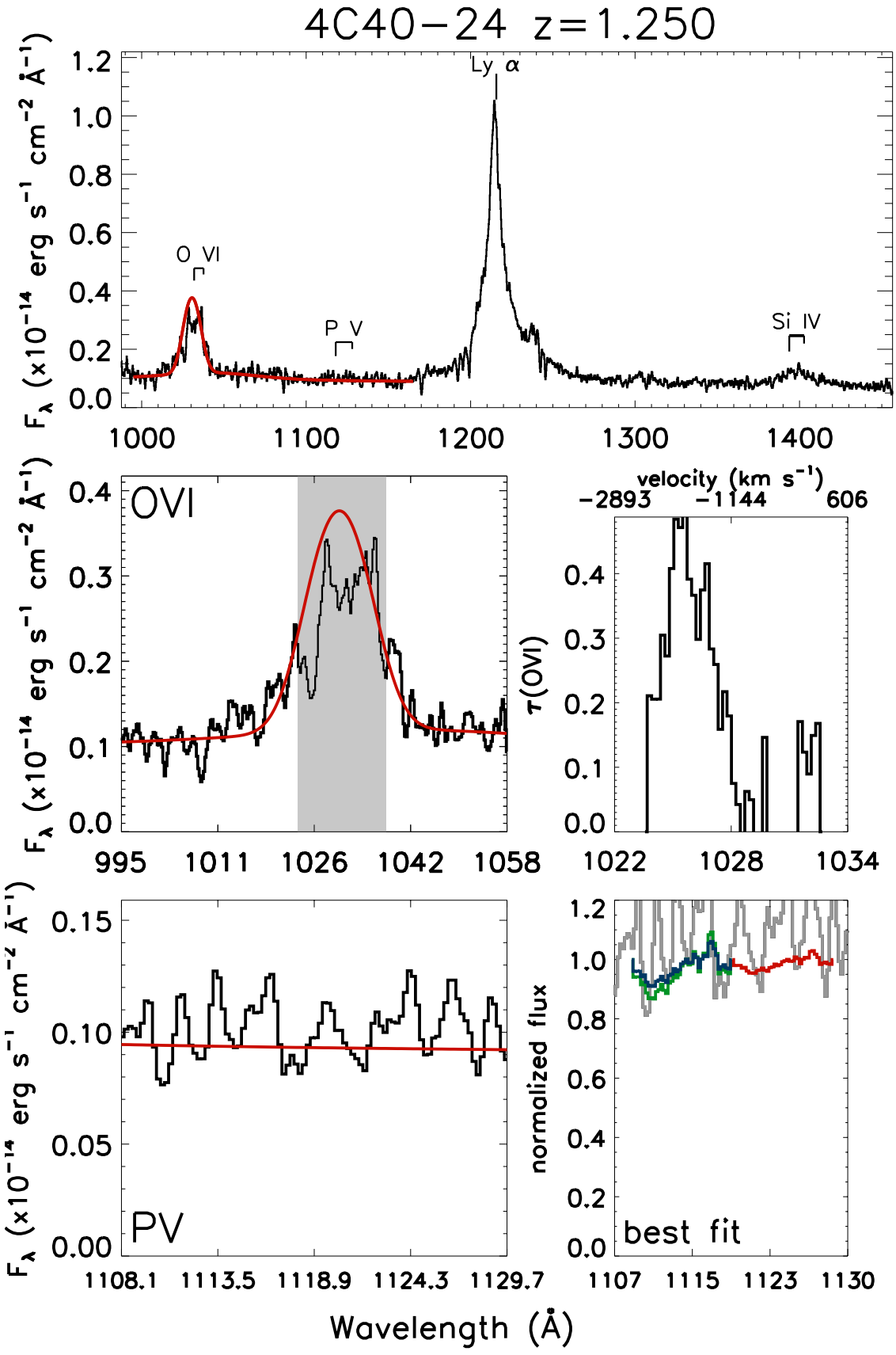
4C40−24 z=1.250
Ly α
O VI
P V
Si IV
OVI
velocity (km s⁻¹)
−2893
−1144
606
τ(OVI)
PV
best fit
normalized flux
Wavelength (Å)

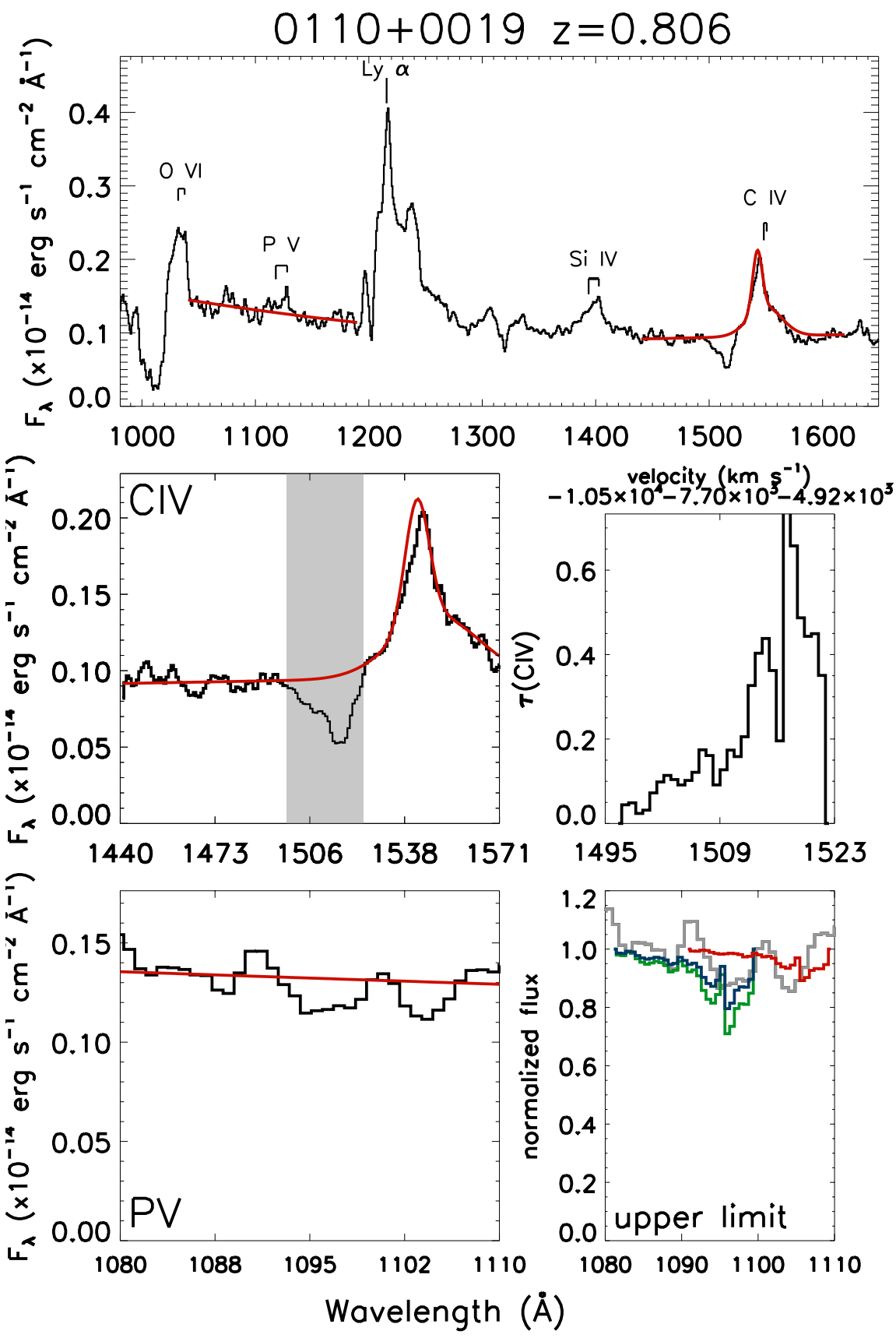
0110+0019 z=0.806
Ly α
O VI
P V
Si IV
C IV
F_λ (x10^{-14} erg s^{-1} cm^{-2} Å^{-1})
CIV
PV
velocity (km s^{-1})
−1.05×10^4 −7.70×10^3 −4.92×10^3
τ(CIV)
normalized flux
upper limit
Wavelength (Å)

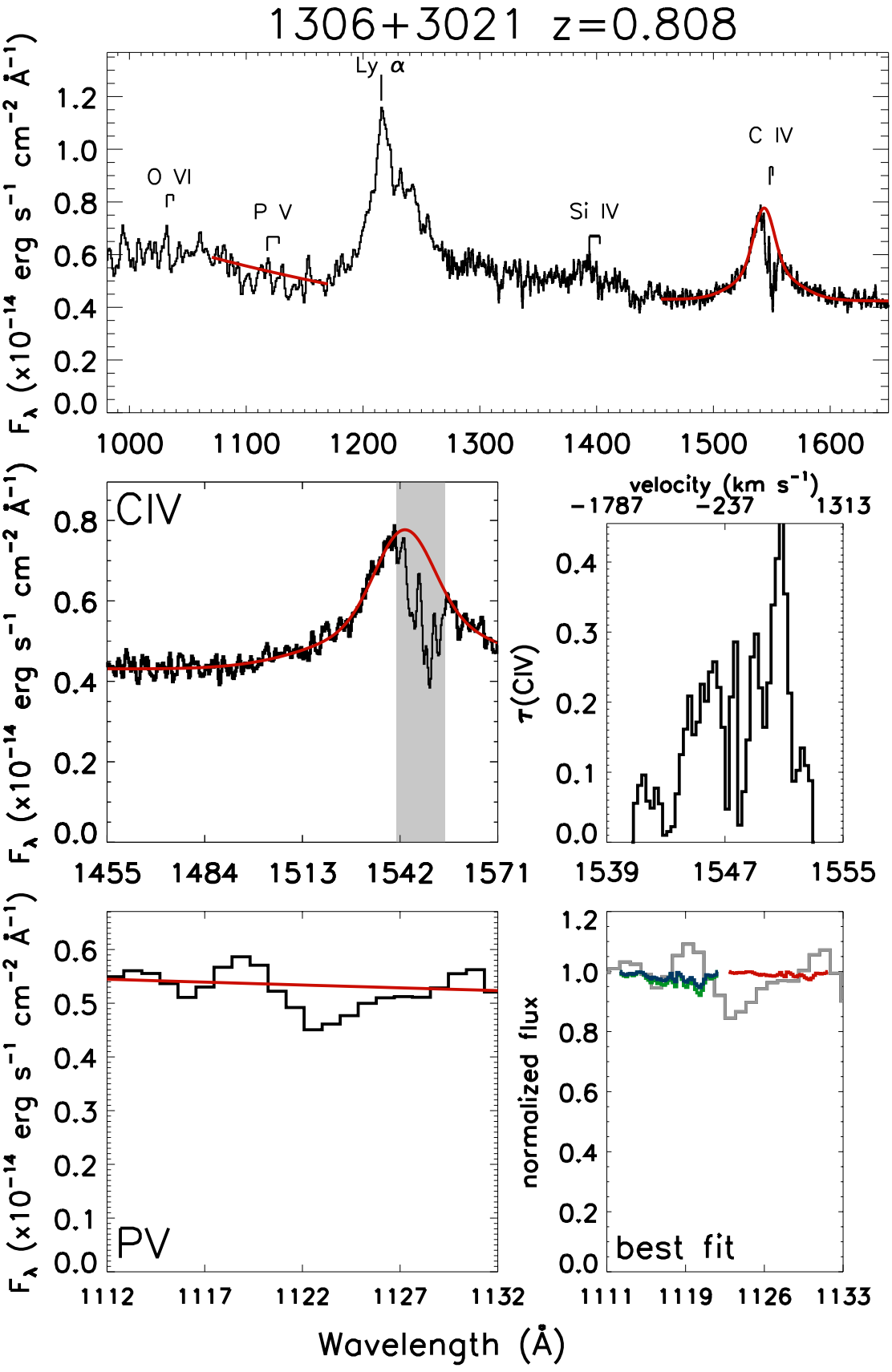
1306+3021 z=0.808
Ly α
O VI
P V
Si IV
C IV
F_λ (x10^{-14} erg s^{-1} cm^{-2} Å^{-1})
1000
1100
1200
1300
1400
1500
1600
CIV
velocity (km s^{-1})
−1787
−237
1313
τ(CIV)
1455
1484
1513
1542
1571
1539
1547
1555
PV
best fit
normalized flux
1112
1117
1122
1127
1132
1111
1119
1126
1133
Wavelength (Å)

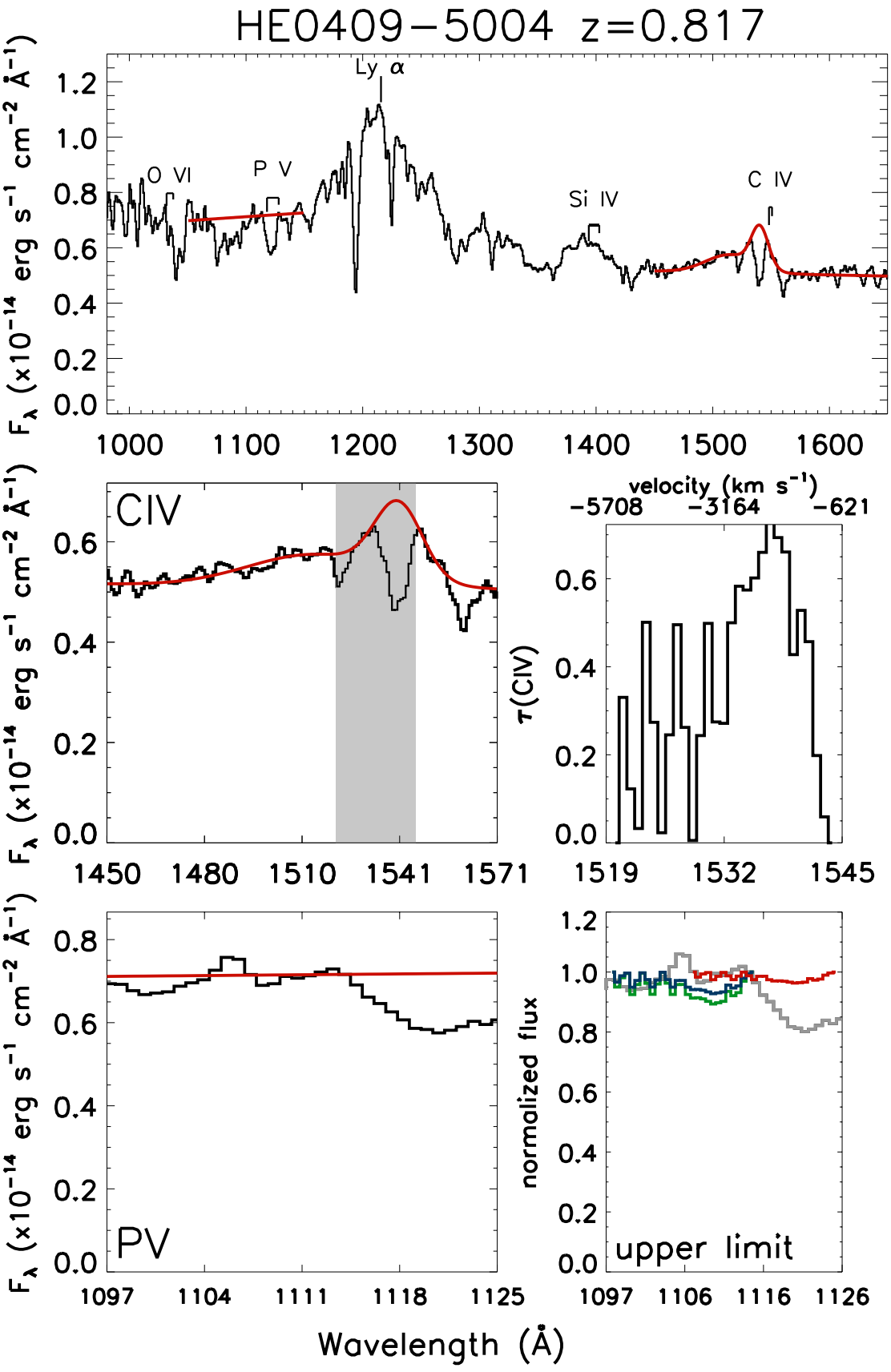
HE0409−5004 z=0.817
Ly α
O VI
P V
Si IV
C IV
CIV
PV
velocity (km s⁻¹)
−5708
−3164
−621
τ(CIV)
normalized flux
upper limit
Wavelength (Å)

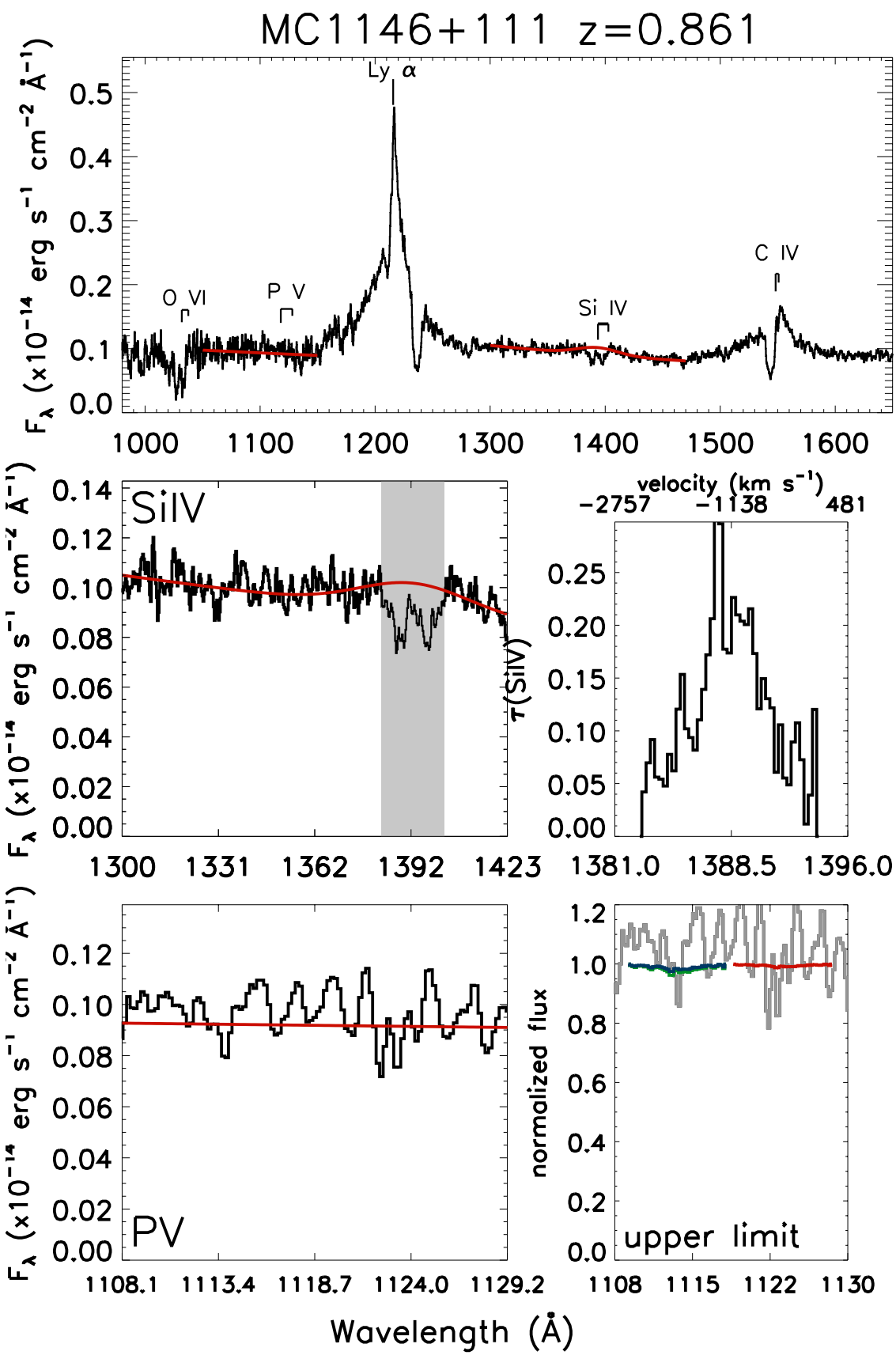
MC1146+111 z=0.861
Ly α
O VI
P V
Si IV
C IV
F_λ (x10^{-14} erg s^{-1} cm^{-2} Å^{-1})
SiIV
velocity (km s^{-1})
−2757
−1138
481
τ(SiIV)
PV
normalized flux
upper limit
Wavelength (Å)

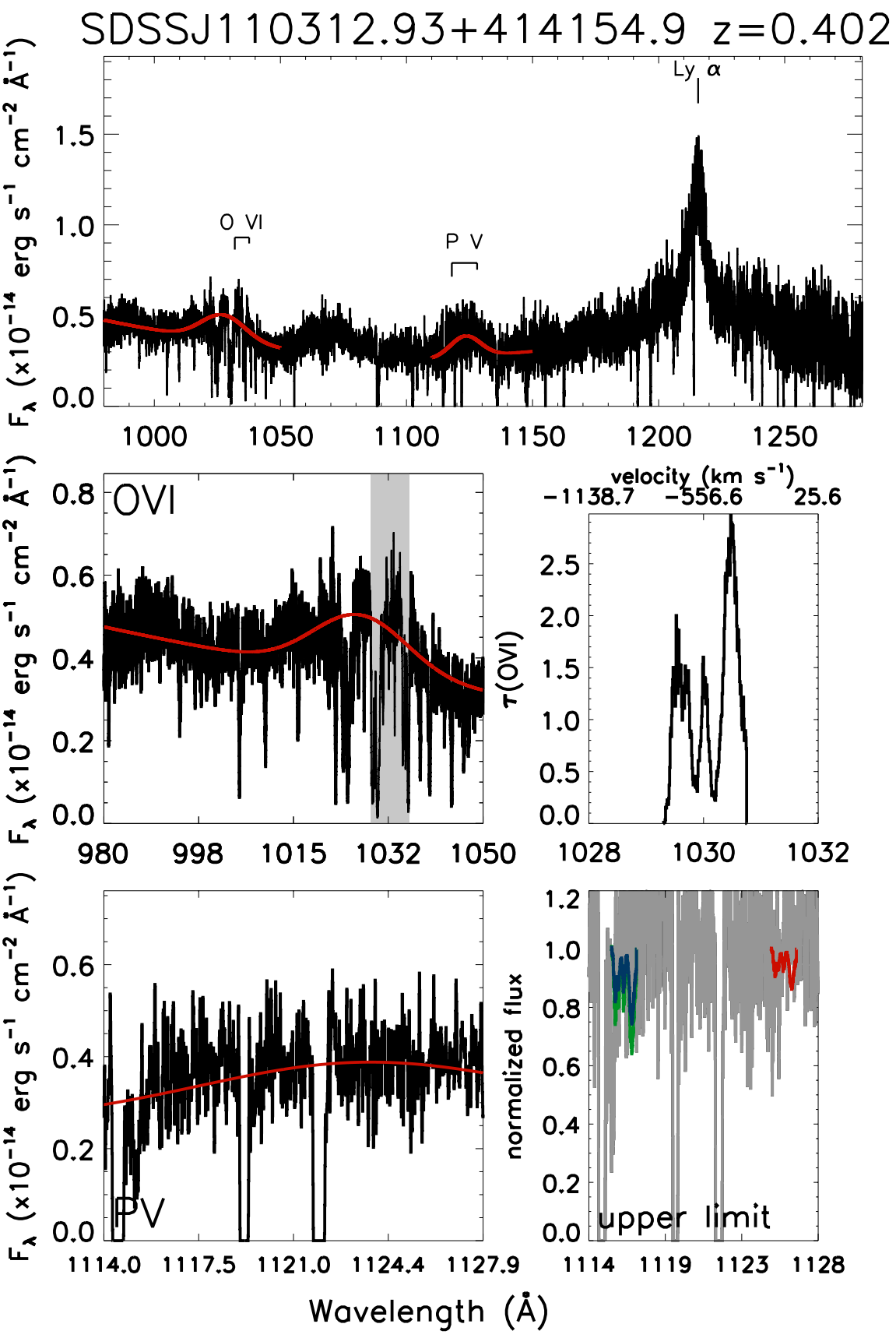
SDSSJ110312.93+414154.9 z=0.402
Ly α
O VI
P V
OVI
PV
velocity (km s⁻¹)
−1138.7
−556.6
25.6
τ(OVI)
normalized flux
upper limit
Wavelength (Å)

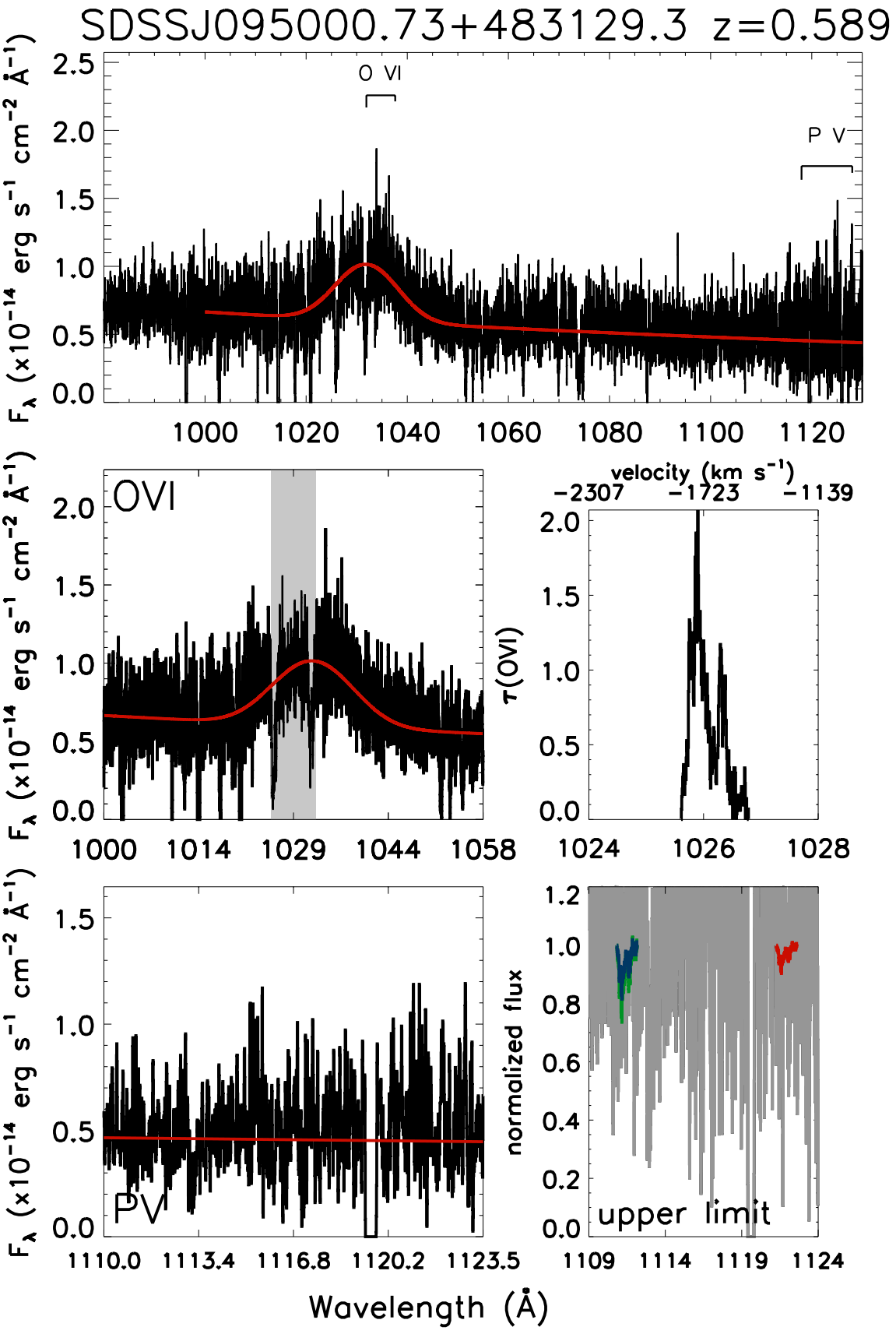
SDSSJ095000.73+483129.3 z=0.589
O VI
P V
OVI
PV
velocity (km s^{-1})
−2307
−1723
−1139
τ(OVI)
normalized flux
upper limit
F$_\lambda$ (x10^{-14} erg s^{-1} cm^{-2} Å^{-1})
Wavelength (Å)

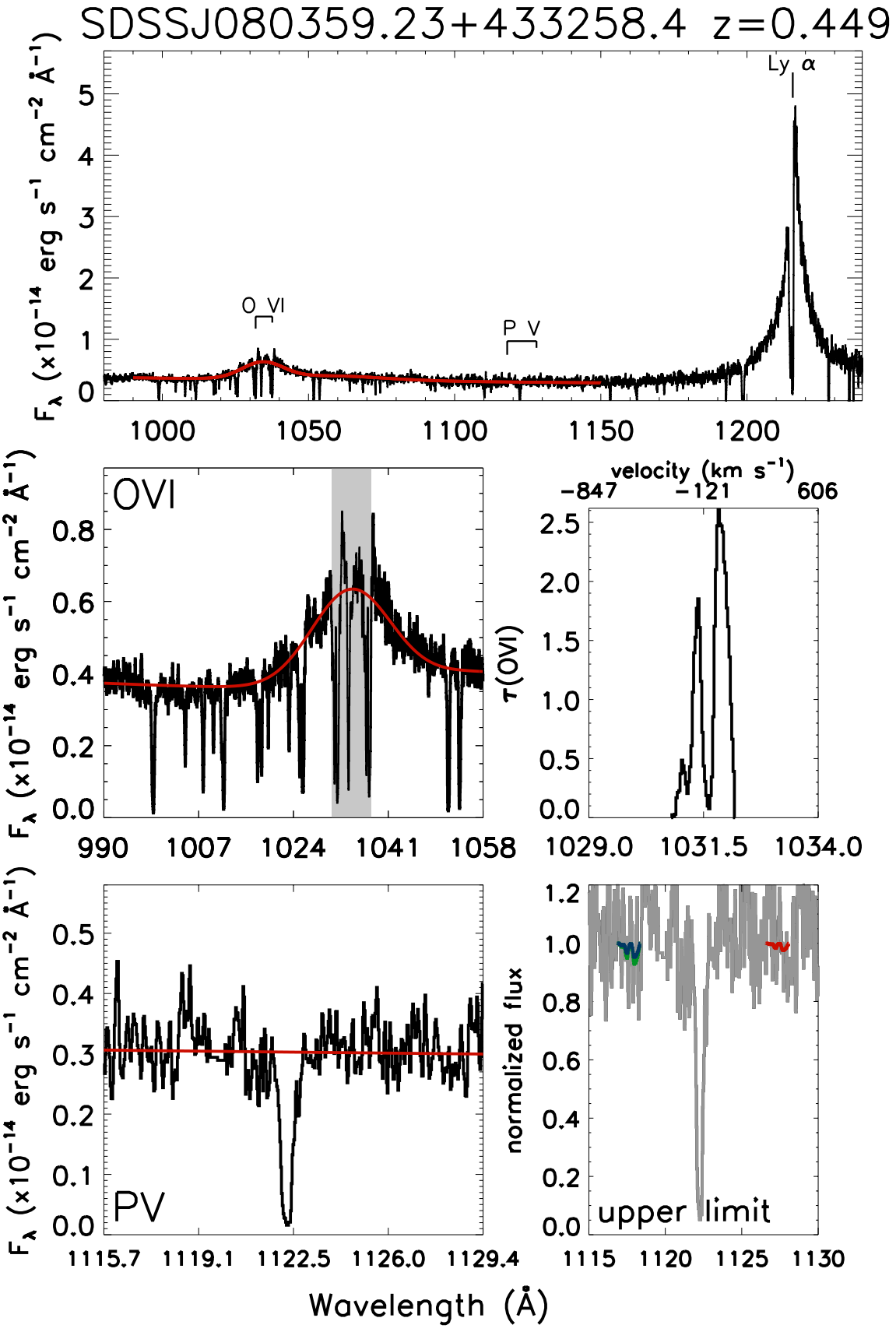
SDSSJ080359.23+433258.4 z=0.449
Ly α
O VI
P V
OVI
PV
velocity (km s⁻¹)
−847
−121
606
τ(OVI)
normalized flux
upper limit
Wavelength (Å)

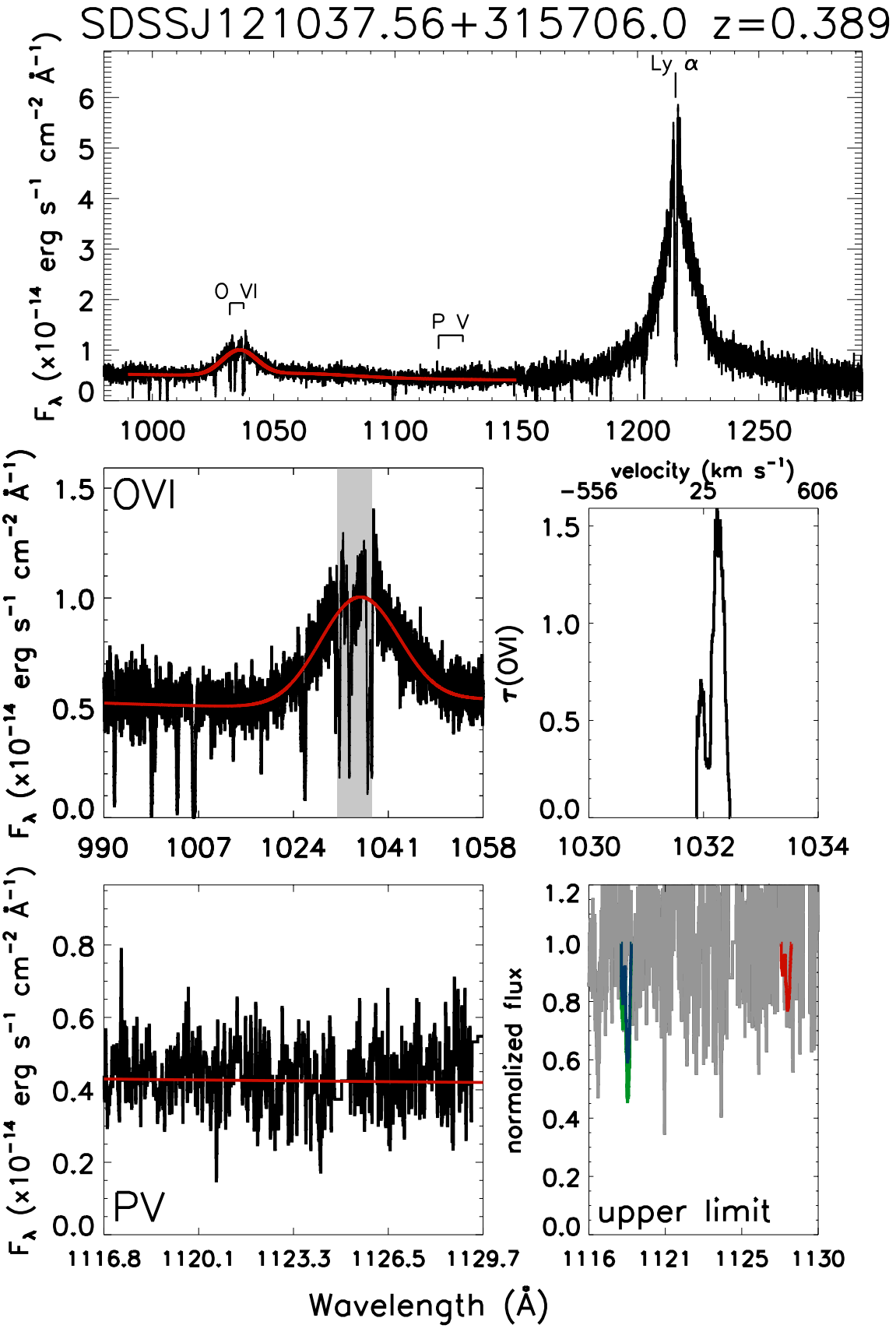
SDSSJ121037.56+315706.0 z=0.389
Ly α
O VI
P V
F_λ (x10^{-14} erg s^{-1} cm^{-2} Å^{-1})
1000
1050
1100
1150
1200
1250
OVI
velocity (km s^{-1})
−556
25
606
τ(OVI)
990
1007
1024
1041
1058
1030
1032
1034
PV
normalized flux
upper limit
1116.8
1120.1
1123.3
1126.5
1129.7
1116
1121
1125
1130
Wavelength (Å)

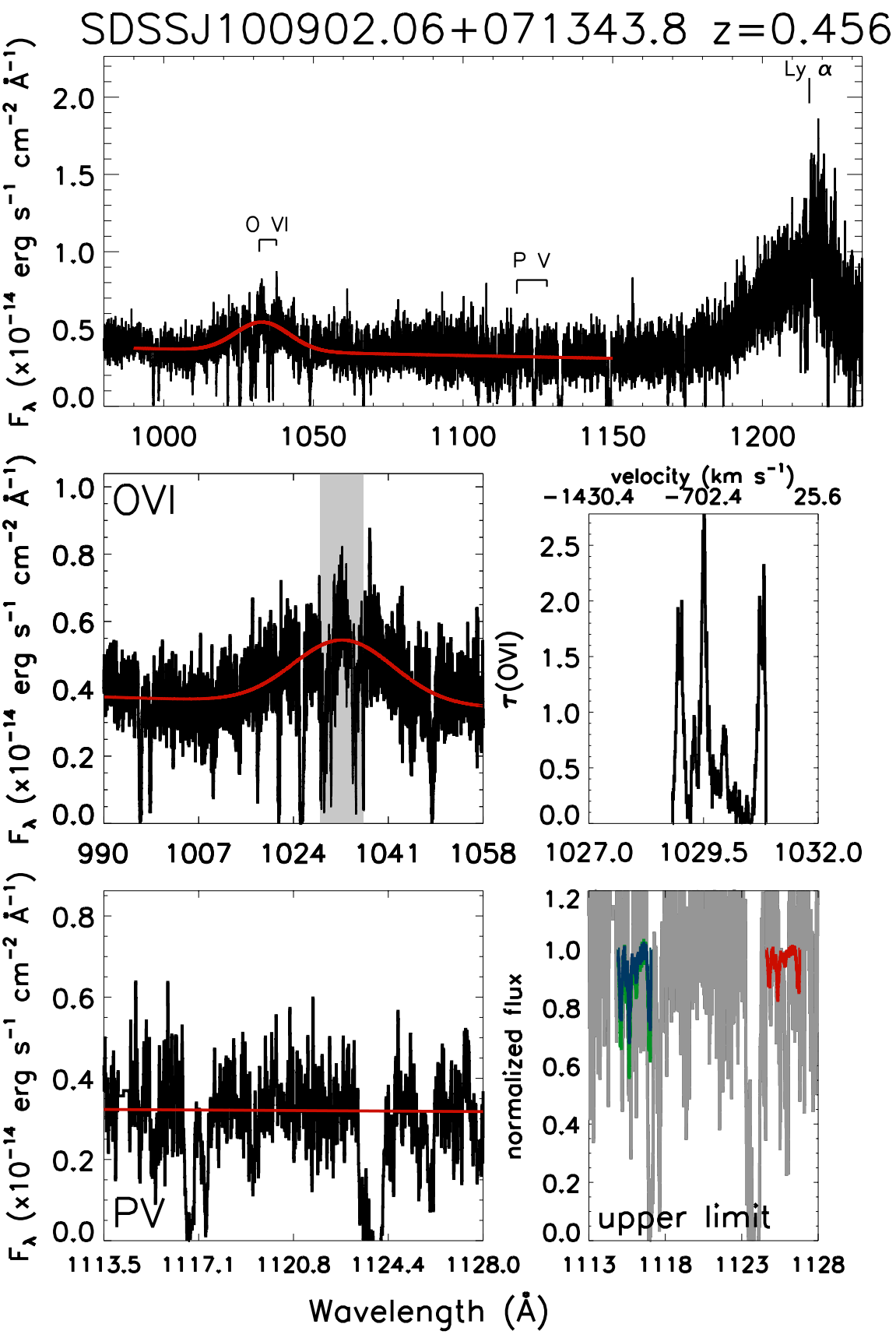
SDSSJ100902.06+071343.8 z=0.456
Ly α
O VI
P V
OVI
PV
velocity (km s⁻¹)
−1430.4
−702.4
25.6
τ(OVI)
normalized flux
upper limit
F_λ (x10⁻¹⁴ erg s⁻¹ cm⁻² Å⁻¹)
Wavelength (Å)

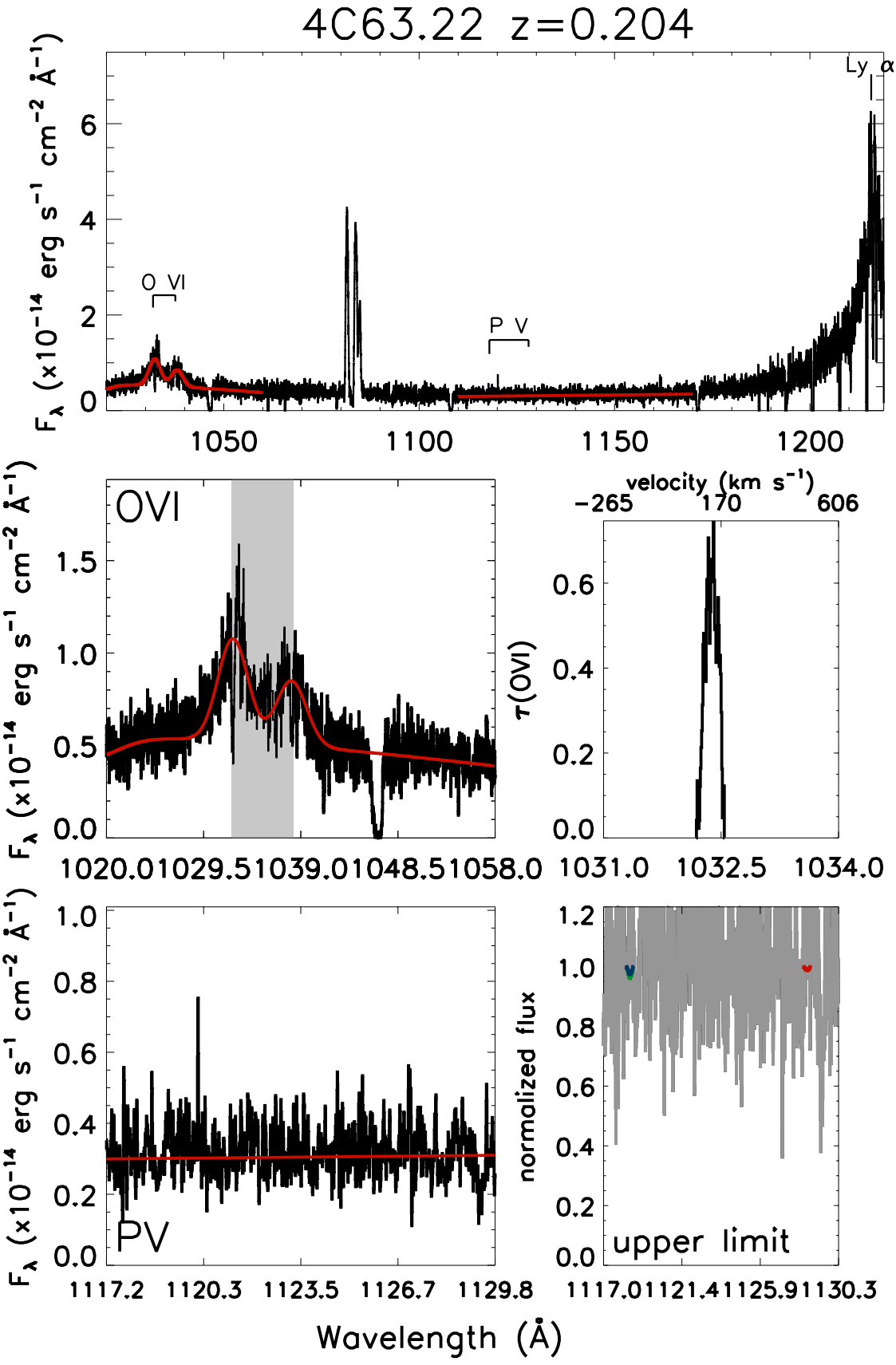
4C63.22 z=0.204
Ly α
O VI
P V
F_λ ($\times 10^{-14}$ erg s^{-1} cm^{-2} Å^{-1})
1050
1100
1150
1200
OVI
velocity (km s^{-1})
−265
170
606
τ(OVI)
1020.0
1029.5
1039.0
1048.5
1058.0
1031.0
1032.5
1034.0
PV
normalized flux
upper limit
1117.2
1120.3
1123.5
1126.7
1129.8
1117.0
1121.4
1125.9
1130.3
Wavelength (Å)

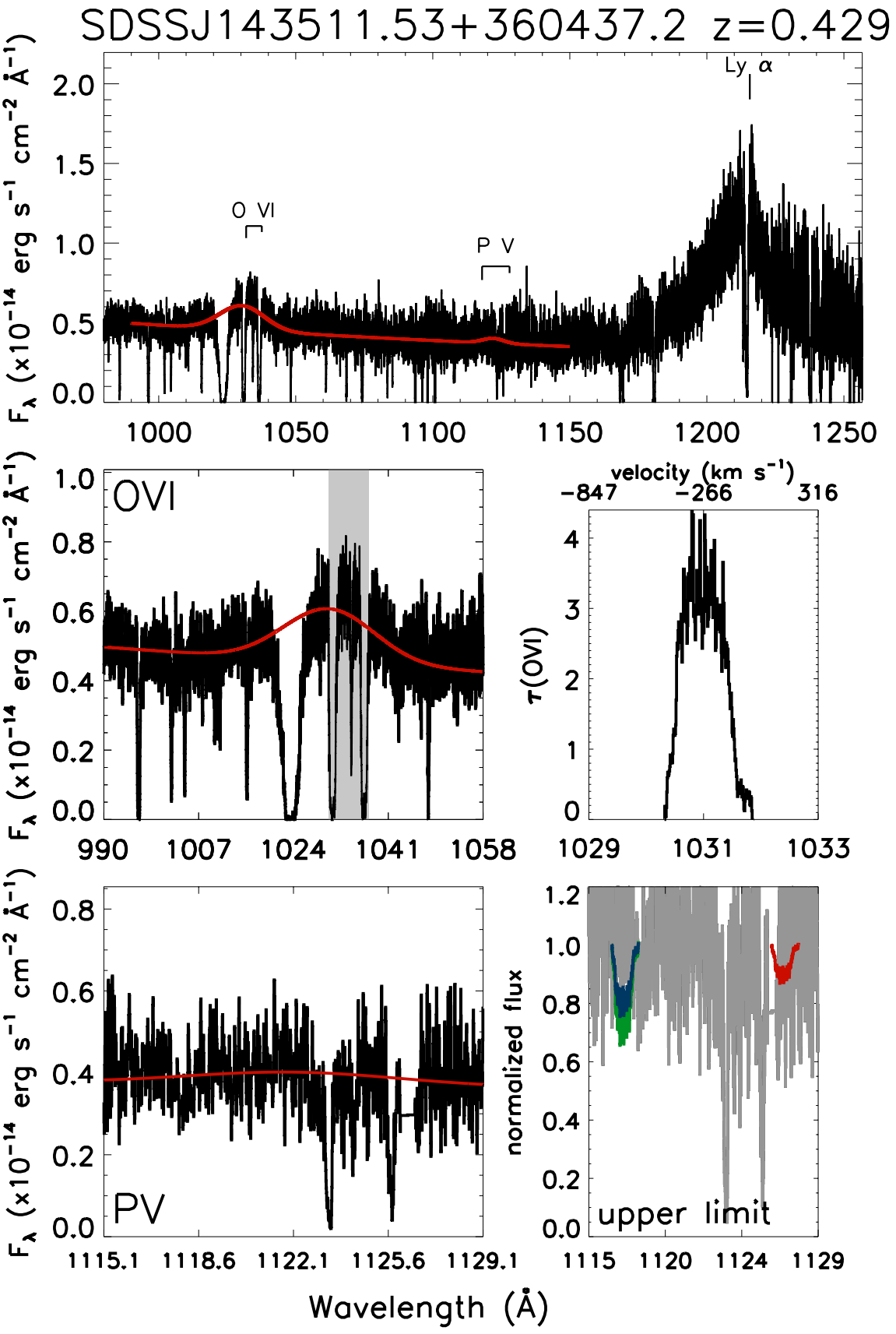
SDSSJ143511.53+360437.2 z=0.429
Ly α
O VI
P V
OVI
PV
velocity (km s⁻¹)
−847
−266
316
τ(OVI)
normalized flux
upper limit
Wavelength (Å)

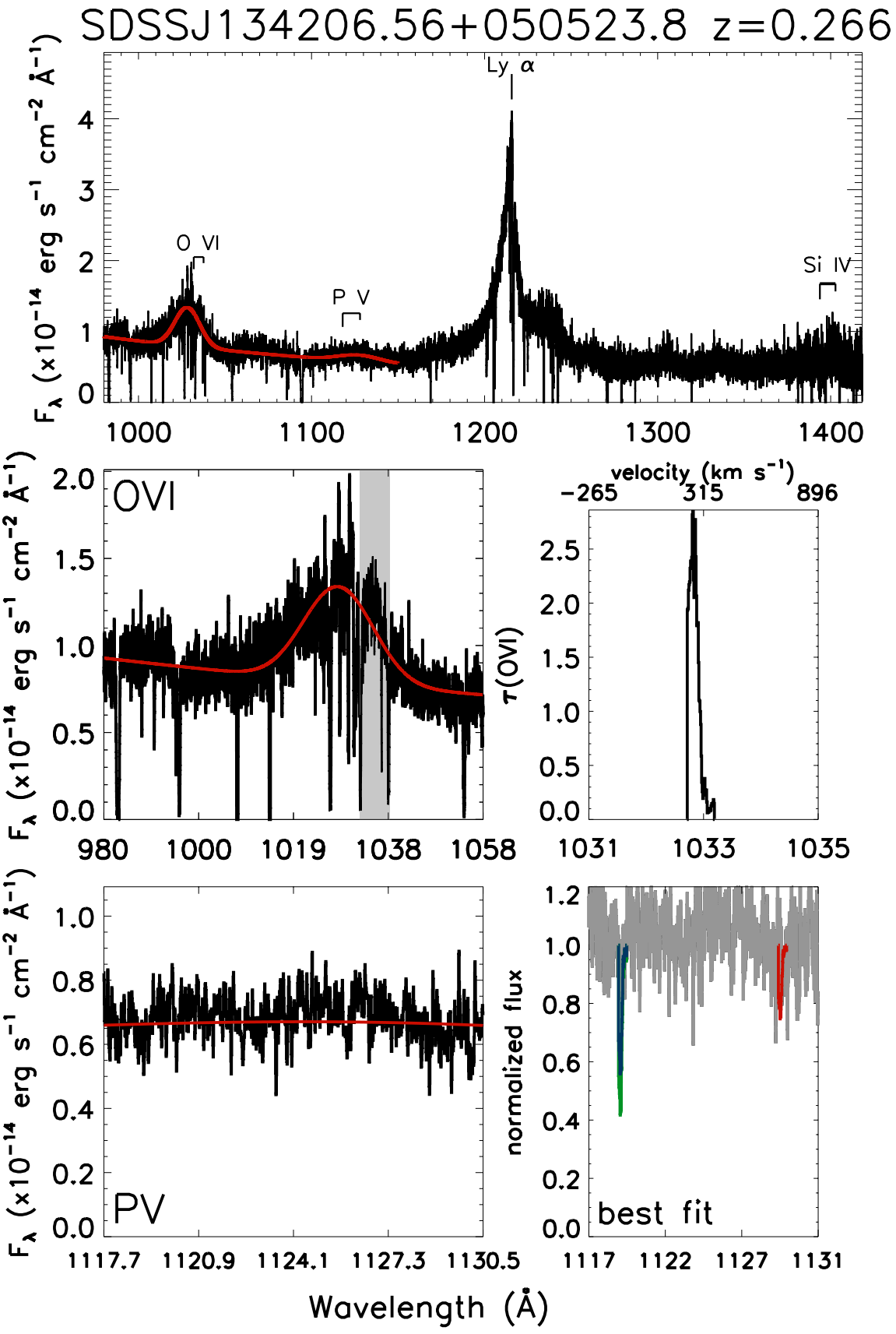
SDSSJ134206.56+050523.8 z=0.266
Ly α
O VI
P V
Si IV
F_λ ($\times 10^{-14}$ erg s^{-1} cm^{-2} Å^{-1})
OVI
PV
velocity (km s^{-1})
−265
315
896
τ(OVI)
normalized flux
best fit
Wavelength (Å)

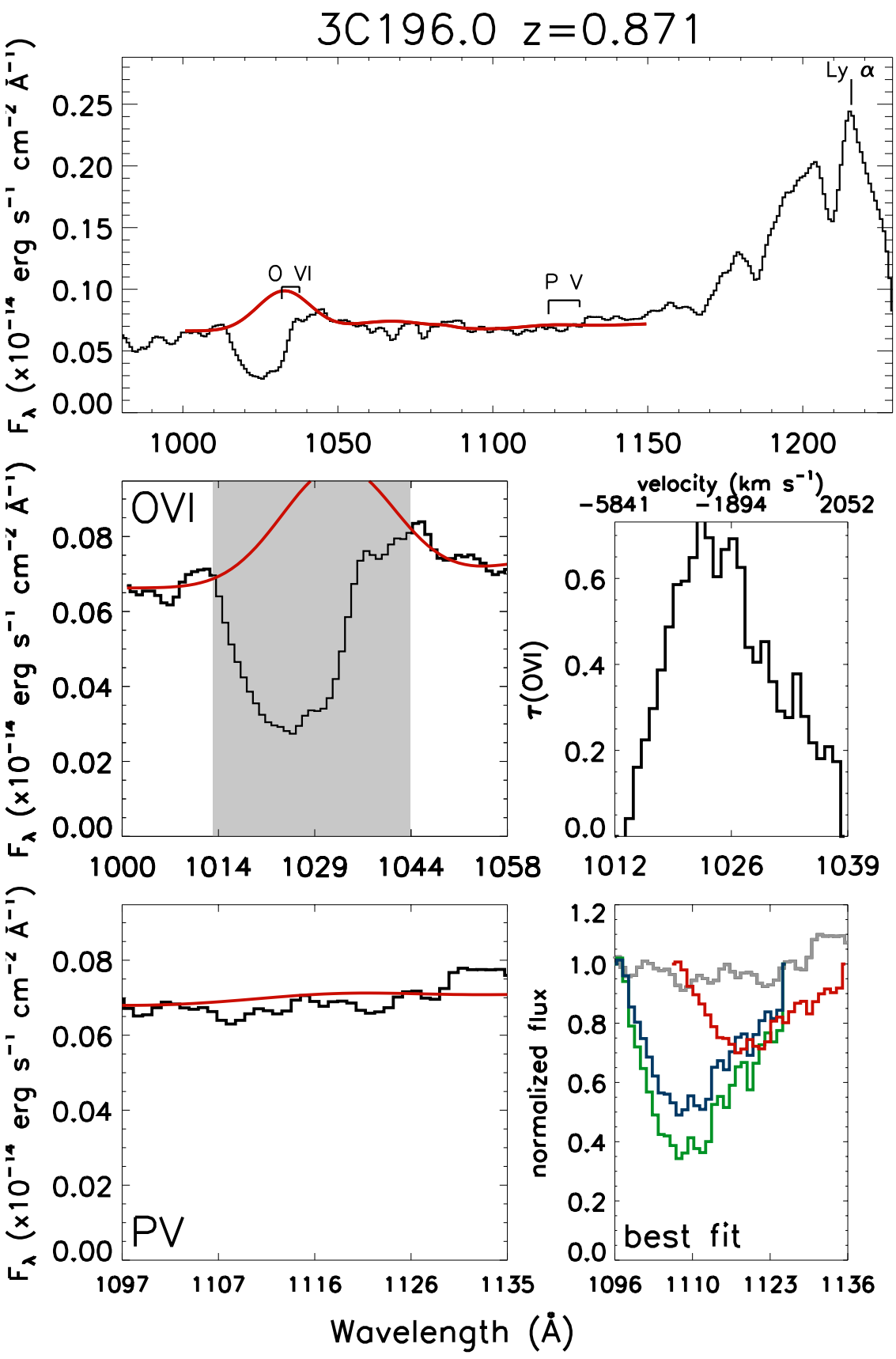
3C196.0 z=0.871
Ly α
O VI
P V
OVI
PV
velocity (km s⁻¹)
−5841
−1894
2052
τ(OVI)
normalized flux
best fit
Wavelength (Å)

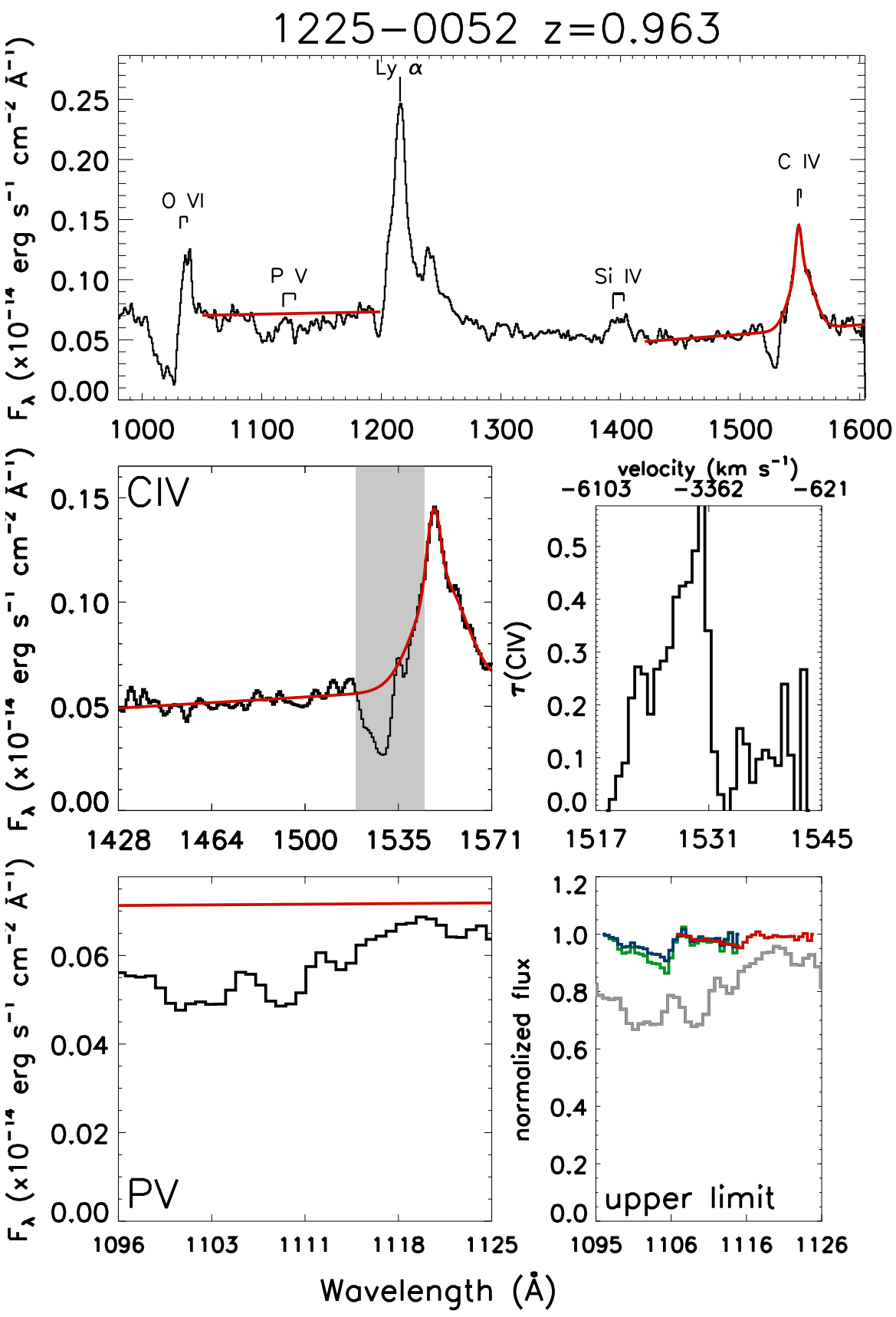
1225−0052 z=0.963
Ly α
O VI
P V
Si IV
C IV
F_λ (x10^-14 erg s^-1 cm^-2 Å^-1)
CIV
velocity (km s^-1)
−6103
−3362
−621
τ(CIV)
PV
normalized flux
upper limit
Wavelength (Å)

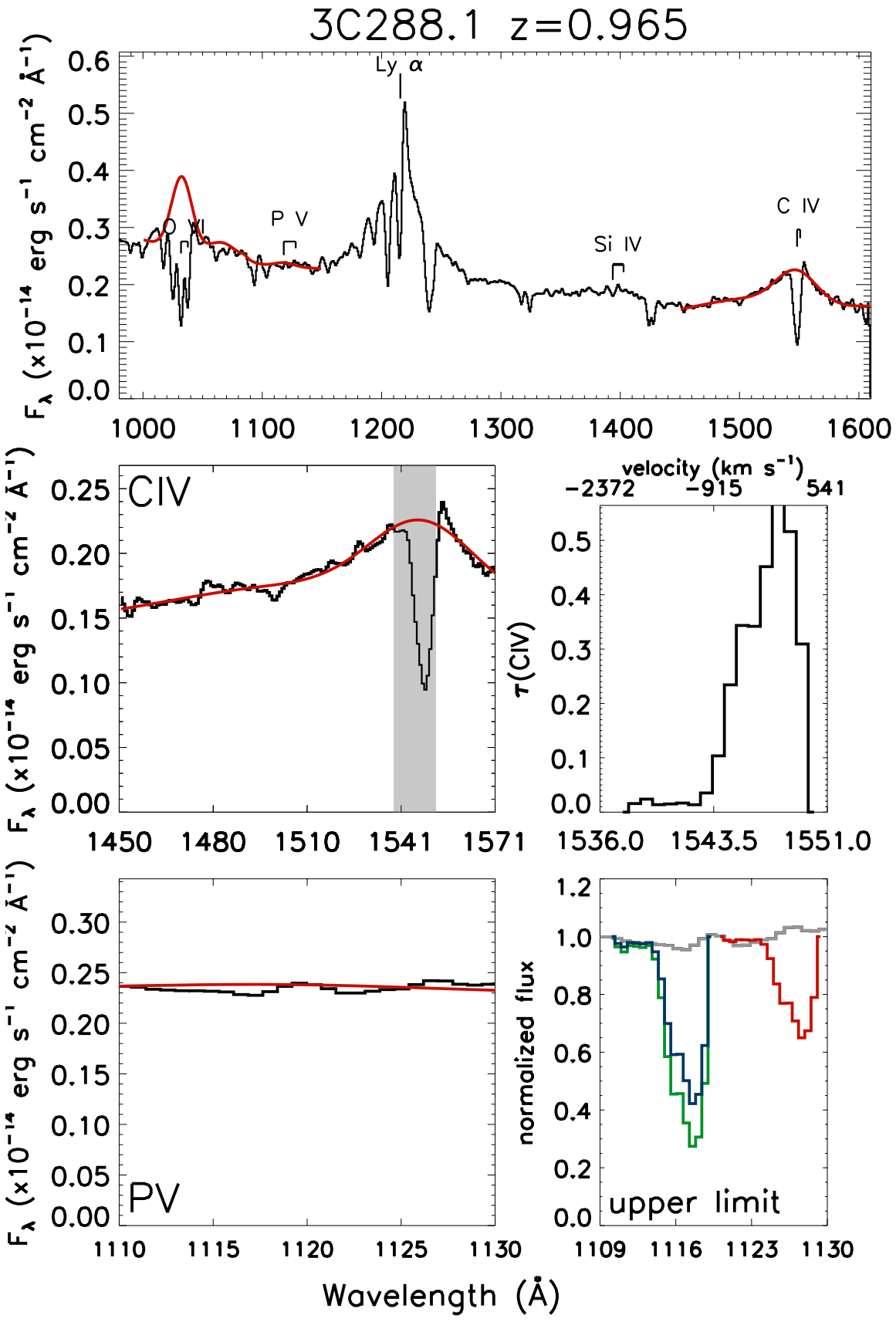
3C288.1 z=0.965
Ly α
O VI
P V
Si IV
C IV
F_λ (x10^{-14} erg s^{-1} cm^{-2} Å^{-1})
CIV
PV
velocity (km s^{-1})
−2372
−915
541
τ(CIV)
normalized flux
upper limit
Wavelength (Å)

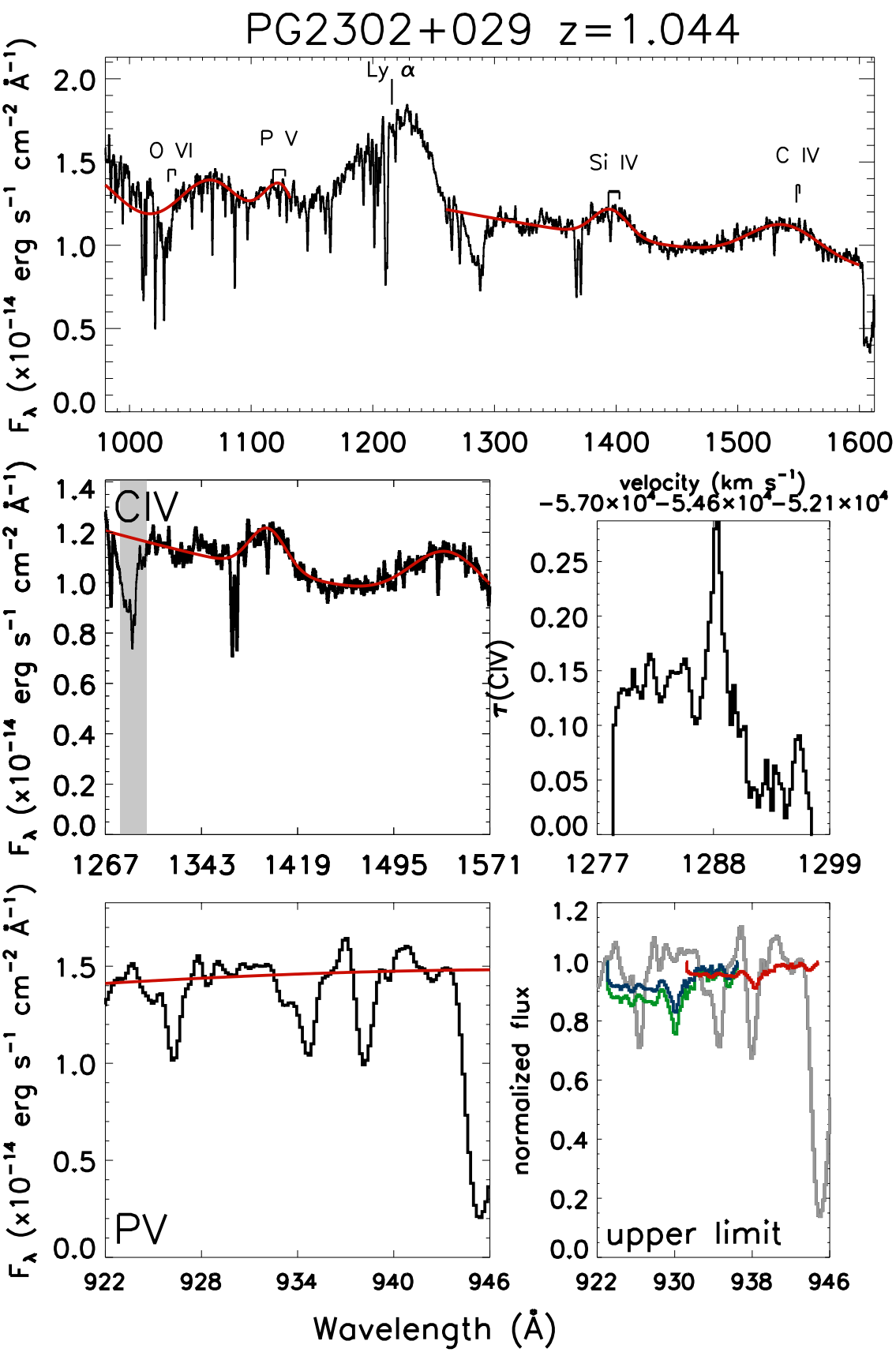
PG2302+029 z=1.044
Ly α
O VI
P V
Si IV
C IV
CIV
PV
velocity (km s⁻¹)
−5.70×10⁴ −5.46×10⁴ −5.21×10⁴
τ(CIV)
normalized flux
upper limit
Wavelength (Å)

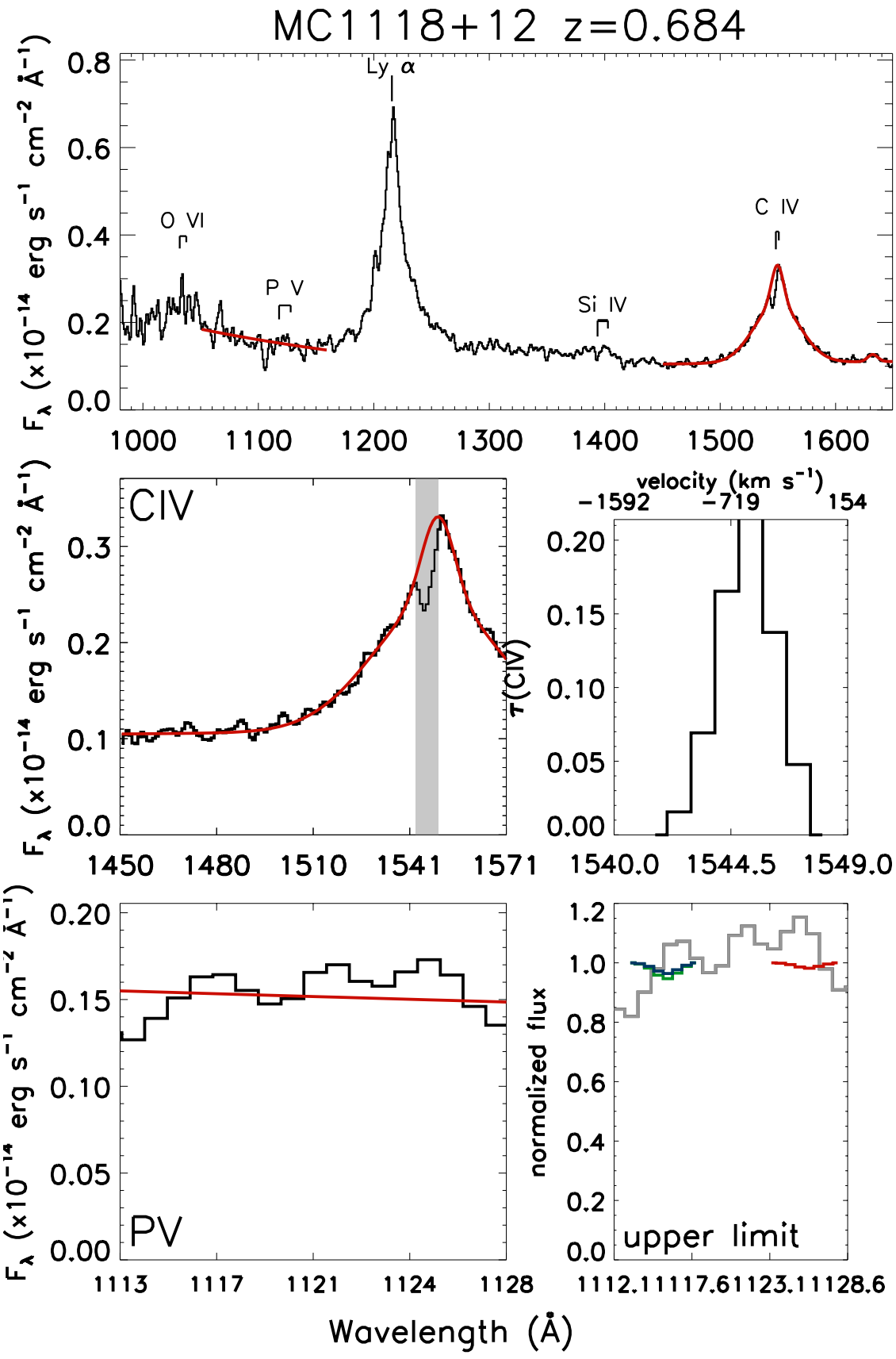
MC1118+12 z=0.684
Ly α
O VI
P V
Si IV
C IV
CIV
PV
velocity (km s⁻¹)
−1592
−719
154
τ(CIV)
normalized flux
upper limit
Wavelength (Å)

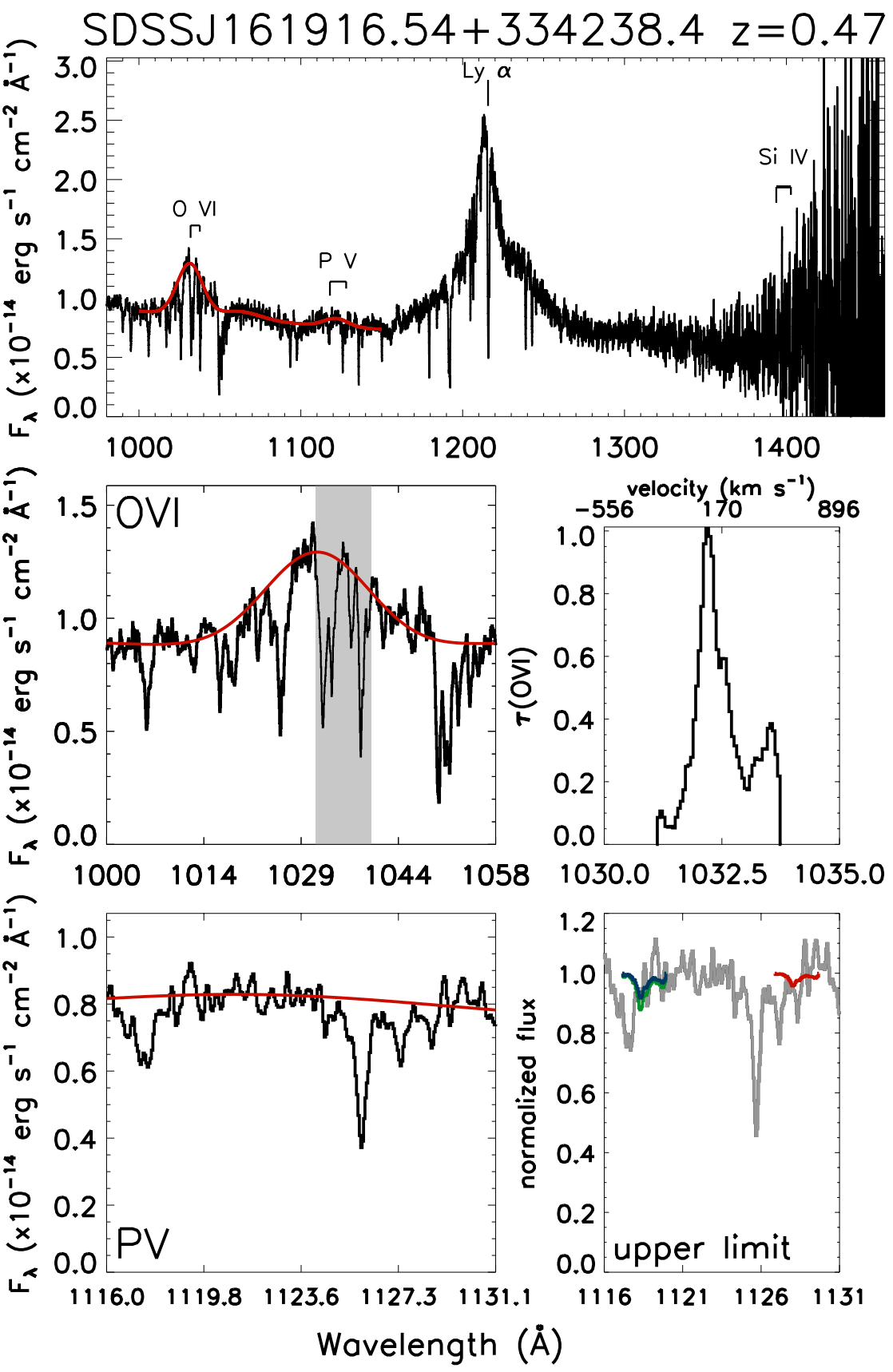
SDSSJ161916.54+334238.4 z=0.471
Ly α
Si IV
O VI
P V
OVI
PV
velocity (km s⁻¹)
−556
170
896
τ(OVI)
normalized flux
upper limit
Wavelength (Å)

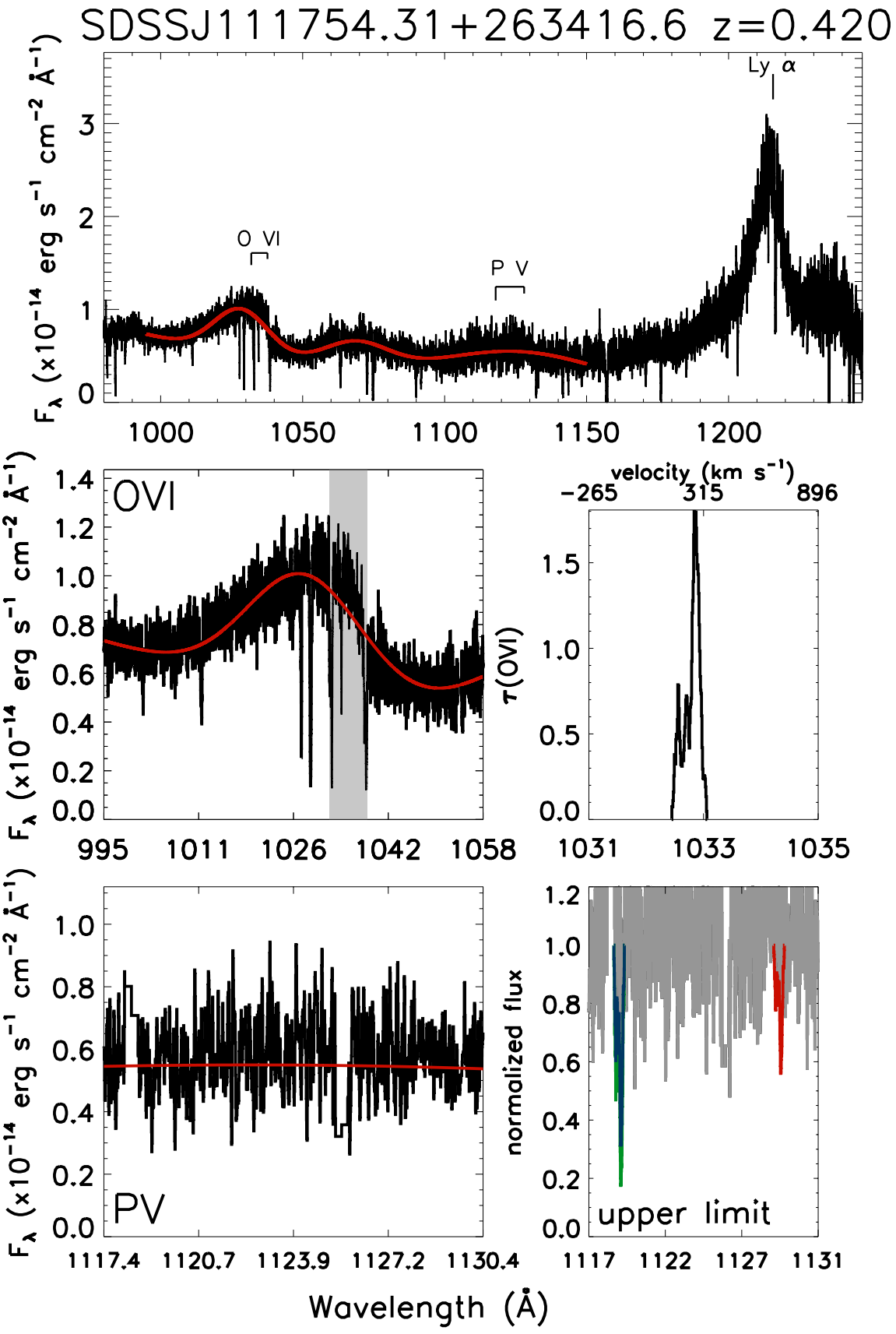
SDSSJ111754.31+263416.6 z=0.420
Ly α
O VI
P V
F_λ (x10^{-14} erg s^{-1} cm^{-2} Å^{-1})
1000
1050
1100
1150
1200
OVI
velocity (km s^{-1})
−265
315
896
τ(OVI)
995
1011
1026
1042
1058
1031
1033
1035
PV
normalized flux
upper limit
1117.4
1120.7
1123.9
1127.2
1130.4
1117
1122
1127
1131
Wavelength (Å)

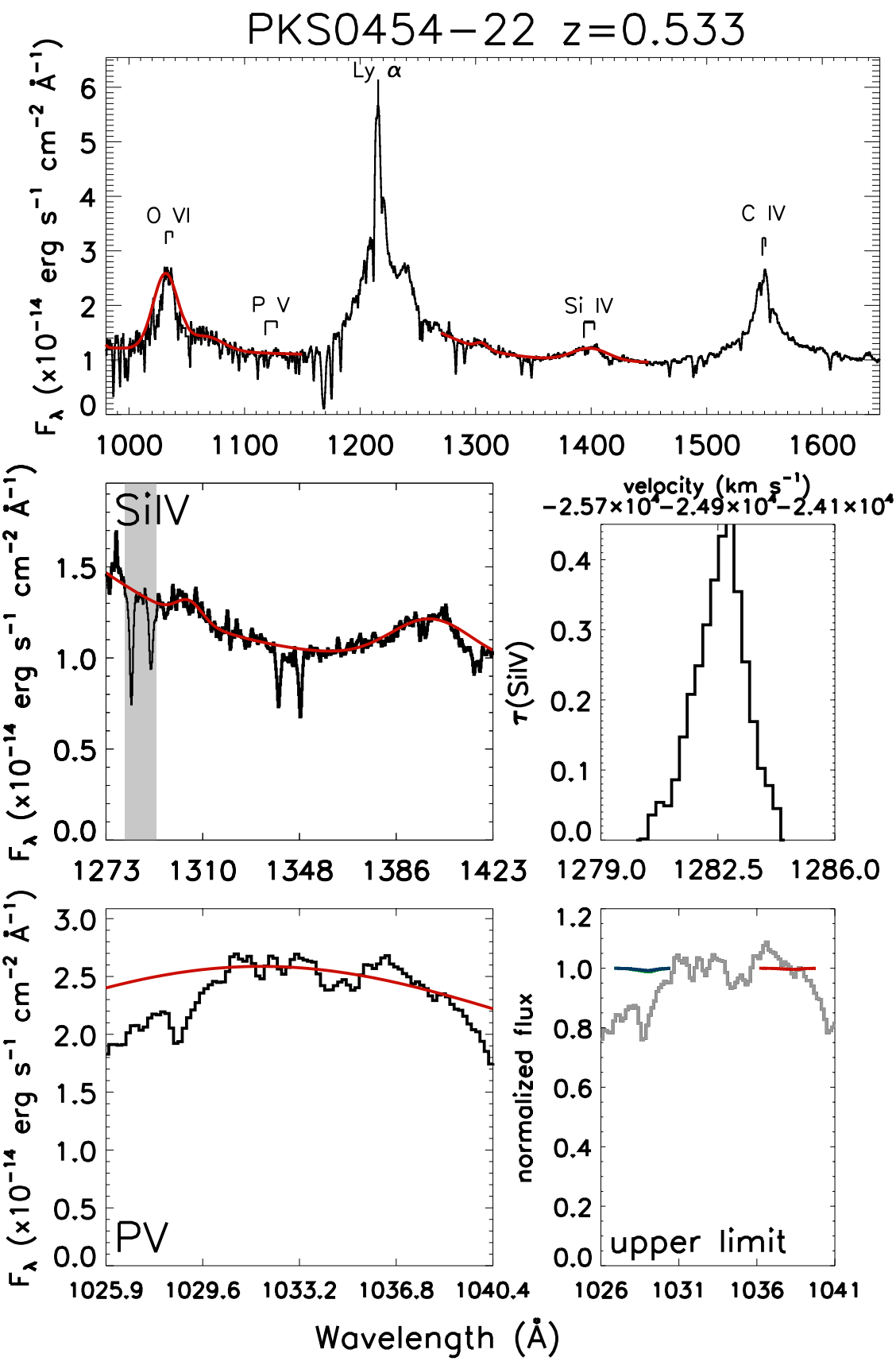
PKS0454−22 z=0.533
Ly α
O VI
P V
Si IV
C IV
F_λ (x10^{-14} erg s^{-1} cm^{-2} Å^{-1})
SiIV
velocity (km s^{-1})
−2.57×10^4 −2.49×10^4 −2.41×10^4
τ(SiIV)
PV
normalized flux
upper limit
Wavelength (Å)

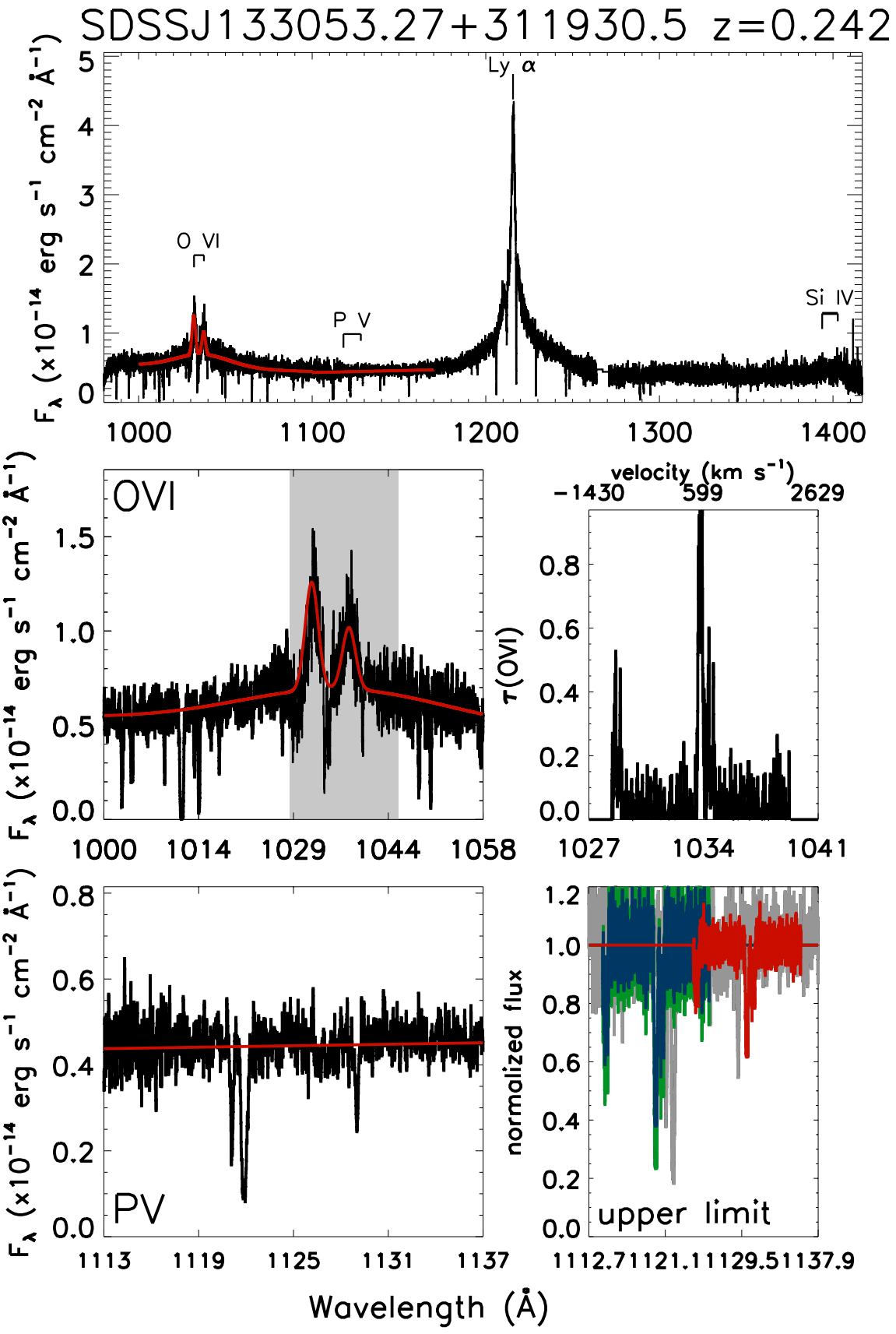
SDSSJ133053.27+311930.5 z=0.242
Ly α
O VI
P V
Si IV
F_λ (x10^-14 erg s^-1 cm^-2 Å^-1)
1000
1100
1200
1300
1400
OVI
velocity (km s^-1)
-1430
599
2629
τ(OVI)
1000
1014
1029
1044
1058
1027
1034
1041
PV
normalized flux
upper limit
1113
1119
1125
1131
1137
1112.7
1121.1
1129.5
1137.9
Wavelength (Å)

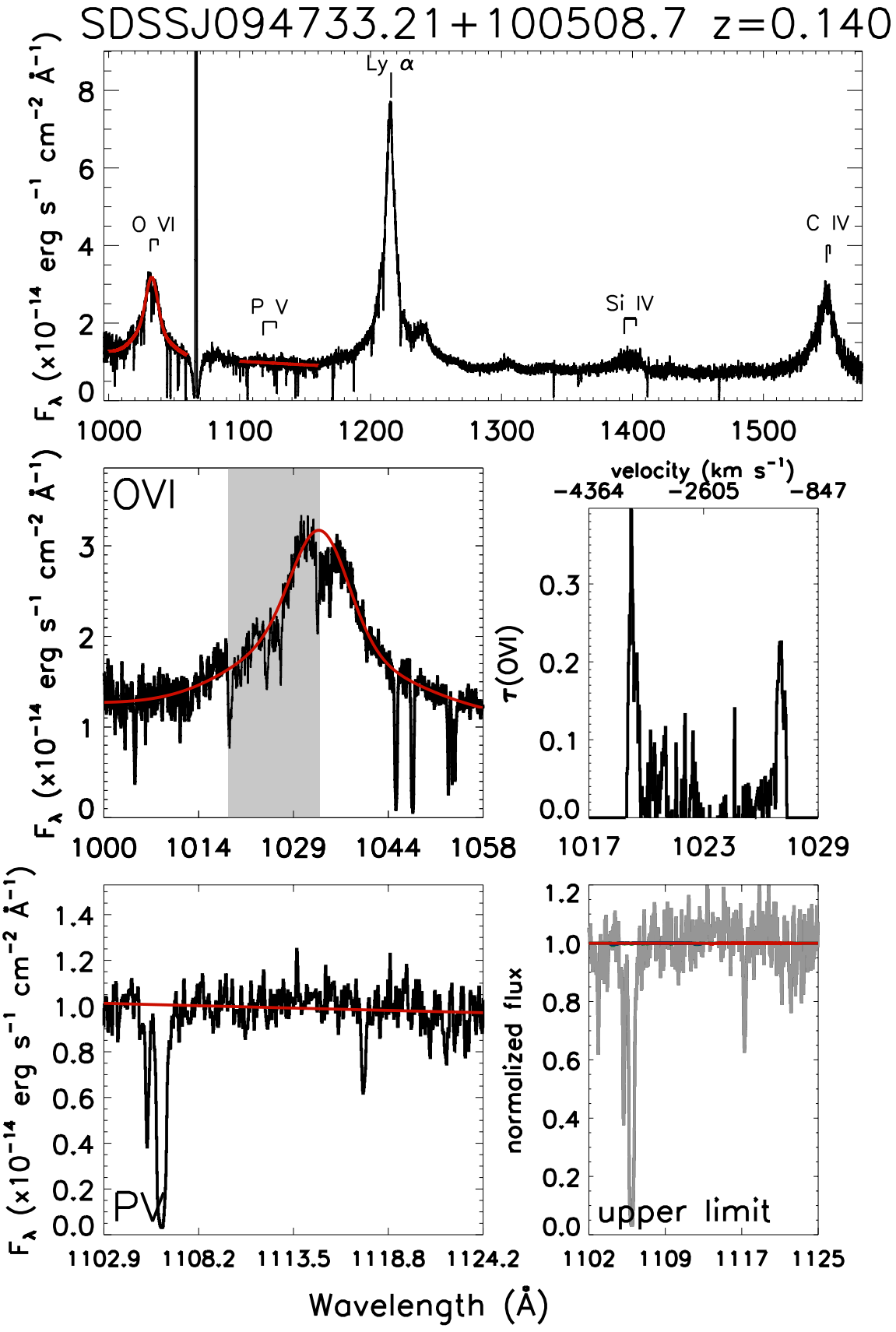
SDSSJ094733.21+100508.7 z=0.140
Ly α
O VI
P V
Si IV
C IV
F_λ ($\times 10^{-14}$ erg s^{-1} cm^{-2} Å^{-1})
1000
1100
1200
1300
1400
1500
OVI
velocity (km s^{-1})
−4364
−2605
−847
τ(OVI)
1000
1014
1029
1044
1058
1017
1023
1029
PV
normalized flux
upper limit
1102.9
1108.2
1113.5
1118.8
1124.2
1102
1109
1117
1125
Wavelength (Å)

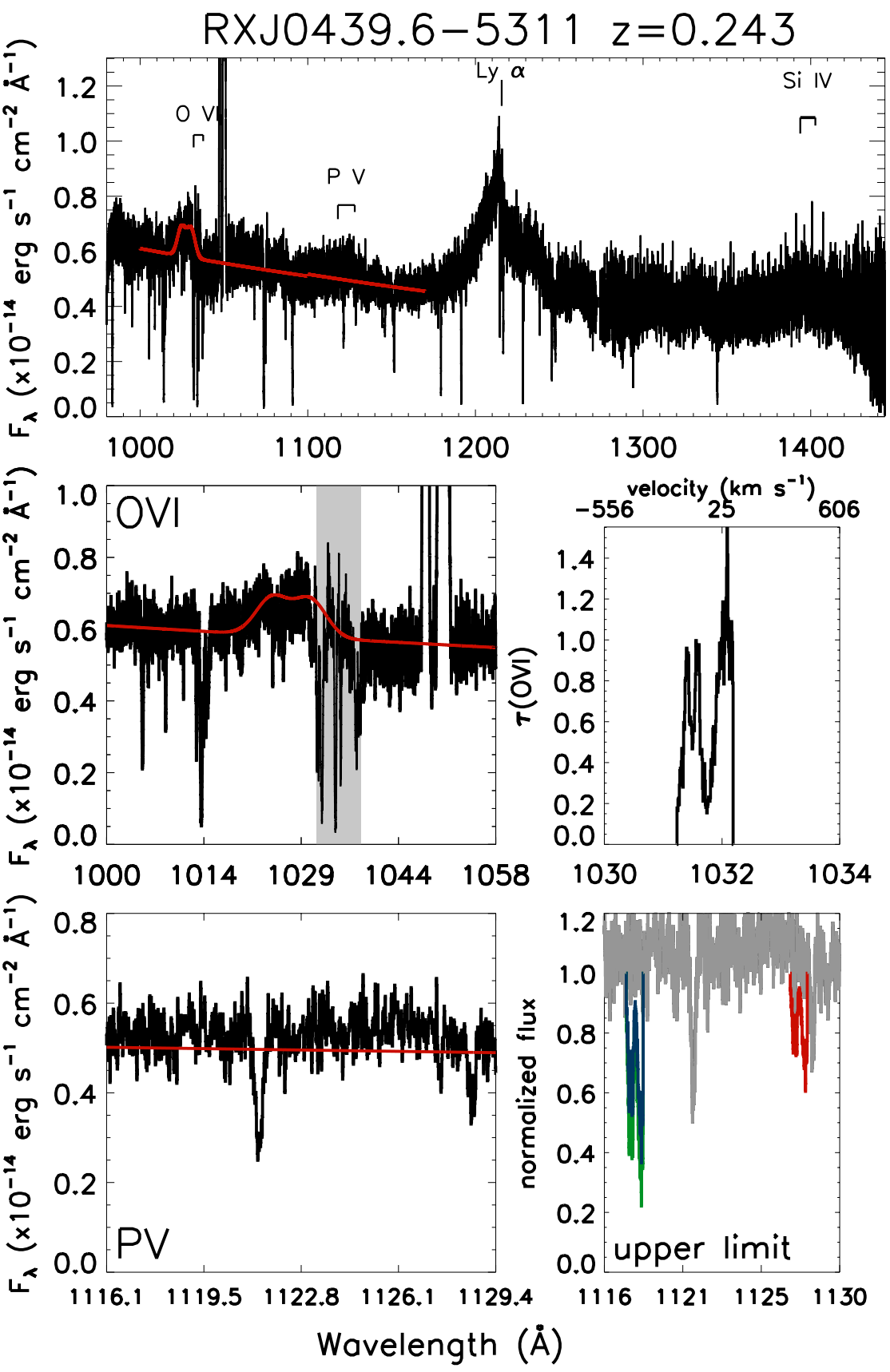
RXJ0439.6−5311 z=0.243
O VI
P V
Ly α
Si IV
OVI
PV
velocity (km s⁻¹)
−556
25
606
τ(OVI)
normalized flux
upper limit
Wavelength (Å)

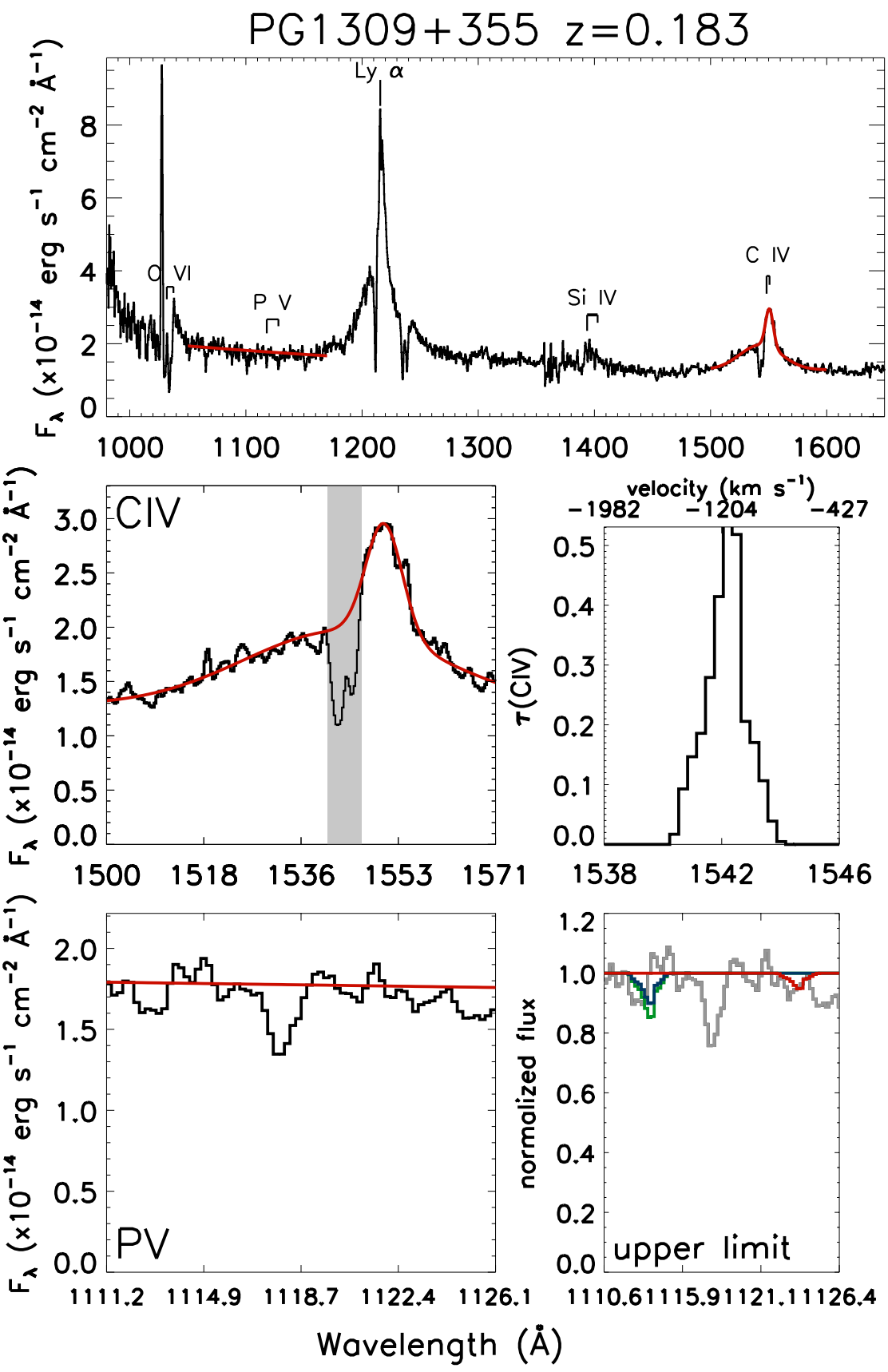
PG1309+355 z=0.183
Ly α
O VI
P V
Si IV
C IV
F_λ (x10^{-14} erg s^{-1} cm^{-2} Å^{-1})
CIV
PV
velocity (km s^{-1})
−1982
−1204
−427
τ(CIV)
normalized flux
upper limit
Wavelength (Å)

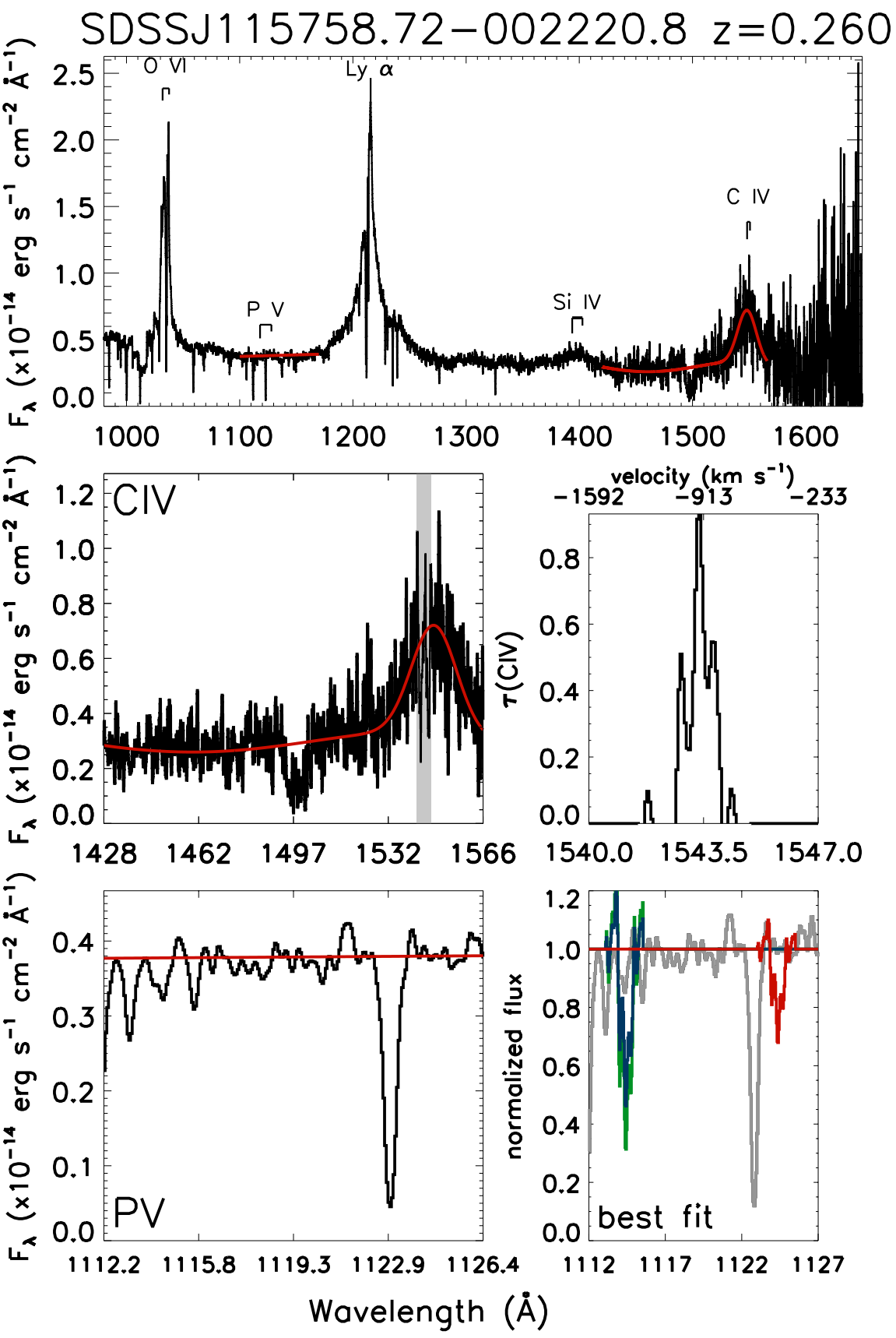
SDSSJ115758.72−002220.8 z=0.260
O VI
Ly α
P V
Si IV
C IV
F_λ (x10^{-14} erg s^{-1} cm^{-2} Å^{-1})
1000 1100 1200 1300 1400 1500 1600
CIV
1428 1462 1497 1532 1566
velocity (km s^{-1})
−1592 −913 −233
τ(CIV)
1540.0 1543.5 1547.0
PV
1112.2 1115.8 1119.3 1122.9 1126.4
normalized flux
best fit
1112 1117 1122 1127
Wavelength (Å)

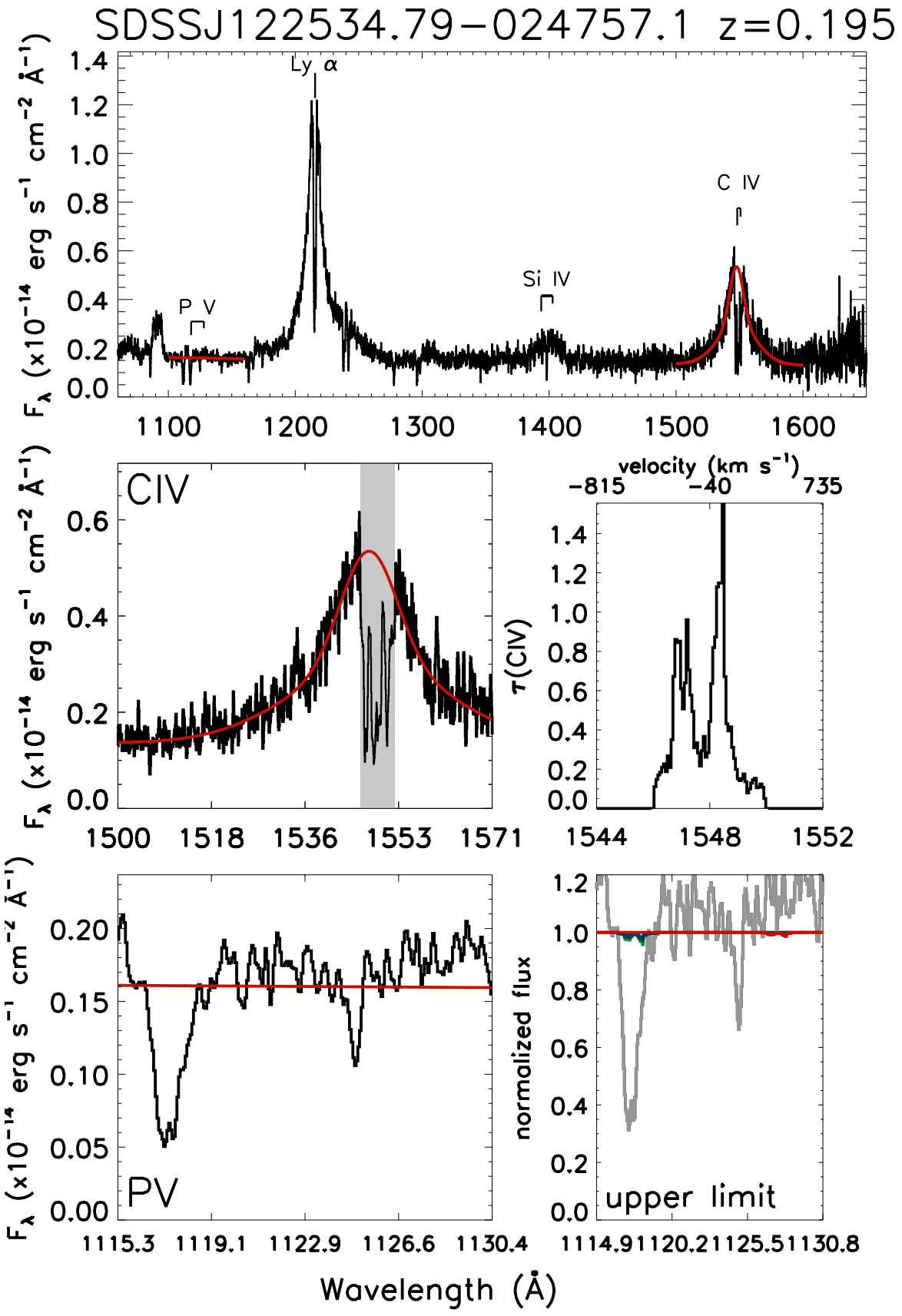
SDSSJ122534.79−024757.1 z=0.195
Ly α
C IV
Si IV
P V
F_λ (x10^{-14} erg s^{-1} cm^{-2} Å^{-1})
1.4
1.2
1.0
0.8
0.6
0.4
0.2
0.0
1100
1200
1300
1400
1500
1600
CIV
0.6
0.4
0.2
0.0
1500
1518
1536
1553
1571
velocity (km s^{-1})
−815
−40
735
τ(CIV)
1.4
1.2
1.0
0.8
0.6
0.4
0.2
0.0
1544
1548
1552
F_λ (x10^{-14} erg s^{-1} cm^{-2} Å^{-1})
0.20
0.15
0.10
0.05
0.00
PV
1115.3
1119.1
1122.9
1126.6
1130.4
normalized flux
1.2
1.0
0.8
0.6
0.4
0.2
0.0
upper limit
1114.9
1120.2
1125.5
1130.8
Wavelength (Å)

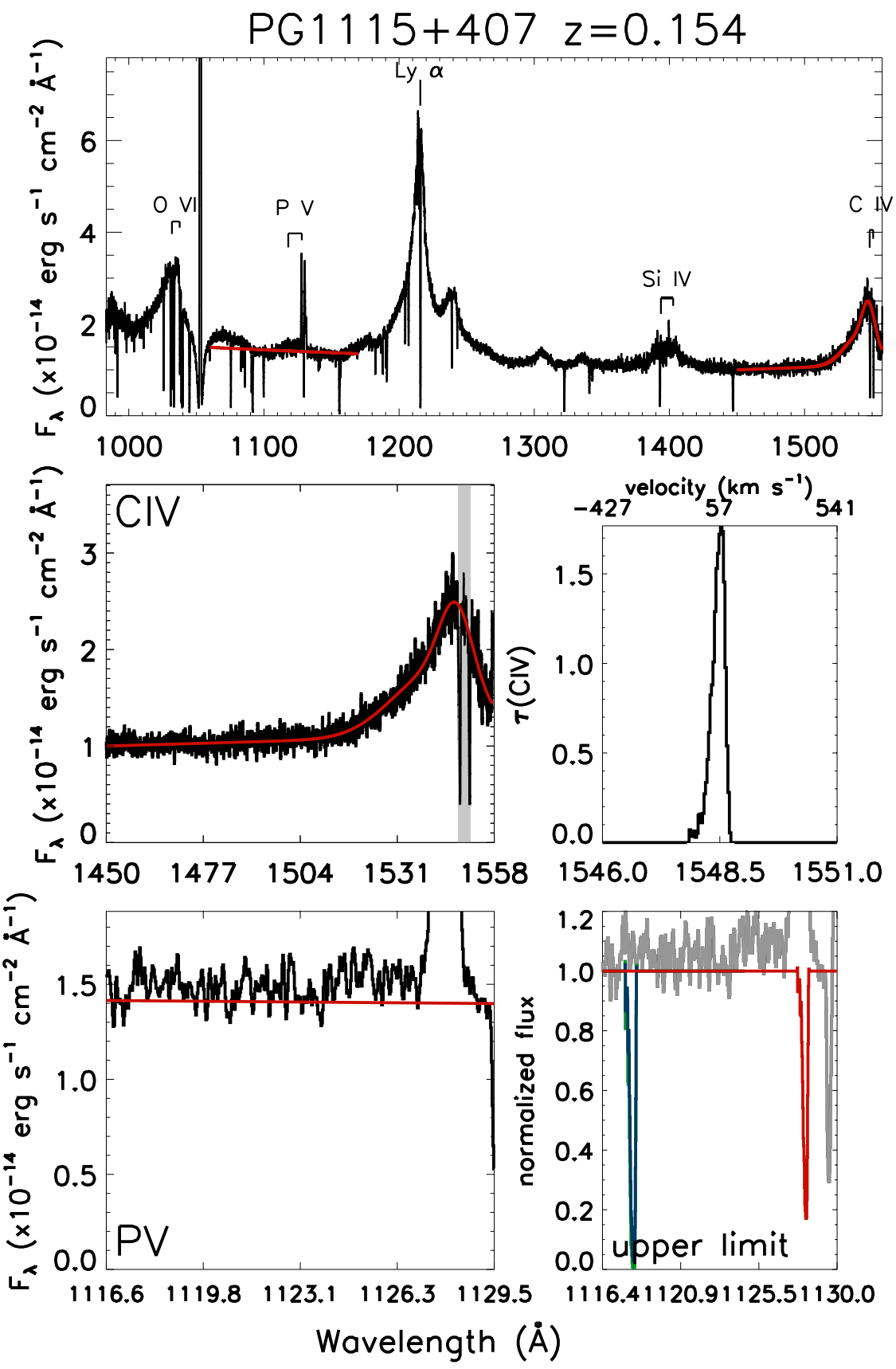
PG1115+407 z=0.154
Ly α
O VI
P V
Si IV
C IV
F_λ ($\times10^{-14}$ erg s^{-1} cm^{-2} Å^{-1})
1000
1100
1200
1300
1400
1500
CIV
velocity (km s^{-1})
−427
57
541
τ(CIV)
1450
1477
1504
1531
1558
1546.0
1548.5
1551.0
PV
normalized flux
upper limit
1116.6
1119.8
1123.1
1126.3
1129.5
1116.4
1120.9
1125.5
1130.0
Wavelength (Å)

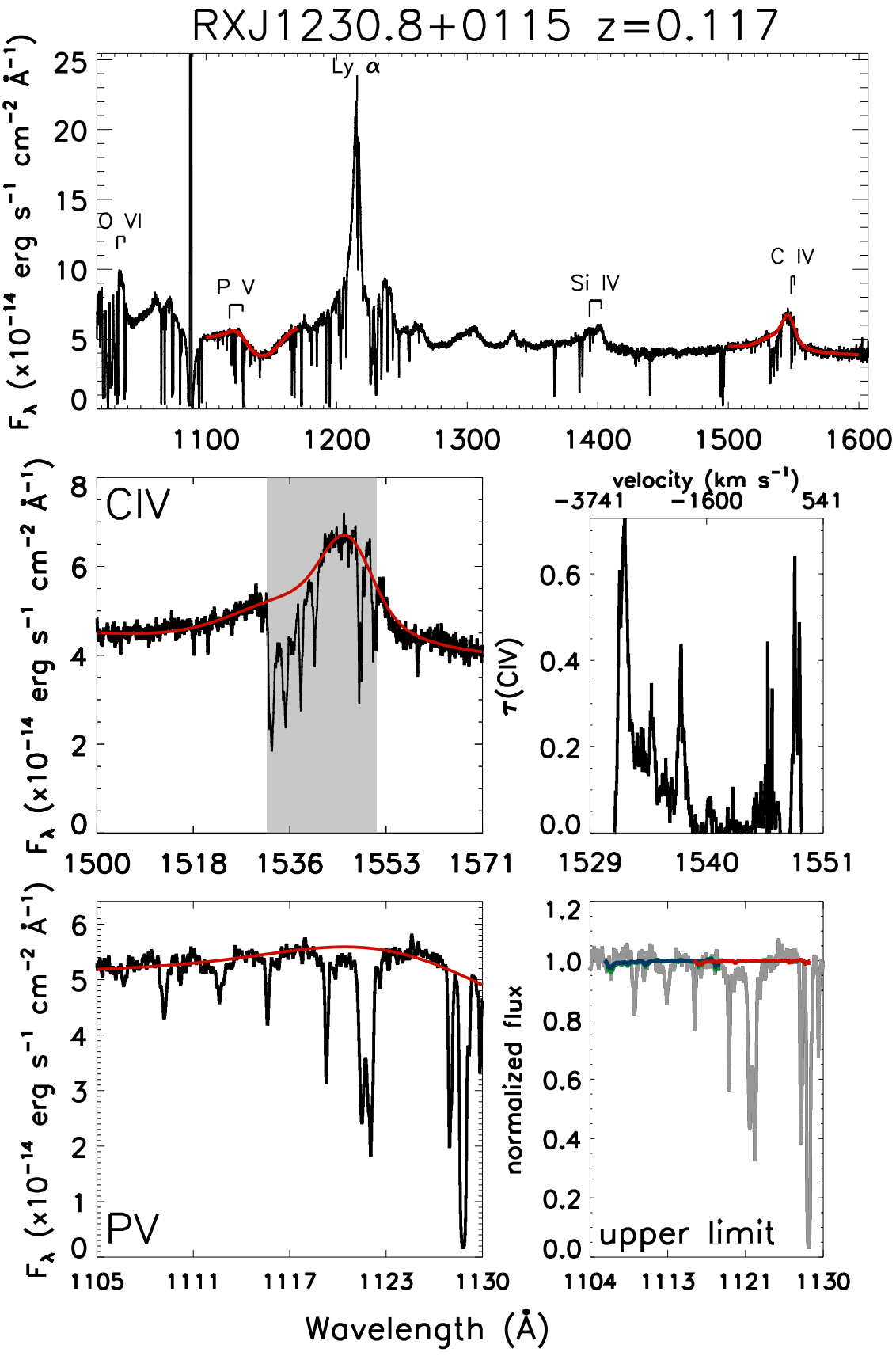
RXJ1230.8+0115 z=0.117
Ly α
O VI
P V
Si IV
C IV
F_λ (x10^{-14} erg s^{-1} cm^{-2} Å^{-1})
CIV
velocity (km s^{-1})
−3741
−1600
541
τ(CIV)
PV
normalized flux
upper limit
Wavelength (Å)

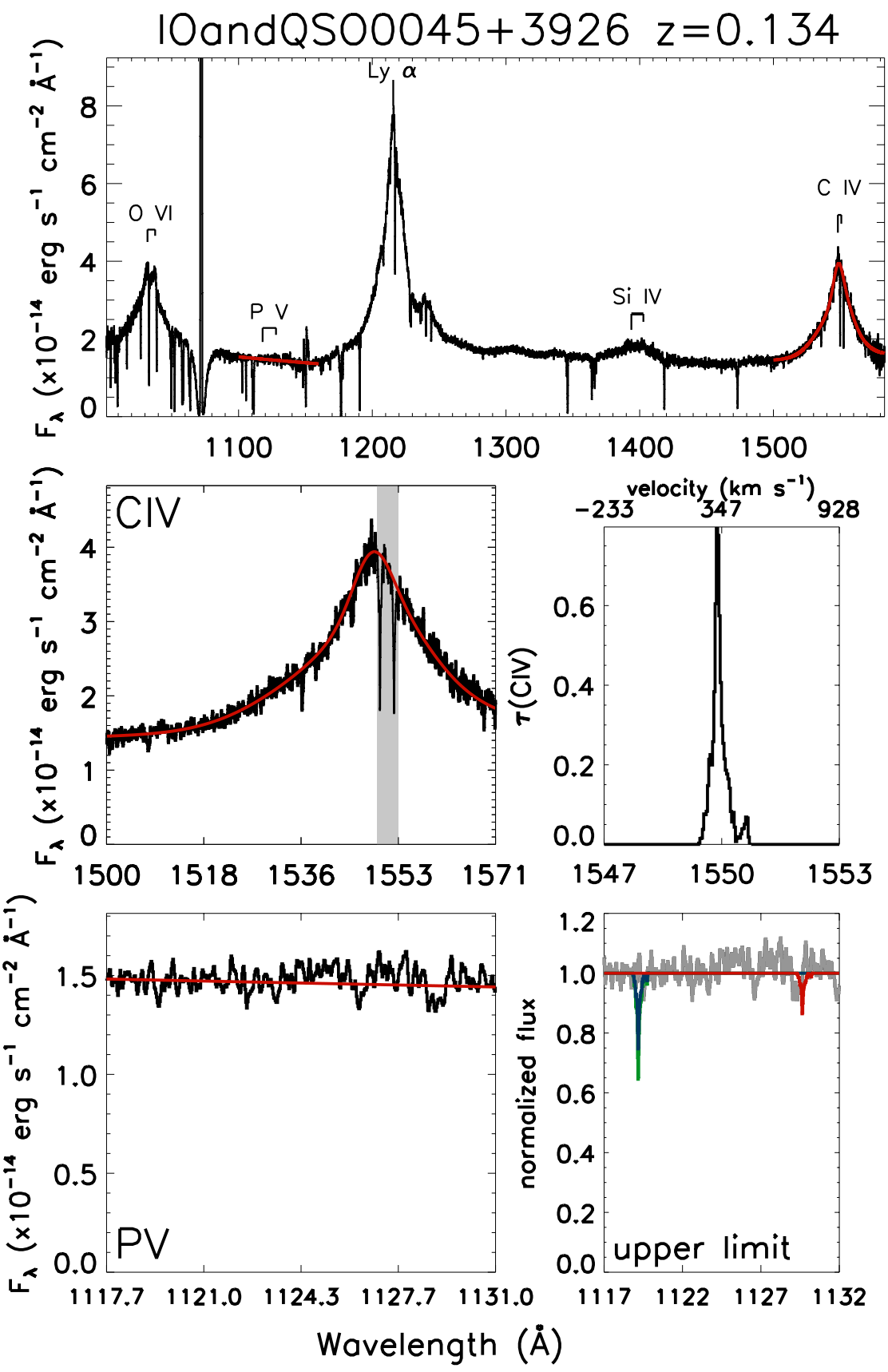
I0andQSO0045+3926 z=0.134
Ly α
O VI
P V
Si IV
C IV
F_λ (x10^{-14} erg s^{-1} cm^{-2} Å^{-1})
CIV
velocity (km s^{-1})
−233
347
928
τ(CIV)
PV
normalized flux
upper limit
Wavelength (Å)

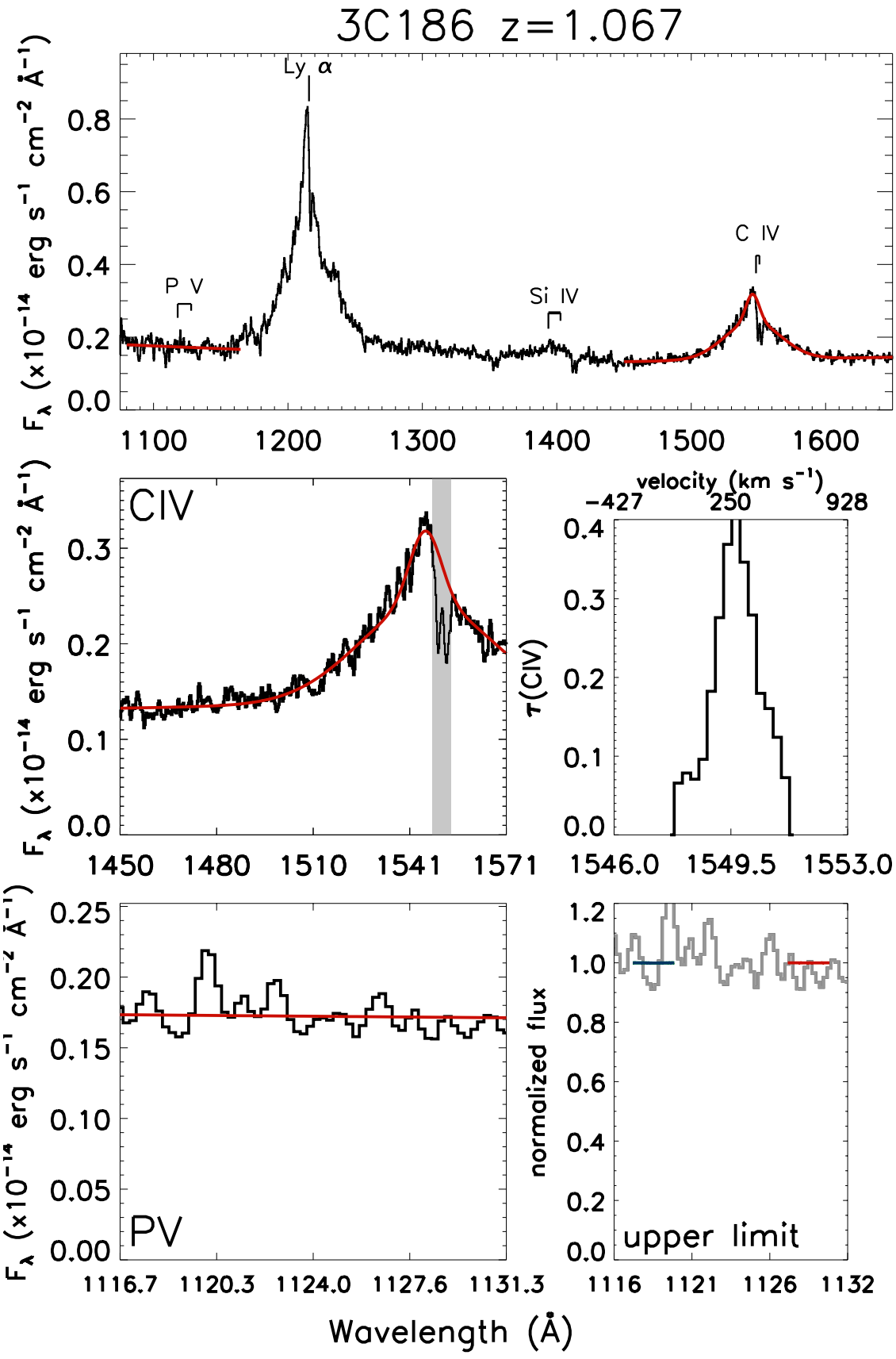
3C186 z=1.067
Ly α
P V
Si IV
C IV
CIV
PV
velocity (km s⁻¹)
−427
250
928
τ(CIV)
normalized flux
upper limit
Wavelength (Å)

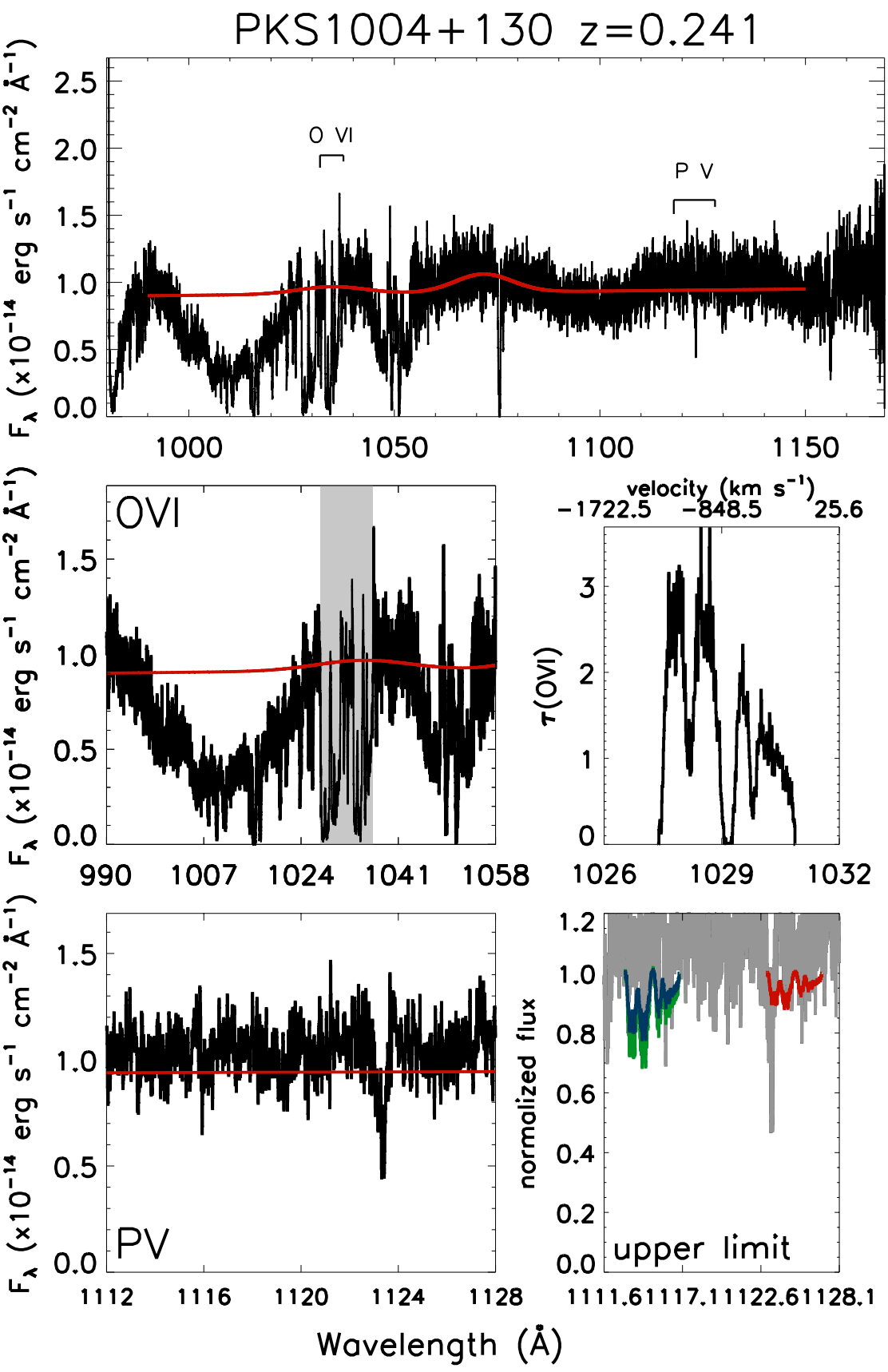
PKS1004+130 z=0.241
O VI
P V
OVI
PV
velocity (km s^{-1})
−1722.5 −848.5 25.6
τ(OVI)
normalized flux
upper limit
F_λ (x10^{-14} erg s^{-1} cm^{-2} Å^{-1})
Wavelength (Å)

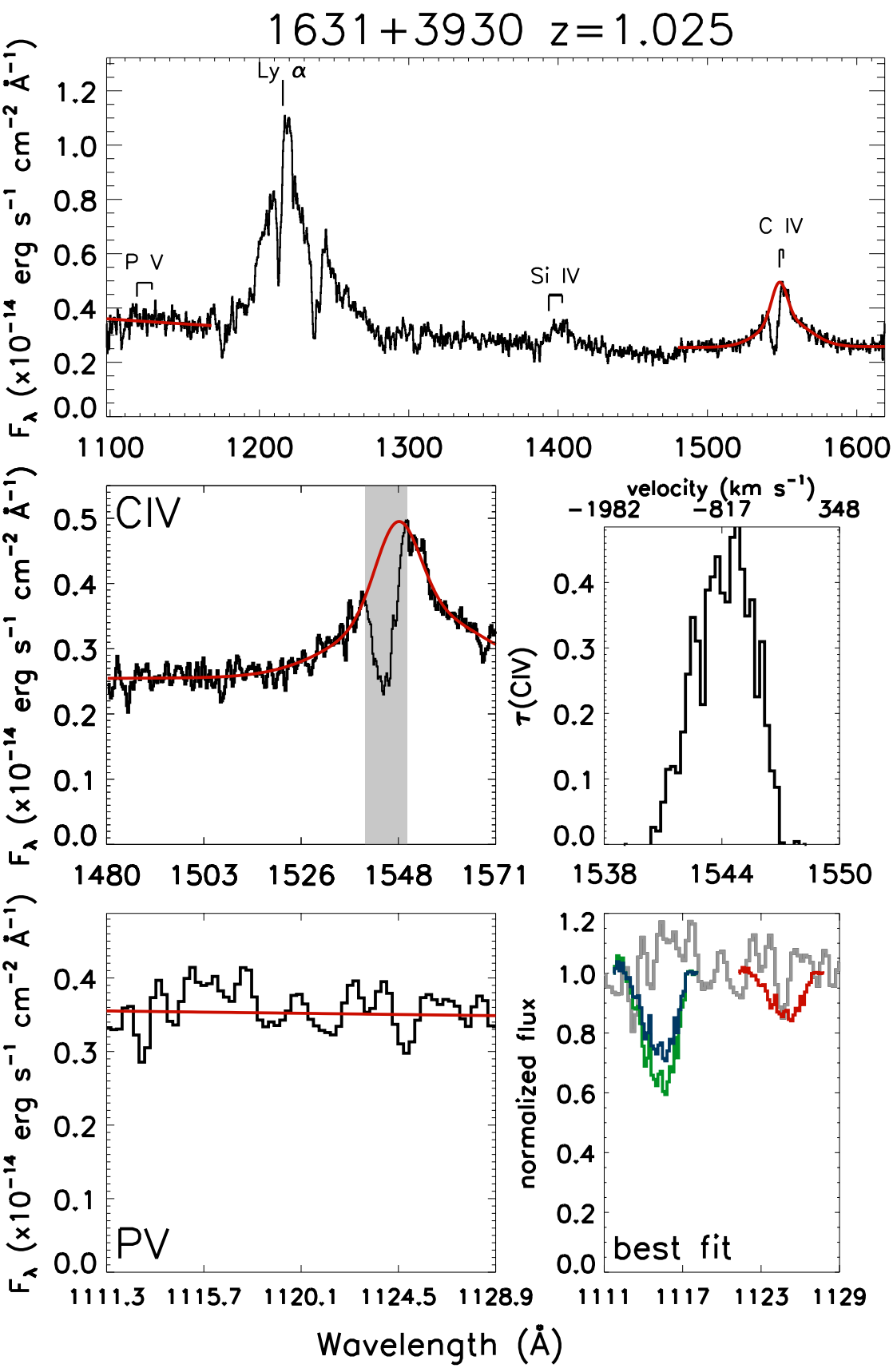
1631+3930 z=1.025
Ly α
P V
Si IV
C IV
CIV
PV
velocity (km s⁻¹)
−1982
−817
348
τ(CIV)
normalized flux
best fit
Wavelength (Å)

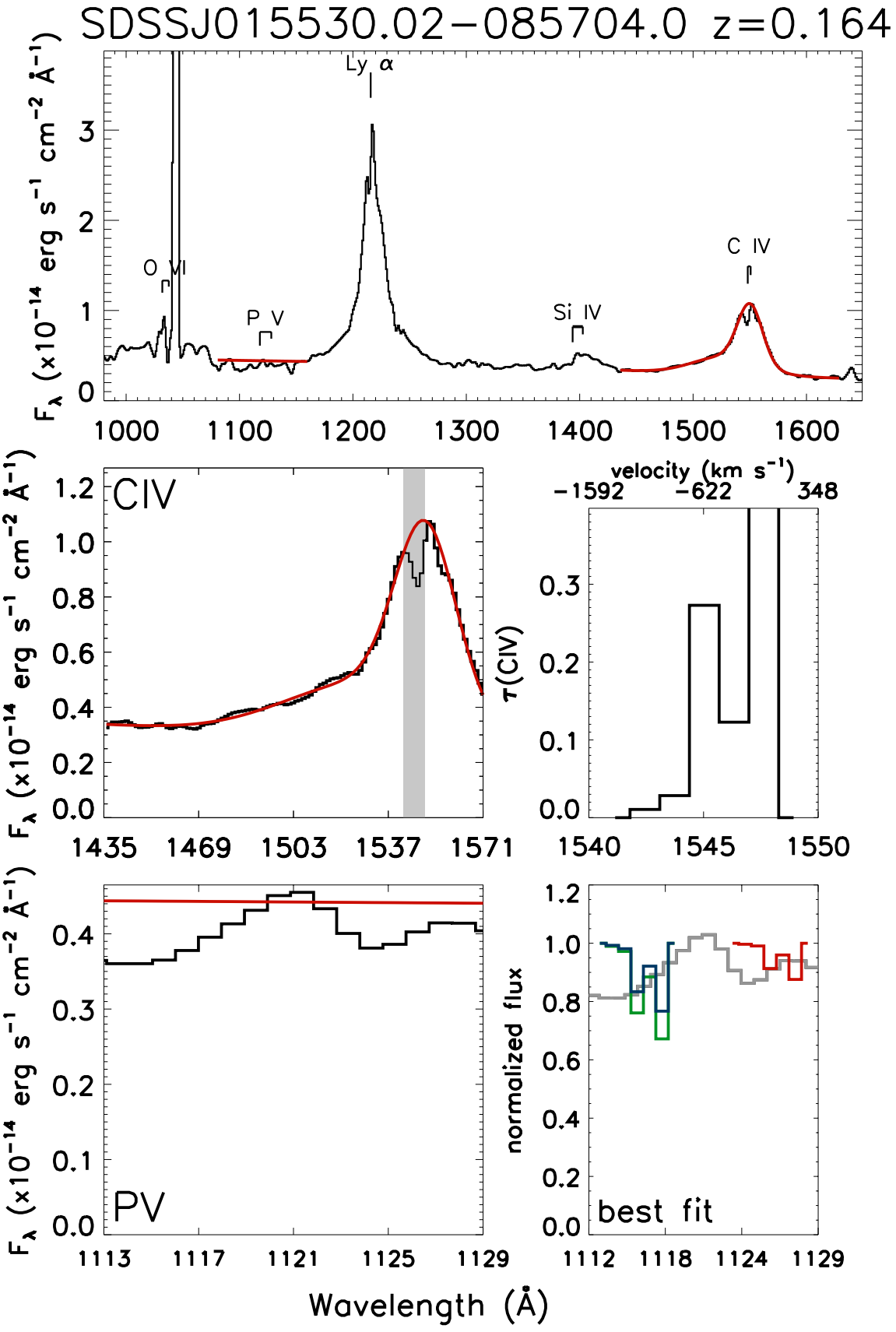
SDSSJ015530.02−085704.0 z=0.164
Ly α
O VI
P V
Si IV
C IV
F_λ (x10^-14 erg s^-1 cm^-2 Å^-1)
1000
1100
1200
1300
1400
1500
1600
CIV
PV
velocity (km s^-1)
−1592
−622
348
τ(CIV)
normalized flux
best fit
Wavelength (Å)

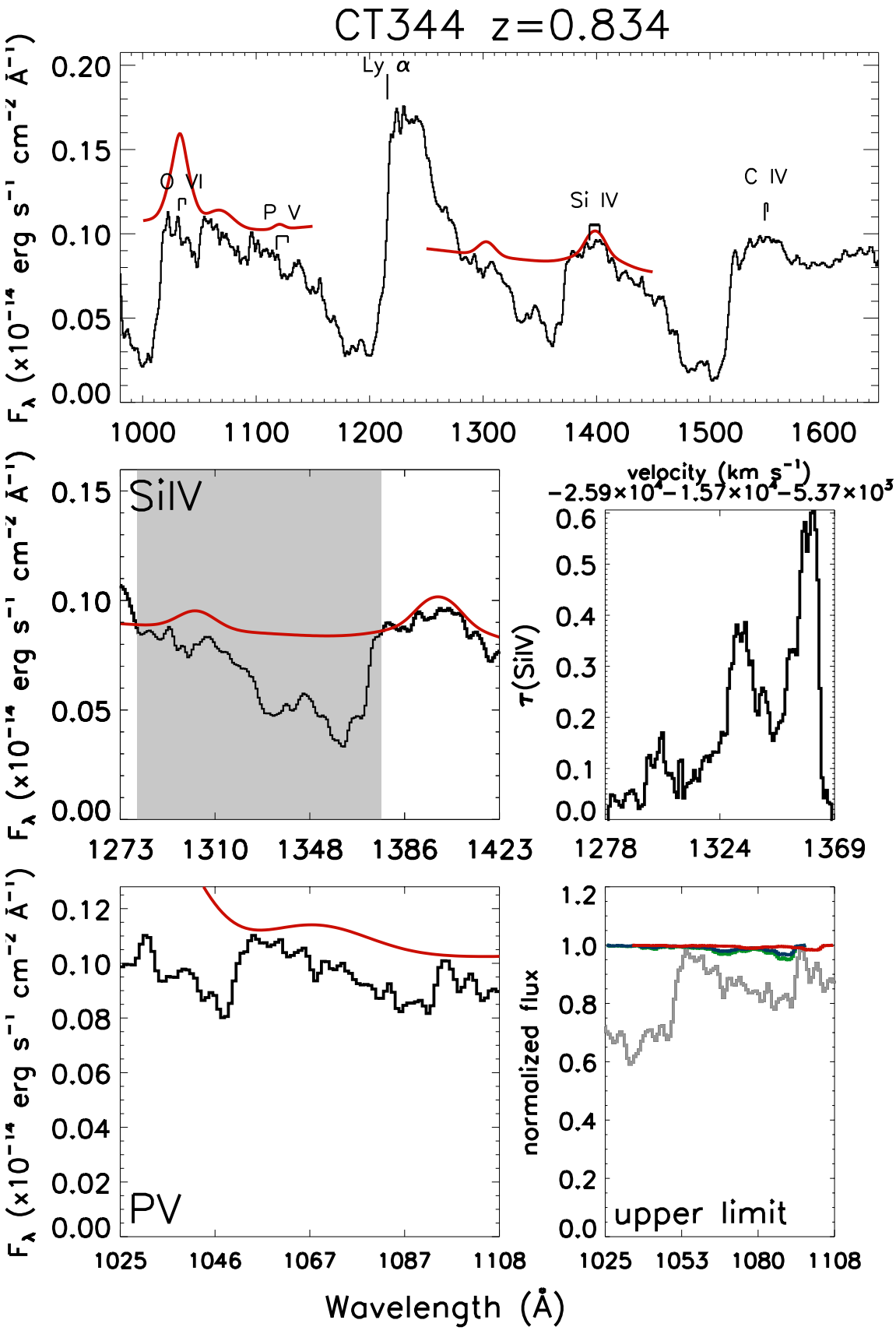
CT344 z=0.834
Ly α
O VI
P V
Si IV
C IV
SiIV
PV
velocity (km s⁻¹)
−2.59×10⁴ −1.57×10⁴ −5.37×10³
τ(SiIV)
normalized flux
upper limit
Wavelength (Å)

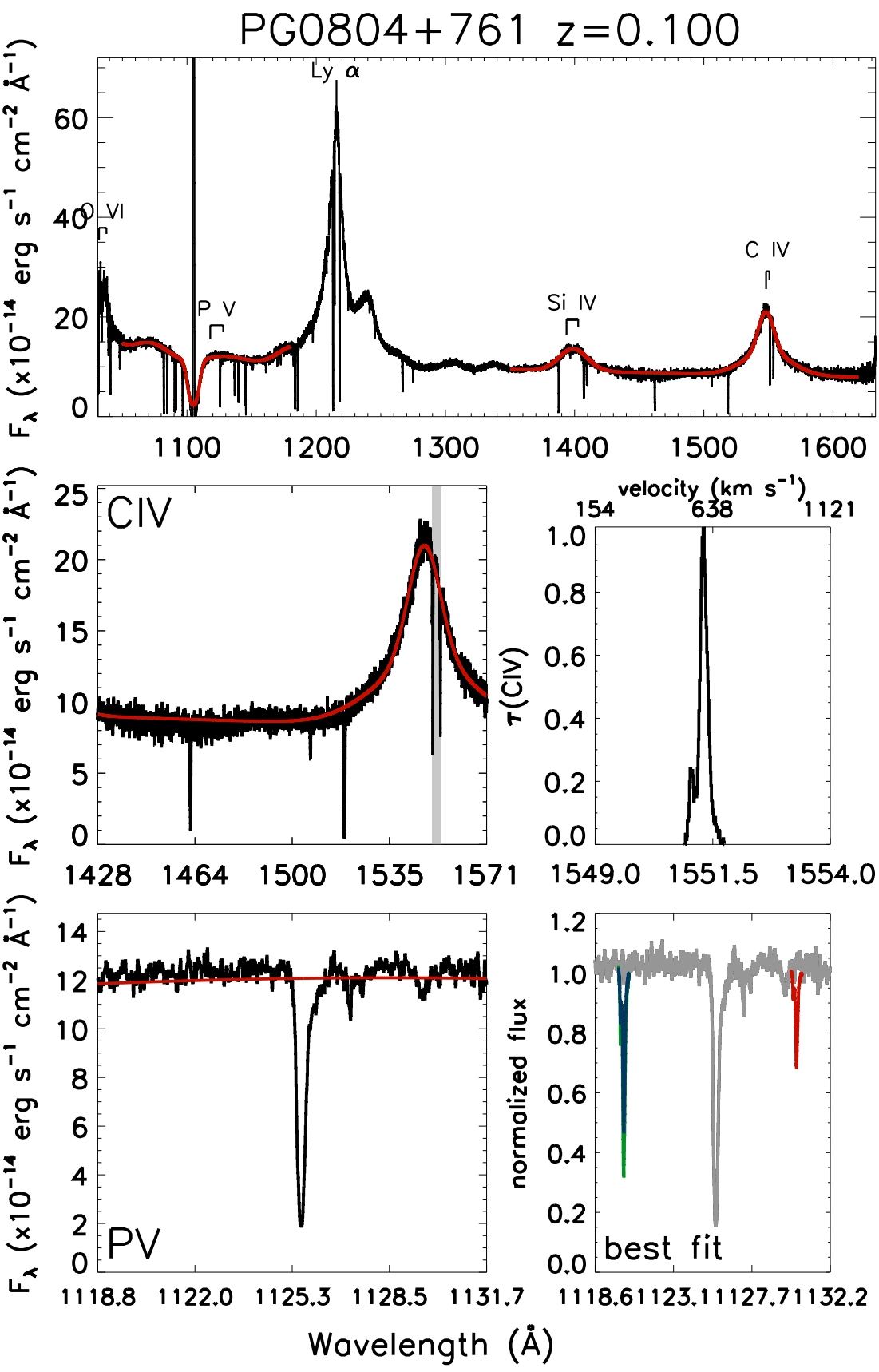
PG0804+761 z=0.100
Ly α
O VI
P V
Si IV
C IV
F_λ ($\times 10^{-14}$ erg s^{-1} cm^{-2} Å^{-1})
1100
1200
1300
1400
1500
1600
CIV
PV
velocity (km s^{-1})
154
638
1121
τ(CIV)
1549.0
1551.5
1554.0
1428
1464
1500
1535
1571
1118.8
1122.0
1125.3
1128.5
1131.7
normalized flux
best fit
1118.6
1123.1
1127.7
1132.2
Wavelength (Å)

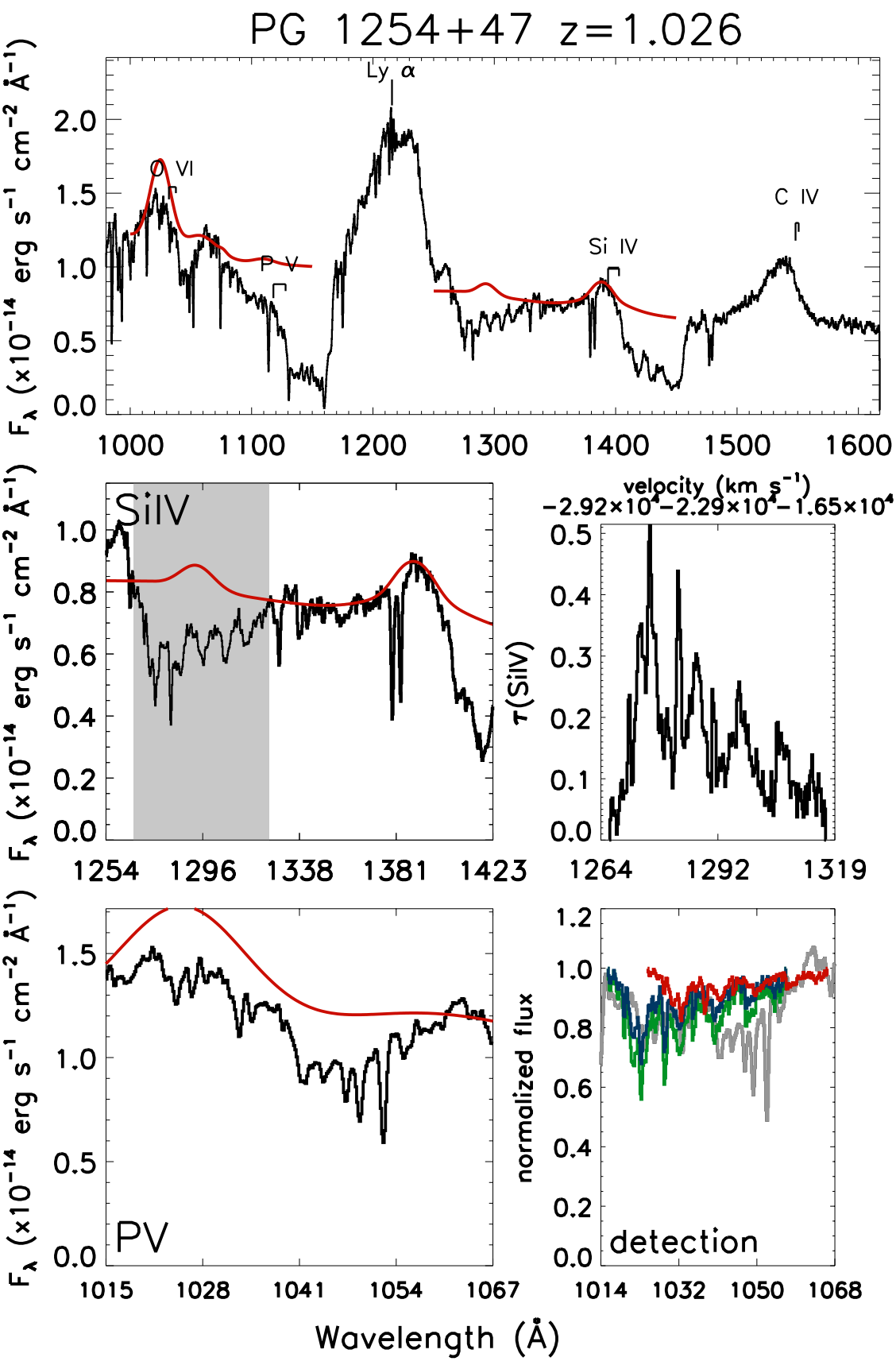
PG 1254+47 z=1.026
Ly α
O VI
P V
Si IV
C IV
SiIV
velocity (km s⁻¹)
−2.92×10⁴ −2.29×10⁴ −1.65×10⁴
τ(SiIV)
PV
detection
normalized flux
Wavelength (Å)

Appendix D

P v Project: Removed Targets

Over the course of developing and applying our method we had to remove some targets from our sample. In this appendix we explain our various reasons for doing so.

D.1 Slit-less Observations

Three of our initial targets were performed as slit-less observations in STIS. Without independent flux measurements we cannot calibrate these spectra and therefore removed them from our sample. These objects are: Kaz102, HE1113+641, and IR07546+3928.

D.2 No Apparent Absorption

After combining the observations of some targets, no apparent absorption was identified in their spectra. We removed these targets from our sample. These targets include: QSO B1435-0645 (STIS, COS), PG 1415+451 (FOS), PKS0252-549 (STIS), and FBQSJ1010+3003 (COS).

D.3 Narrow Lines with Un-Physical τ Ratios

Atomic physics tells us the ratio of optical depths for the blue to red lines of the resonance doublets for all our ions of interest should be 2:1. Partial covering can

reduce the apparent optical depth ratio to as low as 1:1. Anything outside of those ratios is unphysical and therefore the absorption is not due to the ion doublet of interest. We removed the following targets for this reason: SDSSJ122035.10+385316.4, SDSSJ110406.94+314111.4, and HE0226-4110.

D.4 Narrow Lines without Partial Covering

Some narrow absorption from O VI and C IV can be generated from intervening galaxies rather than the AGN itself. [REFERENCE] We required our subset of O VI and C IV targets narrower than $\sim 500(\mathrm{km\,s^{-1}})$ to exhibit partial covering so as not to be confused with potential absorption from intervening galaxies. This requirement of partial covering removes the following targets: SDSSJ122102.49+155447.0 (COS), SDSSJ152139.66+033729.2 (COS), and QSO B1617+1731 (COS).

D.5 O VI BAL blended with Lyα Damping Wings

Three of our initial targets have geocoronal Lyα damped absorption overlapping the O VI absorption. Because we cannot reliably deconvolve this absorption, we remove them from our sample. These three targets are: PG 0923+201 (COS, STIS), 2MASX-J01013113+4229356 (COS) and SDSSJ021218.32-073719.8 (COS).

D.6 Other

PDS456

Appendix E

WPVS007: ISM Line Measurements

We check each nod position (FPPOS and central wavelength) observation for deviations from known ISM lines by modeling them with a linear polynomial and an absorption gaussian in their immediate vicinity using CIAO Sherpa. We then compute a constant shift using the measured deviations and 1σ confidence interval error bars. The results are in Tables E.1, E.2, E.3, E.4 for the June 2010, June 2013, December 2013, and March 2015 data respectively. Lines in some spectra are unable to be measured for various reasons. A comment on why they may not be measurable is given in place of the measured data in the table.

The footnotes are as follows:

(a) Reference positions from Blades et al. [REFERENCE]

(b) Reference positions from the NIST Atomic Lines Database [REFERENCE]

(c) Measured line position from CIAO Sherpa

(d) 1σ confidence interval error bars, rounded to 1 significant digit

(e) Calculated wavelength separation, wavelength separation = measured - NIST, rounded to the same decimal place as the error

Table E.1: WPVS007 HST COS June 2010 ISM Line Measurements

	species	wavelength (Å)				wavelength separation[e] (Å)
		Blades[a]	NIST[b]	measured[c]	error[d]	
LB5A01XYQ SHIFT $= -0.6 \pm 0.1$						
FUV	Si II	1260.421	1260.422	off edge of detector		
	O I	1302.168	1302.168	off edge of detector		
	Si II	1304.370	1304.370	off edge of detector		
	C II	1334.532	1334.532	1335.34	0.01	0.81
	Si II	1526.720	1526.720	1527.47	0.03	0.75
	Fe II	1608.446	1608.446	within noise		
	Al II	1670.787	1670.7867	1671.32	0.1	0.5
LB5A01YFQ SHIFT $= -0.70 \pm 0.09$						
FUV	Si II	1260.421	1260.422	off edge of detector		
	O I	1302.168	1302.168	1303.03	0.03	0.86
	Si II	1304.370	1304.370	1305.16	0.03	0.79
	C II	1334.532	1334.532	1335.58	0.02	1.05
	Si II	1526.720	1526.720	1527.53	0.06	0.81
	Fe II	1608.446	1608.446	1609.06	0.2	0.6
	Al II	1670.787	1670.7867	1671.43	0.08	0.64
LB5A01YFQ SHIFT $= -0.7 \pm 0.1$						
FUV	Si II	1260.421	1260.422	off edge of detector		
	O I	1302.168	1302.168	1303.16	0.03	0.99
	Si II	1304.370	1304.370	1305.25	0.07	0.88
	C II	1334.532	1334.532	1335.64	0.03	1.11
	Si II	1526.720	1526.720	1527.47	0.05	0.75
	Fe II	1608.446	1608.446	within noise		
	Al II	1670.787	1670.7867	1671.44	0.1	0.7

Table E.2: WPVS007 HST COS June 2013 ISM Line Measurements

	species	wavelength (Å)				wavelength separation[e] (Å)
		Blades[a]	NIST[b]	measured[c]	error[d]	
LC2201MJQ SHIFT = 0.2 ± 0.1						
FUV	Si II	1260.421	1260.422	off edge of detector		
	O I	1302.168	1302.168	off edge of detector		
	Si II	1304.370	1304.370	off edge of detector		
	C II	1334.532	1334.532	1334.41	0.07	-0.12
	Si II	1526.720	1526.720	1526.32	0.2	-0.4
	Fe II	1608.446	1608.446	1608.48	0.4	0.0
	Al II	1670.787	1670.7867	1670.52	0.2	-0.3
LC2201MLQ SHIFT = $+0.26 \pm 0.09$						
FUV	Si II	1260.421	1260.422	off edge of detector		
	O I	1302.168	1302.168	1301.75	0.04	-0.42
	Si II	1304.370	1304.370	1303.94	0.07	-0.43
	C II	1334.532	1334.532	1334.53	0.06	-0.00
	Si II	1526.720	1526.720	1526.57	0.2	-0.2
	Fe II	1608.446	1608.446	within noise		
	Al II	1670.787	1670.7867	1670.52	0.6	-0.3
LC2201MNQ SHIFT = 0.06 ± 0.07 = NO SHIFT						
FUV	Si II	1260.421	1260.422	1260.56	0.06	0.14
	O I	1302.168	1302.168	1302.13	0.07	-0.04
	Si II	1304.370	1304.370	1304.09	0.2	-0.3
	C II	1334.532	1334.532	1334.68	0.05	0.15
	Si II	1526.720	1526.720	1526.63	0.09	-0.09
	Fe II	1608.446	1608.446	1608.36	0.4	-0.1
	Al II	1670.787	1670.7867	1670.52	0.1	-0.3
LC2201MPQ SHIFT = 0.00 ± 0.08 = NO SHIFT						
FUV	Si II	1260.421	1260.422	1260.56	0.05	0.14
	O I	1302.168	1302.168	1302.16	0.05	-0.01
	Si II	1304.370	1304.370	1304.57	0.07	0.20
	C II	1334.532	1334.532	1334.85	0.05	0.32
	Si II	1526.720	1526.720	1526.53	0.1	-0.2
	Fe II	1608.446	1608.446	1608.29	0.2	-0.2
	Al II	1670.787	1670.7867	1670.68	0.2	-0.1

Table E.3: WPVS007 HST COS December 2013 ISM Line Measurements

	species	wavelength (Å)				wavelength separation[e] (Å)
		Blades[a]	NIST[b]	measured[c]	error[d]	
LC2202T4Q SHIFT $= -0.35 \pm 0.03$						
FUV	Si II	1260.421	1260.422	off edge of detector		
	O I	1302.168	1302.168	off edge of detector		
	Si II	1304.370	1304.370	off edge of detector		
	C II	1334.532	1334.532	1334.93	0.06	0.40
	Si II	1526.720	1526.720	1527.0	0.1	0.3
	Fe II	1608.446	1608.446	within noise		
	Al II	1670.787	1670.7867	1671.14	0.09	0.35
LC2202T6Q SHIFT $= -0.5 \pm 0.2$						
FUV	Si II	1260.421	1260.422	off edge of detector		
	O I	1302.168	1302.168	1302.19	0.08	0.02
	Si II	1304.370	1304.370	1304.32	0.08	-0.05
	C II	1334.532	1334.532	1335.22	0.07	0.69
	Si II	1526.720	1526.720	1527.11	0.1	0.4
	Fe II	1608.446	1608.446			
	Al II	1670.787	1670.7867	1671.4	0.2	0.6
LC2202TIQ SHIFT $= -0.52 \pm 0.03$						
FUV	Si II	1260.421	1260.422	1260.98	0.09	0.56
	O I	1302.168	1302.168	1302.74	0.09	0.57
	Si II	1304.370	1304.370	1304.88	1	1
	C II	1334.532	1334.532	1335.16	0.07	0.63
	Si II	1526.720	1526.720	1527.25	0.09	0.53
	Fe II	1608.446	1608.446	1609.08	1	1
	Al II	1670.787	1670.7867	1671.21	0.2	0.4
LC2202TLQ SHIFT $= -0.65 \pm 0.05$						
FUV	Si II	1260.421	1260.422	1261.13	0.08	0.71
	O I	1302.168	1302.168	1302.85	0.07	0.68
	Si II	1304.370	1304.370	1304.88	0.08	0.51
	C II	1334.532	1334.532	1335.22	0.07	0.69
	Si II	1526.720	1526.720	1527.28	0.1	0.6
	Fe II	1608.446	1608.446	1608.87	0.2	0.4
	Al II	1670.787	1670.7867	1671.47	0.2	0.7

Table E.4: WPVS007 HST COS March 2015 ISM Line Measurements

	species	wavelength (Å)				wavelength separation[e] (Å)
		Blades[a]	NIST[b]	measured[c]	error[d]	
LCSY01EMQ SHIFT $= -0.27 \pm 0.09$						
FUV	Si II	1260.421	1260.422	1260.65	0.07	0.23
	O I	1302.168	1302.168	heavily blended with airglow		
	Si II	1304.370	1304.370	heavily blended with airglow		
	C II	1334.532	1334.532	1334.91	0.09	0.38
	Si II	1526.720	1526.720	1527.3	0.3	0.6
	Fe II	1608.446	1608.446	1608.7	0.2	0.3
	Al II	1670.787	1670.7867	1671.0	0.2	0.3
LCSY01EOQ SHIFT $= -0.4 \pm 0.1$						
FUV	Si II	1260.421	1260.422	1260.76	0.07	0.3
	O I	1302.168	1302.168	heavily blended with airglow		
	Si II	1304.370	1304.370	heavily blended with airglow		
	C II	1334.532	1334.532	1334.89	0.08	0.4
	Si II	1526.720	1526.720	1526.8	0.3	0.1
	Fe II	1608.446	1608.446	1609.12	0.6	0.7
	Al II	1670.787	1670.7867	1671.2	0.2	0.4
LCSY01EQQ SHIFT $= -0.33 \pm 0.07$						
FUV	Si II	1260.421	1260.422	1260.64	0.08	0.22
	O I	1302.168	1302.168	1302.3	0.2	0.1
	Si II	1304.370	1304.370	1304.5	0.2	0.1
	C II	1334.532	1334.532	1335.04	0.08	0.51
	Si II	1526.720	1526.720	1527.0	0.1	0.2
	Fe II	1608.446	1608.446	1608.7	0.3	0.3
	Al II	1670.787	1670.7867	1671.3	0.3	0.5
LCSY01ESQ SHIFT $= -0.28 \pm 0.08$						
FUV	Si II	1260.421	1260.422	1260.64	0.08	0.21
	O I	1302.168	1302.168	1302.82	0.06	0.65
	Si II	1304.370	1304.370	1304.66	0.06	0.29
	C II	1334.532	1334.532	1334.85	0.09	0.32
	Si II	1526.720	1526.720	1526.9	0.1	0.2
	Fe II	1608.446	1608.446		within noise	
	Al II	1670.787	1670.7867	1671.1	0.3	0.3

Appendix F

WPVS007: Modeling Normalized Flux

F.1 Singlet

For a singlet line, at each wavelength (λ), only one velocity contributes to the absorption. In the simplest case, the normalized intensity looks like:

$$\frac{I}{I_0}(\lambda) = e^{-\tau(v)}$$

In the case where the absorber only partially covers the source, we need to take the covering fraction into account. Traditionally this looks like:

$$\frac{I}{I_0}(\lambda) = (1 - C_f(v)) + C_f(v)e^{-\tau(v)}$$

The term $(1 - C_f(v))$ is the uncovered fraction at velocity, v. Photons not going through the absorber get through without being attenuated, so for the fractional area $(1 - C_f)$, $I = I_0$. Photons going through the absorber, of fractional area $C_f(v)$, are attenuated in the normal way, where $I = I_0 e^{-\tau}$. For a single line, there are no additional constraints on the shape of the covering fraction as a function of velocity, $C_f(v)$.

We can rewrite the above equation to think instead about the effect absorption

has on the normalized intensity:

$$\frac{I}{I_0}(\lambda) = 1 - C_f(v) * (1 - e^{-\tau(v)})$$

Now we can more easily see the reduction in normalized intensity caused by the absorber, where $C_f(v)$ is the fraction of the source covered by the absorber, and $(1 - e^{-\tau(v)})$ is the fraction of light that gets absorbed.

For the special case of full covering, $C_f(v) = 1$ and we recover the simplest case, $\frac{I}{I_0} = e^{-\tau}$. For the trivial case of no absorption, $C_f(v) = 0$ and we recover the fact that $I = I_0$.

F.2 Doublet

For a doublet line, with velocity separation Δv, two velocities contribute to the absorption at each wavelength, λ. At a given λ, atoms traveling with velocity v can absorb the shorter wavelength of the doublet (the blue line), and atoms traveling with velocity $v + \Delta v$ can absorb the longer wavelength of the doublet (the red line). Optical depth is related to the number of absorbers by:

$$\tau \sim f_{ij} * \lambda * N$$

where f_{ij} is the oscillator strength for absorption from lower level i to upper level j and λ is the wavelength of the line. So the optical depth profiles of the doublet lines are related by the ratio of their $f * \lambda$s:

$$\frac{\tau_b}{\tau_r} = \frac{f_{ij} * \lambda_b}{f_{ik} * \lambda_r}$$

if the blue line absorbs from level i to j and the red line from i to k. For the special case of the UV resonance lines this ratio is ~ 2 (see TABLE F.1).

λ(Å)	f_{ij}	τ_b/τ_r
O VI		
1031.912	0.133	2.0040795849
1037.613	0.0660	
P V		
1117.98	0.450	2.0180936909
1128.01	0.221	
N V		
1238.821	0.156	1.9935903006
1242.804	0.0780	
Si IV		
1393.76	0.513	1.9988431293
1402.77	0.255	
C IV		
1548.202	0.190	1.9924882346
1550.774	0.0952	

Table F.1: Resonance Line Data

So if the blue line optical depth is $\tau(v)$, then at the same wavelength, λ the red line optical depth is $\frac{1}{2}\tau(v + \Delta v)$.

F.2.1 Full Covering, $C_f(v) = 1$

Let's explore the case of full covering. For the case where the blue line absorbs first, at the point where the blue line is absorbed,

$$I = I_0 e^{-\tau(v)}$$

Moving to the point where the red line is absorbed, the incident intensity on the red line gas is the resultant intensity from the blue line gas. So the final intensity is:

$$I = (I_0 e^{-\tau(v)}) e^{-\frac{1}{2}\tau(v+\Delta v)}$$

which reduces to

$$I = I_0 e^{-(\tau(v)+\frac{1}{2}\tau(v+\Delta v))}$$

and shows that τ is commutative. Let's check: For the case where the red line absorbs first, at the point where the blue line is absorbed,

$$I = I_0 e^{-(\frac{1}{2}\tau(v+\Delta v))}.$$

Moving to the point where the blue line is absorbed, the incident intensity on the blue line gas is the resultant intensity from the red line gas. So the final intensity is:

$$I = (I_0 e^{-\frac{1}{2}\tau(v+\Delta(v))}) e^{-\tau(v)}$$

which reduces to

$$I = I_0 e^{-(\frac{1}{2}\tau(v+\Delta v)+\tau(v))}$$

which is indeed commutative.

F.2.2 Constant Partial Covering, $C_f(v) = constant$

Now we'll take a look at partial covering, but start simple with a covering fraction constant in velocity. For simplicity, we assume maximal overlap in the gas geometry. If the blue line absorbing gas absorbs first:

```
[source] -------> {blue} -------> {red}
```

From the source, before we have any absorption, $I/I_0 = 1$. From above, we know the effect the blue line absorbing gas cloud has is

$$-C_f(1 - e^{-\tau(v)})$$

By assuming maximal overlap and a constant covering fraction, the red line absorbing gas fully covers the blue line absorbing region. The incident intensity into the red line absorbing gas is $I_0 e^{-\tau(v)}$, so the contribution to the normalized intensity from the red line absorbing gas is

$$-C_f e^{-\tau(v)}(1 - e^{-\frac{1}{2}\tau(v+\Delta v)})$$

Putting it together, the final emerging normalized intensity is

$$\frac{I}{I_0} = 1 - C_f(1 - e^{-\tau(v)}) - C_f e^{-\tau(v)}(1 - e^{-\frac{1}{2}\tau(v+\Delta v)})$$

$$\frac{I}{I_0} = 1 - C_f + C_f e^{-\tau(v)} - C_f e^{-\tau(v)} + C_f e^{-(\tau(v)+\frac{1}{2}\tau(v+\Delta v))}$$

$$\frac{I}{I_0} = (1 - C_f) + C_f e^{-(\tau(v)+\frac{1}{2}\tau(v+\Delta v))}$$

The normalized intensity for a doublet with a constant covering fraction looks just like partial covering for a singlet, but with the optical depth profile for the full covering of a doublet. Again, the optical depths commute, but for completeness, let's check. If the red line absorbing gas absorbs first:

```
[source] -------> {red} -------> {blue}
```

From the source, before we have any absorption, $I/I_0 = 1$. From above, we know the effect the red line absorbing gas cloud has is

$$-C_f(1 - e^{-\frac{1}{2}\tau(v+\Delta v)})$$

By assuming maximal overlap and a constant covering fraction, the red line absorbing gas fully covers the blue line absorbing region. The incident intensity into the blue line absorbing gas is $I_0 e^{-\frac{1}{2}\tau(v+\Delta v)}$, so the contribution to the normalized intensity from the red line absorbing gas is

$$-C_f e^{-\frac{1}{2}\tau(v+\Delta v)}(1 - e^{-\tau(v)})$$

Putting it together, the final emerging normalized intensity is

$$\frac{I}{I_0} = 1 - C_f(1 - e^{-\frac{1}{2}\tau(v+\Delta v)}) - C_f e^{-\frac{1}{2}\tau(v+\Delta v)}(1 - e^{-\tau(v)})$$

$$\frac{I}{I_0} = 1 - C_f + C_f e^{-\frac{1}{2}\tau(v+\Delta v)} - C_f e^{-\frac{1}{2}\tau(v+\Delta v)} + C_f e^{-(\frac{1}{2}\tau(v+\Delta v)+\tau(v))}$$

$$\frac{I}{I_0} = (1 - C_f) + C_f e^{-(\frac{1}{2}\tau(v+\Delta v)+\tau(v))}$$

So indeed the optical depth is commutative.

F.2.3 Non-Constant Partial Covering

Let's now consider each line of the doublet having its own covering fraction. Each wavelength, λ, ties the optical depth profiles at two velocities, v and $v + \Delta v$. So if we start by making the simple consideration that either $C_f(v) > C_f(v + \Delta v)$ or $C_f(v) < C_f(v + \Delta v)$, then C_f has to be either a monotonically decreasing or monotonically increasing function of velocity, respectively.

Monotonically Decreasing Covering Fraction: $C_f(v) > C_f(v + \Delta v)$

Again assuming maximum overlap of the absorbing gas regions, starting with the case where the blue line gas absorbs first and has the larger covering fraction:

```
[source] -------> {BLUE} -------> {red}
```

From the source, before we have any absorption, $I/I_0 = 1$. From above, we know the effect the blue line absorbing gas cloud has is

$$-C_f(v)(1 - e^{-\tau(v)})$$

If the red line absorbing gas has a smaller covering fraction and completely overlaps the blue line absorbing gas, then it fully covers the blue line absorbing gas. The incident intensity into the red line absorbing gas is $I_0 e^{-\tau(v)}$. So the effect of the red line absorbing gas on the normalized intensity is

$$-C_f(v+\Delta v)e^{-\tau(v)}(1-e^{-\frac{1}{2}\tau(v+\Delta v)})$$

Putting it together, the final emerging normalized intensity is:

$$\frac{I}{I_0} = 1 - C_f(v)(1-e^{-\tau(v)}) - C_f(v+\Delta v)e^{-\tau(v)}(1-e^{-\frac{1}{2}\tau(v+\Delta v)})$$

$$\frac{I}{I_0} = 1 - C_f(v) + C_f(v)e^{-\tau(v)} - C_f(v+\Delta v)e^{-\tau(v)} + C_f(v+\Delta v)e^{-(\tau(v)+\frac{1}{2}\tau(v+\Delta v))}$$

$$\frac{I}{I_0} = (1 - C_f(v)) + (C_f(v) - C_f(v+\Delta v))e^{-\tau(v)} + C_f(v+\Delta v)e^{-(\tau(v)+\frac{1}{2}\tau(v+\Delta v))}$$

where $(1-C_f(v))$ is the uncovered fraction, $(C_f(v)-C_f(v+\Delta v))e^{-\tau(v)}$ is the fraction covered by the blue line absorbing region and NOT the red line absorbing region, and

$$C_f(v+\Delta v)e^{-(\tau(v)+\frac{1}{2}\tau(v+\Delta v))}$$

is the fraction covered by BOTH the blue and red line absorbing regions. We know that absorption is commutative (that it does not matter whether the blue line absorbing region or the red line absorbing region absorbs first), so let's check. Now the red line absorbing region absorbs first but still has the smaller covering fraction:

```
[source] -------> {red} -------> {BLUE}
```

From the source, before we have any absorption, $I/I_0 = 1$. From above, we know the effect the red line absorbing gas cloud has is

$$-C_f(v+\Delta v)(1-e^{-\frac{1}{2}\tau(v+\Delta v)})$$

Considering maximal overlap and that the blue line absorbing gas has a larger covering fraction, the blue line absorbing gas fully covers the red line absorbing region. The incident intensity into the blue line absorbing gas that covers the red line absorbing gas is $I_0 e^{-\frac{1}{2}\tau(v+\Delta v)}$. The contribution to the normalized intensity from the blue line absorbing gas has two parts, the fraction that covers the red line absorbing gas:

$$-C_f(v+\Delta v)e^{-\frac{1}{2}\tau(v+\Delta v)}(1-e^{-\tau(v)})$$

and the fraction that does not:

$$-(C_f(v)-C_f(v+\Delta v))e^{-(\tau(v)+\frac{1}{2}\tau(v+\Delta v))}$$

Putting it together, the final emerging normalized intensity is

$$\begin{aligned}\frac{I}{I_0} = 1 - C_f(v+\Delta v)(1-e^{-\frac{1}{2}\tau(v+\Delta v)}) - C_f(v+\Delta v)e^{-\frac{1}{2}\tau(v+\Delta v)}(1-e^{-\tau(v)}) \\ - (C_f(v)-C_f(v+\Delta v))(1-e^{-\tau(v)})\end{aligned}$$

$$\frac{I}{I_0} = 1 - C_f(v+\Delta v) + C_f(v+\Delta v)e^{-\frac{1}{2}\tau(v+\Delta v)} - C_f(v+\Delta v)e^{-\frac{1}{2}\tau(v+\Delta v)}$$
$$+ C_f(v+\Delta v)e^{-(\frac{1}{2}\tau(v+\Delta v)+\tau(v))} - C_f(v) + C_f(v+\Delta v)$$
$$+ C_f(v)e^{-\tau(v)} - C_f(v+\Delta v)e^{-\tau(v)}$$

$$\frac{I}{I_0} = (1 - C_f(v)) + (C_f(v) - C_f(v+\Delta v))e^{-\tau(v)} + C_f(v+\Delta v)e^{-(\frac{1}{2}\tau(v+\Delta v)+\tau(v))}$$

So indeed the optical depth is commutative.

Monotonically Increasing Covering Fraction: $C_f(v) < C_f(v+\Delta v)$

Again assuming maximum overlap of the absorbing gas regions, but starting with the case where the red line gas absorbs first and has the larger covering fraction:

```
[source] -------> {RED} -------> {blue}
```

From the source, before we have any absorption, $I/I_0 = 1$. From above, we know the effect the red line absorbing gas cloud has is

$$-C_f(v+\Delta v)(1 - e^{-\frac{1}{2}\tau(v+\Delta v)})$$

If the blue line absorbing gas has a smaller covering fraction and completely overlaps the red line absorbing gas, then it fully covers the red line absorbing gas. The incident intensity into the red line absorbing gas is $I_0 e^{-\frac{1}{2}\tau(v+\Delta v)}$. So the effect of the blue line absorbing gas on the normalized intensity is

$$-C_f(v+\Delta v)e^{-\frac{1}{2}\tau(v+\Delta v)}(1 - e^{-\tau(v)})$$

Putting it together, the final emerging normalized intensity is:

$$\frac{I}{I_0} = 1 - C_f(v+\Delta v)(1 - e^{-\frac{1}{2}\tau(v+\Delta v)}) - C_f(v)e^{-\frac{1}{2}\tau(v+\Delta v)}(1 - e^{-\tau(v)})$$

$$\frac{I}{I_0} = 1 - C_f(v+\Delta v) + C_f(v+\Delta v)e^{-\frac{1}{2}\tau(v+\Delta v)} - C_f(v)e^{-\frac{1}{2}\tau(v+\Delta v)} + C_f(v)e^{-(\frac{1}{2}\tau(v+\Delta v)+\tau(v))}$$

$$\frac{I}{I_0} = (1 - C_f(v)) + (C_f(v) - C_f(v+\Delta v))e^{-\tau(v)} + C_f(v+\Delta v)e^{-(\tau(v)+\frac{1}{2}\tau(v+\Delta v))}$$

where $(1-C_f(v))$ is the uncovered fraction, $(C_f(v)-C_f(v+\Delta v))e^{-\tau(v)}$ is the fraction covered by the blue line absorbing region and NOT the red line absorbing region, and

$$C_f(v+\Delta v)e^{-(\tau(v)+\frac{1}{2}\tau(v+\Delta v))}$$

is the fraction covered by BOTH the blue and red line absorbing regions. We know that absorption is commutative (that it does not matter whether the blue line absorbing region or the red line absorbing region absorbs first), so let's check. Now the red line absorbing region absorbs first but still has the smaller covering fraction:

```
[source] -------> {red} -------> {BLUE}
```

From the source, before we have any absorption, $I/I_0 = 1$. From above, we know the effect the red line absorbing gas cloud has is

$$-C_f(v+\Delta v)(1 - e^{-\frac{1}{2}\tau(v+\Delta v)})$$

Considering maximal overlap and that the blue line absorbing gas has a larger covering fraction, the blue line absorbing gas fully covers the red line absorbing region. The incident intensity into the blue line absorbing gas that covers the red line absorbing gas is $I_0 e^{-\frac{1}{2}\tau(v+\Delta v)}$. The contribution to the normalized intensity from the blue line absorbing gas has two parts, the fraction that covers the red line absorbing gas:

$$-C_f(v+\Delta v)e^{-\frac{1}{2}\tau(v+\Delta v)}(1-e^{-\tau(v)})$$

and the fraction that does not:

$$-(C_f(v)-C_f(v+\Delta v))e^{-(\tau(v)+\frac{1}{2}\tau(v+\Delta v))}$$

Putting it together, the final emerging normalized intensity is

$$\frac{I}{I_0} = 1 - C_f(v+\Delta v)(1-e^{-\frac{1}{2}\tau(v+\Delta v)}) - C_f(v+\Delta v)e^{-\frac{1}{2}\tau(v+\Delta v)}(1-e^{-\tau(v)}) - (C_f(v)-C_f(v+\Delta v))(1-e^{-\tau(v)})$$

$$\frac{I}{I_0} = 1 - C_f(v+\Delta v) + C_f(v+\Delta v)e^{-\frac{1}{2}\tau(v+\Delta v)} - C_f(v+\Delta v)e^{-\frac{1}{2}\tau(v+\Delta v)} + C_f(v+\Delta v)e^{-(\frac{1}{2}\tau(v+\Delta v)+\tau(v))} - C_f(v) + C_f(v+\Delta v) + C_f(v)e^{-\tau(v)} - C_f(v+\Delta v)e^{-\tau(v)}$$

$$\frac{I}{I_0} = (1-C_f(v)) + (C_f(v)-C_f(v+\Delta v))e^{-\tau(v)} + C_f(v+\Delta v)e^{-(\frac{1}{2}\tau(v+\Delta v)+\tau(v))}$$

So indeed the optical depth is commutative.

Appendix G

Measures of Balnicity

G.1 Balnicity Index

Weymann et al. (1991) defined the balnicity index, BI, to quantitatively describe the BAL-ness of quasar broad absorption lines. It is defined in the following way:

$$\mathrm{BI} = -\int_{25{,}000}^{3{,}000} \Big[1 - \frac{\mathrm{f(v)}}{0.9}\Big] \mathrm{C(v)dv} \tag{G.1}$$

$f(v)$ is the normalized flux as a function of velocity displacement from the line center. C(v) is a step function that only becomes 1 when the quantity $[1 - \frac{\mathrm{f(v)}}{0.9}]$ has been > 0 over a consecutive span of $2,000\,(\mathrm{km\,s^{-1}})$. The first $2,000\,(\mathrm{km\,s^{-1}})$ do not contribute to the index. The $3,000\,(\mathrm{km\,s^{-1}})$ lower velocity limit ensures the emission line does not interfere with the BAL trough. Because this quantity was defined with C IV BALs in mind, the $25,000\,(\mathrm{km\,s^{-1}})$ upper limit ensures that the Si IV $\lambda\lambda 1393, 1402$ emission line doublet does not interfere with the higher velocity end of the C IV BAL.

G.2 Absorption Index

Hall et al. (2002) defined an absorption index, AI, to relax some of the restrictions Weymann et al. (1991) imposed on the balnicity index. The lower limit on the velocity is extended back to zero, the emission line center. The requirement on the

step function, C(v) is relaxed to require only a continuous 450 ($\mathrm{km\,s^{-1}}$) produce a positive value for $[1 - \frac{\mathrm{f(v)}}{0.9}]$. The first 450 ($\mathrm{km\,s^{-1}}$) do not contribute to the index. The definition looks like

$$\mathrm{AI} = \int_{0}^{25{,}000} \Big[1 - \frac{\mathrm{f(v)}}{0.9}\Big] \mathrm{C(v)dv} \tag{G.2}$$

G.3 Detection Index

Pâris et al. (2012) defined a detection index, DI, to relax to include the contribution of the first 2,000 ($\mathrm{km\,s^{-1}}$). It otherwise retains the same definition as Weymann et al. (1991):

$$\mathrm{DI} = -\int_{25{,}000}^{3{,}000} \Big[1 - \frac{\mathrm{f(v)}}{0.9}\Big] \mathrm{C(v)dv} \tag{G.3}$$

but now the step function, C(v), is equal to 1 wherever $[1 - \frac{\mathrm{f(v)}}{0.9}] > 0$ for a minimum width of 2,000 ($\mathrm{km\,s^{-1}}$), not just the velocities beyond the first 2,000 ($\mathrm{km\,s^{-1}}$).